Understanding aspects of cardiovascular physiology and disease via a multi-physics modelling methodology

by

Alberto Coccarelli

A thesis submitted in partial fulfillment

of the requirement for the degree of Doctor of Philosophy

School of Medicine, Cardiff University, UK

2018

Declaration

This work has not been submitted in substance for any other degree or award at this or any other university or place of learning, nor is being submitted concurrently in candidature for any degree or other award.

Signed ..... (candidate) Date .....

Statement 1

This thesis is being submitted in partial fulfillment of the requirements for the degree of PhD.

Signed ..... (candidate) Date .....

Statement 2

This thesis is the result of my own independent work/investigation, except where otherwise stated, and the thesis has not been edited by a third party beyond what is permitted by Cardiff University's Policy on the Use of Third Party Editors by Research Degree Students. Other sources are acknowledged by explicit references. The views expressed are my own.

Signed ..... (candidate) Date .....

Statement 3

I hereby give consent for my thesis, if accepted, to be available online in the University's Open Access repository and for inter-library loan, and for the title and summary to be made available to outside organisations.

Signed ..... (candidate) Date .....

To my family,
for their love and encouragement.

Acknowledgements

Firstly, my greatest thanks go to my principal supervisors Dr. Dimitris Parthimos and Prof. Perumal Nithiarasu, for their guidance, enthusiasm, patience and the inestimable value they gave to my research. I feel extremely fortunate for having them as mentors, and their contribution has been fundamental for my professional growth. My gratitude goes also to my other supervisor Dr. Davids Hughes Edwards, for his continuous support during 'tough times' and for sharing his profound knowledge and passion on experimental vascular medicine. I want also to thank you Dr. Chennakesava Kadapa and Dr. Ankush Aggarwal for the friendly and instructive chats we had on finite elements programming, FSI and continuum mechanics. I cannot forget my office-mate Dr. Rhiannon Roberts, with whom I had lovely time during lunch breaks. She has been a kind of living British dictionary, teaching me several colloquial expressions and helping me out with all the bureaucratic stuff. Many thanks go also to my Swansea colleagues and friends Mr. Hayder Hasan, Mr. Osama Ibrahim, Dr. Simona Di Fraia and Dr. Etienne Boileau, for sharing the same lifestyle at the Bay Campus.

I feel double lucky because outside the academic environment I met and built profound friendships with a very large number of fabulous people. I start from my former Cardiff friends Mike G., Dave, Elin, Vito and Mike B., which have been my rocks during these 4 years. A special thanks goes to my awesome flatmates and close friends Manuel, Chloe, Alessandra and Nicolo', for having done so many activities together and ran some memorable house-parties. In the last couple of years, the weekends would have not been the same without Fabio and Silvia, which I thank so much for the enthusiasm and for having such a

big southern-Italian heart. Another massive thank you to my brilliant friends Federico, Paulo, Jakub, Marcin, Alessandra and Carlotta, for having shared several nights out and funny time. I am also grateful to each member of Biohazard football team for those glorious moments during the Sunday league, and to all friends from Cardiff school of pharmacy, which have always been very welcoming.

This last paragraph is obviously dedicated to the special people I had before starting such a great experience in Wales. I just want to say thank you to all my old best Italian friends Checco, Krasty, Randalf, Sora, Gigi, Miki and Luca, for maintaining our friendships unaltered despite the distance between us. All this would have not been possible without the support provided by my parents, Grazia and Fernando, my brother Alessandro and my grandparents Luigi and Lidia, and the rest of my family. Finally, I want to express my infinite gratitude to my wonderful girlfriend Antea, for having been so patient and for always believing in me. I will never be able to thank you enough.

Abstract

The overall aim of this study is to develop and analyse the performance of a multiscale framework involving arterial wall dynamics and blood flow in realistic vascular architectures that can facilitate the understanding of the onset and progression of vascular disease. This comprehensive modelling framework will also allow the virtual testing and ultimately inform the design of novel pharmacological probes. To achieve this aim, we need to deliver an arterial model able to account for i) the wall contractility triggered by biochemical processes at the cellular level ii) the interaction between the flow and vessel deformation, and iii) the transport phenomena along the arterial systemic circulation. For each problem component, a solution procedure has been proposed and validated against benchmark theoretical results and experimental measurements. First we characterised the structural behaviour of the arterial media layer and its response to the active contractile activity modulated by the smooth muscle Ca^{2+} dynamics. In this study, we modelled the activation, modulation and inhibition of the smooth muscle contraction by pharmacological interventions. Subsequently we have focused on the fluid structure interaction between wall mechanics and hemodynamics. This work required coupling a traditional incompressible arterial fluid model to a solid boundary, which represents the elastic arterial wall. The methodology proposed has been validated against a set of classical benchmark cases and exhibits improved numerical efficiency and significant memory savings. The third component of the work focuses on modelling transport and diffusion phenomena along the arterial branching network and within surrounding tissues. For the purpose of this study, a network of vessels was embedded within a solid tissue model of the human body. This model was able to predict how a property (in this application energy,

but equivalently drug concentrations) is transported and diffused from the blood vessels to the tissues.

Refereed Journal Publications

Part of the work done during my doctoral studies has been published in peer-reviewed journals. These are listed below.

1. **Coccarelli, A.,** Hasan, H.M., Carson, J., Parthimos, D., Nithiarasu, P. Modelling ageing effects on human arterial flow and heat transfer: a review. *International Journal for Numerical Methods in Biomedical Engineering*. In press.

2. **Coccarelli, A.**, Edwards, D.H., Aggarwal, A., Nithiarasu, P., Parthimos, D. (2018). A multiscale active structural model of the arterial wall accounting for smooth muscle dynamics, *Journal of The Royal Society Interface.* *http://dx.doi.org/10.1098/rsif.2017.0732.*

3. Hasan, H.M., **Coccarelli, A.**, Nithiarasu, P. (2018). Novel semi-implicit, locally conservative Galerkin (SILCG) methods: Application to blood flow in a systemic circulation. *Computer Methods in Applied Mechanics and Engineering* 332, 217-233.

4. **Coccarelli, A.**, Boileau, E., Parthimos, D., Nithiarasu, P. (2017). Modeling Accidental Hypothermia Effects on a Human Body under different Pathophysiological Conditions. *Medical & Biological Engineering & Computing* 55(12), 2155-2167.

5. **Coccarelli, A.**, Boileau, E., Parthimos, D., Nithiarasu, P. (2016). An advanced computational bioheat transfer model for a human body with an embedded systemic circulation. *Biomechanics and Modeling in Mechanobiology* 15(5), 1173-1190.

6. **Coccarelli, A.**, Nithiarasu, P. (2015). A Robust Finite Element Modeling Approach to Conjugate Heat Transfer in Flexible Elastic Tubes and Tube Networks. *Numerical heat transfer part A-Applications* 67, 513-530.

It is important to state that chapters 3 and 5 are, respectively, extended versions of the journal papers 2 and 5. Although these publications have other co-authors, their contribution was no greater than it would otherwise have been for a regular thesis chapter.

List of Figures

List of Tables

Contents

List of Acronyms

AC Artificial Compressibility

ALE Arbitrary Lagrangian Eulerian

AV Aortic Valve

AVA Arterio-Venous Anastomoses

CB Cross-Bridge

CBS Charatcteristic Based Split

CICR Ca^{2+} Induced-Ca^{2+} Release

CIVD Cold Induced Vasodilation

CPA Cyclopiazonic Acid

CU Contractile Unit

FE Finite Element

FSI Fluid-Structure Interaction

HIVC Heat Induced Vasoconstriction

HR Heart Rate

L-NAME NG-Nitro-L-Arginine Methyl Ester

LCG Locally Conservative Taylor Galerkin

LV Left Ventricle

MQ Multi Quadratic Biharmonic

MVQN Multi Vector Quasi-Newton

NCX Na^{+}-Ca^{2+} Exchange

NO Nitric Oxide

NR Newton-Raphson

NSCC Non-Specific Cation Channel

Phe Phenylephrine

RBF Radial Basis Function

Rya Ryanodine

RyR Ryanodine Receptor

SERCA Sarco/Endoplasmic Reticulum Ca^{2+}-ATPase

SMC Smooth Muscle Cell

SOCC Store-Operated Ca^{2+} Channel

SR Sarcoplasmic Reticulum

VOCC Voltage Operated Ca^{2+} Channel

Nomenclature

Latin letters

A	Vessel cross-sectional area
A_0	Vessel stress free cross-sectional area
A_{ext}	External surface area
A_{in}	Internal surface area
A_S	SOCC parameter
$\mathbf{a}$	Current fibre direction
$\mathbf{a}_0$	Reference fibre direction
$\mathbf{B}$	Deformation matrix
B_{SR}	SR uptake rate
$\mathbf{b}$	Left Cauchy deformation tensor
$\mathbf{C}$	Right Cauchy deformation tensor
$\mathbf{C}_F$	Convection matrix
$\mathbf{C}_{F,stab}$	Convection stabilization matrix
C_{Ry}	RyR CICR rate
$\mathbf{c}$	Relative fluid velocity
c_F	Specific heat at constant pressure of fluid
c_{max}	Maximum intrinsic wave speed
c_{p1},c_{p2}	Wall material parameters
c_s	Intrinsic wave speed
c_t	Specific heat at constant pressure of wall

D	Characteristic length
$\mathbf{D}_{eT}$	Element matrix for temperature diffusion in fluid
D_{EX}	Ca^{2+} extrusion by ATPase pump rate
$\mathbf{D}_T$	Tangent modulus matrix
$\mathbf{d}$	Displacement vector
$\mathbf{E}$	Green strain tensor
E_{Ca}	VOCC influx cell conductance
E_{Cl}	Cl^- channels cell conductance
E_K	K^+ efflux cell conductance
E_{NCX}	NCX cell conductance
E_s	Specific energy
$\mathbf{F}$	Deformation gradient tensor
$\mathbf{F}_\mathbf{F}$	Convective and Taylor Galerkin fluxes
$\mathbf{f}$	External force vector
f_{cl}	Clothing surface factor
$\mathbf{f}_{\Gamma e}$	Boundary terms at element boundaries
$\bar{\mathbf{G}}_F$	Diffusion vector
$\mathbf{G}_F$	Gradient matrix
$\mathbf{G}_{p,stab}$	Pressure stabilization matrix
$\mathbf{g}$	Body force
$\mathbf{H}^*$	Laplacian matrix
$\mathbf{H}_F$	Matrix of convection term
h	Tube wall thickness
h_{ele}	Element characteristic length
h_{ext}	External heat transfer coefficient
h_{in}	Internal heat transfer coefficient
h_{rad}	Radiative heat transfer coefficient
$\mathbf{I}_d$	Identity matrix
$\bar{I}_i$	ith invariant

J	Determinant of Deformation gradient
$\bar{J}$	Dilation coefficient
$\bar{J}_C, \bar{J}_V$	Intercellular currents
$\mathbf{J}_I$	Interface coupling Jacobian
$\mathbf{J}_{x,\xi}$	Mapping Jacobian
$\mathbf{K}_e$	Element matrix for convection and Taylor Galerkin terms
$\mathbf{K}_{eT}$	Element matrix for temperature convection and Taylor Galerkin terms
k_{Ex}	Ca^{2+} extrusion by ATPase pump constant
k_F	Fluid thermal conductivity
$\mathbf{K}_F$	Viscosity matrix
$\mathbf{K}_T$	Tangent stiffness matrix
k_t	Wall thermal conductivity
L	Tube length
$\bar{L}_0$	Relative filament overlap
$\mathbf{L}_e$	Element matrix of source terms
$\mathbf{L}_{eT}$	Element matrix of temperature source terms
$\bar{\mathbf{L}}_F$	Eigenmatrix
$\mathbf{L}_F$	Eigenvectors
L_{SR}	SR leak rate constant
$\mathbf{M}$	Mass matrix
$\mathbf{M}_e$	Element mass matrix
$\mathbf{M}_{eT}$	Element mass matrix for temperature
m_{Ry}	RyR CICR Hill coefficient
$\dot{m}_{skin}$	Skin perfusion flow
$\dot{m}_{swea}$	Sweating flow
$\mathbf{N}$	Shape function vector
N	Shape function

$\mathbf{n}$	Surface normal
$n_M, n_{Mp}, n_{AM}, n_{AMp}$	CB kinetic states
n_{SR}	SR uptake Hill coefficient
$\mathbf{P}$	Stress force vector
P_a	CU filament sliding resistance/averaged First Piola-Kirchhoff stress tensor
P_c	CB stress force
p	Pressure
p_{ext}	External pressure
p_{in}	Input pressure value
p_m	Polynomial function
p_{out}	Ambient water vapour pressure
p_{Ry}	RyR CICR Hill coefficient
p_{skin}	Skin water vapour pressure
Q	Flow rate
$\mathbf{Q}_F$	Jacobian matrix of source
Q_{shiv}	Shivering power
q_{bre}	Breathing heat flux
$q_{con,out}$	Convective heat flux
q_m	Metabolic heat production
q_{rad}	Radiative heat flux
q_{swe}	Evaporative heat flux
$\mathbf{q}_{\Gamma e}$	Element boundary term for energy equation
$\mathbf{R}$	Residual
R_{Ca}	VOCC influx max slope of activation sigmoid
R_{Ex}	Ca^{2+} extrusion by ATPase pump constant
R_K	K^+ efflux max. slope of K_{Ca} activation sigmoid
$R_{swe,cl}$	Clothing sweating resistance
R_t	Terminal reflection coefficient

R_{Vr}	Valve reflection coefficient
r	Radial coordinate
r_{in}	Vessel internal radius
r_{ext}	Vessel external radius
Re	Reynolds number
$\mathbf{S}$	Second Piola-Kirchhoff stress tensor
$\bar{\mathbf{S}}_{\mathbf{F}}$	Source vector
T	Fluid temperature
T_{core}	Core temperature
T_{out}	Outside environment temperature
T_{shiv}	Shivering temperature threshold
T_{skin}	Mean skin temperature
T_{swe}	Sweating temperature threshold
T_t	Tissue temperature
$T_{w,in}$	Inner wall temperature
t	Time
$\mathbf{t}_f$	Traction force
$\bar{\mathbf{U}}_F$	Primitive variable vector of area, velocity and temperature
U_{vol}	Potential energy
$\mathbf{u}$	Fluid velocity
$\bar{u}_{cb}$	Normalized average CB elongation
$\bar{u}_{fs}$	Normalized average relative filament sliding in a CU
$\bar{u}_{fs}^{opt}$	Material parameter
$\mathbf{u}_g$	Grid velocity
u_{inl}	Inlet velocity
$\dot{W}_{shear}$	Loss due to viscous effect
$\dot{W}_{wall}$	Work by wall forces
w_1, w_2, w_3	Characteristic variables

w_{skin}	Skin wetness
$\mathbf{X}$	Reference coordinates
$\mathbf{x}$	Current coordinates
$\bar{x}_0$	Material parameter
x_{Cl}	Cl^- channels Ca^{2+} sensitivity
x_{NCX}	NCX half point of Ca^{2+}activation
x_{Ry}	RyR CICR half point of CICR activation sigmoid
x_{SR}	SR uptake half point of ATPase activation sigmoid
Y	Young's modulus
y_{Ry}	RyR CICR half point of Ca^{2+} efflux sigmoid
$\mathbf{Z}$	Interpolation function
z_{Ca1}	VOCC influx reversal potential
z_{Ca2}	VOCC influx half point of activation sigmoid
z_{Ca3}	K^+ efflux half point of activation sigmoid
z_{Cl}	Cl^- channels reverse potential
z_{Ex}	Ca^{2+} extrusion by ATPase pump constant
z_K	K^+ efflux reverse potential
z_{NCX}	NCX reversal potential

Greek letters

α_a	Active material parameter
α_C	Cellular Ca^{2+} diffusivity
α_F	Fluid thermal diffusivity
α_f, α_m	α method parameter
α_V	Cellular voltage diffusivity
α_Z	Interpolation coefficient
β	Vessel elastic parameter
β_a	Active material parameter
β_C	Incompressibility parameter/maximum velocity

β_K	K^+ efflux Ca^{2+} sensitivity of K_{Ca} channel activation sigmoid
β_N	Newmark method parameter
β_Z	Polynomial coefficient
β_α	α method parameter
Γ	Domain surface
γ_m	Membrane potential scaling factor
γ_N	Newmark method parameter
γ_α	α method parameter
Δt	Time step
$\delta_{i,j}$	Kronecker delta
ϵ	Strain tensor
ζ	Store Ca2+ concentration
ζ_S	SOCC parameter
η	Membrane potential
$\theta_1,\theta_2,\theta_3,\theta_4$	CBS time integration parameters
θ_k	Enhancement kinetics coefficient
κ	Bulk modulus
κ_{AM}	Parameter related to the force-bearing capacity of a dephosphorylated CB during muscle extension
κ_{AMp}	Parameter related to the force of a power-stroke of a single CB
$\bar{\mathbf{\Lambda}}_F$	Eigenvalues
λ	Stretching ratio
μ_a	Active shear modulus
μ_F	Fluid dynamic viscosity
μ_p	Passive shear modulus
μ_S	Solid shear modulus
ν_{air}	Air velocity

ν_{Pois}	Poisson's ratio
$\boldsymbol{\xi}$	Parametric coordinates
ρ_{∞}^{h}	Spectral radius parameter
ρ_F	Fluid density
ρ_S	Solid density
ρ_t	Tissue density
$\boldsymbol{\sigma}$	Cauchy stress tensor
τ_0	CB kinetic model fitting parameter
$\tau_1, \tau_2, \tau_3, \tau_4, \tau_5, \tau_7$	CB kinetic rates
τ_F	Fluid shear stress
$\Phi_A, \Phi_B, \Phi_C, \Phi_{Cl}, \Phi_D, \Phi_K, \Phi_L, \Phi_N, \Phi_S, \Phi_V$	Ca^{2+} cellular fluxes
$\dot{\Phi}_{cond}$	Heat diffusion flux
$\dot{\Phi}_{conv}$	Heat convection flux
Φ_{pF}	Numerical pressure flux
ϕ_{perf}	Perfusion rate
ϕ_Z	Radial Basis function
χ	Intracellular Ca2+ concentration
χ_0	Kinetic saturation constant
Ψ	Strain energy function
Ω	Reference spatial domain
Ω'	Deformed spatial domain
ω_R	Relaxing factor

Chapter 1

Introduction

This thesis presents the development of a modelling framework for the study of fundamental mechanisms responsible for the onset and progression of cardiovascular disease. The formulation of a comprehensive in silico system allows for the non-invasive testing of pathogenic hypotheses and may inform the design of novel drugs. The first part of this chapter provides a characterisation of the arterial system by defining the main physiological, morphological and structural features. This outline focuses on the contractile activity of the arterial wall that occurs under physiological conditions or induced by specific pharmacological interventions. A concise summary on the current state of the vascular modelling techniques is then presented. The aims of the work and the global methodology adopted are finally outlined.

1.1 Characterisation of the arterial system

The arterial systemic circulation consists of a branching network of blood vessels and provides the means by which the oxygenated and nutrient-rich blood is transported from the left cardiac ventricle to the body soft tissues. Classification of these blood vessels is commonly based on their size and type. Large arteries (lumen >10 mm) are characterised by their elastic behaviour (thus also called elastic arteries) and convey large volume of arterial blood from the core region towards the main organs and the peripheral regions. Among these large vessels are the aorta, its main branches and the pulmonary arteries. These vessels branch into muscular/distributing arteries (lumen between 0.1-10.0 mm) which become smaller in diameter as they get further from the parent branch. By comparison to the elastic vessels, which store and dissipate the energy generated by the heart's pumping, the muscular vessels are characterised by a thick layer of smooth muscle, which enables the control of blood flow by actively changing the vessel lumen diameter. Small arteries, called arterioles, are characterised by a proximal diameter of around 50-100 μm which narrows down to 15 μm as they penetrate into the tissues and form capillary networks. The terminal part of the arterial network is also known as microcirculation and forms the level at which the exchange of oxygen between blood and cells takes place. Consequently, microvessels are extremely important for the cellular environment homeostasis. Arterial circulation is complemented by

the venous system, which is deputed to drain blood from the tissues to the pumping heart, forming a closed loop for the blood circulation. By comparison to veins of the same size, arteries are characterised by a thicker wall and smaller lumen, as well as by the absence of any internal valves for flow regulation. The arterial system can be also considered to act as a pressure reservoir, as only one-quarter of the blood volume resides in arteries at high transmural pressure, while the remaining is located in veins at low pressure. The rhythmic blood ejection from the left ventricle, combined with the compliance of the arterial wall, results in pulsatile circulation flow [10]. The resulting pressure and flow signals are characterised by irregular patterns, as the propagation of the waveform along the arterial tree is disturbed by reflections occurring at the singularities of the network, e.g. aortic valve, branching points and terminals. The arterial blood is considered a non-Newtonian fluid, and the viscous effect is extremely relevant when the pulsatile flow is separated at bifurcation points [11]. For the vast majority of arterial vessels, including arterioles, the flow is laminar. Turbulence may develop in large arteries, such as the ascending and descending aorta segments (Reynolds number>3300) [12] but such a condition is limited to the proximity of branching points or associated with pathological situations. In most cases, blood in large-medium arteries can be treated as a homogeneous and incompressible fluid.

1.1.1 Arterial wall

Due to the high variability in flow and pressure along the arterial tree, each blood vessel exhibits unique structural properties in order to sustain the physiological fluid load. The vessel structure is generally very complex, as it is arranged in layers performing different functions and constituted by several components, such as endothelium, smooth muscle, elastin, collagen and connective tissue. The macroscopic wall mechanical response depends on how the tissue components are arranged within each layer. A morphological characterisation of the wall at microscopic scale is therefore necessary for elucidating the structural behaviour of the material [13, 14]. The composite collagen/elastin, located in the extracellular space, is the main load carrying element in the structure [15]. Collagen is a protein able to confer

exceptional strength, toughness and mechanical stability to the tissue as it is able to re-arrange its hierarchical structure, which is based on fibres called collagen fibrils (with thickness around 50-300 *nm*). By comparison to collagen, elastin is much more flexible allowing the vessel to sustain larger deformation and stress. The synthesis of both these proteins occurs in the smooth muscle, the cellular layer that is responsible for the active contractility of the wall. The smooth muscle is fundamental to the flow regulation by means of the mechanisms of vasoconstriction and vasodilation. Vascular contraction is governed by a framework of smooth muscle cells, whose contractile machinery is driven by the phosphorylation of the myosin motors, associated with the sub-cellular contractile units and regulated by complex intracellular Ca^{2+} dynamics. The endothelial cells regulate these processes by releasing factors able to inhibit or activate specific ionic pathways within the smooth muscle [16].

Layers of the structure

The arterial wall is arranged in a multi-layered structure: the innermost layer, called intima, the media layer and the external layer, called adventitia (see Figure 1.1).

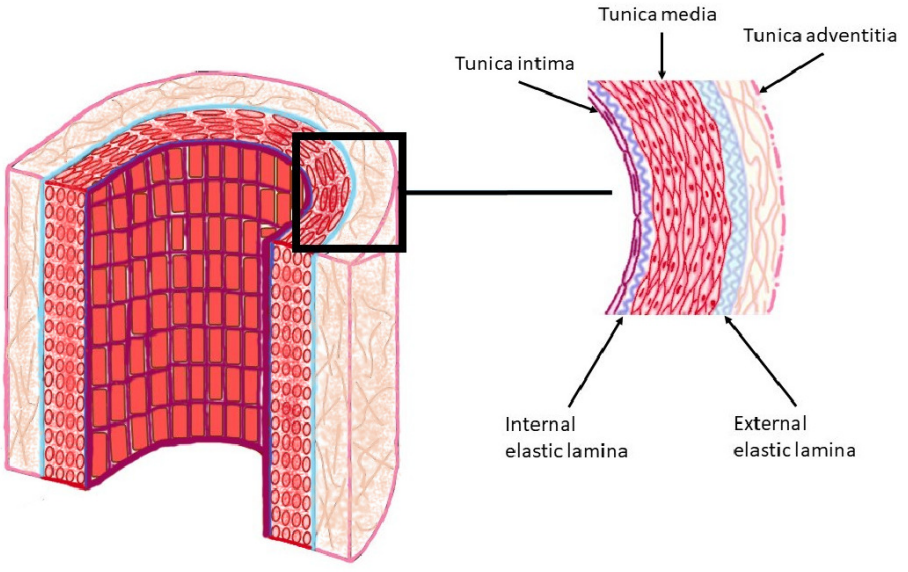

Figure 1.1: Multi-layered structure of the arterial wall.

Intima Consists of a monolayer of endothelial cells lining the inner surface of the blood vessels and supported by the internal elastic lamina, a thick membrane made mostly of collagen. It represents the interface for the transport of molecules from the bloodstream to the media and vice versa. The endothelium layer is present in all arterial vessels. It is important to note that, under healthy conditions, the intima itself does not confer any significant structural property to the wall.

Media A layer consisting of smooth muscle cells embedded in an extracellular matrix made of collagen and elastin. The arrangement of smooth muscle cells and elastic fibres follow a concentric lamellar pattern. The fibres are mainly aligned along the circumferential direction of the vessel. The relative amount of smooth muscle tissue increases in vessels having vasoactive capabilities, such as muscular arteries and arterioles [17, 18].

Adventitia The adventitia tunica confines the inner layers and mainly consists of thick bundles of collagen fibres arranged in helical structures. A loose connective tissue surrounds the outer surface of the layer. In a large artery, this layer represents almost 10 % of the wall thickness, while in a muscular blood vessel this fraction can increase significantly. The artery may also have one or more internal elastic laminae, lying between the layers, able to increase the resistance and the elastic response of the vessel. The presence of these laminae is much more relevant in large rather than in muscular arteries [19]. In Figures 1.2 and 1.3 confocal microscope images show how the tissue morphology may differ depending on the artery. Figure 1.2 shows a confocal image of a cross section of a rabbit ear central artery. For this artery it is easy to distinguish the internal elastic lamina, but the external lamina is indistinct and multifaceted. The structural morphology significantly changes when we look at the arterial section from a rabbit carotid artery (see Figure 1.3). The image shows that other than the internal lamina, the wall layers are much more complex in character. The elastin of the laminae intertwines between the muscle layers, which themselves become more complex and indeed form coils, or ropes, of muscle cells that wrap around and through the media of the artery.

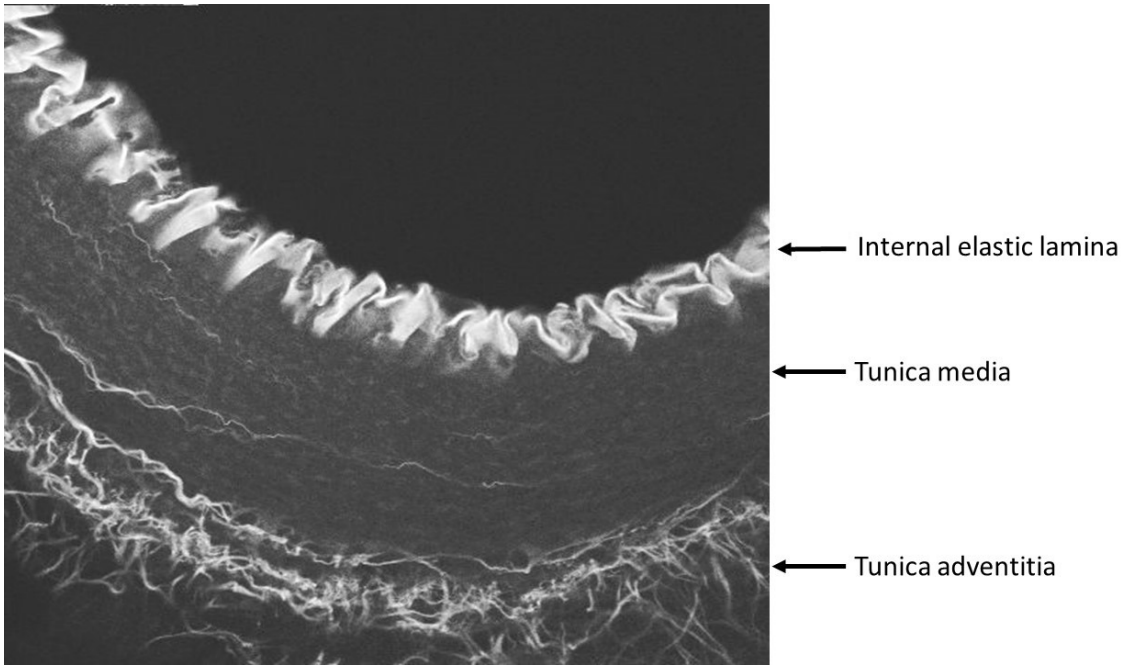

Figure 1.2: Confocal image of a longitudinal section of the arterial wall from a rabbit central ear artery (image generated in our laboratory by Dr. D. Edwards).

Structural properties

The macroscopic mechanical response of the vascular wall is characterised by a nonlinear stress/strain relationship, anisotropy, incompressibility and viscous effects. By isolating the elastin and collagen contributions, Roach and Burton [20], found that for low tension conditions the wall response is dominated by elastin, while for high stress, the tissue exhibits the characteristic stiffening of collagen. The arrangement of the dispersed collagen fibres in both media and adventitia implies a considerable anisotropy of the material. Large arteries are rich in elastic material, while smaller vessels present a stiffer behaviour, which is in line with the increase of pulse wave velocity from core to peripheral regions [18]. Incompressibility may generally be assumed, due to the high water content within the tissues. The mechanical response is also affected by viscosity which makes the material inelastic. Hysteresis phenomena are exhibited when arteries are subjected to cyclic loading but they are particularly relevant during the initial loading phase. After this preconditioning, hysteresis tends to remain the same over time and the stress-strain curve becomes repeatable. The importance of the pre-

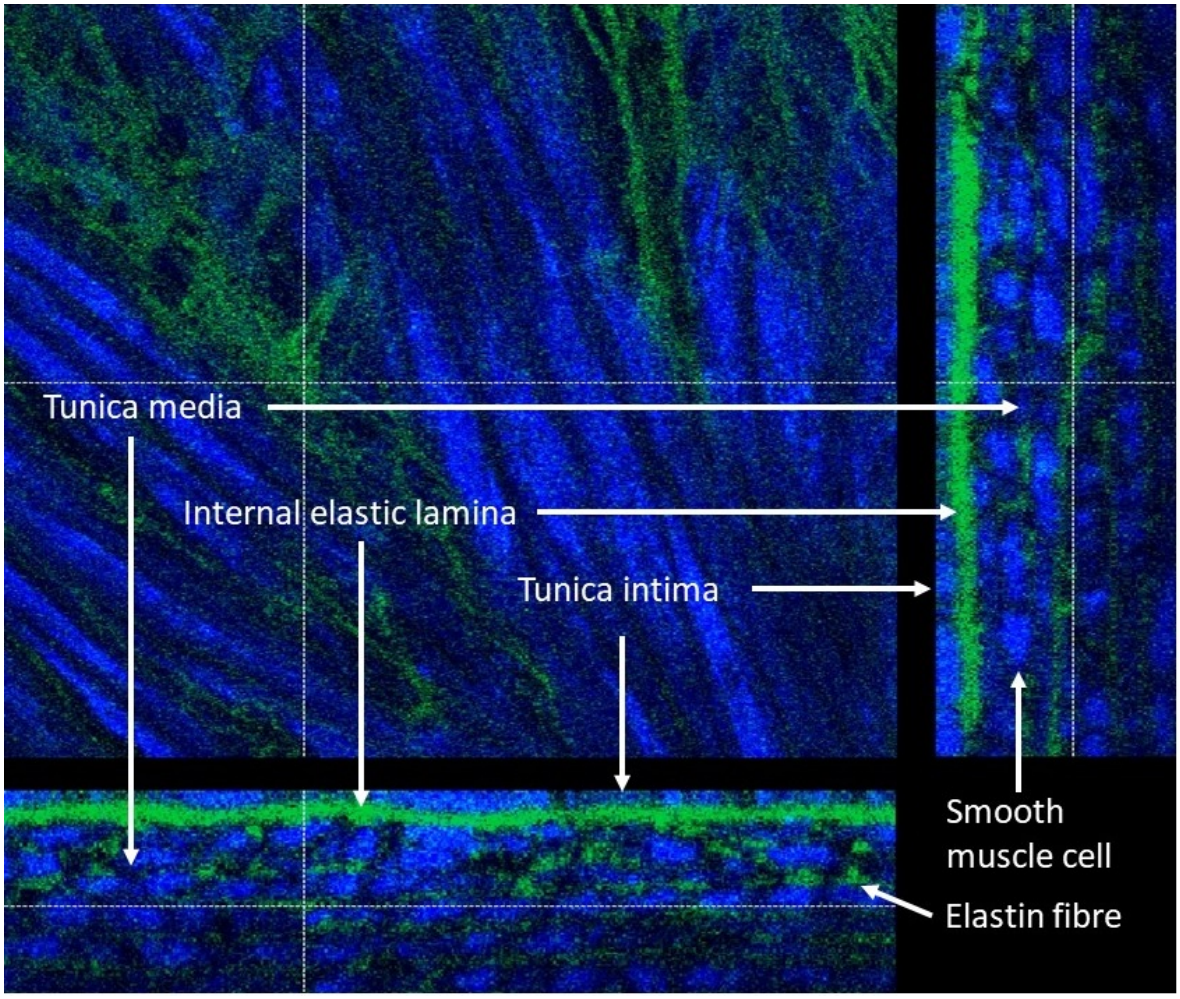

Figure 1.3: Confocal image of the arterial wall. Longitudinal and transversal sections from a rabbit carotid artery (image generated in our laboratory by Dr. D. Edwards).

stress in the unloaded configuration of the wall was pointed out by Fung [21]. Across the lifetime of an artery, several growing and remodelling processes may occur, involving continuous and irreversible changes in the structure. These residual stresses are destined to vary with age and eventual pathological conditions. The residual stresses in the wall, as well as the viscoelastic effects, are not taken into account in this study, in order to simplify the complex modelling process.

1.1.2 Flow regulation

Arterial pressure control is necessary in order to ensure a sufficient and timely blood supply to the vital organs and peripheral regions. At the capillary level, pressure control is fundamental for maintaining the tissue volume and the interstitial fluid composition within well defined physiological ranges. The mean arterial pressure is regulated by changes in cardiac output, which are driven mainly by neurohumoral mechanisms and systemic vascular resistance. The response associated with the nervous system relies on different receptors located at various sites along the arterial tree, in order to monitor the state of the heart and the vascular system [11]. The neural signals are transmitted, either in an individual or integrated manner, from the receptors to the brain. The autonomous nervous system has two principal components: the sympathetic system and the parasympathetic nervous system. If sympathetic nerves are stimulated, the rate and contractile force of the heart rises and vasoconstriction occurs, with a consequent increase in arterial blood pressure. Stimulation of the parasympathetic system causes the opposite effects, with a resulting decrease in arterial blood pressure. These two subsystems can be located in two functionally different areas of the medullary cardiovascular centre and known as pressor and depressor regions [18]. Muscular arteries and arterioles are able to modulate their lumen in order to regulate the blood perfusion in the tissues. Microcirculation [22] represents the site of greatest pressure drop in the arterial blood circuit. For this reason, arterioles play a dominant role in peripheral vascular resistance, which affects the cardiac output [23]. The myogenic response represents an important mechanism in the local regulations of blood flow, involving vasoconstriction when intravascular pressure is high and, conversely, the dilation of the vessel at low pressure [24]. Experiments on isolated rabbit ear arteries demonstrated that such a mechanism has the capacity to minimise changes in smooth muscle cell contractility over the full physiological range of pulsatile intravascular pressure [25]. The relationship between flow and the vessel dilation is modulated by the endothelium-derived relaxing factor nitric oxide (NO), which maintains a fourth-power relationship between lumen and flow so that, in each vessel, the pressure gradient tends asymptotically to a constant value for high flow rates [26]. Different

studies [27, 28] found analogies between such myogenic mechanism and the phenomenon called vasomotion, a spontaneous and rhythmic contractile activity, manifested by low frequency oscillations in vessel caliber [29]. It is pointed out that such diameter oscillations do not depend on the pulsating regime of the flow. Vasomotion has been predominantly found in microcirculation [30, 31], but it also plays a significant role for large muscular arteries [32, 33]. Although the precise physiological function of vasomotion is still not fully understood, this mechanism is relevant in small arteries and arterioles for regulating perfusion, filtration and lymphatic drainage, and maintaining homeostasis [34, 35]. For large arteries, the role of vasomotion is still a matter of debate, although it seems to affect considerably the elastic properties of the arterial wall [36]. Vasomotion has also been proposed as a protective mechanism under conditions of ischemia [37]. Mechanical factors affecting the endothelium, such as the lumen shear stress, seem to be involved in the modulation of vasomotion [38, 39, 40], although there is no a clear evidence on how these factors are linked to the emergence of the phenomenon. Several studies [41, 42, 43] support the claim that vasomotion may originate from fluctuations in the cytosolic concentration of calcium ions. Variations in Ca^{2+} concentration observed in smooth muscle cells are the result of the continuous calcium ion uptake/release through the cellular membrane (sarcolemma). Intracellular Ca^{2+} is of huge importance for media tissue contractility as it is the primary catalyst for the phosphorylation of cross-bridge formation that occurs within each smooth muscle cell, and which facilitates the contractile response of the cellular cytoskeleton. Intercellular coupling within the smooth muscle promotes the long distance entrainment of Ca^{2+} dynamics and the emergence of synchronised contractile activity within the arterial wall.

Integration of all these mechanisms is therefore required to shed light on the effects of cellular dysregulation onto macroscopic level events such as physiologically significant vascular flow changes.

1.2 Vascular modelling

A review of the main contributions to the field of vascular computational mechanics is presented here.

1.2.1 Advanced arterial wall models

Due to the structural complexity of the arterial wall, the models available in the literature generally account for only a subset of the features described in Section 1.1.1. Nevertheless advanced computational models of the vascular structure have become very useful for the study of pathological conditions that may involve the dysfunction of arterial wall components. One of the early fundamental contribution in this field was due to Fung [44, 21], who proposed a non-linear continuum mechanical formulation described in terms of a strain energy function. Many other relevant models were derived from this reference work [45, 46, 19, 47]. Holzapfel et al. [19] added an isotropic Neo-Hookean contribution and reformulated the exponential form of Fung in terms of tensor invariants. In this work the anisotropy of the structure is introduced through the reinforcing collagen fibre contributions. This type of (micro-)structural model was able to capture the characteristic *S-shaped* stress-strain relationship, and became popular over the last two decades, giving rise to different extensions that included visco-elasticity, fibre remodelling and fibre dispersion [48, 49, 50]. These models were intended to simulate the passive response of arterial wall without taking into account the active media layer contractility. The theoretical work by Rachev and Hayashi [51] was one of the earliest to model the effects of smooth muscle contraction on strain and stress distributions in arteries. Several methodologies have been subsequently proposed for simulating the smooth muscle contractility [51, 52, 53, 54, 55, 8], that translate the kinetics occurring within the smooth muscle contractile units into a macroscopic tissue structural response.

At the same time a number of works accounting for the cellular Ca^{2+} dynamics has been proposed [7, 56, 57]. These models have been systematically validated against a broad range

of pharmacological interventions that specifically inhibit individual transport mechanisms and modulate endothelial nitric oxide (NO) synthesis. The methodology proposed for single cell dynamics has been subsequently extended to arrays of coupled cells with realistic architectures of arterial vessels [58, 6]. This led to the study of Ca^{2+} synchronisation and wave formation on the arterial wall under varying cellular coupling conditions. For an extended review on structural modelling of arteries, the reader is referred to [59, 60].

1.2.2 Computational hemodynamics

With regard to arterial flow modelling, a large variety of computational methodologies has been developed in the last three decades. They range from simple lumped parameter models (0-D) [61], which consider a uniform distribution of the fundamental variables, to one-dimensional (1-D) models [62, 63, 64, 65, 1, 66, 67] accounting for flow/pressure propagation along the arterial network, to three dimensional (3-D) models, which may be characterised by more realistic features, ie, detailed interaction with the wall (fluid structure interaction) or realistic vascular geometry (patient-specific) [68, 69, 70, 71, 72]. Each computational strategy has its own advantages and limitations and the choice must depend on the scale relevant to the hemodynamics of the problem treated [73]. The 0-D models represent a computationally inexpensive and mathematically simple choice, optimal for carrying out a global analysis of the system. These models do not provide any spatial definition of the problem and are therefore not suitable for modelling flow propagation/advection phenomena. The one-dimensional methodologies allow the description of wave propagation along extensive arterial vessel networks by requiring affordable computational cost, even for long time simulations. The 1-D description of the flow, however, is not able to capture detailed flow features such as the velocity and stress field distribution on the wall interface boundary. This information may be extremely relevant in the study of certain pathological scenarios, such as stenosis and aneurysms. Despite the enormous computational resources requested, the multidimensional approach is probably the best candidate for representing complex flow in realistic geometries and, in the case of coupling with the vascular structure, to account for both active and

passive dynamic properties of the wall. A limiting factor to these approaches is the accurate estimation of model parameters, such as material properties, vascular geometry and boundary conditions which fundamentally affect the simulated outcome, regardless of the computational methodology adopted. A way to overcome this constrain was suggested in [72], where it was showed that accurate results can be obtained for different patient-specific models (1-D/0-D and 3-D/0-D) even when parametric data were obtained through non-invasive techniques. For multidimensional fluid structure interaction problems, many computational methods are available ranging from monolithic strategies [74, 75, 76, 77], where all the field equations are solved at the same time in a unique block, to segregated strategies [78, 79, 80, 81], which compute the solution by treating each subsystem in a segregated fashion. The choice of the numerical method, however, has a significant impact on the computational time. The partitioned schemes generally guarantee lower computational costs but at the same time may suffer numerical issues, such as added mass effect or incompressibility dilemma [82, 83, 84], due to a lack of robustness of the coupling algorithm. FSI remains a research area in continuous expansion, within which the cardiovascular system constitutes one of the most important and challenging application cases [85]. Several hemodynamics FSI studies have been carried out by considering a variety of complex vascular domains, ranging from idealised aneurysms to geometries derived from MRI scans [71, 86, 87, 88]. There is still however the need to render such algorithms computationally more efficient, in order to extend the FSI analysis to larger portions of the arterial system. More importantly, in light of the present work, the number of FSI works employing advanced wall structural models is extremely limited. A successful compromise can be achieved by employing multiscale strategies, such as in [89], where a localised, detailed arterial model is coupled with an extensive model of systemic circulation, modelled with a reduced order methodology. In this case the reduced model can impose "realistic" boundary conditions at the interface with the more sophisticated component. This allows modelling simplifications as well as significant computational savings.

1.2.3 Modelling blood transport and diffusive processes along the arterial tree

A fundamental understanding of blood transport in the human body is important for studying a broad range of situations, such as the effect of temperature controlled surgeries and the impact of dramatic change in atmospheric or surrounding temperature. The thermal manipulation of body temperature has been used for a long time in cryosurgery and cancer treatment (hyperthermia) [90, 91, 92]. It is also known that dramatic changes in weather (extremely cold seasons or heat waves) can lead to adverse health conditions and in some cases death. In thermally controlled surgeries, understanding the heat or cold dissipation mechanism in a human body can be critically important. In a more ordinary situation, seasonal changes in atmospheric temperature require the body to adapt fast to keep the stimuli under control. Despite all the regulatory mechanisms of the human body, whenever temperature reaches a threshold value, tissue damage and/or alterations to biological processes may occur. When subjected to varying temperature conditions, the thermo-regulatory system enables the control mechanisms of the body to keep tissue temperature within the threshold limit. Modelling such a control mechanism and resulting temperature behaviour in time and space within a human body is extremely complex.

A number of modelling attempts have been made in the past using lumped models or models that have only accounted for conduction and perfusion to understand the heat transfer in a human body. While these models provide a good starting point, they are not comprehensive as they do not include the effect of pulsatility and flow in arteries. A brief overview of the existing models is given below. The available bio-heat transfer models for a human body may be conveniently divided into lumped models, segmented models and multidimensional models. In addition, there are models that fall between these categories. The lumped models are the simplest as they treat the human body as a single point with temperature change allowed only in time. Since the thermo-regulation effects and heat transfer processes within the body were not accounted in the lumped models, applications of such models are extremely limited. By comparison, fully three dimensional models represent thermal changes

in a human body close to reality. Such representations are however complex, extremely expensive computationally and difficult to implement. Thus, the segmented models that carefully account for various biological and physical processes are probably the best templates for understanding the human body bio-heat transfer. Alternatives to lumped models were developed in the late sixties and the first of such models consist of two nodes, representing a human body by two concentric shells. The first, central shell represents internal organs, bone, muscle and subcutaneous tissue and the second, outer shell represents the skin layer. The model presented by Gagge *et al.* [93] is one of the best-known two-node models. It calculates the thermal response by means of two energy balance equations, one for the core node and one for the skin node. Gagge *et al.*'s model accounts for the effects of heat accumulation, conductive and convective heat transfer via blood flow between the core and skin shells, metabolic heat generated during exercise and shivering. The energy exchange with the environment has been modelled by considering respiration, convection, radiation and evaporation of moisture. Gagge *et al.*'s model is simple to use, but it can only be applied to situations with moderate levels of activity and uniform environmental conditions. Although this model is an improvement on lumped models, it does not allow for the computation of detailed body temperature distribution. An obvious extension to the two node model is to introduce multi-nodes to discretely represent different parts of the body. Stolwijk and co-workers [94, 95, 96] divided the human body into five cylindrical parts to individually represent the trunk, arms, hands, legs and feet and a spherical body part for the head. Each part was further divided into four concentric shells representing the core, muscle, fat and skin layers. In this model, the blood circulation system is represented by a blood pool located in the trunk. The trunk is connected to all tissue nodes by a network of blood vessels. The heat transfer between tissue nodes occur by conduction while between the central blood node and the adjacent tissue nodes by convection. The energy balance equation includes heat accumulation, blood convection, tissue conduction, metabolic activity, respiration and heat transfer to the environment by convection, radiation and evaporation. A thermal control system is also included. A fundamental limitation of this methodology is that it is restricted to isothermal blood flow. The model developed by Wissler [97, 98], consists of 6 (later

15) elements connected by a vascular system. The vascular network is composed of arteries, veins and capillaries and the blood temperatures are assumed to be uniform. Arteries connect the heart to the arterial pool of each element and further into the capillaries. From the capillaries, the blood circulates to the venous pool of the element and back to the heart. Between large arteries and large veins countercurrent heat exchange is modelled. It also accounts for breathing losses and is able to simulate transient states. The 3-D transient multi-element model developed by Smith [99] is based on a more realistic representation of the entire human body than previous models. The body here is composed of 15 elements, which are connected by the central macrocirculation and superficial veins. For the blood network, 1-D steady-state Newtonian flow is assumed. An accurate evaluation of breathing losses is proposed by considering the respiration cycle. In this thermo-regulatory system proposed, variation of skin blood vessel radii during vasomotor response, the sweat rate and the shivering metabolic rate are functions of the core and mean skin temperatures. The 3-D approach makes the model suitable for situations with high temperature gradients or highly non-uniform thermal conditions. However in such model fat and skin layers are modelled as a single layer; this may affect the heat convection to the skin surface carried by blood flow and thus the entire body thermal response. Moreover, blood perfusion occurring in capillary beds is not considered. Another relevant work is that of Fiala et al. [100, 101], who divide the body into cylindrical and spherical elements. Such subdivision was enforced whenever a significant change of body tissue properties occurred. The heat produced within the body is dispersed to the environment by convection, radiation and moisture evaporation at the skin, and in the lungs/respiratory tract. Such multi-layered model consists of annular concentric tissue layers and uses seven different tissue materials: brain, lung, bone, muscle, viscera, fat and skin. For the solid conduction problem 1-D Pennes' equation was used. Body elements are supplied with warm blood from the central pool by the major arteries. Along the pathway, arterial blood exchanges energy with returning veins as in a countercurrent heat exchanger. This was introduced in order to obtain a more realistic distribution of the arterial blood temperature instead of assuming a constant arterial blood temperature for all body elements equal to the temperature of the central blood pool. Perfusion is used as the

mechanism of exchange between blood and tissues. The effects of the thermo-regulatory system are also accounted. Cropper et al. [102] coupled the human model of [100] with a CFD for external airflow and obtained a tool able to predict the response of body temperature to several detailed local environmental conditions. Tanabe et al. [103] modelled human thermal system in a similar way. In this case each individual body elements consists of a core layer and a skin layer and in the centre of each core layer there are artery and vein blood pools. Between the artery and the superficial vein blood pools, an additional vessel is introduced to account for changes in blood flow due to changes in the ambient environment. The model developed by Huizenga et al. [104] is based on the Stolwijk model [94, 95, 96] as well as on work by Tanabe [103], but includes several significant improvements, as it can simulate an arbitrary number of human body segments. Each of these segments consists of four body layers (core, muscle, fat, and skin tissues) while a clothing node has been added to model heat and moisture capacitances. The improved blood flow model includes central artery/vein countercurrent heat exchange and blood perfusion model to estimate blood flow to local tissue. The model also calculates the heat transfer by conduction to surfaces in contact with the body. A better estimation of the convection and radiation transfer coefficients, an explicit radiation heat transfer calculation using angle factors and the addition of a radiation heat flux model are notable additions. Besides this, the model allows simulation of any sequential combination of environmental, clothing and metabolic conditions. Although the latter models with arterial systems [100, 101, 103, 104] represent a step forward, they do not explicitly include a systemic circulation and the resulting inner convection occurring between the arterial blood and wall. Other notable models include the one developed by The National Renewable Energy Laboratory (NREL) [105], which contains a detailed simulation of human internal thermal physiological systems and thermo-regulatory responses. Another multi-segmented human thermal model developed by Salloum et al. [106] for bare human body consists of a comprehensive blood network. Flow rates are based on exact physiological data, real dimensioning and anatomic positions of the arteries in the body. Holopainen [9] combined the human thermal modelling with a thermal sensation and comfort model inside a simulated building. The models by Karaki et al. [107] and Rida et al. [108] also incorporate

dynamic thermal response associated with arterio-venous anastomoses (AVA) functions. Several works including [109, 110] and [111] report that AVAs in the distal parts of the extremities play a significant role in the heat exchange with the environment. For example, exposure to extremely cold environment, causing cold induced vasodilation (CIVD) to protect hands or feet from cold injury and very high temperature environments causing heat induced vasoconstriction (HIVC) so that the warm blood cannot reach the human core easily. However, as reported in [109], these two exceptions for the AVA function during CIVD and HIVC do not apply to the vasoconstriction or vasodilation of the arterial system triggered by decreased or increased body core temperature. The ability to appropriately characterise the inner convection between tissue and vessels, introduced here, has been a weak point in many recent models. Following the work by Smith [99], Sun [112] derived a comprehensive 3-D model that is able to highlight the heat transfer for walking conditions. Although a blood network was included within solid tissues, this was under the assumption that blood nodes exchange heat with surrounding tissue only via conduction. Moreover, vessels were considered inelastic and thus pulsatile velocity was not accounted for. Ferreira and Yanagihara [113] proposed a 3-D conduction model, where arterial and venous flows are considered as reservoirs and the tissue temperature does not account for any flow temperatures. In subsequent work Ferreira and Yanagihara [114] modelled heat transfer at a steady state in the upper limbs. Although tissue matter was modelled via partial differential equations, the conditions considered were stationary. Furthermore only two different tissues were used, while a reduced, arterial network was adopted.

In the literature there is no clear evidence on the role of the venous system on the global thermal balance of the body. Indeed the importance of the heat exchanged between arteries and veins is still a matter of debate, as highlighted by an analytical model by Mitchell and Myers [115], demonstrating no significant counter-current effect in the human arm. This can be mainly justified because the distance between large arterial and venous vessels is significant; the high velocity blood flow and the too short length of the vessels may affect further the counter-current heat exchange. Vanggaard [116] confirmed that counter-current heat exchange is of minor importance in total heat exchange. He concluded that counter-

current heat exchange either had to be always 100% effective or negligible, and naturally opted for the latter. Some studies have reported heat transfer in the blood but without the surrounding body tissues. For example, Craciunescu and Clegg [117] analysed the effect of a pulsating blood velocity field on temperature. In their studies they obtained some important results on the relationship between the pulsating axial velocity and temperature profile and the effect of the Womersley number variation. In the work proposed by Bommadevara et al. [118] a sophisticated bio-heat transfer model representing neck is presented. They evaluate temperatures along common and internal carotid arteries for various environmental conditions. However, blood vessels in this study are treated as rigid tubes and thus the effects of area variations are not accounted for. Ying et al. [119] proposed a thermo-fluid model valid for a circulation system of the upper limb which involves arteries, capillaries, and veins. Here, the temperature is evaluated along the network by considering the effects of blood flow rate, transmural pressure, cross-sectional area and elasticity. However, this model is not comprehensive as reflections due to variations in vessel topology and properties are not accounted for.

1.3 Aims of the work

As discussed in Section 1.1, characterisation of the interaction between the blood flow and the vascular wall is vital for a better understanding of the mechanisms underlying the transport and regulation of the flow. Phenomena like vasomotion are the result of intimate coupling between cellular biochemical processes, wall structural mechanics and blood flow. With this work we aim to develop and validate an arterial fluid model accounting for smooth muscle dynamics and wall-blood flow interaction in a robust multiscale formulation. The designed framework will provide a platform for testing hypothesis on the mechanistic origin of vascular disease and suggest pharmacological interventions able to inhibit pathogenic processes at the cellular level. This methodology may provide the foundation for future applications, such as the study of vascular disease in diabetes and tumour neovascularisation. Figure 1.4 illustrates the global modelling methodology we intend to develop, highlighting

the main focus of the present work (A,B) along with potential future applications (C,D,E).

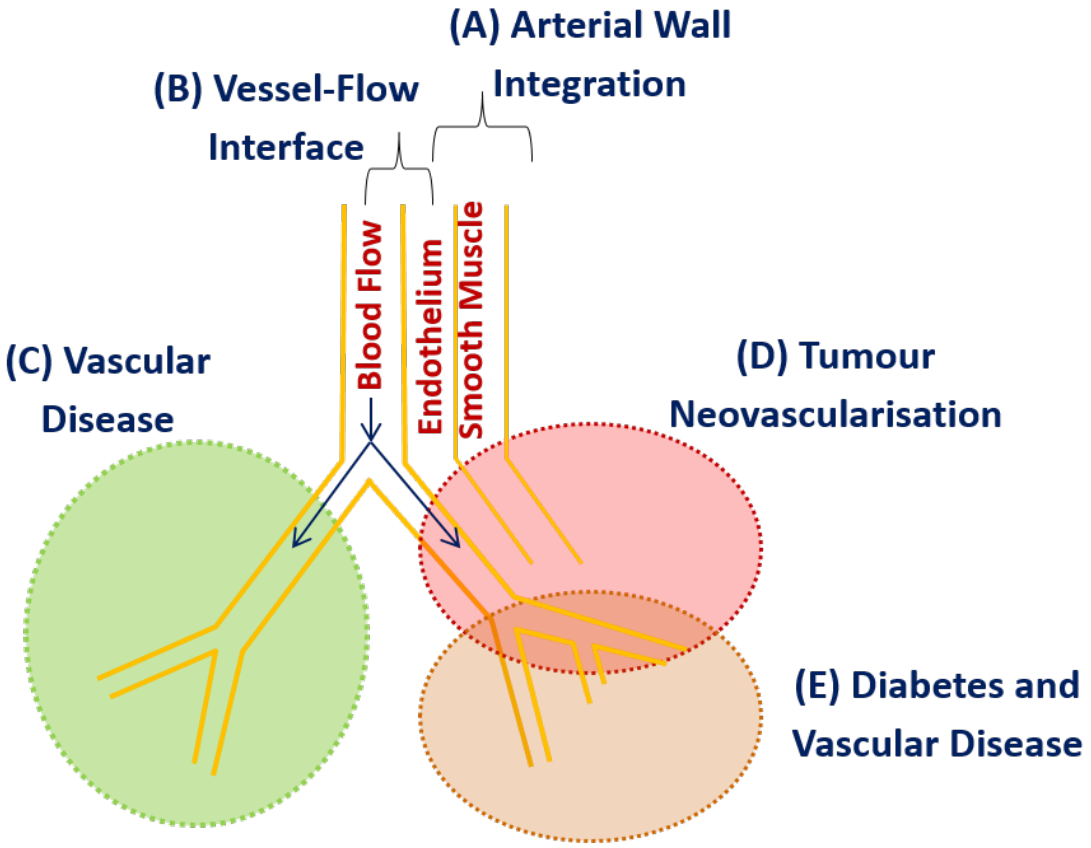

Figure 1.4: Schematic of integrated framework (A,B) and potential applications (C,D,E).

This methodology requires integration of a fluid dynamics framework for collapsible vessel with a model describing the wall contractile behaviour. The arterial wall can be seen as a control system of the blood flow and its subsystems/layers dependencies, depicted in Figure 1.5. Unlike a common collapsible-passive vessel, the arterial wall includes a smooth muscle cellular layer which forms an active source of contractility. Concentration of Ca^{2+} ions in the cytosol plays a fundamental role in the excitation of the smooth muscle's contraction. Such contractile mechanism acts in parallel to fluid traction load in wall deformation and is regulated by the endothelium monolayer. The adventitia has no active contractile capacity but plays a fundamental role in the passive response of the material.

This multiscale approach will allow us to study the effect of localised (e.g. cellular) dysregulation

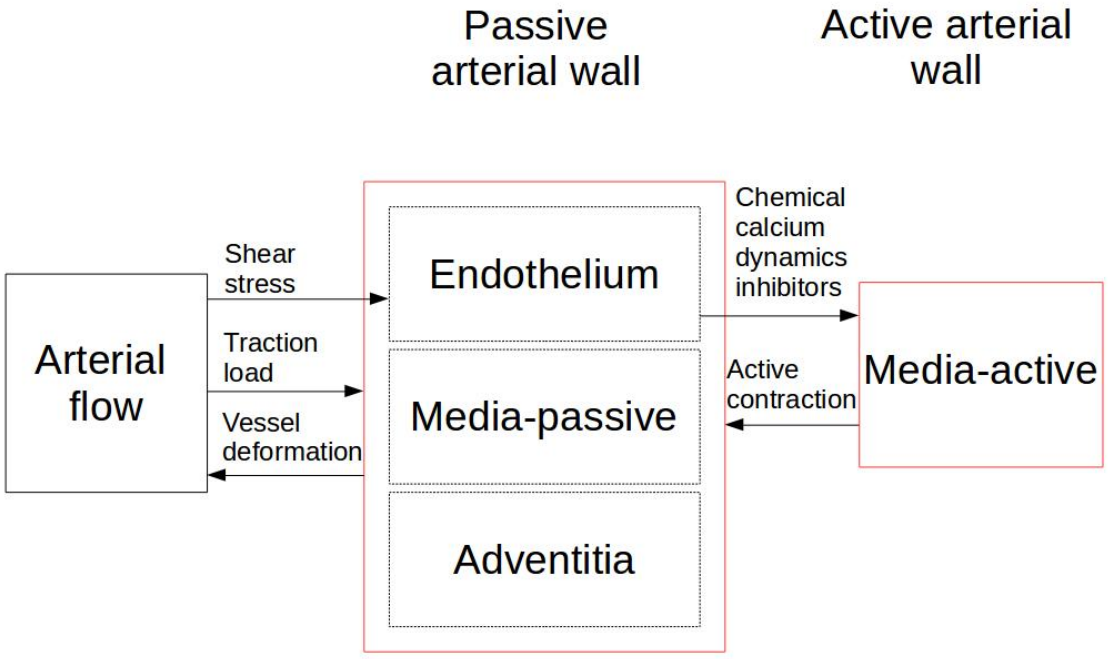

Figure 1.5: Virtual artery system components.

as manifested in global circulatory dysfunction. Integration of this multi-physics platform will be performed along three distinct steps:

- **Coupling arterial wall mechanics with Ca^{2+} dynamics**.
  The contractile state of the vascular wall constitutes one side of the non-linear relationship between stress and deformation of the wall structure. In absence of arterial flow, the smooth muscle layer becomes the only driving force that may cause wall deformation. In this area of the work, we aim to integrate the cellular Ca^{2+} dynamics into a tissue structural model, so that the resulting structural response of the media will be able to account for different levels of contractility driven by the cellular biochemical processes.

- **Development of efficient fluid structure interaction for hemodynamics problems**
  To describe the interaction between the vascular wall and the blood flow, an FSI

scheme needs to be developed. For this purpose we adopt one of the best tested approaches: the partitioned coupling scheme which utilises subsequent solutions of both the fluid and the structure sub-problems, thus enabling existing fluid and structure solvers to be re-used. To overcome any numerical instability issues, we employ a strongly coupled scheme which utilises multiple iterations per time step (dual time stepping) to converge to the monolithic solution. The use of such dual time stepping allows us to employ a larger time step, resulting in a considerable improvement in efficiency.

- **Modelling transport along the systemic circulation**

  Computing the transport of drugs and fluid properties within the tissues requires coupling the vascular network with the solid tissues system. To represent the arterial systemic circulation we adopted the model proposed in [64, 1]. The methodology allows the computation of 1-D flow along a network composed by 63 blood elastic vessels (Figure 1.6). This approach results in a comprehensive model as reflections due to variations in vessel topology and properties, and aortic valve effects are accounted for. Since temperature is a fundamental blood property (e.g. in terms of drug solubility and viscosity) we extended the model proposed in [64, 1] by incorporating fluid energy conservation equations. We thus developed a novel thermal model able to account for embedded arterial circulation. Importantly, this multi-branching circulatory model of blood flow-body tissue interaction can be used to describe a variety of diffusive processes, such as drug delivery into tissue in 1-D blood flow, as it relies on the same transport equations employed for fluid energy conservation.

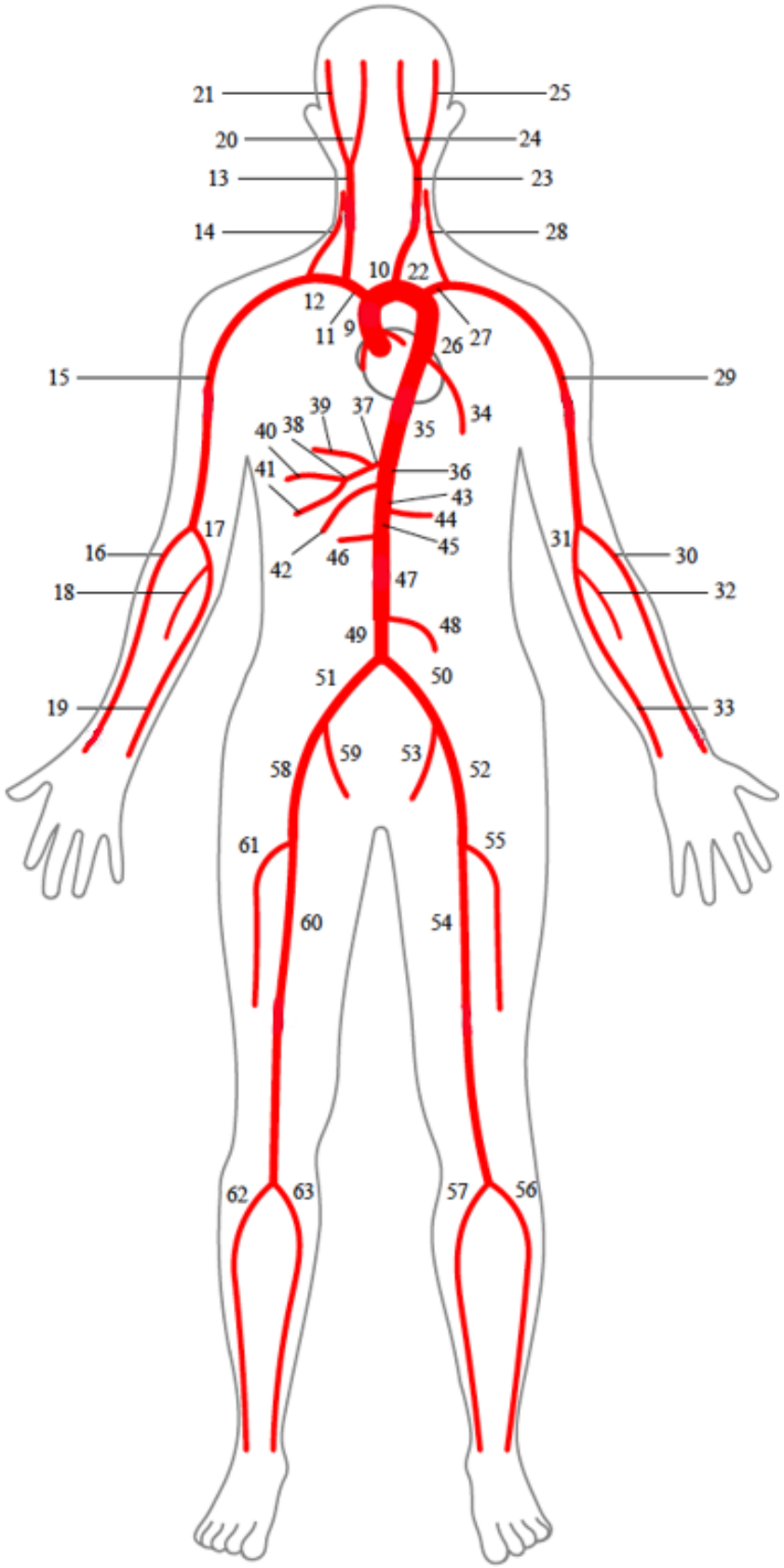

Figure 1.6: Arterial systemic circulation (from [1]).

Chapter 2

General methods

The theoretical background underlying the numerical solution procedures employed for solving the problems identified in Section 1.3 is presented below. A more detailed presentation of the methodology employed for each section of the work is provided within the relevant results chapters. The latter part of the chapter outlines the experimental techniques used to investigate arterial tissue contractility.

2.1 Computational methods

A wide variety of physical field problems can be described by a set of partial different equations in conjunction with conditions imposed at the spatial border, called boundary conditions. In seeking a solution difficulties may arise from the problem formulation and/or the geometry of the physical domain. There is thus the need to adopt robust numerical techniques in order to limit as much as possible eventual numerical issues. The finite element method has emerged as one of the most reliable and widely used techniques for solving this type of problems. In this section, we introduce the basics of the computational procedure necessary to advance from the solid mechanics governing equations to the numerical solution. Although the presented procedure is an introduction to finite element method, it also represents the common methodological basis underlying a broad range of problems, including fluid dynamics and fluid-structure interaction. For a more rigorous introduction to the finite element method, we address the reader to more systematic reference works [120, 121, 122].

2.1.1 Kinetics and deformations

Space is defined with respect to a Cartesian coordinate system (c_1, c_2, c_3). A continuous body is assumed to deform from a reference configuration Ω to a deformed configuration Ω'. For any of its points, the position can be represented in terms of reference (material) coordinates $\mathbf{X}=(X_1, X_2, X_3)$ or current (spatial) ones $\mathbf{x}=(x_1, x_2, x_3)$.

The deformation gradient tensor $\mathbf{F}$, describing the deformation from configuration Ω to Ω',

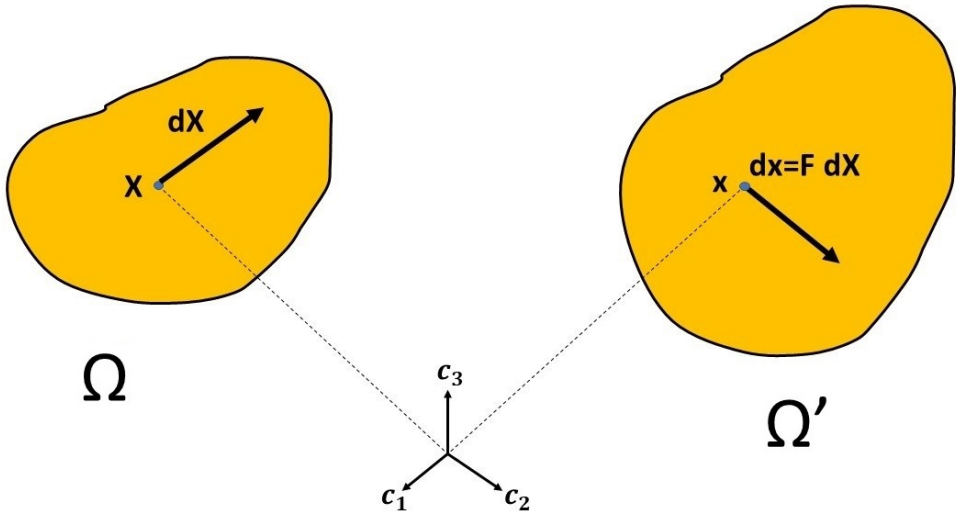

Figure 2.1: Deformation from a reference configuration Ω to a deformed configuration Ω′.

is defined as

$$\mathbf{F} = \begin{bmatrix} \frac{\partial x_1}{\partial X_1} & \frac{\partial x_1}{\partial X_2} & \frac{\partial x_1}{\partial X_3} \\ \frac{\partial x_2}{\partial X_1} & \frac{\partial x_2}{\partial X_2} & \frac{\partial x_2}{\partial X_3} \\ \frac{\partial x_3}{\partial X_1} & \frac{\partial x_3}{\partial X_2} & \frac{\partial x_3}{\partial X_3} \end{bmatrix} \tag{2.1}$$

Thus, it is possible to write the differential of $\mathbf{x}$ as

$$d\mathbf{x} = \mathbf{F}\, d\mathbf{X} \tag{2.2}$$

Spatial coordinates are also related to material ones by means of the following kinematic relationship

$$\mathbf{x} = \mathbf{X} + \mathbf{d} \tag{2.3}$$

where $\mathbf{d}$ is the displacement vector with respect to reference coordinates.

The relationship between the strain tensor $\boldsymbol{\epsilon}$ and the displacement $\mathbf{d}$ is expressed in matrix form via

$$\boldsymbol{\epsilon} = \mathbf{B}\,\mathbf{d} \tag{2.4}$$

where

$$\mathbf{B}^T = \begin{bmatrix} \frac{\partial}{\partial x_1} & 0 & 0 & \frac{\partial}{\partial x_2} & 0 & \frac{\partial}{\partial x_3} \\ 0 & \frac{\partial}{\partial x_2} & 0 & \frac{\partial}{\partial x_1} & \frac{\partial}{\partial x_3} & 0 \\ 0 & 0 & \frac{\partial}{\partial x_3} & 0 & \frac{\partial}{\partial x_2} & \frac{\partial}{\partial x_1} \end{bmatrix} \tag{2.5}$$

The Green strain tensor $\mathbf{E}$ can be written as:

$$\mathbf{E} = \frac{1}{2}(\mathbf{F}^T\mathbf{F} - \mathbf{I}_d) = \frac{1}{2}(\nabla\mathbf{d} + \nabla^T\mathbf{d} + \nabla\mathbf{d}\nabla^T\mathbf{d}) \tag{2.6}$$

in which $\mathbf{I}_d$ is the identity matrix. We note that if a linearity assumption is made for the material (as in the case of the fluid), the product of displacement gradients in Equation (2.6) is negligible; thus each component of tensor $\mathbf{E}$ becomes

$$\mathbf{E} \approx \frac{1}{2}(\nabla\mathbf{d} + \nabla^T\mathbf{d}) \tag{2.7}$$

Extremely important for computational mechanics calculations are the Left Cauchy deformation tensor $\mathbf{b}$, which can be written as

$$\mathbf{b} = \mathbf{F}\mathbf{F}^T \tag{2.8}$$

and the Right Cauchy deformation tensor $\mathbf{C}$, defined as

$$\mathbf{C} = \mathbf{F}^T\mathbf{F} \tag{2.9}$$

Notes on tensors

For a generic tensor $\mathbf{A}$, the deviatoric part $\bar{\mathbf{A}}$, also called $dev(\mathbf{A})$, is given as

$$\bar{\mathbf{A}} = \mathbf{A} - tr(\mathbf{A}) \tag{2.10}$$

where $tr(\mathbf{A})$ is the trace of $\mathbf{A}$, calculated as

$$tr(\mathbf{A}) = \frac{\sum_{i=1}^{3} \mathbf{A}_{ii}}{3} \mathbf{I}_d \tag{2.11}$$

in which $\mathbf{I}_d$ is the identity matrix.

2.1.2 Governing Equations

A generic field problem can be generally described by means of one or more conservation equations. If an infinitesimal solid volume $d\Omega$ is considered, the balance of linear momentum along the ith direction may be written as

$$\sigma_{ij,j} + g_i = \rho_S \ddot{d}_i \quad i,j = 1,2,3 \tag{2.12}$$

where $\sigma_{ij,j}$ ($\sigma_{ij,j}$=$\frac{\partial \sigma_{ij}}{\partial x_j}$) are components of the Cauchy stress, ρ_S is the material density, g_i and $\ddot{d}_i$ are the body force and material acceleration components, respectively. The stress tensor $\boldsymbol{\sigma}$ is defined by means of a constitutive relationship, which depends on the type of material assumed. For each equilibrium equation, it is possible to associate a weak form by multiplying the equation by an appropriate arbitrary function, integrating over the problem's domain Ω, and setting this quantity equal to zero. For the formulation of the non-linear elasticity problem we start from the *virtual work* variational principle, which applied to

Equation (2.12), leads to the following form [123]

$$\int_{\Omega} \delta d_i [\rho_S \ddot{d}_i - g_i - \sigma_{ij,j}] d\Omega = 0 \tag{2.13}$$

where δd_i is the virtual displacement. Integration by parts of the stress components yields

$$\int_{\Omega} \delta d_i \rho_S \ddot{d}_i d\Omega - \int_{\Omega} \delta d_i g_i d\Omega + \int_{\Omega} \delta \varepsilon_{ij} \sigma_{ij} d\Omega - \int_{\Gamma} \delta d_i t_{f,i} d\Gamma = 0 \tag{2.14}$$

where $\delta \varepsilon_{ij}$ is the virtual strain components and $t_{f,i}$ is the current traction vector acting on the surface Γ. Equation (2.14) may be expressed also in a matrix form (neglecting the body force component) as

$$\int_{\Omega} \delta \mathbf{d}^T \rho_S \ddot{\mathbf{d}} d\Omega + \int_{\Omega} \delta (\mathbf{B}\mathbf{d})^T \boldsymbol{\sigma} d\Omega - \int_{\Gamma} \delta \mathbf{d}^T \mathbf{t}_f d\Gamma = 0 \tag{2.15}$$

Enforcing incompressibility

In order to prevent volumetric locking a three field Hu-Washizu formulation can be used as an alternative to the virtual work principle. The functional Π_{HW} depends on the state of deformation (ϕ), the volume change independently of the motion ($\bar{J}$) and the pressure (p) that is a Lagrange multiplier enforcing the condition that $J = \bar{J}$, as follows

$$\Pi_{HW}(\phi, \bar{J}, p) = \int_{\Omega} \bar{\Psi}(\mathbf{C}) d\Omega + \int_{\Omega} U_{vol}(\bar{J}) d\Omega + \int_{\Omega} p(J - \bar{J}) d\Omega - \Pi_{ext}(\phi) \tag{2.16}$$

where $\bar{\Psi}$ is the deviatoric component of the energy stored during the deformation, whilst $\Pi_{ext}(\phi)$ depends on the external forces.

Given a direction $\delta\boldsymbol{\nu}$, the stationary conditions of Equation (2.16) with respect to ϕ, $\bar{J}$ and p yield the virtual work principle and the constitutive and kinematic relationships associated

with the volumetric conditions

$$\begin{cases} D\Pi_{HW}(\phi,\bar{J},p)[\delta\boldsymbol{\nu}] = \int_{\Omega'} \boldsymbol{\sigma} : \delta\mathbf{d}\, d\Omega' - \delta W_{ext}(\phi,\delta\boldsymbol{\nu}) = 0 \\ D\Pi_{HW}(\phi,\bar{J},p)[\delta\bar{J}] = \int_{\Omega} (\frac{dU_{vol}}{d\bar{J}} - p)\delta\bar{J}\, d\Omega = 0 \\ D\Pi_{HW}(\phi,\bar{J},p)[\delta p] = \int_{\Omega} (J-\bar{J})\delta p\, d\Omega = 0 \end{cases} \tag{2.17}$$

where J is the pointwise jacobian such that $J = \frac{d\Omega'}{d\Omega}$. As $\delta\bar{J}$ and δp can be any arbitrary functions, Equation (2.17) gives $\bar{J} = J$ and $p = \frac{dU_{vol}}{d\bar{J}}$. We note that in this system of equations the first expression is the virtual work principle. More details on the procedure can be found in [124].

2.1.3 Finite element procedure

If the finite element approximation is adopted for discretizing the space, the domain of interest, Ω, is divided into a set of sub-domains (called elements), Ω_e, such that

$$\Omega \approx \hat{\Omega} = \sum_e \Omega_e \tag{2.18}$$

The same treatment applies for the boundary

$$\Gamma \approx \hat{\Gamma} = \sum_e \Gamma_e \tag{2.19}$$

Equation (2.15) for the problem domain $\hat{\Omega}$ is written as a sum over the element domains

$$\sum_e \Big[\int_{\Omega_e} \delta\mathbf{d}^T \rho_S \ddot{\mathbf{d}} d\Omega + \int_{\Omega_e} \delta(\mathbf{Bd})^T \boldsymbol{\sigma} d\Omega - \int_{\Gamma_e} \delta\mathbf{d}^T \mathbf{t}_f d\Gamma \Big] = 0 \tag{2.20}$$

With the Galerkin method, the virtual variables are defined as approximations of the independent variables of the variational form. It is also required that the highest derivative in Equation (2.20) must be at least piecewise continuous over the considered domain, so that all integrals exist.

Approximation of displacement

For each element the displacement field may be approximated as

$$\mathbf{d}(\mathbf{x},t) \approx \hat{\mathbf{d}} = \sum_b N_b(\mathbf{x})\tilde{\mathbf{d}}_b(t) = \mathbf{N}(\mathbf{x})\tilde{\mathbf{d}}(t) \tag{2.21}$$

where N_b are element shape functions, $\tilde{\mathbf{d}}_b(t)$ are nodal displacements and the sum ranges over the number of nodes associated with the element.

The element coordinates may be also defined with a parametric mapping ξ (see Figure 2.2 for the two-dimensional quadrilateral).

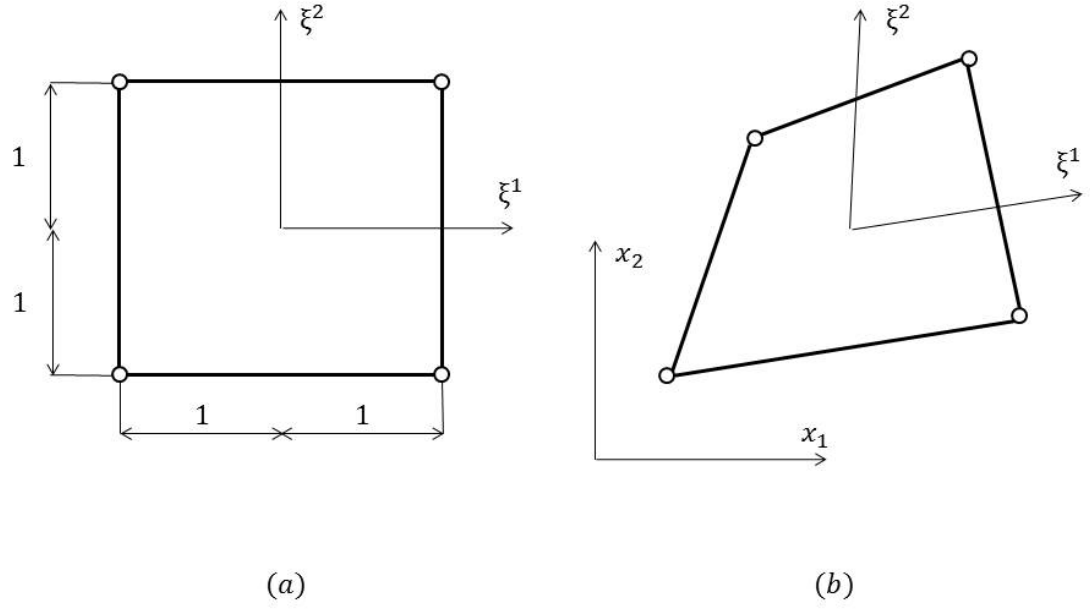

Figure 2.2: Isoparametric map for four-node quadrilateral: (a) element defined in local coordinates (ξ) and element in cartesian coordinates (x).

For such *isoparamteric* elements the displacement $\mathbf{x}$ can be written as

$$\mathbf{x}(\boldsymbol{\xi}) = \sum_b N_b(\boldsymbol{\xi})\tilde{\mathbf{x}} \tag{2.22}$$

where $\tilde{\mathbf{x}}$ represents the nodal coordinate parameters. Thus the displacement field can be also defined as

$$\mathbf{d}(\boldsymbol{\xi},t) \approx \tilde{\mathbf{d}}(\boldsymbol{\xi},t) = \sum_b N_b(\boldsymbol{\xi})\tilde{\mathbf{d}}_b(t) = \mathbf{N}(\boldsymbol{\xi})\tilde{\mathbf{d}}(t) \tag{2.23}$$

Shape function derivatives

The weak formulation introduced previously requires the calculation of the first derivatives of displacements with respect to $\mathbf{x}$. For the isoparametric approximation, it is possible to establish a relationship between derivatives for $\mathbf{x}$ and $\boldsymbol{\xi}$ systems

$$\frac{\partial N_a}{\partial \boldsymbol{\xi}} = \mathbf{J}_{x,\xi}\frac{\partial N_a}{\partial \mathbf{x}} \tag{2.24}$$

in which

$$\frac{\partial N_a}{\partial \mathbf{x}} = \begin{bmatrix} \frac{\partial N_a}{\partial x_1} \\ \frac{\partial N_a}{\partial x_2} \\ \frac{\partial N_a}{\partial x_3} \end{bmatrix}, \qquad \mathbf{J}_{x,\xi} = \begin{bmatrix} \frac{\partial x_1}{\partial \xi^1} & \frac{\partial x_2}{\partial \xi^1} & \frac{\partial x_3}{\partial \xi^1} \\ \frac{\partial x_1}{\partial \xi^2} & \frac{\partial x_2}{\partial \xi^2} & \frac{\partial x_3}{\partial \xi^2} \\ \frac{\partial x_1}{\partial \xi^3} & \frac{\partial x_2}{\partial \xi^3} & \frac{\partial x_3}{\partial \xi^3} \end{bmatrix}, \qquad \frac{\partial N_a}{\partial \boldsymbol{\xi}} = \begin{bmatrix} \frac{\partial N_a}{\partial \xi^1} \\ \frac{\partial N_a}{\partial \xi^2} \\ \frac{\partial N_a}{\partial \xi^3} \end{bmatrix} \tag{2.25}$$

where $\mathbf{J}_{x,\xi}$ is the Jacobian transformation between $\mathbf{x}$ and $\boldsymbol{\xi}$. Thus

$$\frac{\partial N_a}{\partial \mathbf{x}} = \mathbf{J}_{x,\xi}^{-1}\frac{\partial N_a}{\partial \boldsymbol{\xi}} \tag{2.26}$$

Strain-displacement equation

From the strain-displacement relationship defined in Equation (2.4), it is possible to write

$$\boldsymbol{\epsilon} = \mathbf{B}\,\mathbf{d} \approx \sum_b (\mathbf{B}N_b)\,\tilde{\mathbf{d}}_b = \sum_b \mathbf{B}_b^*\,\tilde{\mathbf{d}}_b = \mathbf{B}^*\tilde{\mathbf{d}} \tag{2.27}$$

For the three dimensional problem, the matrix $\mathbf{B}_b^*$ is defined as

$$\mathbf{B}_b^{*T} = \begin{bmatrix} \frac{\partial N_b}{\partial x_1} & 0 & 0 & \frac{\partial N_b}{\partial x_2} & 0 & \frac{\partial N_b}{\partial x_3} \\ 0 & \frac{\partial N_b}{\partial x_2} & 0 & \frac{\partial N_b}{\partial x_1} & \frac{\partial N_b}{\partial x_3} & 0 \\ 0 & 0 & \frac{\partial N_b}{\partial x_3} & 0 & \frac{\partial N_b}{\partial x_2} & \frac{\partial N_b}{\partial x_1} \end{bmatrix} \tag{2.28}$$

Semi-discrete form

Substituting Equations (2.21) and (2.27) into the weak formulation given in Equation (2.20) yields

$$\sum_e \delta\mathbf{d}^T \Big[\int_{\Omega_e} \mathbf{N}^T \rho_S \mathbf{N} \ddot{\tilde{\mathbf{d}}} d\Omega + \int_{\Omega_e} \mathbf{B}^{*T} \boldsymbol{\sigma} d\Omega - \int_{\Gamma_e} \mathbf{N}^T \mathbf{t}_f d\Gamma \Big] = 0 \tag{2.29}$$

As the virtual parameter $\delta\mathbf{d}$ is arbitrary, the previous equation can be re-written in the following compact matrix form

$$\mathbf{M}\ddot{\tilde{\mathbf{d}}} + \mathbf{P}(\boldsymbol{\sigma}) = \mathbf{f} \tag{2.30}$$

where

$$\mathbf{M} = \sum_e \mathbf{M}^{(e)} = \sum_e \int_{\Omega_e} \mathbf{N}^T \rho_S \mathbf{N} d\Omega \tag{2.31}$$

$$\mathbf{P}(\boldsymbol{\sigma}) = \sum_e \mathbf{P}^{(e)} = \sum_e \int_{\Omega_e} \mathbf{B}^{*T} \boldsymbol{\sigma} d\Omega \tag{2.32}$$

$$\mathbf{f} = \sum_e \mathbf{f}^{(e)} = \sum_e \int_{\Omega_e} \mathbf{N}^T \mathbf{t}_f d\Gamma \tag{2.33}$$

The integrals of Equations (2.31), (2.32) and (2.33) are generally performed numerically via (second order) Gauss-Legendre integration [123]. The vector $\mathbf{P}$ is referred to as *stress force* term.

Boundary conditions

In order to construct the solution from a weak form, two different boundary conditions can be imposed: traction conditions that are satisfied naturally by the variational form and displacement conditions, which must be imposed separately. A displacement condition requires imposing the value $\bar{\mathbf{d}}$ directly at the node

$$(\tilde{d}_a)_i = \bar{d}_i \tag{2.34}$$

where $(\tilde{d}_a)_i$ is the value at node a in the direction i.

Imposing a traction (different from zero) on the boundary Γ_t requires an integration over the surface of each element. Thus for a boundary node a it is necessary to evaluate the following integral

$$\mathbf{f}_a = \sum_e \int_{\Gamma_t} N_a \mathbf{t}_f d\Gamma_t \tag{2.35}$$

where e ranges over all elements belonging to Γ_t that include node a.

2.1.4 Time integration

To solve any transient problem, a discretization in time is necessary. Such approximation will transform the system described by Equation (2.30) into a set of algebraic equations. The solution of the problem is approximated as

$$\tilde{\mathbf{d}}(t_{n+1}) \approx \mathbf{d}_{n+1}, \qquad \dot{\tilde{\mathbf{d}}}(t_{n+1}) \approx \dot{\mathbf{d}}_{n+1}, \qquad \ddot{\tilde{\mathbf{d}}}(t_{n+1}) \approx \ddot{\mathbf{d}}_{n+1} \tag{2.36}$$

The force $\mathbf{P}$ may be written directly in terms of displacement $\mathbf{d}_{n+1}$

$$\mathbf{P}(\boldsymbol{\sigma}) = \int_{\Omega} \mathbf{B}^{*T} \boldsymbol{\sigma}(\mathbf{d}_{n+1}) d\Omega = \mathbf{P}(\mathbf{d}_{n+1}) \tag{2.37}$$

Equation (2.30) may now be written in a residual form for each time step t_{n+1}

$$\mathbf{R}_{n+1} = \mathbf{f}_{n+1} - \mathbf{M}\ddot{\mathbf{d}}_{n+1} - \mathbf{P}(\mathbf{d}_{n+1}) = 0 \tag{2.38}$$

We note that Equation (2.30) is not valid for the inelastic case, as vector $\mathbf{P}$ would depend on internal state variables. We point out that the system described above is second order in time as it presents second order time derivatives. A practical procedure for tackling this class of problems is the Newmark method [125], which relates the discrete displacement, velocity and acceleration by the following formulas

$$\mathbf{d}_{n+1} = \mathbf{d}_n + \Delta t \dot{\mathbf{d}}_n + (\frac{1}{2} - \beta_N)\Delta t^2 \ddot{\mathbf{d}}_n + \beta_N \Delta t^2 \ddot{\mathbf{d}}_{n+1} = \breve{\mathbf{d}}_n + \beta_N \Delta t^2 \ddot{\mathbf{d}}_{n+1} \tag{2.39}$$

$$\dot{\mathbf{d}}_{n+1} = \dot{\mathbf{d}}_n + (1 - \gamma_N)\Delta t \ddot{\mathbf{d}}_n + \gamma_N \Delta t \ddot{\mathbf{d}}_{n+1} = \breve{\dot{\mathbf{d}}}_n + \gamma_N \Delta t \ddot{\mathbf{d}}_{n+1} \tag{2.40}$$

where Δt=$t_{n+1} - t_n$ is the time step, $\breve{\mathbf{d}}_n$ and $\breve{\dot{\mathbf{d}}}_n$ are predicted variables depending only on the previous time step t_n, whilst β_N and γ_N are parameters for controlling the stability and

accuracy of the scheme. Importantly, the choice of parameter β_N leads to either explicit or implicit treatment of the time-related variables.

Explicit method

For β_N=0, it is possible to obtain

$$\mathbf{d}_{n+1} = \breve{\mathbf{d}}_n \tag{2.41}$$

and therefore, from Equation (2.30),

$$\mathbf{M}\ddot{\breve{\mathbf{d}}}_{n+1} = \mathbf{f}_{n+1} - \mathbf{P}(\breve{\mathbf{d}}_n) \tag{2.42}$$

The right hand side of Equation (2.42) is a known term at time step t_{n+1}; this leads to a linear system having $\ddot{\breve{\mathbf{d}}}_{n+1}$ as an unknown variable. The mass matrix may be approximated by a diagonal/lumped form

$$M^L_{ab} = \delta_{ab} \int_\Omega N_a d\Omega \tag{2.43}$$

In this way the inversion of $\mathbf{M}^L$ is trivial, leading to another diagonal matrix

$$\mathbf{M}^{L-1} = \begin{bmatrix} 1/M^L_{11} & & \\ & \ddots & \\ & & 1/M^L_{mm} \end{bmatrix} \tag{2.44}$$

where m is the total number of equations in the system. Such diagonalization allows the computation of $\ddot{\breve{\mathbf{d}}}_{n+1}$ explicitly via

$$\ddot{\breve{\mathbf{d}}}_{n+1} = \mathbf{M}^{L-1}\left[\mathbf{f}_{n+1} - \mathbf{P}(\breve{\mathbf{d}}_n)\right] \tag{2.45}$$

Computing the solution in explicit manner is extremely convenient when the priority is saving RAM memory, as no matrix needs to be stored. However, explicit schemes are *conditionally stable* and thus the maximum time step Δt must be lower than a critical time step Δt_{crit}, which is related to the wave propagation velocity across the element. For long transient problems, it is generally more efficient to adopt implicit schemes as they allow the employment of larger time steps.

Implicit method

In an implicit scheme it is generally convenient to use $\mathbf{d}_{n+1}$ as the basic variable and to compute $\dot{\mathbf{d}}_{n+1}$ and $\ddot{\mathbf{d}}_{n+1}$ by means of Equations (2.39) and (2.40). Thus, Equation (2.38) becomes

$$\mathbf{R}_{n+1} = \mathbf{f}_{n+1} - \frac{1}{\beta_N \Delta t^2}\mathbf{M}\left[\mathbf{d}_{n+1} - \breve{\mathbf{d}}_{n+1}\right] - \mathbf{P}(\mathbf{d}_{n+1}) = 0 \tag{2.46}$$

If the resulting system is linear, a vast variety of solution techniques can be employed ranging from direct methods, such as LU factorization, to iterative methods, such as Jacobi or conjugate gradient methods. For more details about linear system solvers we address the reader to reference [126].

If any term of Equation (2.46) is non-linear, an iterative process is required for solving the system. The Newton Raphson (NR) method represents the basis for most of the schemes used for this type of problems. In this method the residual at iteration $k+1$ can be written as

$$\mathbf{R}_{n+1}^{k+1} \approx \mathbf{R}_{n+1}^{k} + d\mathbf{R}_{n+1}^{k} = 0 \tag{2.47}$$

where the differential $d\mathbf{R}_{n+1}^{k}$ is

$$d\mathbf{R}_{n+1}^{k} = -\Big[\frac{1}{\beta_N \Delta t^2}\mathbf{M} + \frac{\partial \mathbf{P}_{n+1}}{\partial \mathbf{d}_{n+1}}\Big|_{n+1}^{k}\Big] d\mathbf{d}_{n+1}^{k} = -\mathbf{A}_{T,n+1}^{k} d\mathbf{d}_{n+1}^{k} \tag{2.48}$$

For each element the derivative of $\mathbf{P}$ may be computed as

$$\frac{\partial \mathbf{P}^{(e)}_{n+1}}{\partial \mathbf{d}_{n+1}}|^{k}_{n+1} = \int_{\Omega_e} \mathbf{B}^{*T} \mathbf{D}^{k}_{T} \mathbf{B}^{*} d\Omega \equiv \mathbf{K}^{k}_{T} \tag{2.49}$$

in which $\mathbf{D}^{k}_{T}$ is the *tangent modulus matrix* for the stress-deformation relation and $\mathbf{K}_T$ is the *tangent stiffness matrix*. We note that the load vector $\mathbf{f}_{n+1}$ has been considered independent of deformation. Combining Equations (2.47) and (2.49) yields

$$\mathbf{R}^{k}_{n+1} = \mathbf{A}^{k}_{T,n+1} d\mathbf{d}^{k}_{n+1} \tag{2.50}$$

from which it is possible to compute the displacement increment $d\mathbf{d}^{k}_{n+1}$. Direct elimination methods or iterative techniques can be used for solving the linear equations associated with each nonlinear iteration. Such a displacement correction is used for updating the solution via

$$\mathbf{d}^{k+1}_{n+1} = \mathbf{d}^{k}_{n+1} + d\mathbf{d}^{k}_{n+1} \tag{2.51}$$

$$\ddot{\mathbf{d}}^{k+1}_{n+1} = \frac{1}{\beta_N \Delta t^2} \left[\mathbf{d}^{k+1}_{n+1} - \breve{\mathbf{d}}_{n+1} \right] \tag{2.52}$$

$$\dot{\mathbf{d}}^{k+1}_{n+1} = \breve{\dot{\mathbf{d}}}_{n+1} + \gamma_N \Delta t \ddot{\mathbf{d}}^{k+1}_{n+1} \tag{2.53}$$

At the initial iteration of each time step, it is common practice to initialise the variable with the value of the previous time step

$$\mathbf{d}^{1}_{n+1} = \mathbf{d}_n \tag{2.54}$$

The iterative process continues until a convergence criterion of the form

$$\frac{\|\mathbf{R}_{n+1}^{k}\|}{\|\mathbf{R}_{n+1}^{1}\|} \leq \varepsilon_{tol} \tag{2.55}$$

is satisfied for a given tolerance ε_{tol}.

2.1.5 Strain energy function

A common approach to non-linear elasticity is defining a potential energy Ψ, also called *strain energy function*, which represents the energy stored in the material due to deformation. If this expression is known, it is possible to derive the constitutive relationships for $\boldsymbol{\sigma}$ and $\mathbf{D}_T$. The scalar quantity Ψ depends on the current deformation

$$\Psi = \Psi(\boldsymbol{\epsilon}) = \Psi(\mathbf{C}) \tag{2.56}$$

and is generally used for defining the *Second Piola-Kirchhoff* stress tensor $\mathbf{S}$

$$\mathbf{S} = 2\frac{\partial \Psi}{\partial \mathbf{C}} \tag{2.57}$$

This is related to the Cauchy stress tensor $\boldsymbol{\sigma}$ via

$$\boldsymbol{\sigma} = J^{-1}\mathbf{F}\mathbf{S}\mathbf{F}^{T} \tag{2.58}$$

Therefore the tangent modulus $\mathbf{D}_T$ can be computed, by using the *push forward* operator ϕ_* defined in [124], as

$$\mathbf{D}_T = J^{-1}\phi_*[2\frac{\partial \mathbf{S}}{\partial \mathbf{C}}] = J^{-1}\phi_*[4\frac{\partial^2 \Psi}{\partial \mathbf{C}\partial \mathbf{C}}] \tag{2.59}$$

2.2 Experimental methods

The contractile ability of an artery may be altered by specific pharmacological interventions, which primarily influence the ionic homeostasis of the smooth muscle cells where the contractile apparatus is located. Arterial smooth muscle cells may be thought as a system communicating with the external environment via a range of channel-specific ionic currents. These currents synergistically affect the levels of cytosolic Ca^{2+}, which is the catalyst for actin-myosin phosphorylation and cross-bridges kinetics. Importantly, Ca^{2+} is sequestered within intracellular stores, called Sarcoplasmic Reticulum (SR), able to regulate cytosolic Ca^{2+} concentrations. The scheme presented in Figure 2.3 shows a drug intervention specifically affecting a single cellular channel type. In this example the flux through CHAN1, is increased following the intervention. This single channel intervention will generally affect Ca^{2+} equilibrium in both the cytosol and the sarcoplasmic reticulum.

Drugs that have been used for experimental probing in the present study are phenylephrine (Phe), ryanodine (Rya) and cyclopiazonic acid (CPA). Each having a specific effect on vascular contractility based on their ability to affect Ca^{2+} homeostasis. From a modelling point of view, the action of Phe at the cellular level can be mimicked by simply increasing the cellular Ca^{2+} uptake via specific Ca^{2+} influx channels. Similarly, the action of CPA, an inhibitor of the SERCA pump responsible for re-filling the SR, and Ryanodine, which affects Ca^{2+} release from the SR, can each be simulated by varying the corresponding model parameters.

2.2.1 Preparation

In vitro experiments modulating vascular tissue tone can be carried out by using two different protocols: the cannulated method and the wire-myograph/ring method [127]. Each experimental approach can extract specific characteristics of the vessel physiological response. The main features of each method are reported below. In the ring preparation the vessel is segmented in a number of arterial rings of $\sim$2 *mm* in length. These rings are mounted on steel hooks/wires

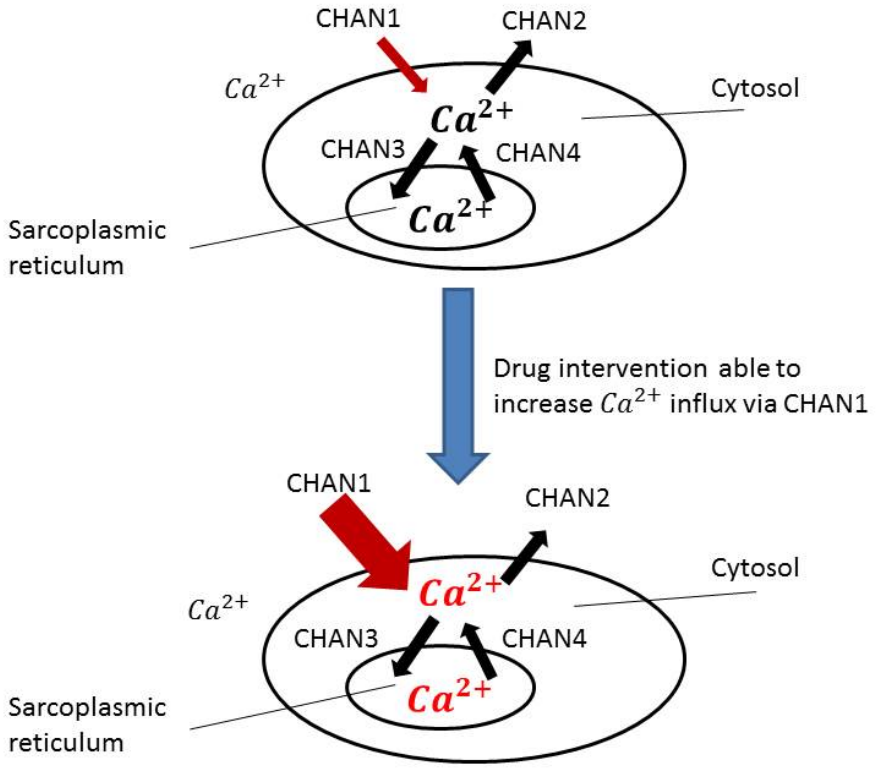

Figure 2.3: Ca^{2+} currents in the smooth muscle cell under a pharmacological intervention.

in a myograph containing normally oxygenated (95 % O_2-5 % CO_2) buffer, with the temperature kept constant around physiological values ∼37.0 ^oC. Figure 2.4 shows a scheme of the device. Prior to any pharmacological intervention, the ring is stretched radially by means of a loading mechanism connected to the wires in order to activate the contractile machinery of the media. This loading phase is often performed in a cyclic manner in order to avoid the rupture of the tissue. Once the luminal diameter reaches the optimal value, the hooks are fixed. From this stage onwards, the operating conditions are isoparametric and the force developed at the hooks is recorded for a constant inner diameter.

In the cannulated method an intact vascular segment is mounted on a pressure gauge, with both extremities cannulated with small glass cannulae. The upstream cannula is connected to a feeding reservoir, where different types of solution, including fluorescent dye tracer,

Figure 2.4: Wire myograph with four chambers (DMT, Aarhus, Dk).

may be contained. A downstream reservoir is connected to the other cannula in order to receive the perfusate. Figure 2.5 shows a cannulated rabbit central ear artery (G_0) and its generations (G_1 And G_2). The vessel is subjected to transmural pressure and is allowed to deform in diameter. The luminal pressure is recorded continuously by connecting a pressure transducer to the reservoir and may be adjusted by varying the relative height between the two reservoirs. Before starting any drug intervention, the cannulated segments and the lumen vessel may be superfused with a gas mixture containing high volume percentage of oxygen ($\sim 95\ \%\ O_2$). The temperature is maintained constant in order to recreate physiological tissue conditions. The chamber of the vessel is generally placed under a microscope, equipped with a fluorescent attachment, which allows the continuous measurement of the luminal cross-sectional area.

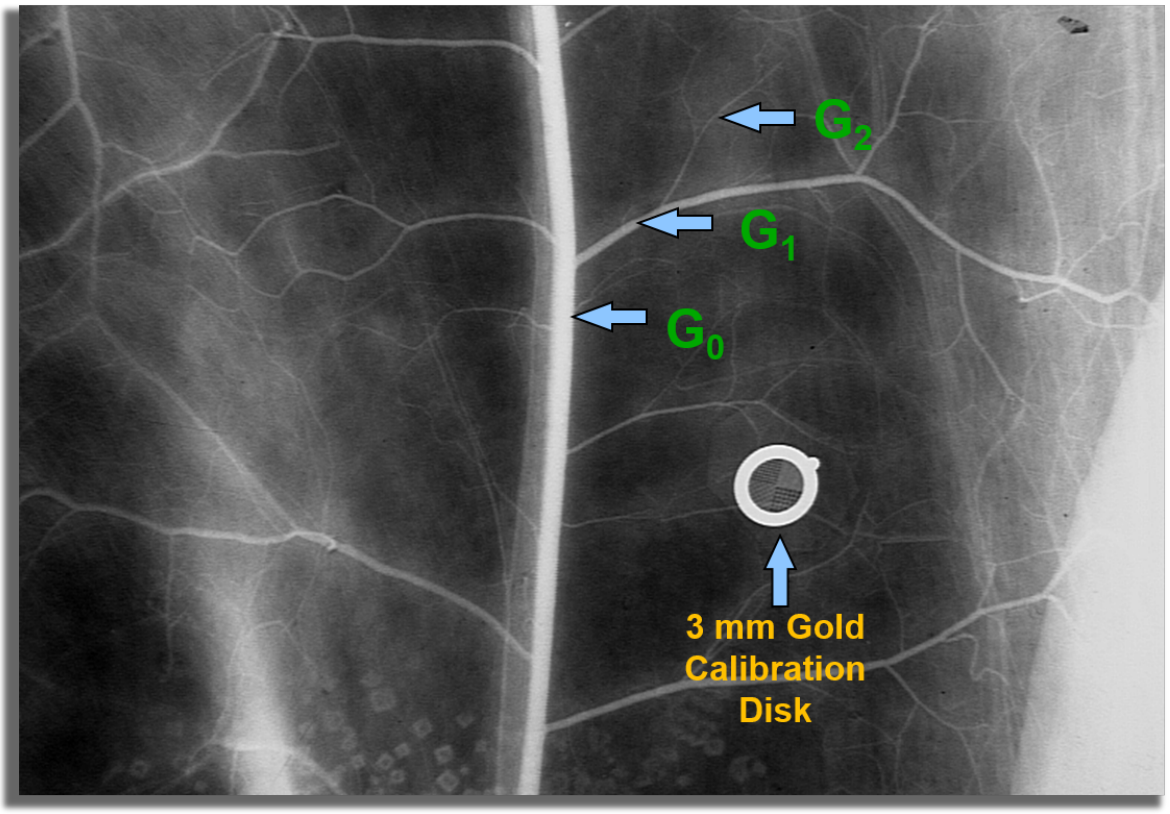

Figure 2.5: Rabbit central ear artery G_0 and its generations G_1 and G_2 (image generated in our laboratory).

2.3 Concluding remarks

Through this chapter we have provided the background on the modelling and experimental methodologies adopted in this study. The description of the theoretical/numerical strategy includes the mathematical formulation of a generic elastic problem and the subsequent discretization of the equations. For the space discretization, the finite element method is used, whilst for the time integration, both explicit and implicit techniques are presented. Details on the iterative solution procedure, typical of the non-linear finite element analysis (such as the Netwon-Raphson method), are also reported. In the latter part of the chapter, we have also outlined the experimental techniques which are commonly used for investigating arterial tissue contractility.

Chapter 3

Structural behaviour of the arterial wall with emphasis on the media layer

The vascular wall represents one fundamental component of the framework proposed in Section 1.3. The current chapter introduces a theoretical model able to reproduce the active structural response of the arterial tissue for various mechanical and biochemical conditions. The design of the proposed study allows us to focus on the solid tissues properties, avoiding any effect due to the interaction with the blood flow.

3.1 Background

As mentioned in Section 1.1, the arterial wall can be viewed as a control system able to regulate blood flow in order to satisfy local tissue oxygenation and nutrition requirements. This function is principally performed by spontaneous fluctuations in vascular tone and diameter, known as vasomotion, and is facilitated by the contractile apparatus located within the smooth muscle layer of the arterial wall [128]. Arteries form an anisotropic structure composed of three primary layers that perform distinct functions. The outermost layer, adventitia, is made of a tissue with fiber dispersion which confines the inner arterial structures. Active vascular contractility is governed by the smooth muscle cells (SMCs) located in the second layer, called media. The endothelium, a cellular monolayer lining the inner surface of the blood vessels, operates as an active interface which translates and amplifies the electrochemical signal between the blood flow and the medial layer. Much of the mechano-elastic properties of the vascular wall are conveyed by the external and internal elastic laminae, which lie between the three layers previously described [129]. The active contractile machinery of SMCs, driven by the phosphorylation of the actin-myosin motors, is catalyzed by intracellular Ca^{2+}. Under physiological conditions the intracellular Ca^{2+} concentration exhibits modest variations, however, when operative conditions deviate far from normal, such as in the case of injury or under pharmacological interventions, significant fluctuations in intracellular Ca^{2+} concentrations may occur that are reflected in the pronounced dynamical variation in vascular tone [130, 131, 132]. The complex structure and function of the arterial wall, even in the absence of blood flow, suggest that a mathematical/computational multi-physics approach is necessary in order to elucidate the dynamical intricacy of the underlying biological system

and to address questions that so far evade experimental investigations. To address this problem, a considerable number of multiscale/multi-component models for the arterial wall have been proposed in recent years [133, 134, 135, 136]. The development of models accounting for the elastic behaviour of the vascular wall has been based on extensive experimentation on the mechanical properties of vascular tissue under a variety of stress-strain conditions [29, 19, 47, 137, 138]. Based on these findings, several methodologies have been proposed in the last decade for simulating the smooth muscle contractility [51, 52, 53, 54, 55, 8]. In spite of considerable advances, the active component of vascular contractility, centered on the cellular Ca^{2+} dynamics of the smooth muscle has not been incorporated in a systematic way. This is particularly important as, according to classification by Fischer [139], the smooth muscle responsible for arterial vasomotion can be considered of the "fast type" from a mechano-elastic point of view, and is therefore markedly sensitive to the cellular wall dynamics. Detailed modelling of vasomotion as an expression of multi-channel ionic signalling that regulates arterial smooth muscle Ca^{2+} dynamics, has been proposed in [7, 56]. This work was extensively validated against a broad range of pharmacological interventions that specifically inhibit individual transport mechanisms. Extended cellular arrays of coupled smooth muscle cells were subsequently used to study the emergence of large scale synchronization [58].

3.2 Objectives

In the present work we employ a hybrid model, based on [7, 56], to integrate the active contractile behaviour of the media smooth muscle layer with the structural response of the arterial wall. The computational model developed incorporates two distinct scales: the cellular, where cytosolic Ca^{2+} catalyzes cross-bridge kinetics, and the continuous where the contractile units (CU), and therefore the arterial tissue, exhibit deformation and stress. Evaluation of the cross-bridges kinetics at cellular level relies on a modified version of the Hai and Murphy model [140, 141]. The cellular network finite element design follows the anatomical morphology of the tissue considered. For the mechano-elastic characterisation of the arterial wall we follow the work of [53, 55, 8]. From the structural point of view the tissue

is assumed to be a fiber reinforced hyper-elastic material [19, 50] and incompressibility is enforced by means of a standard penalty method. To validate the proposed methodology we employ an experimental protocol involving the placement of arterial rings excised from central rabbit ear arteries on a myograph that records vascular tone under isometric conditions. In the absence of fluid flow, the relationship between stress and deformation of the vascular structure becomes the only stress/deformation-generator mechanism. In addition, we are able to minimise the role of the endothelium on the contractile activity at the smooth muscle, by the administration of L-NAME, well before the onset of any experimental probing. L-NAME is shown to suppress NO production at the endothelium, while in the context of a central rabbit ear artery only a small NO-independent component remains [142]. The performance of the modelling framework is tested against a number of cellular Ca^{2+} dynamics scenarios, induced by drug interventions able to specifically modulate the SMCs contractile machinery.

The objectives of such work can be summarised as follows

- to introduce a novel multiscale methodology able to predict the structural response for a medium/small arterial vessel activated by drug interventions
- to analyse the effects of different level of cellular coupling on Ca^{2+} transport
- to test such model in a case study consisting of an arterial section under isometric conditions and subjected to different pharmacological interventions. Such interventions are able to stimulate, modulate and inhibit the contractility of the SMC tissue.

In the next two sections, a description of the arterial wall model is presented. A subsection is dedicated to each sub-model level followed by a description of the coupling strategy. Section 3.6 outlines the case study, including the experimental setup, the model initialisation and the comparison between experimental and theoretical/computational results. The concluding remarks are made in Section 3.7.

3.3 Modelling methodology of the media layer

In the following subsections a description of the multiscale modelling methodology for the arterial media layer is reported. The model accounts for the dynamics occurring at two different levels, each constituted by more than one subsystems. Figure 3.1 shows how each subsystem is allocated in the model and exchanges information with the others. At cellular level the Ca^{2+} dynamics is described by a model whose variables are the cytosolic Ca^{2+} concentration (χ), the store Ca^{2+} concentration (ζ) and the membrane potential (η). These variables' behaviour may be affected by drug interventions, which can be simulated by opening or blocking some specific cellular channels. The kinetics related to the formation of cross-bridges and subsequent contraction generation occurs within the cell in the contractile units. In this subsystem four different states that represent the kinetics are taken into account (n_M, n_{Mp}, n_{AM}, n_{AMp}). The rate associated with the phosphorylation of myosin and actin (either attached or detached) strongly depends on the intracellular Ca^{2+} concentration (χ). Since χ is a constant quantity over a cell, the variables representing the kinetic states are also assumed to be spatially uniform within a cell. The stress and deformation of the system are computed at continuous level. From the cellular level, the cross-bridges (CB) state describing the fractions of actin myosin filaments attached (n_{AM}, n_{AMp}) serves as an input for the contractile unit model. The mechano-chemical model of the CU also uses the variable λ, describing the deformation of the CU as an input. This quantity is computed as the stretch ratio in the tissue structure model and passed to the calculations at the next time step. All the calculations performed in the CU model depend on the internal variable $\bar{u}_{fs}$, which represents the current relative sliding between the filaments. The derivatives of the active free energy function with respect to the fourth invariant ($\frac{\partial \bar{\Psi}_a}{\partial \bar{I}_4}$, $\frac{\partial^2 \bar{\Psi}_a}{\partial \bar{I}_4^2}$), calculated at the CU subsystem, are then passed directly to the tissue structural mechanics model (displacement u and pressure p as variables), which evaluate the total (passive and active) tissue stress and deformation.

In the following sub-sections descriptions of the subsystems, coupling and solution procedure are reported. All the parameters of the cellular and continuous level models are listed, respectively, in Tables 3.1 and 3.2.

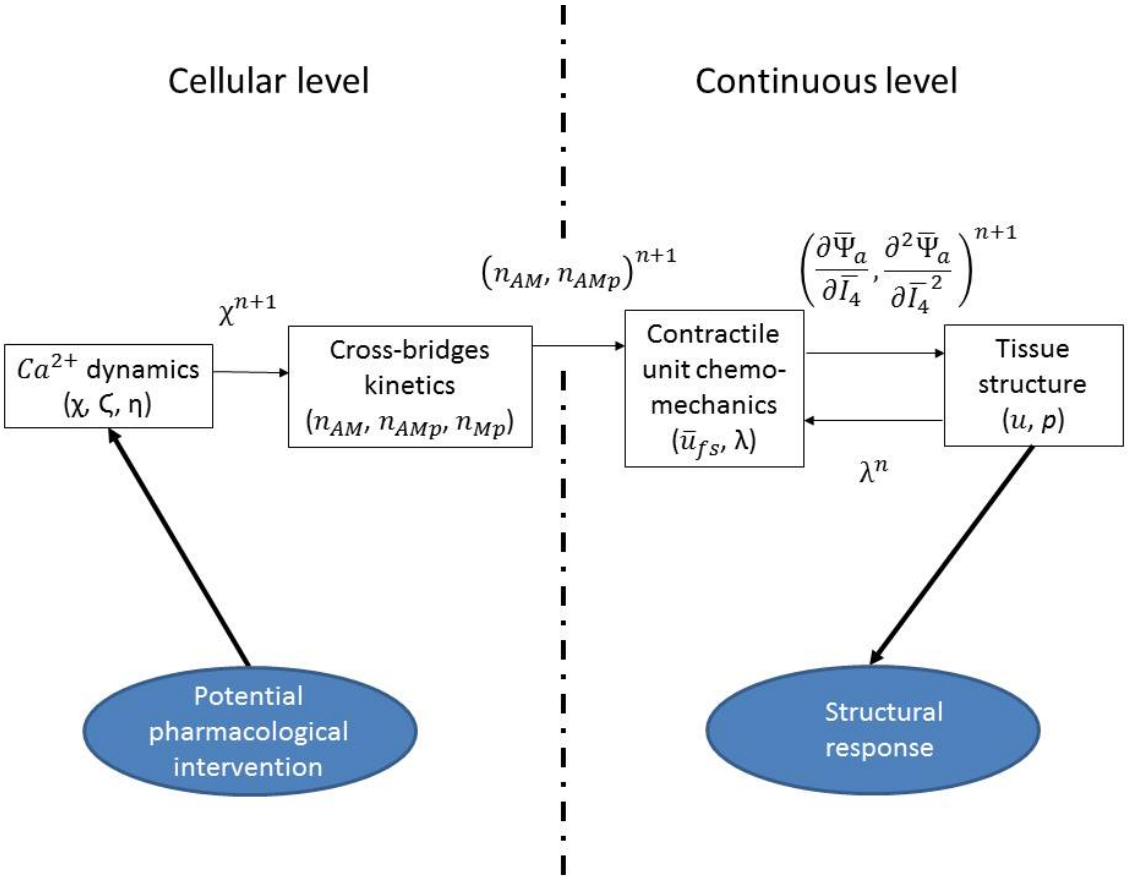

Figure 3.1: Levels and subsystems of the media multiscale model (from [2]). Thin arrows indicate quantities transmitted between the subsystems. Variables in the boxes are internal variables of the subsystems. Thick arrows represent the input and output of the model.

3.3.1 Cellular level model

Cellular Ca^{2+} dynamics

To describe the Ca^{2+} dynamics occurring in the SMCs, the model proposed in [7, 56] is adopted (see Figure 3.2). For a rigorous methodology we refer the reader to the previously mentioned works. Here, each cell is modelled as a system composed of a membrane and an intracellular oscillator. The mechanism underlying the intracellular variation of Ca^{2+} concentration is known as Ca^{2+} induced-Ca^{2+} release (CICR) from intracellular stores via ryanodine receptors (RyR). Calcium ions entering the cell via Voltage Operated Ca^{2+} Channels

(VOCCs) and Non-Specific Cation Channels (NSCCs) are primarily sequestered within intracellular stores via the sarco/endoplasmic reticulum Ca^{2+}-ATPase (SERCA) pump. A small subsequent rise in cytosolic Ca^{2+} will initiate a rapid Ca^{2+} by opening the ryanodine-sensitive Sarcoplasmic Reticulum (SR)-Ca^{2+} release channel. Once released into the cytosol, Ca^{2+} is partly pumped out of the cell, and partly re-sequestered by the stores, thus resetting the process that sustains oscillatory activity. Membrane potential is mainly influenced by the balance between K^+ and Cl^- gradients, and by the reverse mode Na^+-Ca^{2+} exchange (NCX), depending on whether the exchanger operates in forward or reverse mode.

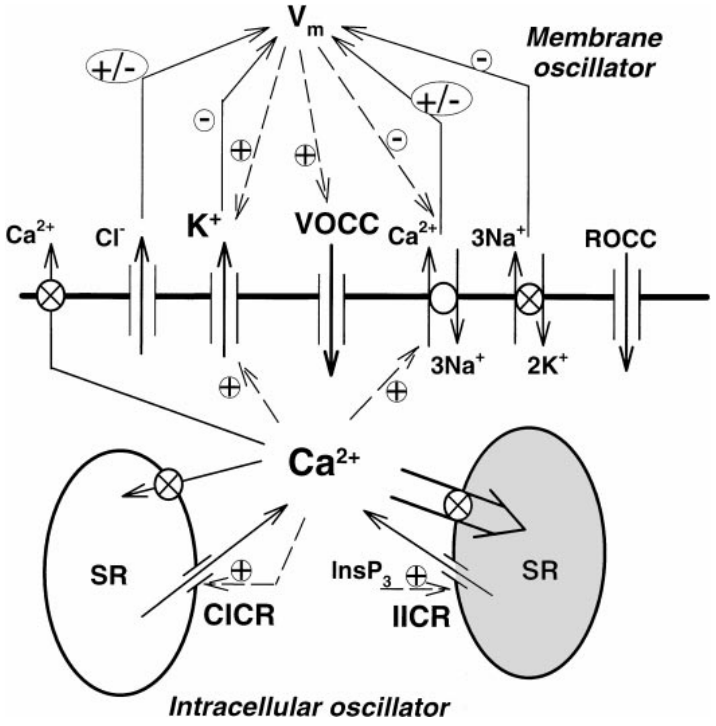

Figure 3.2: Cellular Ca^{2+} model constituted by the membrane and intracellular oscillators (from [2]).

Ionic channels The extracellular influx is the sum of the concentration currents Φ_A, Φ_S, Φ_V and Φ_N, which represent the Ca^{2+} permeable Non-Selective Cation Channels (NSCCs), Store-Operated Ca^{2+} Channels (SOCCs), Voltage Operated Ca^{2+} Channels (VOCCs) and reverse mode Na^+-Ca^{2+} exchange (NCX), respectively. In the present study the first current is assumed to be constant whilst the others depend on χ and η via the following equations:

$$\Phi_S(\zeta) = A_S(\zeta_S - \zeta) \tag{3.1}$$

$$\Phi_V(\eta) = E_{Ca}\left[\frac{\eta - z_{Ca1}}{1 + exp(-(\eta - z_{Ca1})/R_{Ca})}\right] \tag{3.2}$$

$$\Phi_N(\chi,\eta) = E_{NCX}\left[\frac{\chi}{\chi + x_{NCX}}(\eta - z_{NCX})\right] \tag{3.3}$$

where A_S, ζ_S, E_{Ca}, z_{Ca1}, R_{Ca}, E_{NCX}, x_{NCX} and z_{NCX} are cellular model parameters.The sarcoplasmic reticulum (SR) acts as an inner store, uptaking cytosolic Ca^{2+} by means of the SERCA pump ($\Phi_B(\chi)$) and releasing it into the cytosol through ryanodine-sensitive SR-Ca^{2+} release channel ($\Phi_C(\chi,\zeta)$). Store leakage ($\Phi_L(\chi,\zeta)$) is also accounted for. These fluxes are described through the following expressions:

$$\Phi_B(\chi) = B_{SR}\left[\frac{(\chi)^{n_{SR}}}{(\chi)^{n_{SR}} + (x_{SR})^{n_{SR}}}\right] \tag{3.4}$$

$$\Phi_C(\chi,\zeta) = C_{Ry}\left[\frac{\chi^{p_{Ry}}}{\chi^{p_{Ry}} + (x_{Ry})^{p_{Ry}}}\frac{(\zeta)^{m_{Ry}}}{(\zeta)^{m_{Ry}} + (y_{Ry})^{m_{Ry}}}\right] \tag{3.5}$$

$$\Phi_L(\zeta) = L_{SR}\zeta \tag{3.6}$$

where B_{SR}, n_{SR}, x_{SR}, C_{Ry}, p_{Ry}, m_{Ry}, x_{Ry}, y_{Ry} and L_{SR} are cellular model constants. The Ca^{2+} extrusion from cytosol by ATPase pump ($\Phi_D(\chi,\eta)$) is modelled as:

$$\Phi_D(\chi,\eta) = D_{EX}(\chi)^{k_{Ex}}(1 + \frac{\eta - z_{Ex}}{R_{Ex}}) \tag{3.7}$$

where D_{EX}, k_{EX}, z_{EX} and R_{EX} are cellular model parameters.

The chloride ($\Phi_{Cl}(\chi,\eta)$) and potassium ($\Phi_K(\chi,\eta)$) ion membrane fluxes are modelled as:

$$\Phi_{Cl}(\chi,\eta) = E_{Cl}\left[\frac{\chi}{\chi + x_{Cl}}(\eta - z_{Cl})\right] \tag{3.8}$$

$$\Phi_K(\chi,\eta) = E_K\left[(\eta - z_K)\frac{\chi}{\chi + \beta_K exp(-(\eta - z_K)/R_K)}\right] \tag{3.9}$$

where E_{Cl}, x_{Cl}, z_{Cl}, E_K, z_K, β_K and R_K are cellular model constants.

Intercellular communication In a cellular cluster each cell is able to communicate with its neighbours by exchanging Ca^{2+} ions (J_{Ca}) and voltage (J_V) gradients. If the cellular size (ratio between the volume and surface) is uniform along the grid, we can define the net fluxes $\bar{J}_{C,i}$ and $\bar{J}_{V,i}$ exchanged by the ith cell as:

$$\bar{J}_{C,i} = \alpha_C \sum_{j=1}^{nNeigh} (\chi_i - \chi_j) \tag{3.10}$$

$$\bar{J}_{V,i} = \alpha_V \sum_{j=1}^{nNeigh} (\eta_i - \eta_j) \tag{3.11}$$

where $nNeigh$ is the number of adjacent elements and $\bar{\alpha}_C$ and $\bar{\alpha}_V$ are the intercellular diffusion coefficients.

Global cellular balance The system variables χ, ζ and η evolve in time according to the following system of non linear ordinary differential equations:

$$\dot{\chi} = \Phi_A + \Phi_S(\zeta) - \Phi_V(\eta) + \Phi_N(\chi,\eta) - \Phi_B(\chi) + \Phi_C(\chi,\zeta) - \Phi_D(\chi,\eta) + \Phi_L(\zeta) + \bar{J}_{C,i} \tag{3.12}$$

$$\dot{\zeta} = \Phi_B(\chi) - \Phi_C(\chi,\zeta) \tag{3.13}$$

$$\dot{\eta} = -\gamma_m(\Phi_{Cl}(\chi,\eta) + 2\Phi_V(\eta) + \Phi_N(\chi,\eta) + \Phi_K(\chi,\eta)) + \bar{J}_{V,i} \tag{3.14}$$

where γ_m is a scaling factor relating the net movement of ion fluxes to the membrane potential.

Cross-bridges kinetics

Following [140, 141], the kinetics is described through four different states representing the fraction of i) CB attached and dephosphorylated (n_{AM}), ii) CB attached and phosphorylated (n_{AMp}), iii) CB detached and dephosphorylated (n_A) and iv) CB detached and phosphorylated (n_{Ap}). The temporal evolutions of these variables are described through the following system of ordinary differential equations:

$$\dot{n}_M = -\tau_1 n_M + \tau_2 n_{Mp} + \tau_7 n_{AM} \tag{3.15}$$

$$\dot{n}_{Mp} = \tau_1 n_M - (\tau_2 + \tau_3) n_{Mp} + \tau_4 n_{AMp} \tag{3.16}$$

$$\dot{n}_{AMp} = \tau_3 n_{Mp} - (\tau_2 + \tau_4) n_{AMp} + \tau_1 n_{AM} \tag{3.17}$$

$$\dot{n}_{AM} = \tau_2 n_{AMp} - (\tau_1 + \tau_7) n_{AM} \tag{3.18}$$

where τ_2, τ_3, τ_4 and τ_7 are the kinetic rate constants and τ_1 depends on the intracellullar Ca^{2+} concentration (χ) via:

$$\tau_1 = \tau_0 \left[\frac{\chi^2}{\chi^2 + {\chi_0}^2} \right] \tag{3.19}$$

where τ_0 and χ_0 are material constants. The four state kinetics is shown in Figure 3.3. Since n_M+n_{Mp}+n_{AMp}+n_{AM}=1, then one state (n_M in the current work) can be rewritten as dependent on the other three states, leading to a three independent variables system.

Parameter	Description	Value
Ca^{2+} **dynamics**		
Φ_A	Ca^{2+} influx via NSCC	0.6 (μM/s)
L_{SR}	SR leak rate constant	0.025 (s^{-1})
γ_m	Scaling factor	1.0 ($V/\mu M$)
A_S	SOCC parameter	0.0 (s^{-1})
ζ_S	SOCC parameter	4.0 (μM)
E_{Ca}	VOCC influx cell conductance	12.0 ($\mu M/(Vs)$)
z_{Ca1}	VOCC influx reversal potential	0.13 (V)
z_{Ca2}	VOCC influx half point of activation sigmoid	-0.024 (V)
R_{Ca}	VOCC influx max slope of activation sigmoid	0.0085 (V)
E_{NCX}	NCX cell conductance	43.8 ($\mu M/(Vs)$)
z_{NCX}	NCX reversal potential	-0.04 (V)
x_{NCX}	NCX half point of Ca^{2+}activation	0.5 (μM)
B_{SR}	SR uptake rate	400.0 (μM/s)
x_{SR}	SR uptake half point of ATPase activation sigmoid	4.4 (μM)
n_{SR}	SR uptake Hill coefficient	2 (-)
C_{Ry}	RyR CICR rate	1250.0 (μM/s)
y_{Ry}	RyR CICR half point of Ca^{2+} efflux sigmoid	8.9 (μM)
x_{Ry}	RyR CICR half point of CICR activation sigmoid	0.9 (μM)
m_{Ry}	RyR CICR Hill coefficient	2 (-)
p_{Ry}	RyR CICR Hill coefficient	4 (-)
D_{EX}	Ca^{2+} extrusion by ATPase pump rate	6.25 (μM/s)
z_{Ex}	Ca^{2+} extrusion by ATPase pump constant	-0.1 (V)
R_{Ex}	Ca^{2+} extrusion by ATPase pump constant	0.25 (V)
k_{Ex}	Ca^{2+} extrusion by ATPase pump constant	2
E_{Cl}	Cl^- channels cell conductance	65.0 ($\mu M/(Vs)$)
z_{Cl}	Cl^- channels reverse potential	-0.025 (V)
x_{Cl}	Cl^- channels Ca^{2+} sensitivity	0.0 (μM)
E_K	K^+ efflux cell conductance	43.0 (μM/s)
z_K	K^+ efflux reverse potential	-0.095 (V)
z_{Ca3}	K^+ efflux half point of activation sigmoid	-0.027 (V)
R_K	K^+ efflux max. slope of K_{Ca} activation sigmoid	0.012 (V)
β_K	K^+ efflux Ca^{2+} sensitivity of K_{Ca} channel activation sigmoid	0.0 (μM)
α_C	Cellular Ca^{2+} diffusivity	1.0 (s^{-1})
α_V	Cellular voltage diffusivity	1.0 (s^{-1})
CB kinetics		
τ_0	Kinetic model fitting parameter	1.7 (s^{-1})
τ_2	Kinetic rate	0.5 (s^{-1})
τ_3	Kinetic rate	0.4 (s^{-1})
τ_4	Kinetic rate	0.1 (s^{-1})
τ_5	Kinetic rate	1.0 (s^{-1})
χ_0	Kinetic saturation constant	0.6 (μM)
θ_k	Enhancement kinetics coefficient	1.0 (-)

Table 3.1: Table of parameters: Ca^{2+} dynamics and cross-bridges kinetics. Parametric values associated with Ca^{2+} dynamics are taken from [6], while parameters for CB kinetics are from [7].

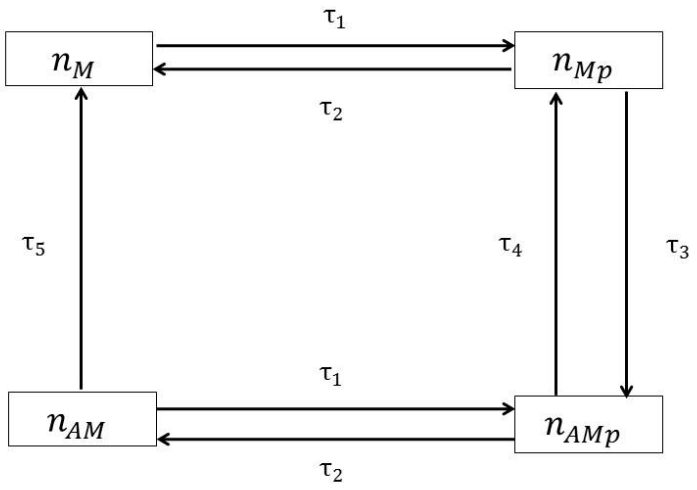

Figure 3.3: Four states of the actine-myosin cross-bridges kinetics (from [2]). Each arrows represents a transition between two states and it is associated to a specific kinetic rate. The arrow's direction indicates the final state of the transition.

3.3.2 Continuous level model

Contractile unit mechanics

In order to model the mechanics occurring at the CUs the works done by Murtada et al. [53, 55, 8] are followed. Both phosphorylated and de-phosphorylated attached cross-bridges (n_{AMp}, n_{AM}) are considered elastic with the same mechanical stiffness. As mentioned previously λ is the current stretch of the CU and it can also be defined as ratio between the current and reference CU length. Thus the average elastic elongation of the attached cross-bridge ($\bar{u}_{cb}$) can be calculated as:

$$\bar{u}_{cb} = \lambda - 1 - \bar{u}_{fs} \tag{3.20}$$

We note that both $\bar{u}_{fs}$ and $\bar{u}_{cb}$ are normalised with respect to the reference CU length and

are taken to be negative for contraction. The relative actin-myosin filament sliding $\bar{u}_{fs}$ in the CU can be driven either by the myosin power-stroke or the external force/deformation. This internal variable is thus decomposed into a chemical ($\bar{u}_{fs}^{chem}$) and mechanical ($\bar{u}_{fs}^{mech}$) component. The temporal evolution of the chemical component $\bar{u}_{fs}^{chem}$ can be derived from the following force balance:

$$(P_a + \alpha_a)(-\dot{\bar{u}}_{fs}^{chem} + \beta_a) = \beta_a(P_c + \alpha_a) \tag{3.21}$$

where P_c is the stress associated with the driving force from the cross-bridges whilst β_a and α_a are fitting parameters. The internal driving stress P_c depends on the contraction/relaxation state of the CU, ie,

$$P_c = \begin{cases} \bar{L}_0 \kappa_{AMp} n_{AMp} \;\; if \;\; P_a < \bar{L}_0 \kappa_{AMp} n_{AMp} \;\; \text{(contraction state)} \\ \bar{L}_0(\kappa_{AMp} n_{AMp} + \kappa_{AM} n_{AM}) \;\; if \;\; P_a > \bar{L}_0(\kappa_{AMp} n_{AMp} + \kappa_{AM} n_{AM}) \;\; \text{(relaxation state)} \\ P_a \;\; else \;\; \text{(neutral state)} \end{cases} \tag{3.22}$$

where κ_{AMp} is a parameter related to the force of a power-stroke of a single cross-bridge and κ_{AM} is related to the force-bearing capacity of a dephosphorylated cross-bridge during muscle extension.

The energy stored in the CU is related to the filament sliding resistance from the surrounding matrix (P_a), which can also be seen as the (averaged) first Piola-Kirchhoff stress over the CU:

$$P_a = \mu_a \bar{L}_0 (n_{AMp} + n_{AM}) \bar{u}_{cb} \tag{3.23}$$

where μ_a behaves like an active shear modulus and $\bar{L}_0$ defines the relative filament overlap

as a parabolic function of $\bar{u}_{fs}$:

$$\bar{L}_0 = (\bar{u}_{fs} - \frac{\bar{u}_{fs}^2}{2\bar{u}_{fs}^{opt}} + \bar{x}_0) \tag{3.24}$$

where $\bar{u}_{fs}^{opt}$ and $\bar{x}_0$ are material parameters.

Tissue structure

From the structural point of view the medial tissue is considered as a hyper-elastic fiber reinforced material, with the fibres aligned along the circumferential direction [19, 50]. The free energy function (Ψ^{med}) is split into volumetric (Ψ_{vol}^{med}) and isochoric components; the latter is then decomposed into active ($\bar{\Psi}_a^{med}$), accounting for the CU chemo-mechanics, and passive parts ($\bar{\Psi}_p^{med}$), ie,

$$\Psi^{med} = \Psi_{vol}^{med} + \bar{\Psi}_a^{med} + \bar{\Psi}_p^{med} \tag{3.25}$$

Both $\bar{\Psi}_a^{med}$ and $\bar{\Psi}_p^{med}$ depend on the CU stretch (λ), that can also be related to the fourth invariant as

$$\lambda = \sqrt{\bar{I}_4^{med}} = \sqrt{\mathbf{a}_0^{med} \cdot \bar{\mathbf{C}}\mathbf{a}_0^{med}} \tag{3.26}$$

where $\bar{\mathbf{C}}$ is the deviatoric part of the right Cauchy deformation tensor and $\mathbf{a}_0^{med}$ is the direction of the media unstressed fibre.

The active component depends directly on the cross-bridges attached (n_{AMp}, n_{AM}), ie,

$$\bar{\Psi}_a^{med} = \frac{\mu_a \bar{L}_0}{2}(n_{AMp} + n_{AM})(\bar{u}_{cb})^2 \tag{3.27}$$

The passive part is modelled as a classical anisotropic material with one fiber aligned with the smooth muscle cells as

$$\bar{\Psi}_p^{med} = \frac{\mu_p^{med}}{2}(\bar{I}_1^{med} - 3) + \frac{c_{p1}^{med}}{2c_{p2}^{med}}\{\exp[c_{p2}^{med}(\bar{I}_4^{med} - 1)^2] - 1\} \tag{3.28}$$

where μ_p^{med}, c_{p1}^{med} and c_{p2}^{med} are material constants.

Parameter	Description	Value
CU mechanics		
α_a	Material parameter	26.68 (kPa)
β_a	Material parameter	0.00833 (s^{-1})
κ_{AMp}	Parameter related to the force of a power-stroke of a single cross-bridge	203.71 (kPa)
κ_{AM}	Parameter related to the force-bearing capacity of a dephosphorylated cross-bridge during muscle extension	61.14 (kPa)
$\bar{u}_{fs}^{opt}$	Material parameter	0.48 $(-)$
$\bar{x}_0$	Material parameter	0.4255 $(-)$
Tissue structure		
κ	Bulk modulus	4.0 (kPa)
μ_a	Active shear modulus	5301.0 (kPa)
μ_p	Passive shear modulus	0.84 (kPa)
c_{p1}	Material parameters	3.15 (kPa)
c_{p2}	Material parameter	0.035 (-)

Table 3.2: Table of parameters: Contractile units mechanics and tissue structure. All parametric values reported in the table are from [8].

Details on Cauchy stress calculation for the media layer can be found in the Appendix.

3.4 Modelling methodology of the adventitia layer

3.4.1 Tissue structure

This layer, that is passive, is modelled as a Neo-Hookean material reinforced by two family of collagenous fibres, characterised by two reference direction vectors $\mathbf{a}_{0i}^{adv}$ with i=4,5. Under high pressure regimes, the resistance to stretch is mostly borne by these fibres and such mechanical response is modelled by means of an anisotropic function [19].

The free energy function of the adventitia (Ψ^{adv}) is constituted by a volumetric and an isochoric components

$$\Psi^{adv} = \Psi_{vol}^{adv} + \bar{\Psi}^{adv} \tag{3.29}$$

The volumetric part is assumed to be proportional to the energy potential as

$$\Psi_{vol}^{adv} = \kappa \frac{(J-1)^2}{2} \tag{3.30}$$

where κ and J are respectively the penalty number and the determinant of the deformation tensor $\mathbf{F}$ ($J = \det\mathbf{F}$). The isochoric strain energy function of the adventitia is written as

$$\bar{\Psi}^{adv} = \frac{\mu_p^{adv}}{2}(\bar{I}_1^{adv} - 3) + \sum_{i=4,5} \frac{c_{p1}^{adv}}{2c_{p2}^{adv}} \{exp[c_{p2}^{adv}(\bar{I}_i^{adv} - 1)^2] - 1\} \tag{3.31}$$

where μ_p^{adv}, c_{p1}^{adv} and c_{p2}^{adv} are material parameters, whilst the invariants $\bar{I}_i^{adv}$, which describe the deformation of the fibres, are computed as

$$\bar{I}_i^{adv} = \mathbf{a}_{0i}^{adv} \cdot \bar{\mathbf{C}}\mathbf{a}_{0i}^{adv} \quad with \;\; i = 4,5 \tag{3.32}$$

Fibre direction under the current deformation are computed as

$$\mathbf{a}_i^{adv} = \bar{\mathbf{F}}\mathbf{a}_{0i}^{adv} \quad with \;\; i = 4,5 \tag{3.33}$$

Details on Cauchy stress calculation for the adventitia layer can be found in the Appendix.

3.4.2 Multiscale coupling and solution procedure

Space Discretization

Each level of the framework is discretized by a spatial grid. The cellular network grid reflects the morphology of the tissue, so that each element represents a "real" cell. For the continuous level, a finite element discretization of the domain was carried out. By assigning each smooth muscle cell to each finite element the connectivity of the cellular grid and the mesh coincide. The variables computed at the cellular level (i.e. Ca^{2+} dynamics and CB kinetics) may be considered as internal variables in the finite element framework. The contractile unit variables ($\bar{u}_{fs}$, λ, etc.) are evaluated at the Gauss integration points of the finite element, in order to take into account the spatial diversity of deformation over the element. For the structural problem, staggered finite elements are used in which the displacement field is interpolated linearly whilst the pressure and dilation coefficient are constant over each element. The non-linear problem is solved via a classical Newton-Raphson procedure.

Time integration

The models/subsystems constituting the framework are solved in a block segregated fashion, as depicted in Figure 3.1. As there is no feedback between the subsystems, it is possible to employ a different and optimal time integration strategy for each of them. Thus, the Ca^{2+} dynamics is solved by an explicit and adaptive scheme (Runge Kutta Merson), whereas the time-dependent equations for both the CB kinetics and CU mechanics are solved by the Forward Euler method (as in [8]). Note that for computing the CU mechanics the deformed

configuration (expressed in terms of λ) of the previous time step is used. By comparison, the tissue mechanics problem is solved in an implicit manner. The methodology proposed is valid for either quasi static or dynamic problems, depending on whether the case considered is under isometric or non-isometric conditions. The same time step was employed for all subsystems. The solution procedure is presented step by step in Table 3.3.

Cellular level (solving consecutively two linear problems for n_{AM} and n_{AMp})

1. Loop over the temporal discretization $\Delta\tau_1$ points
2. Loop over the cell framework (the FE mesh in the current work)
3. Computing Ca^{2+} variables explicitly (Runge-Kutta) from Equations (3.12,3.13,3.14)
4. Compute rate constant τ_1
5. Compute CB kinetic states explicitly (Forward Euler) from Equation (3.15, 3.16,3.17,3.18)
6. $t = t + \Delta\tau_1$

Continuous level (solving a non linear problem for u and p)

1. Loop over the temporal discretization $\Delta\tau_2$ points
2. Newton-Raphson (NR) algorithm
3. Loop over the finite elements
4. If it is the first NR iteration
   then interpolate CB kinetic states in time from $\Delta\tau_1$ to $\Delta\tau_2$
   (also in space if cellular and FE meshes do not match)
5. Loop over the Gauss integration points
6. Compute CB mechano-chemical variables, Equations (3.20,3.23,3.24,3.21,3.22)
7. Compute first and second order derivatives of $\bar{\Psi}_a$ with respect to $\bar{I}_4$
8. Compute total stress and elastic moduli
9. Assemble stiffness matrix and residual vector
10. Solve linearized system and variables updating
11. If the residual error condition is satisfied
    then $t = t + \Delta\tau_2$ and go to 2.

Table 3.3: Solution procedure for evaluating all the system variables along the time (from [2]).

3.5 Experimental study

The pharmacological studies employed in the validation of the modelling methodology along with the model setup developed to reproduce the experimental settings are reported below.

3.5.1 Experimental protocol

Isolated rabbit ears were obtained as described previously [128], the central ear artery was removed and cleaned of adherent fat and connective tissue. To measure force, 2 *mm* wide rings were mounted on 0.25 *mm* diameter steel hooks in a myograph (model 610M, Danish Myotechnology, Aarhus, Denmark) containing oxygenated (95% O_2; 55% CO_2) Holman's buffer (composition in *mM*: $NaCl$ 120, KCl 5, NaH_2PO_4 1.3, $NaHCO_3$ 25, $CaC(12)$ 2.5, glucose 11, and sucrose 10) at 37.0 ^oC. Prior to any pharmacological interventions the rings were maintained at a resting tension of 1 *mN* over a 60 *min* equilibration period, with frequent readjustments in baseline tension to correct for stress relaxation. The average inner and outer diameters of the annular segments were approximately 0.7 and 0.8 *mm*, respectively (see Figure 3.4a). Following the loading phase, the arterial rings obtained the deformed configuration shown in Figure 3.5, by considering a Cartesian reference system, the loading is applied along the x direction.

In order to considerably reduce the effect of the endothelium as a control mechanism on the smooth muscle contractile apparatus, preparations were incubated for 30 *min* with both the endothelial nitric oxide synthase inhibitor NG-nitro-l-arginine methyl ester (L-NAME, 300 μM) and the cyclooxygenase inhibitor indomethacin (10 μM) to inhibit prostanoid formation. Rings were then constricted with phenylephrine (Phe, 1 μM) and, once constrictor responses had reached a stable plateau, cumulative concentration-response curves to CPA and/or ryanodine were obtained.

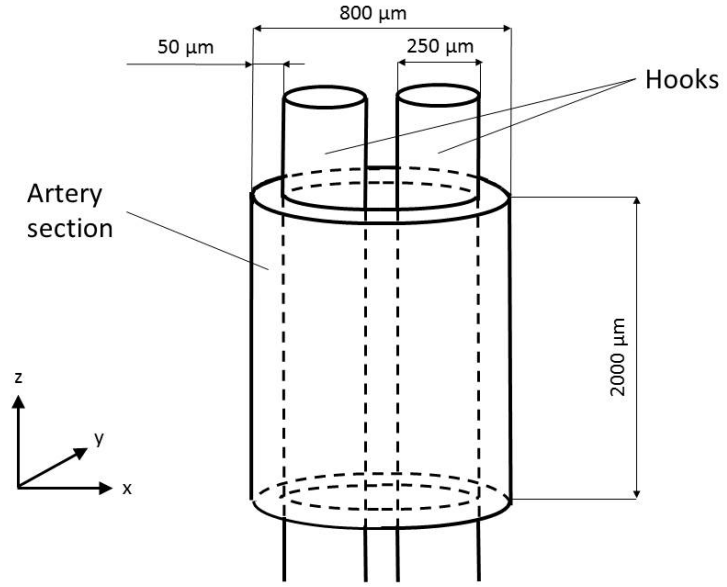

(a)

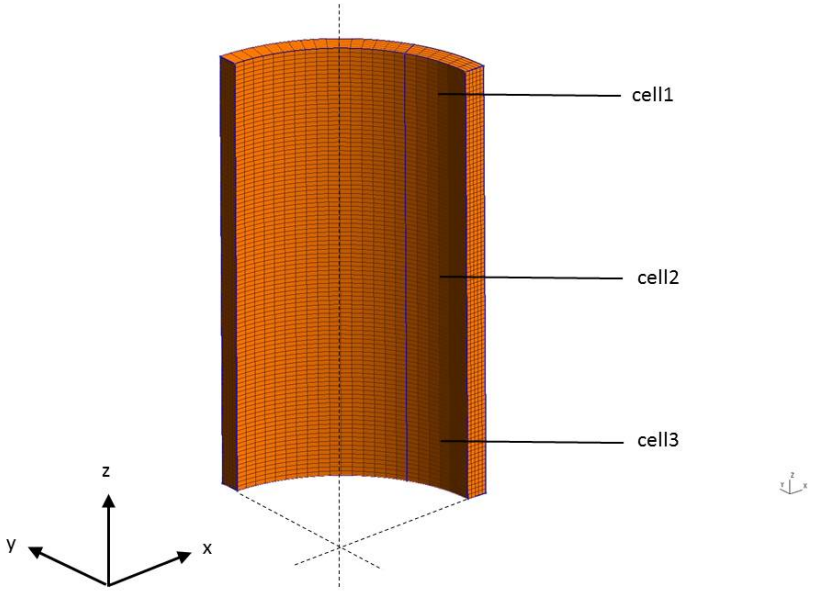

(b)

Figure 3.4: Figure 3.4a (top): Size and geometry of the arterial section set in the myograph through two hooks. Figure 3.4b (bottom): Location of cell1, cell2 and cell3 in the 3D mesh representing one eight of the arterial section (from [2]).

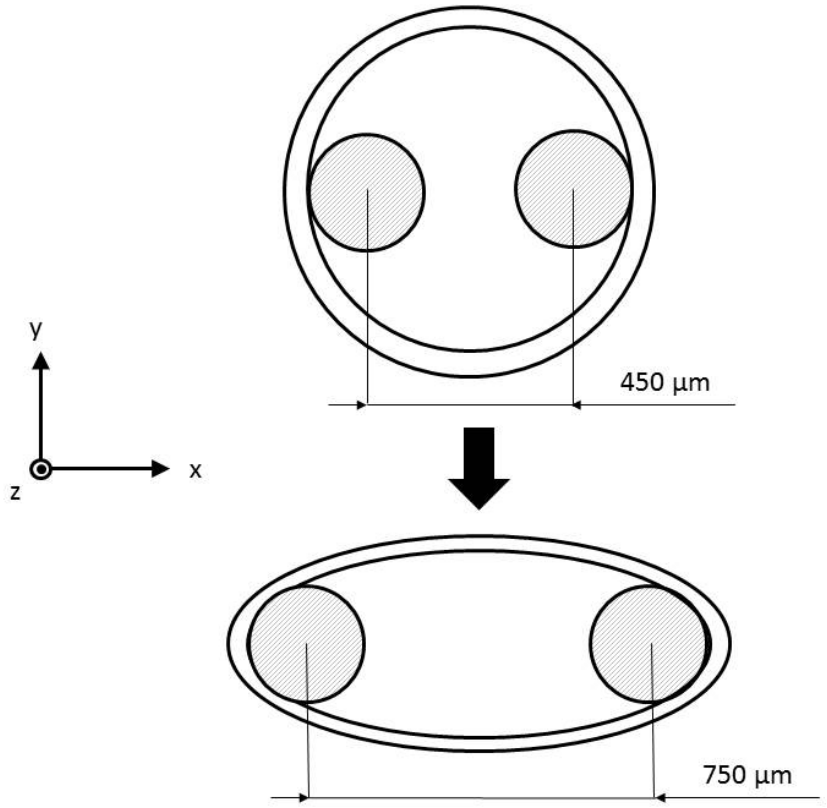

Figure 3.5: Arterial section deformation during the loading phase, initial (top) and stretched (bottom) configurations (from [2]).

3.5.2 Model settings

From a structural point of view, each ring is assumed to deform symmetrically with respect to the x plane, while no translations along y and in the longitudinal direction (z) are expected. The system can thus be reduced to one eighth of the ring. A finite element mesh consisting of 11000 linear hexahedral elements is used in the calculations (see Figure 3.4b). For the cellular cluster, each cell was associated with one element. At sub-cellular level we associate a CU to each Gauss integration point. The values for all model parameters can be found in Tables 3.1 and 3.2. To account for cellular variability (e.g. size, rates of Ca^{2+} uptake/extrusion) the term corresponding to the influx via Ca^{2+} permeable non-selective cation channels (Φ_A) is randomised with a normal distribution (mean value=1.0 $\mu M/s$ and

standard deviation=0.1 $\mu M/s$). For all simulations, the initial values for χ, ζ and η are set equal to 0.1 μM, 0.2 μM and -0.02 mV, respectively. The reference set of kinetic rates (τ_0, τ_2, τ_3, τ_4, τ_5) necessary for solving the cross-bridge dynamics are taken from [7].

3.6 Results

3.6.1 Cellular coupling conditions

The proposed analysis is carried out for varying levels of cellular coupling in order to establish the dependency between the diffusion coefficients α_C, α_V and the global Ca^{2+} dynamics. These simulations are carried out for an unloaded ring configuration. The variables associated with the Ca^{2+} dynamics are monitored for three different cells: cell1, cell2 and cell3 (see Figure 3.4b). In Figure 3.6 the time evolution of χ for (α_C,α_V) equal to 0.0, 0.1, 1.0 s^{-1} are shown. The plot shows clearly that coupling does not affect significantly the amplitude of χ signal. The cellular coupling tends to synchronise the χ beating pattern along the cluster.

The spatial distribution of χ for two coupling levels (weakly coupled: (α_C,α_V)=0.1 s^{-1}, strongly coupled: (α_C,α_V)=1.0 s^{-1}) at two different time instants (t=0.1 s, t=6.0 s) are shown in Figure 3.7. It is evident that coupling promotes the formation of travelling waves along the annular domain.

3.6.2 Framework validation

A range of pharmacological interventions associated with the activation/inhibition of specific cellular mechanisms was employed for the validation of the model. To mimic the diffusion of pharmacological agents, parametric changes were applied in a graded fashion to all the cells constituting the network. The interventions selected (i.e. phenylephrine, CPA and ryanodine), are associated with the modulation of the cellular Ca^{2+} homeostasis which is reflected in the contractile state of the smooth muscle. The actions of these pharmacological

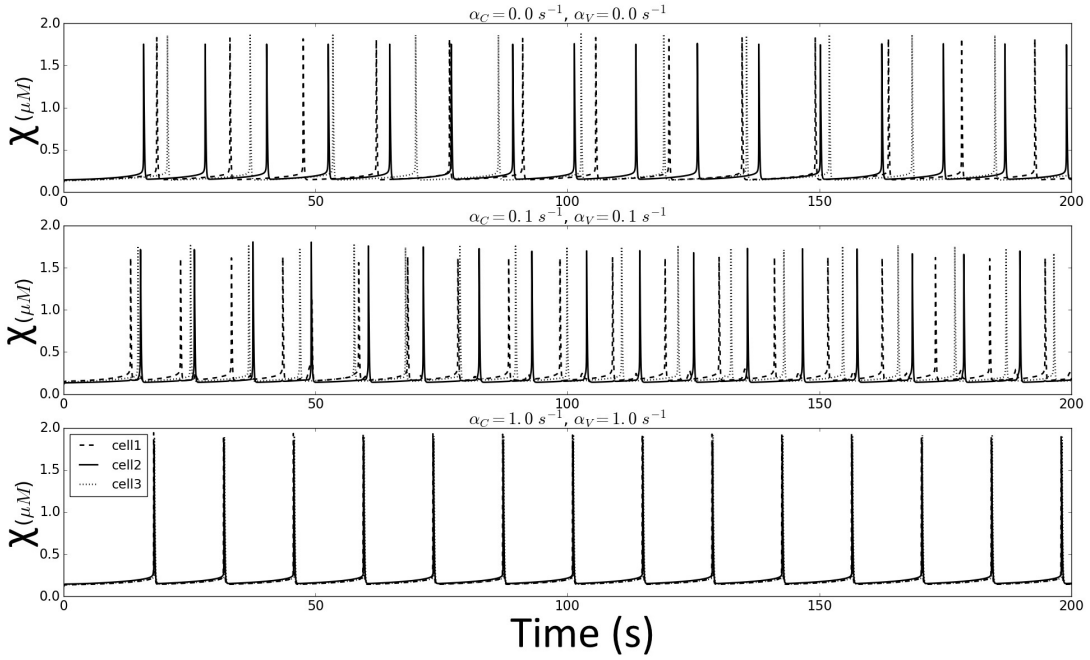

Figure 3.6: Temporal evolutions of χ at three different cells (labelled cell1, cell2, cell3) for different α_C and α_V (from [2]).

probes were simulated by the gradual variations of the associated model parameters, reported in Table 3.4. The actin and myosin filaments are assumed to be detached for t=0 s (n_M =0.5 and n_{Mp} =0.5), whilst the initial $\bar{u}_{fs}$ is set equal to 0 for each CU. Cells are assumed to be strongly coupled with (α_C,α_V) set equal to 1.0 s^{-1}. The simulated drug interventions were performed only after the Ca^{2+} and CB variables reached stationary conditions. For each plotted result the drug intervention occurred at t=0 s unless otherwise stated.

Parameter	Phenylephrine	CPA	Ryanodine
Φ_A (μM s^{-1})	0.6 $\rightarrow$ 4.2 in Var s	0.8	0.8
B_{SR} (μM s^{-1})	400	400 $\rightarrow$ 200 in 1000 s	400
C_{Ry} (μM s^{-1})	1250	1250	1250 $\rightarrow$ 312.5 in 2000 s
A_S (s^{-1})	0.0	0.0	0.1
θ_k	1.0	30.0	0.5

Table 3.4: Ca^{2+} dynamics and CB kinetics parameters for simulating the drug interventions. The variation of parameters is carried out linearly.

As the ring is clamped at the hooks, the resultant between internal and external forces at the

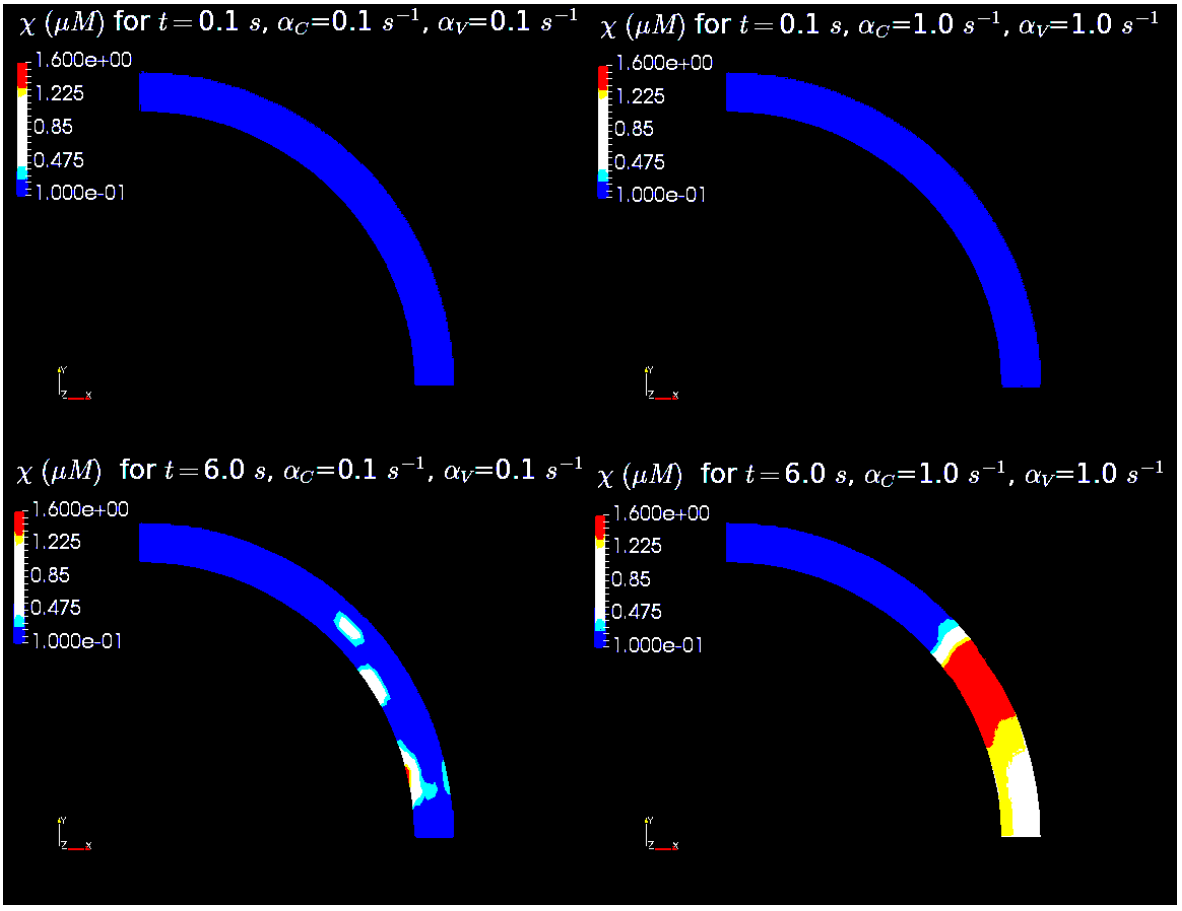

Figure 3.7: Temporal evolutions of χ along the spatial domain for (α_C,α_V)=0.1 s^{-1} and (α_C,α_V)=1.0 s^{-1} (from [2]). At the top of the figure χ is showed at t=0.1 s for a weakly coupled cluster of cells (left) and a strongly coupled cluster one (right). At the bottom part the figure χ is shown at t=6.0 s for a weakly coupled cluster of cells (left) and a strongly coupled one (right).

nodes in contact with the hooks must be null. In the current study we are mainly interested in the global force developed at the hooks, which can be seen as the sum of nodal contributions along the contact surface. In addition to this, we consider also the force developed locally at cell1, which is assumed to be proportional to the sum n_{AMp}+n_{AM} [7].

Phenylephrine intervention

Phenylephrine is a selective agonist of α-adrenergic receptors, associated with vasoconstriction. The action of phenylephrine at cellular level was modelled by increasing the cytosolic Ca^{2+}

influx via NSCCs. A more complete picture of the action of phenylephrine involves an initial Ca^{2+} release from the sarcoplasmic reticulum, via inositol 1,4,5-trisphosphate-sensitive Ca^{2+} release channels (IP3R channels), followed by sustained Ca^{2+} influx into the cytosol through NSCCs [143]. Although Ca^{2+} release from intracellular stores affects the superficial oscillatory characteristics of the response, it has been previously shown theoretically that it cannot account for sustained increase in arterial tone [7]. The prolonged contractile response is therefore due to the raised levels of intracellular Ca^{2+} which in turn promote the formation of actin/myosin cross-bridges, reflected in increase of variables n_{AMp} and n_{AM}. To simulate the action of phenylephrine, coefficient Φ_A was increased linearly from 0.5 to 2.5 $\mu M/s$. Two different drug dilution times (Δt_{dil} =50 and 100 s) were used, as shown in Figure 3.8. With the increasing of the cytosolic Ca^{2+} uptake, χ in cell1 starts beating periodically. This pattern is reflected also in the store Ca^{2+} concentration variations (Figure 3.8). As expected, higher Δt_{dil} involves longer transient before reaching stationary conditions.

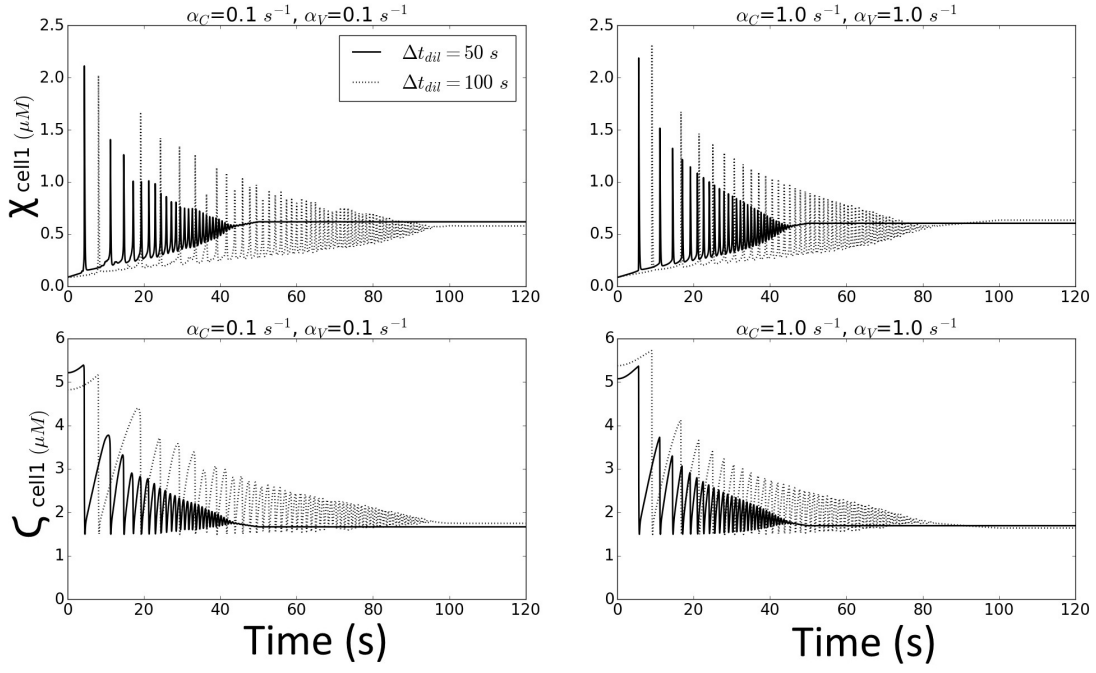

Figure 3.8: Time evolutions of χ cell1 and ζ cell1 for a simulated phenylephrine intervention (from [2]). The results are shown for different drug dilution times (Δt_{dil}=50 and 100 s) and coupling conditions ((α_C,α_V)=0.1 s^{-1} and (α_C,α_V)=1.0 s^{-1}).

The forces generated by this intervention, normalised with respect to the force developed at the beginning of the intervention, are shown in Figure 3.9, where three responses are shown for different dilution times (Δt_{dil}) and different cellular coupling (α_C, α_V). By comparison to the simulated results, it appears that the drug was able to activate the muscle tissue at a dilution time $\Delta t_{dil} \sim 50\ s$. We also observe that the final magnitude of the simulated and measured force is very similar.

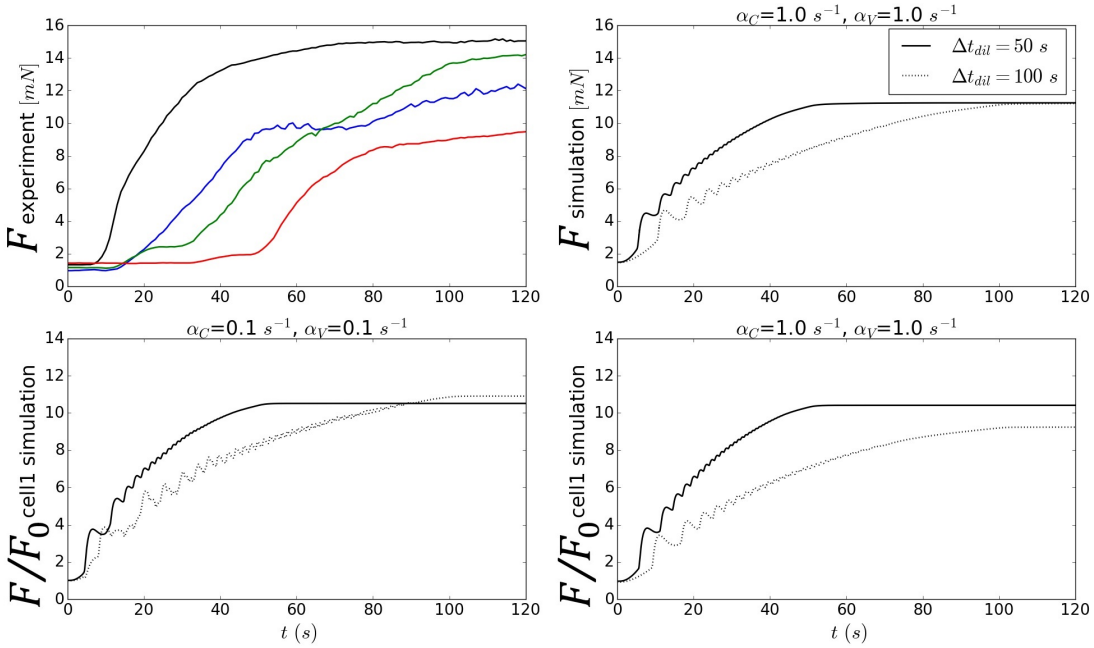

Figure 3.9: Time evolutions of the experimental and simulated forces at the hooks for a simulated phenylephrine intervention (from [2]). Experimental forces (coloured lines) are plotted for four different ring measurements. The theoretical results are shown for different drug dilution times (Δt_{dil}=50 and 100 s) and coupling conditions ((α_C,α_V)=0.1 s^{-1} and (α_C,α_V)=1.0 s^{-1}). The cellular forces values are normalised with respect to the initial force F_0.

CPA intervention

Cyclopiazonic acid (CPA) is an inhibitor of the SERCA pump, preventing refilling of the store and is thus associated with Ca^{2+} store depletion. The effect of CPA, in terms of modulating the intracellular Ca^{2+} oscillator, is highly dose-dependent as shown previously [144].

CPA was administered through a sequence of concentration increases from 10 μM up to 30 μM. For simulation purposes, the action of CPA was reproduced by linearly decreasing coefficient B_{SR} from 400 to 350 μM in 2000 s. In both the experiment and simulations CPA caused a small reduction in the oscillatory amplitude, while a regular waveform was maintained throughout the intervention (Figure 3.10). A comparison between the experimental and simulated time series is shown in Figures 3.11 and 3.12.

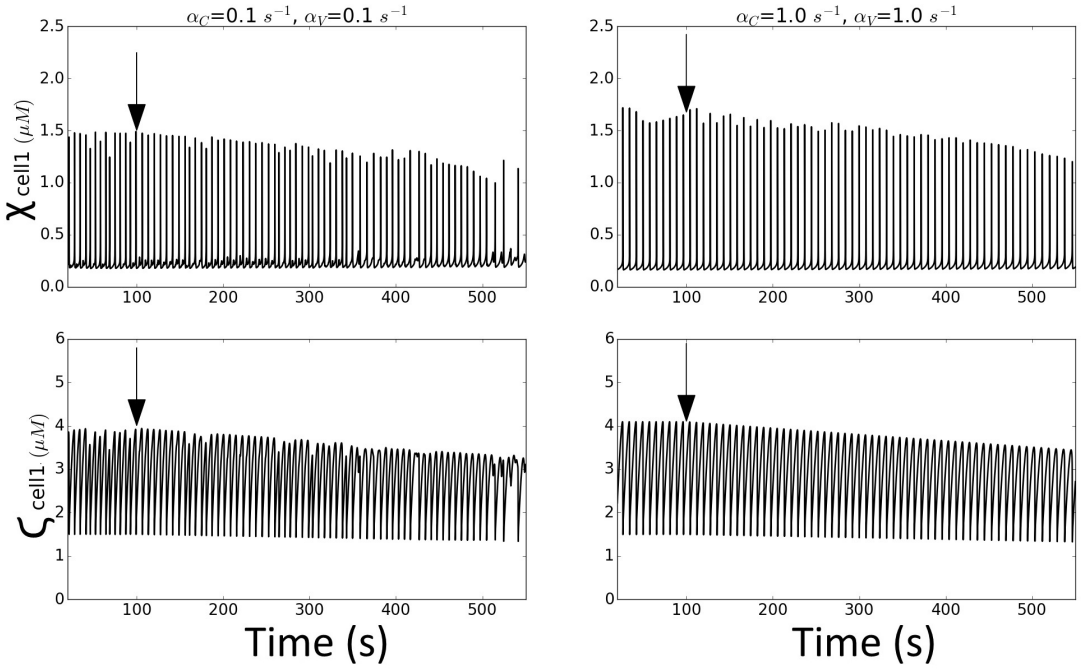

Figure 3.10: Time evolutions of χ cell1 and ζ cell1 for a simulated CPA intervention for different coupling conditions ((α_C,α_V)=0.1 s^{-1} and (α_C,α_V)=1.0 s^{-1}) (from [2]). Black arrows show the intervention time.

The shrinking effect on the oscillatory amplitude is visible in both curves, while the period of the oscillations is almost the same.

Ryanodine intervention

Increasing concentrations of ryanodine (from 10 μM after 100 s up to 30 μM) were administrated at each arterial sample. As discussed previously, the action of ryanodine can be simulated

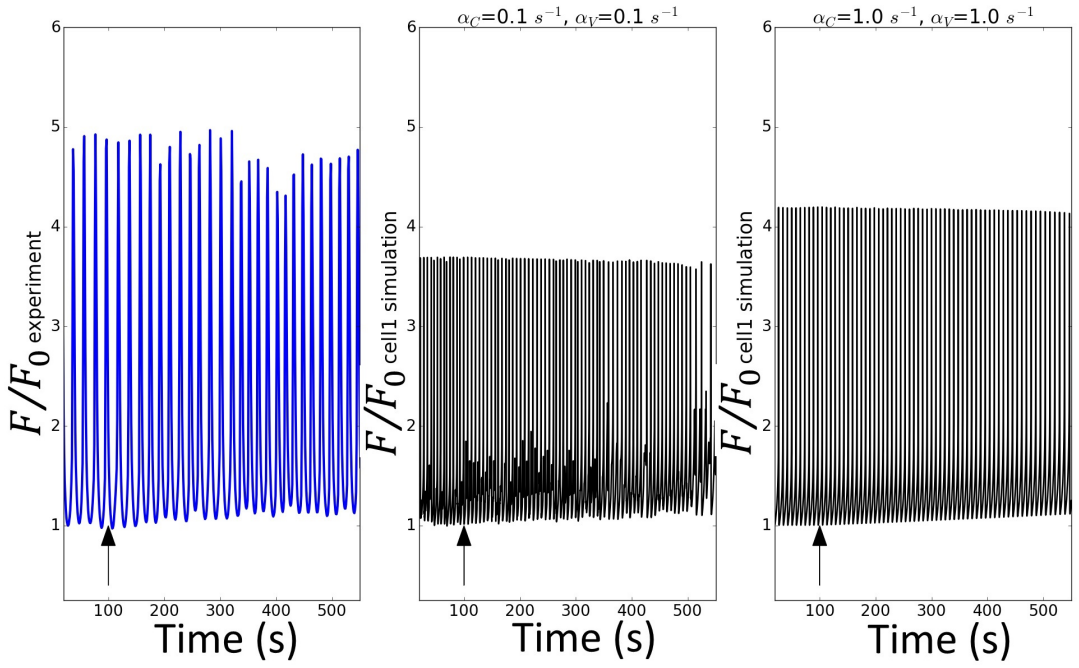

Figure 3.11: Time evolutions of the experimental and simulated cellular forces at the hooks for a simulated CPA intervention for different coupling conditions ((α_C,α_V)=0.1 s^{-1} and (α_C,α_V)=1.0 s^{-1}) (from [2]). Black arrows show the intervention time. The plotted values are normalised with respect to the initial force F_0.

in different ways depending on the dosage [7, 56]. This is due to the complex multi-stage configuration of the ryanodine receptor tetramer. For the concentrations of ryanodine used in the present study, it is accepted that the compound will block Ca^{2+} release from the sarcoplasmic reticulum in a concentration related fashion. The action of ryanodine was simulated according to [7], by decreasing linearly the coefficient C_{Ry} at t=100 s from 1250 $\mu M/s$ down to 312.5 $\mu M/s$. The temporal evolution of variables χ cell1 and ζ cell1 within the reference cell is shown in Figure 3.13 for different cellular coupling conditions ((α_C,α_V)=0.1 s^{-1} and (α_C,α_V)=1.0 s^{-1}). Gradual attenuation of Ca^{2+} release via the ryanodine receptor channels is associated with a decrease in frequency. This pattern is consistent with experimental observations, presented in Figures 3.14 and 3.15.

The forces obtained from the model are compared against the experimental values in Figures 3.14 and 3.15. In this case coefficient θ_k was equal to 0.5. The pattern of the forces follows

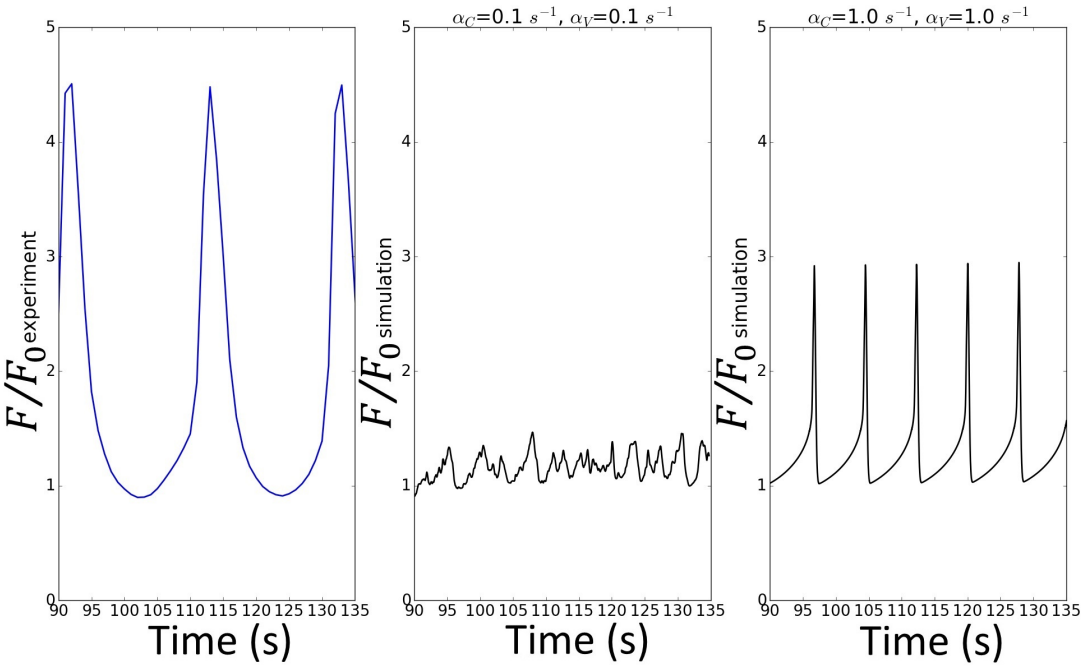

Figure 3.12: Time evolutions of the experimental and simulated forces at the hooks for a simulated CPA intervention for different coupling conditions ((α_C,α_V)=0.1 s^{-1} and (α_C,α_V)=1.0 s^{-1}) (from [2]). The plotted values are normalised with respect to the initial force F_0.

the Ca^{2+} variables, with the same gradual decreasing magnitude. To simulate this aspect of the experimental traces, we needed to employ the term in Equation (3.1) associated with store-operated Ca^{2+} entry, which is triggered in response to levels of sarcoplasmic reticulum Ca^{2+}. Note that this mechanism only had a minor effect in the simulation of the phenylephrine and CPA responses.

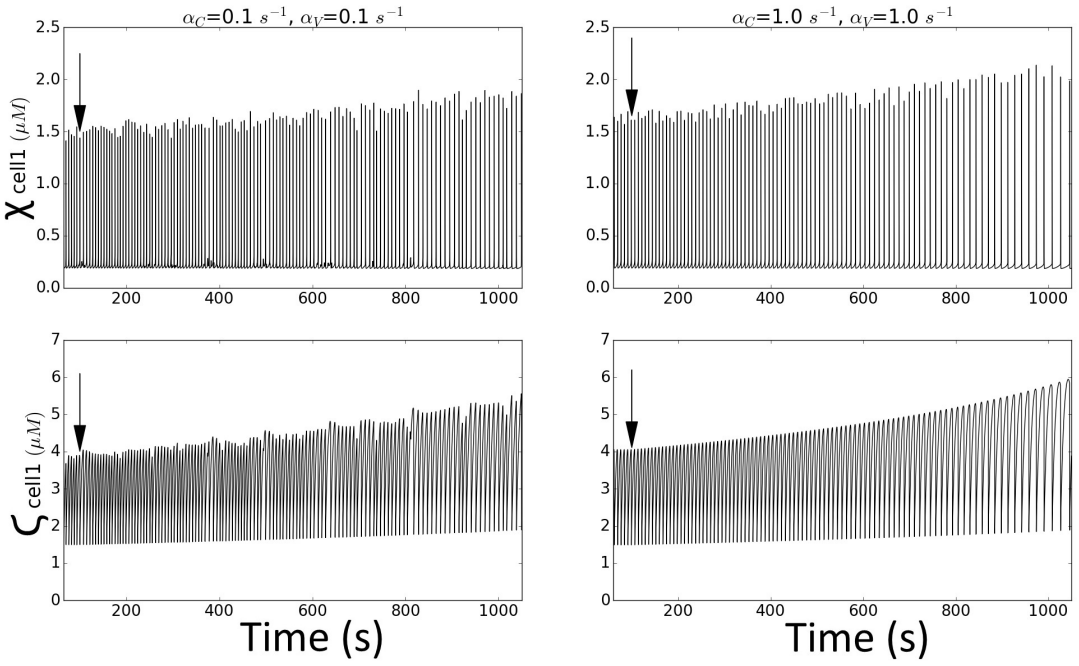

Figure 3.13: Time evolutions of χ cell1 and ζ cell1 for a simulated ryanodine intervention for different coupling conditions ((α_C,α_V)=0.1 s^{-1} and (α_C,α_V)=1.0 s^{-1}) (from [2]). Black arrows show the intervention time.

3.7 Concluding remarks

We have developed a multi-component mathematical modelling framework that accounts for the structural response of the arterial wall under the active contractile activity of the media smooth muscle layer. The methodology was applied to a set of pharmacological interventions that probe the contractile apparatus at the cellular level. The multiscale modelling approach combines dynamics and mechanics occurring at different levels, each requiring a specific solution strategy. Regarding the mechano-elastic component, the study was performed under isometric conditions, and thus the inertial force is neglected. This allowed us to deal with a simplified system, in which the evaluation of a number of dynamic parameters (such as density) was not necessary. Moreover, the ability to choose a finite element discretization that conformed to the cellular grid, eliminated the need for spatial and temporal interpolation between the two subsystems. As a consequence, it was possible to adopt the same time step

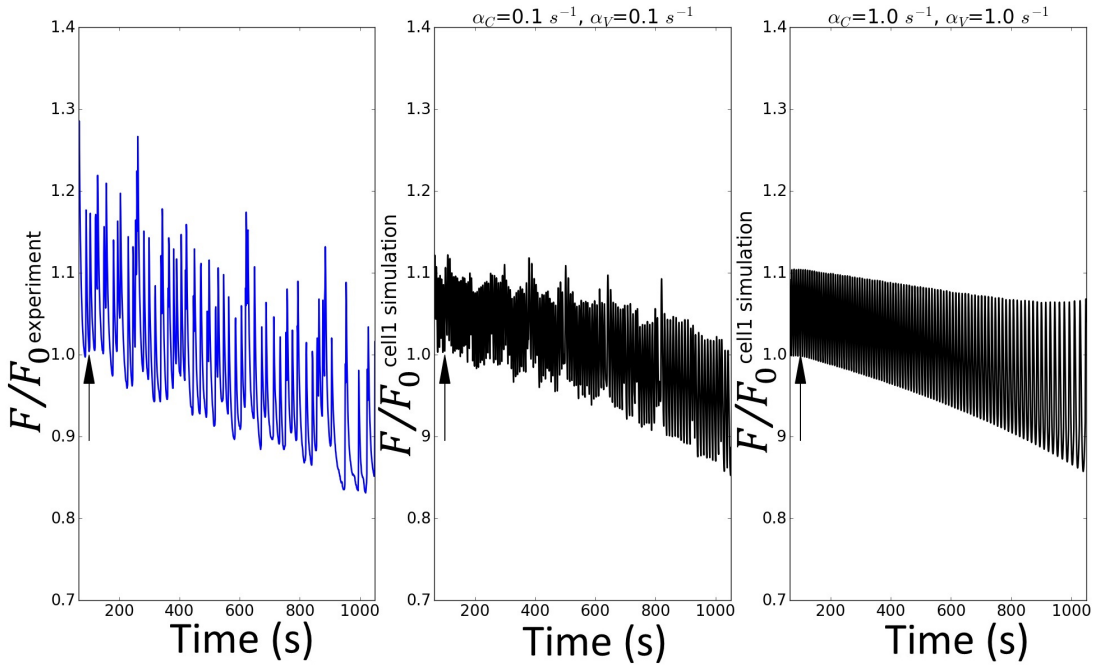

Figure 3.14: Time evolutions of the experimental and simulated cellular forces at the hooks for a simulated ryanodine intervention for different coupling conditions ((α_C,α_V)=0.1 s^{-1} and (α_C,α_V)=1.0 s^{-1}) (from [2]). Black arrows show the intervention time. The plotted values are normalised with respect to the initial force F_0.

for all elements of the model. In general, however, different integration steps can be selected for each model level if required by the specific problem. This strategy can be implemented in conjunction with interpolation techniques that allow information transmission between the various contributing systems. Although necessary in many cases, this approach can result in loss of accuracy. All experiments in the present study were performed following administration of L-NAME to eliminate the inhibitory effect of endothelium derived nitric oxide on the smooth muscle contractile apparatus [145]. The involvement of secondary endothelium produced electrochemical factors in the contractile activity of the arterial wall has not been included, and should form the basis for further elaboration of the current model [146, 128]. The main focus of the present work has been the integration of the smooth muscle based contractile apparatus and the mechano-elastic properties of the arterial wall. To probe this fundamental interaction in the genesis of arterial tone, we have employed a series of experimental studies that probe distinct aspects of these mechanisms [7, 56]. By

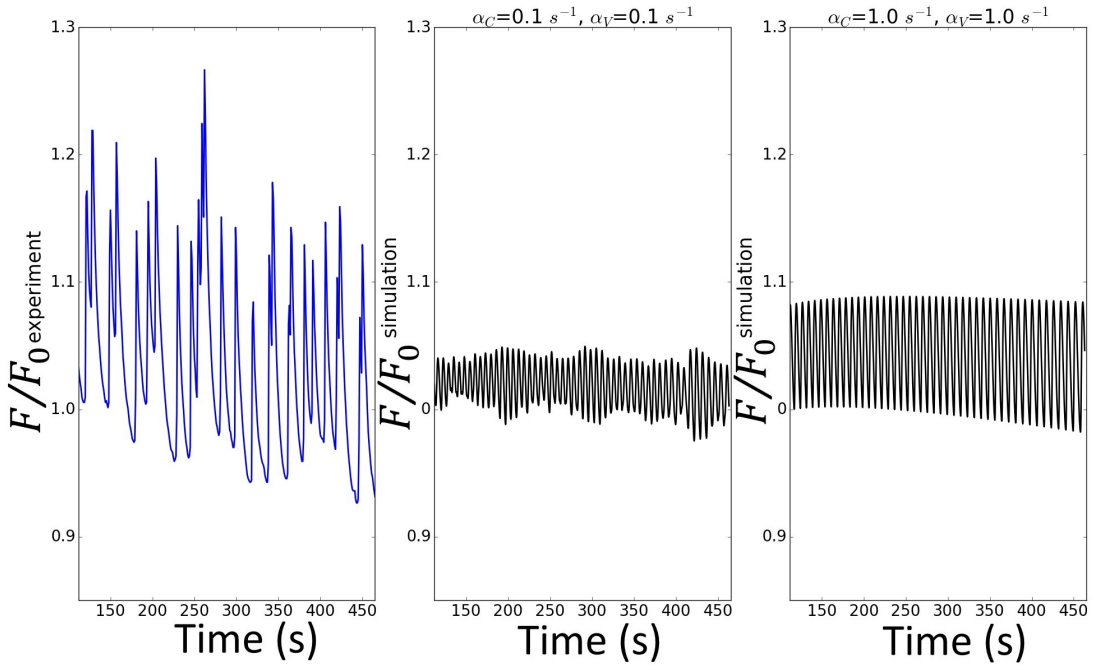

Figure 3.15: Time evolutions of the experimental and simulated forces at the hooks for a simulated ryanodine intervention for different coupling conditions ((α_C,α_V)=0.1 s^{-1} and (α_C,α_V)=1.0 s^{-1}) (from [2]). The plotted values are normalised with respect to the initial force F_0.

simulating experimental findings with the vasoconstrictor phenylephrine, we were able to match the response time of the drug, and demonstrate the direct link between cellular Ca^{2+} dynamics and the development of force at the tissue level. Indeed, the cellular events occur at the same time-scale as the global tissue contraction. This finding is correlated to the increased cytosolic Ca^{2+} concentrations associated with the administration of phenylephrine. This observation highlights the central role of Ca^{2+} uptake in the generation of vascular tone and the onset of oscillatory activity observed in both experiments and simulations. It has been previously shown that the levels of Ca^{2+} influx can determine other ionic signalling pathways in a specific, clinically relevant manner [7]. The potential of Ca^{2+} influx to determine the natural frequency of the cell's contractile apparatus was the main reason that parameter Φ_A was selected for randomisation across the cellular population. By comparison, cellular dynamics are considerably less sensitive to variations of other system parameters, associated with alternative ionic fluxes [6]. Blockage of the SERCA pump with CPA resulted in a

modest reduction in oscillatory activity that highlights the robustness of the store-refilling mechanism. The resilience of Ca^{2+} dynamics under CPA was reproduced by the simulations. A noteworthy aspect of the function of CPA is its ability to transform arterial vasomotion in a controlled manner that follows hallmark transition routes out of chaotic behaviour [144, 147]. Evidence of this behaviour is shown in Figures 3.11 and 3.12 although detailed investigation of nonlinear oscillatory transitions was not an aim of the present work. Ryanodine receptor dysregulation is implicated in a range of neuromuscular disorders and arrhythmogenesis in cardiovascular diseases [130]. This is mainly due to the complex inter-and intra-subunit interactions within the ryanodine receptor homotetramer [131, 132]. Considering the intricate multi-stage dynamics of the ryanodine channel, computational simulation work can elucidate some of the dominant components of the mechanism. In this case, we were able to highlight the role of store-operated Ca^{2+} entry associated with the suppression of the Ca^{2+}- induced Ca^{2+} release mediated by the ryanodine channel. Although studied here in isolation, dysregulation of the ryanodine channel has been associated with up-regulation of the SERCA pump protein, to allow for the maintenance of a level of sustainable homeostasis [57, 148]. Such findings support the proposed methodology as a testing ground for hypotheses on the pathogenesis of vascular disease. For instance, it will be possible predicting and characterizing the effects of a Ca^{2+} cellular dysregulation on the arterial muscular tone. The same kind of testing could be done for a case of electrical coupling dysfunction.

Appendix

Constitutive relationships

Tunica media

For this layer, the Cauchy stress derived from Equation (3.28) is

$$\boldsymbol{\sigma}^{med} = \boldsymbol{\sigma}^{med}_{vol} + \bar{\boldsymbol{\sigma}}^{med}_{a} + \bar{\boldsymbol{\sigma}}^{med}_{p} \tag{3.34}$$

where:

$$\boldsymbol{\sigma}^{med}_{vol} = \kappa \frac{J-1}{J}\mathbf{I}_d \tag{3.35}$$

$$\bar{\boldsymbol{\sigma}}^{med}_{a} = \frac{2}{J}\frac{d\bar{\Psi}^{med}_{a}}{d\bar{I}^{med}_{4}}\mathrm{dev}(\mathbf{a}^{med}\otimes\mathbf{a}^{med}) \tag{3.36}$$

$$\bar{\boldsymbol{\sigma}}^{med}_{p} = \frac{\mu^{med}_{p}}{J}\mathrm{dev}\bar{\mathbf{b}} + \frac{2}{J}\frac{d\bar{\Psi}^{med}_{p}}{d\bar{I}^{med}_{4}}\mathrm{dev}(\mathbf{a}^{med}\otimes\mathbf{a}^{med}) \tag{3.37}$$

with:

$$\frac{d\bar{\Psi}^{med}_{a}}{d\bar{I}_4} = \mu_a \bar{L}_0(n_{AMp}+n_{AM})\frac{\lambda - 1 - \bar{u}_{fs}}{2\bar{I}^{med}_{4}} \tag{3.38}$$

$$\frac{d\bar{\Psi}^{med}_{p}}{d\bar{I}^{med}_{4}} = c^{med}_{p1}(\bar{I}^{med}_{4}-1)\exp\left[c^{med}_{p2}(\bar{I}^{med}_{4}-1)^2\right] \tag{3.39}$$

This structural model is generally discretized by using the finite element procedure previously reported in Section 2.1.3.

Tunica adventitia

The Cauchy stress derived from Equation (3.31) can be written like

$$\boldsymbol{\sigma}^{adv} = \boldsymbol{\sigma}^{adv}_{vol} + \bar{\boldsymbol{\sigma}}^{adv} \tag{3.40}$$

where:

$$\boldsymbol{\sigma}^{adv}_{vol} = \kappa \frac{J-1}{J} \mathbf{I}_d \tag{3.41}$$

$$\bar{\boldsymbol{\sigma}}^{adv} = \frac{\mu_p^{adv}}{J} \mathrm{dev}\bar{\mathbf{b}} + \sum_{i=4,5} \frac{2}{J} \frac{d\bar{\Psi}^{adv}}{d\bar{I}_i^{adv}} \mathrm{dev}(\mathbf{a}_i^{adv} \otimes \mathbf{a}_i^{adv}) \tag{3.42}$$

with

$$\frac{d\bar{\Psi}^{adv}}{d\bar{I}_i^{adv}} = c_{p1}^{adv}(\bar{I}_i^{adv} - 1)\exp\left[c_{p2}^{adv}(\bar{I}_i^{adv} - 1)^2\right] \tag{3.43}$$

As for the media layer, such structural model is discretized by using the finite element procedure presented in Section 2.1.3.

Chapter 4

Developing an efficient method for fluid-structure interaction problems in hemodynamics

As mentioned in Section 1.3, the deformation of the vessel wall is the result of the combination of the media contractile machinery and the blood traction load. In the present chapter we only consider the latter source of deformation, and therefore the wall can be considered a purely *passive* structure. For describing the relationship between flow and wall in a collapsible vessel, a Fluid-Structure interaction (FSI) approach is required. In the following a novel FSI method for hemodynamic problems is presented and validated by means of classical benchmark cases.

4.1 Background

In the last two decades different FSI schemes have been proposed, ranging from partitioned approaches, where the fluid and solid problems are solved separately, to monolithic schemes, where all the solution variables are computed at the same time with a unique solver. Despite recent findings [75, 76] on the superiority of monolithic over partitioned approaches to FSI, there are many advantages that make the latter a valuable alternative [80, 81]. For example, in a segregated approach, individual solution strategies can be employed independently to fluid flow and solid dynamics and they can be coupled through robust interface coupling methods. This allows well-established solution methods to be employed without radically changing the solution strategies for fluid and solid. Strongly coupled segregated schemes demonstrated robustness when an accurate coupling strategy at the interface is employed [149, 150, 151, 80, 81]. Generally, in many FSI problems the fluid side requires a much finer discretization than the solid; which may result in a large difference in terms of degrees of freedom between the two fields. As a consequence, within a partitioned FSI approach, the fluid system efficiency affects enormously the performance of the coupled scheme. This trait becomes crucial once strong coupling between the two systems is adopted.

The characteristic based split scheme [152] is a popular and efficient fractional step method that has been employed for solving both incompressible and compressible fluid problems. Standard versions of the CBS algorithm, such as semi-implicit and quasi-implicit, present

a first order pressure accurate in time due to the complete removal of the pressure term from the momentum equation in the first step of the splitting. This splitting error may have overwhelming effect if this fluid solver is employed into a partitioned strongly coupled FSI scheme. This is because generally the solid solvers rely on higher order methods in time (α-generalised method for instance) for computing the transient solution. The discrepancy in accuracy between the two solvers may cause failure in the convergence of the scheme. Among the strategies for eliminating this error, the dual time stepping for the fluid solver has been demonstrated as a promising candidate [153, 154] based on simplicity and efficiency.

4.2 Objectives

In the current work we propose the employment of the Characteristic Based Split method augmented with artificial compressibility within a strongly coupled partitioned FSI framework. The dual time step approach in a CBS scheme has been initially introduced by Nithiarasu [153] in conjunction with artificial compressibility (AC-CBS). We note that no scheme from the CBS family combined with dual time stepping has ever been used for dealing with FSI problems. In the CBS procedure the pressure gradient in the momentum equation is considered a source evaluated apart. The convective term can thus be treated by numerical techniques valid for "Convection dominated problems". By using AC, the incompressible fluid states are considered as the steady state solutions of a compressible system. For each dual time step procedure we need to define a "pseudo time step" (Δt) and a "real time step" (Δt_R). To implement this, we need to add a true transient term to the momentum equation; the solution converges to a prescribed pressure residual (an instantaneous steady state) by pseudo time-stepping within each real time step. If the dual time stepping is combined with AC all fluid variables are computed explicitly and no matrix coefficient storing is required. This make the solver extremely fast and efficient as no linear system need to be solved; this results in important savings in terms of RAM memory. Furthermore, the stabilising properties of the CBS algorithm allow the employment of low order elements (linear isoparametric triangles in this case) without violating the Babuska-Brezzi condition. All these features

make the current approach very suitable for large scale simulations of bio-medical and industrial problems.

The solid is assumed to be under large strain regime and constitutive relationships are defined through a hyper-elastic potential. The structural problem is dealt with a mixed (Jacobian-pressure) finite element formulation. The displacement field is linearly interpolated whilst for the other variables discontinuous functions are used. For the temporal discretization the standard α-method is used. Fluid variables are computed through an Arbitrary Lagrangian Eulerian (ALE) frame. Both fluid grid updating and information transmission at the interface between the two systems are carried out via Radial Basis Function (RBF) interpolation. This technique is extremely appealing in terms of efficiency as no connectivity information between nodes is required.

Regarding the coupling between fluid and solid, different techniques have been employed. We initially tested simple approaches such as fixed point or Aitken methods. We also employed a more sophisticated technique, that is a variant of the Quasi-Newton method recently proposed by Bogaers et al. [155]. This strong coupling strategy allows us to deal with high mass ratio cases. By comparison, methods such as fixed point techniques often fail [156, 155].

The proposed methodology represents a novel approach in the FSI field, as a dual time step is adopted in computing the solution. Considering the solid and coupling time step limitations, this method may lead to a larger time step used. Moreover, since the fluid solver is explicit/matrix free, significant computer memory savings are guaranteed.

The objectives of the present work can be summarised in the following points:

- to test each sub-component of the framework by using benchmark cases
- to verify the efficiency of the fluid solver employed
- to investigate the temporal stability and robustness of the global FSI scheme
- to propose a representative case for the arterial system

In Section 4.3 we present a brief theoretical background on solid and fluid dynamics, while the numerical procedure is outlined in Section 4.4. Benchmark cases for validating the framework are proposed in Section 4.5 followed by concluding remarks (Section 4.6).

4.3 Governing equations

In a generic FSI problem the space domain Ω can be split into fluid and solid sub-domains (Ω_F and Ω_S respectively) interacting through a separating interface Γ_I (see Figure 4.1).

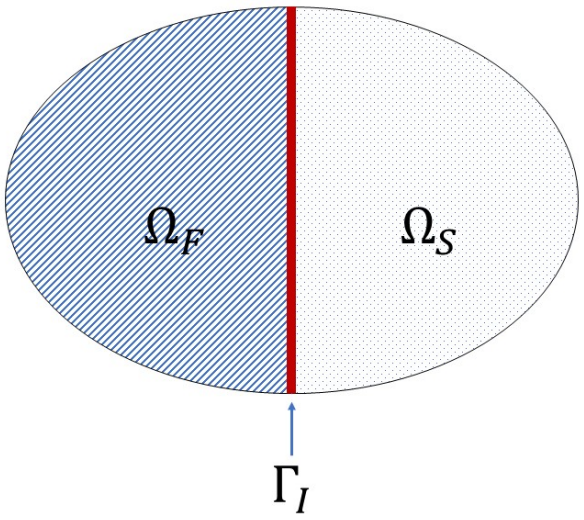

Figure 4.1: Domains of FSI problem. Blue lines identify the fluid domain Ω_F, whilst the white colour indicates the solid Ω_S. These two domains are separated by an interface Γ_I, depicted in red colour.

The field governing and boundary equations for each sub-domain are described below.

4.3.1 Solid domain

With regard to the solid formulation, either Equation (2.15) or (2.17) can be used, depending on whether incompressibility must be enforced. The material is assumed to be nearly-incompressible hyper-elastic and therefore, as anticipated in Section 2.1.5, a strain energy function Ψ needs to be defined. This energy is decomposed into deviatoric $\bar{\Psi}$ and volumetric U components

$$\Psi = \bar{\Psi} + U_{vol} \tag{4.1}$$

A generalised Neo-Hookean model is adopted as constitutive relationship, and thus

$$\bar{\Psi}(\mathbf{C}) = \mu_S(tr\bar{\mathbf{C}} - 3) \tag{4.2}$$

where $\bar{\mathbf{C}}$ is the isochoric Right Cauchy deformation tensor, whereas μ_S is the shear stress. The volumetric strain energy function is defined as follows

$$U_{vol} = \frac{\kappa}{2}(J^2 - 1) \tag{4.3}$$

where κ is a penalty number. According to Equation (2.57) the Cauchy stress tensor yields

$$\boldsymbol{\sigma} = \frac{\mu_S}{J} dev(\bar{\mathbf{b}}) + \kappa \frac{J^2 - 1}{2J} \mathbf{I}_d \tag{4.4}$$

where $\bar{\mathbf{b}}$ is the isochoric Left Cauchy deformation tensor.

4.3.2 Fluid domain

In the current implementation the flow is assumed to be incompressible, Newtonian and laminar. The fluid variables ($\mathbf{u}$,p) are described via the dimensional version of Navier-Stokes

for incompressible flow in an *Arbitrary Lagrangian Euler* (ALE) formulation:

$$\begin{cases} \nabla \cdot \mathbf{U} = 0 \\ \frac{\partial \mathbf{U}}{\partial t}|_{x_0} = -\mathbf{c} \cdot \nabla \mathbf{U} - \nabla p + \nabla \cdot \boldsymbol{\tau_F} \end{cases} \tag{4.5}$$

where $\mathbf{c}$ is the fluid velocity relative to the arbitrarily moving domain, $\mathbf{U}$ is the flow variable ($\mathbf{U} = \rho_F \mathbf{u}$), $\frac{\partial}{\partial t}|_{x_0}$ stands for the time derivative with respect to the initial configuration whereas τ is the deviatoric stress tensor, evaluated as

$$\boldsymbol{\tau_F} = \mu_F (\nabla \mathbf{u} + \nabla \mathbf{u}^T) \tag{4.6}$$

4.3.3 Interface

The intimate coupling between the fluid and structural domain can be described as follows: the flow of the fluid generates a traction which acts upon the structure. This traction on the structure results in a deformation which alters the geometry of the fluid domain and thus also alters the fluid flow. We define Γ_I as the fluid/structure interface boundary and $\mathbf{n}$ the normal at a point of Γ_I. An intimately coupled system like this requires certain coupling conditions to be employed in order to be solved. These are:

$$\dot{\mathbf{d}} = \mathbf{u} \;\; on\, \Gamma_I \tag{4.7}$$

$$\boldsymbol{\sigma} \cdot \boldsymbol{n} = (-p \boldsymbol{I}_d + \boldsymbol{\tau_F}) \cdot \boldsymbol{n} \;\; on\, \Gamma_I \tag{4.8}$$

4.4 Solution procedure

The numerical schemes for each sub-component of the framework are presented below, followed by a description of the strategy employed for coupling the solvers.

4.4.1 Solid discretization

Space discretization

The finite element discretization of the structural problem, outlined in Section 2.1.3, leads to the following formulation

$$\mathbf{f}_S - \int_{\Omega_S} \mathbf{B}^T \boldsymbol{\sigma} d\Omega - \mathbf{M}_S \ddot{\tilde{\mathbf{d}}} = 0 \tag{4.9}$$

where $\mathbf{f}_S$ accounts for all forces acting on the boundary, including the interface load. This system can be re-written (adding damping) in a matrix form:

$$\mathbf{M}_S \ddot{\tilde{\mathbf{d}}} + \mathbf{C}_S \dot{\tilde{\mathbf{d}}} + \mathbf{K}_S(\tilde{\mathbf{d}}) = \mathbf{f}_S \tag{4.10}$$

We note that all integrals for the solid domain are performed numerically via second order Gauss-Legendre integration. Equation (4.10) is non-linear and thus a linearization of the stiffness matrix $\mathbf{K}_S$ is required. This is carried out by using the definition of Equation (2.59). If the problem requires the enforcement of incompressibility constrain, it is necessary to adopt a more sophisticated technique than the standard penalty function. In the current work we adopted the *mean dilation technique* reported in [124].

Time integration

For temporal discretization the α-method is employed. The sought solution is recovered by solving the following system of equations:

$$\begin{cases} \mathbf{M}_S \ddot{\tilde{\mathbf{d}}}^{n+\alpha} + \mathbf{C}_S \dot{\tilde{\mathbf{d}}}^{n+\alpha} + \mathbf{K}_S(\tilde{\mathbf{d}}^{n+\alpha}) = \mathbf{f}_S^{n+\alpha} \\ \tilde{\mathbf{d}}^{n+\alpha} = (1-\alpha_f)\tilde{\mathbf{d}}^{n} + \alpha_f \tilde{\mathbf{d}}^{n+1} \\ \dot{\tilde{\mathbf{d}}}^{n+\alpha} = (1-\alpha_f)\dot{\tilde{\mathbf{d}}}^{n} + \alpha_f \dot{\tilde{\mathbf{d}}}^{n+1} \\ \ddot{\tilde{\mathbf{d}}}^{n+\alpha} = (1-\alpha_m)\ddot{\tilde{\mathbf{d}}}^{n} + \alpha_m \ddot{\tilde{\mathbf{d}}}^{n+1} \\ \tilde{\mathbf{d}}^{n+1} = \tilde{\mathbf{d}}^{n} + \Delta t \dot{\tilde{\mathbf{d}}}^{n} + \Delta t^2((\frac{1}{2}-\beta_\alpha)\ddot{\tilde{\mathbf{d}}}^{n} + \beta_\alpha \ddot{\tilde{\mathbf{d}}}^{n+1}) \\ \dot{\tilde{\mathbf{d}}}^{n+1} = \dot{\tilde{\mathbf{d}}}^{n} + \Delta t((1-\gamma_\alpha)\ddot{\tilde{\mathbf{d}}}^{n} + \gamma_\alpha \ddot{\tilde{\mathbf{d}}}^{n+1}) \\ \beta_\alpha = \frac{1}{4}(1+\alpha_m-\alpha_f)^2 \\ \gamma_\alpha = \frac{1}{2}+\alpha_m-\alpha_f \\ \alpha_f = \frac{1}{1+\rho_\infty^h} \\ \alpha_m = \frac{2-\rho_\infty^h}{1+\rho_\infty^h} \end{cases} \tag{4.11}$$

where ρ_∞^h is defined as the spectral radius for $\Delta t \to 0$, whilst β_α, γ_α, α_f and α_m are time integration parameters. For linear problems, the scheme can be proven to be second order accurate and unconditionally stable for $0 \leq \rho_\infty^h \leq 1$. This can be re-written as a system with only $\tilde{\mathbf{d}}^{n+1}$ as unknown variable. The solution of such a system is sought by employing a Newton-Raphson procedure.

4.4.2 Fluid discretization

To derive the fluid solution in time from the system of Equations (4.5) we use continuous linear finite elements combined with the characteristic based split (CBS) algorithm.

Space-time discretizations

Equations (4.5) are discretized by means of the standard weighted residual Galerkin method with Taylor stabilisation

$$\begin{cases} \int_{\Omega_F} (N_p)^T \nabla \cdot \mathbf{U} d\Omega = 0 \\ \int_{\Omega_F} (\mathbf{N}_u)^T \frac{\Delta \mathbf{U}}{\Delta t}|_{x_0} d\Omega = \int_{\Omega_F} (\mathbf{N}_u)^T \{-\mathbf{c} \cdot \nabla \mathbf{U} - \nabla p + \nabla \cdot \boldsymbol{\tau}_{\boldsymbol{F}} + \frac{\Delta t}{2} [\nabla^T (\mathbf{u}\mathbf{N}_u)]^T [\nabla^T (\mathbf{u}\mathbf{U}) + \nabla p]\} d\Omega \end{cases} \tag{4.12}$$

where N_p and $\mathbf{N}_u$ are the test functions for the continuity and momentum equations, respectively. We note that the time discretization of the right side of Equation (4.12) will be performed in the Section *Characteristic based split method*. After performing integration by parts of the viscous term, the semi-discrete form of these equations can be written in the following matrix form

$$\begin{cases} \mathbf{G}_F \tilde{\mathbf{U}} = 0 \\ \mathbf{M}_F \frac{\Delta \tilde{\mathbf{U}}}{\Delta t} = -\mathbf{C}_F \tilde{\mathbf{U}} - \frac{\mathbf{K}_F}{\rho_F} \tilde{\mathbf{U}} - \mathbf{G}_F \tilde{p} + \frac{\Delta t}{2} (\mathbf{C}_{F,stab} \tilde{\mathbf{U}} + \mathbf{G}_{p,stab} \tilde{p}) + \mathbf{f}_F \end{cases} \tag{4.13}$$

where $\mathbf{M}_F$ is the mass matrix, $\mathbf{C}_F$ is the convection matrix, $\mathbf{K}_F$ is the viscous matrix, $\mathbf{G}_F$ is the gradient matrix, $\mathbf{C}_{F,stab}$ is the convective stabilisation matrix, $\mathbf{G}_{p,stab}$ is the pressure stabilisation matrix, while $\mathbf{f}_F$ is the force obtained by integrating the deviatoric stress component along the boundary.

Characteristic based split method

Before proceeding with the split, the right side of system of Equations (4.13) is discretized in time by using the coefficients θ_1, θ_2, θ_3 and θ_4

$$\begin{cases} \mathbf{G}_F \tilde{\mathbf{U}}^{n+\theta_1} = 0 \\ \mathbf{M}_F \frac{\Delta\tilde{\mathbf{U}}}{\Delta t} = -\mathbf{C}_F \tilde{\mathbf{U}}^{n+\theta_4} - \frac{\mathbf{K}_F}{\rho_F} \tilde{\mathbf{U}}^{n+\theta_3} - \mathbf{G}_F \tilde{p}^{n+\theta_2} + \frac{\Delta t}{2}(\mathbf{C}_{F,stab} \tilde{\mathbf{U}}^{n+\theta_4} + \mathbf{G}_{p,stab} \tilde{p}^{n+\theta_2}) + \mathbf{f}_F^n \end{cases} \tag{4.14}$$

The choice of the time scheme depends on the values adopted for such coefficients. Generally θ_4=0, leading to an explicit evaluation of the convective terms. Setting both θ_2>0 and θ_3>0 leads to the quasi-implicit scheme. We note that if only θ_2>0 the scheme is called semi-implicit and only pressure is calculated implicitly. The fully explicit scheme ($\theta_1 \geq 0$, θ_2=0, θ_3=0, θ_4=0) is generally combined with dual time stepping and artificial compressibility (AC) in order to speed up the calculations [153, 154, 157].

The temporal split is carried out by introducing the intermediary velocity $\mathbf{U}^*$ such that

$$\Delta\tilde{\mathbf{U}} = \Delta\tilde{\mathbf{U}}^* + \Delta\tilde{\mathbf{U}}^{**} = (\tilde{\mathbf{U}}^* - \tilde{\mathbf{U}}^n) + (\tilde{\mathbf{U}}^{n+1} - \tilde{\mathbf{U}}^*) \tag{4.15}$$

This procedure decouples pressure from velocity variables and from the momentum equation we have

$$\mathbf{M}_F \frac{\Delta\tilde{\mathbf{U}}^*}{\Delta t} = -\mathbf{C}_F \tilde{\mathbf{U}}^n - \frac{\mathbf{K}_F}{\rho_F} \tilde{\mathbf{U}}^{n+\theta_3} + \frac{\Delta t}{2} \mathbf{C}_{F,stab} \tilde{\mathbf{U}}^n + \mathbf{f}_F^n \tag{4.16}$$

$$\mathbf{M}_F \frac{\Delta\tilde{\mathbf{U}}^{**}}{\Delta t} = -\mathbf{G}_F \tilde{p}^{n+\theta_2} + \frac{\Delta t}{2} \mathbf{G}_{p,stab} \tilde{p}^{n+\theta_2} \tag{4.17}$$

The scheme for the fully explicit case augmented with artificial compressibility (CBS-AC) is outlined here. This means that the fluid is treated as compressible and the solution is found

iteratively, once the incompressibility limit is reached. This introduces the "pseudo time step" concept which is an artificial time step used to compute the solution for a specific real time step. For transient recovery with the CBS-AC scheme, a dual time stepping procedure is employed. This involves adding an extra source term in the momentum equation, accounting for real time velocity variations. Since it is an explicit method, local calculation of the time step is carried out in order to increase the efficiency of the method. We note that, for the other CBS version, e.g. the quasi-implicit, the procedure is similar except for the viscous and pressure terms, which are treated implicitly. The CBS fractional method requires performing three steps.

Step 1

An intermediate velocity $\tilde{\mathbf{U}}^*$ is evaluated without considering the pressure contribution:

$$\Delta\tilde{\mathbf{U}}^* = -\Delta t\mathbf{M}_F^{-1}[(\mathbf{C}_F + \frac{\mathbf{K}_F}{\rho_F} - \frac{\Delta t}{2}\mathbf{C}_{F,stab})\tilde{\mathbf{U}}^n + \mathbf{f}_F^n] \tag{4.18}$$

Step 2

Once $\tilde{\mathbf{U}}^*$ is known, it is possible to evaluate the pressure from the mass continuity equation accounting for artificial compressibility

$$\int_\Omega (N_p)^T(\frac{1}{c_s^2})\frac{\Delta p}{\Delta t}d\Omega = \mathbf{M}_p\frac{\Delta\tilde{p}}{\Delta t} = -[\mathbf{G}_F\tilde{\mathbf{U}}^n + \theta_1\mathbf{G}_F(\Delta\tilde{\mathbf{U}}^*) - \Delta t\,\theta_1\mathbf{H}^*\tilde{p}^n] \tag{4.19}$$

in which $\mathbf{M}_p$=$\int_\Omega (N_p)^T(\frac{1}{c_s^2})N_p d\Omega$ $\mathbf{H}^*$=$\int_\Omega(\nabla N_p)^T\nabla N_p d\Omega$

where c_s is the speed of sound. We note that the results for such an equation are self-adjoint for the pressure variable, and thus it is possible to apply Galerkin method without any further stabilisation techniques.

Step 3

The velocity correction is found by adding the transient recovery term $\frac{\Delta\tilde{\mathbf{U}}_R}{\Delta t_R}$ to the new

calculated pressure gradient contribution (with stabilisation)

$$\Delta\tilde{\mathbf{U}}^{**} = -\Delta t \mathbf{M}_F^{-1}[(\mathbf{G}_F^T + \frac{\Delta t}{2}\mathbf{G}_{p,stab})\tilde{p}^{n+1} - \frac{\Delta\tilde{\mathbf{U}}_R}{\Delta t_R}] \tag{4.20}$$

where Δt_R is the real time step. The true transient term $\frac{\Delta\tilde{\mathbf{U}}_R}{\Delta t_R}$ is evaluated with a second-order real-time approximation

$$\frac{\Delta\tilde{\mathbf{U}}_R}{\Delta t_R} = \frac{3\tilde{\mathbf{U}}^{n+1} - 4\tilde{\mathbf{U}}^n + \tilde{\mathbf{U}}^{n-1}}{\Delta t} \tag{4.21}$$

Time step restrictions Since the fully explicit method is employed, the local stability limit for the pseudo-time step is

$$\Delta t_{lim} < min(\frac{h_{ele}}{|u| + \beta_C}, \frac{h_{ele}Re}{2}) \tag{4.22}$$

in which h_{ele} is the characteristic element length, Re is the Reynolds number while β_C is a parameter calculated as the maximum between the convective and diffusive velocities.

4.4.3 Mesh movement

If an arbitrary Lagrangian-Eulerian (ALE) approach is employed, a third non-physical mesh field is needed. It accounts for the fluid domain's deformation, an extension of the FSI interface deformation caused by the interaction. After each FSI iteration the fluid grid is updated by using the RBF interpolation technique proposed in [81]. By comparison to classical techniques, such as treating the grid as an elastic solid, this method is very efficient, since only a simple linear system has to be solved. In addition it does not require any information about grid connectivity of the two meshes. This makes it especially appealing for non-conforming meshes.

RBF interpolation

A brief description of the method is reported below. We assume that we want to transmit information from mesh $m1$ to mesh $m2$. We need to build an interpolation function $\mathbf{Z}(\mathbf{x})$ which will be able to provide back a discrete value for any point of the spatial domain. From mesh $m1$ we know n_1 discrete values $\mathbf{g}_{m1}$ and the associated spatial coordinates (or integration points) $\mathbf{x}_{m1}$:

$$g_{m1,i} = \mathbf{Z}(\mathbf{x}_{m1,i}) \;\; i = 1, ..., n_1 \tag{4.23}$$

For mesh $m2$, we want to evaluate n_2 interpolated discrete values $\mathbf{g}_{m2}$ for points located at $\mathbf{x}_{m2}$.

The interpolation function may then be written as:

$$\mathbf{Z}(\mathbf{x}) = \sum_{i=1}^{n_1} \alpha_{Z,i} \phi_Z(||\mathbf{x} - \mathbf{x}_{m1,i}||) + p_m^k(\mathbf{x}) \tag{4.24}$$

where ϕ_Z is a generic radial basis function, $p_m^k(\mathbf{x})$ is a polynomial of degree k, and $\alpha_{Z,i}$ and β_{Zj} are constants to be determined. For the present study we select the multi quadratic biharmonic (MQ) radial basis function regarded as one of the most promising RBF [81]. In our case $p_m(\mathbf{x})$ is a first order polynomial and therefore we need to evaluate 4 polynomial coefficients ($p_m(\mathbf{x}) = \beta_{Z0} + \beta_{Z1}x + \beta_{Z2}y + \beta_{Z3}z$). The coefficients α_{Zi} and β_{Zj} are evaluated by imposing conditions expressed in Equation (4.27) and the following constrains:

$$\sum_{i=1}^{n_1} p_m^k(\mathbf{x}_{m1i}) \alpha_{Zi} = 0 \;\; k = 1, ..., k \tag{4.25}$$

Once the interpolation function $\mathbf{Z}(\mathbf{x})$ has been built, the discrete values can be found by:

$$g_{m2,i} = \mathbf{Z}(\mathbf{x}_{m2,i}) \;\; i = 1, ..., n_2 \tag{4.26}$$

Once the new fluid node coordinates are known it is possible to calculate the grid velocity via:

$$\mathbf{u}_g^{n+1} = \frac{2(\mathbf{d}^{n+1} - \mathbf{d}^n)}{\Delta t} - \mathbf{u}_g^n \tag{4.27}$$

4.4.4 Interface

In an FSI algorithm, all the fluid and solid equations reported above need to be solved with respect to the interface displacement $\mathbf{d}_I$. Operators Υ and Λ are used for indicating the fluid and solid solver respectively. Each field operator can be written, with its input and output, in a compact form as a black box:

$$\mathbf{t}_I = \Upsilon(\mathbf{d}_I) \tag{4.28}$$

$$\bar{\mathbf{d}}_I = \Lambda(\mathbf{t}_I) \tag{4.29}$$

where $\mathbf{t}_I$ is the fluid traction computed at the interface, $\bar{\mathbf{d}}_I$ is the approximation of the interface displacement computed from the solid system.

An FSI cycle leads to the approximation of the interface displacement, that is computed by combining Equations (4.28) and (4.29)

$$\bar{\mathbf{d}}_I^{k+1} = \Lambda(\Upsilon(\mathbf{d}_I^k)) \tag{4.30}$$

From this approximation of the interface displacement, it is possible to calculate the interface displacement $\mathbf{d}_I$ by using a coupling technique. The fluid and solid solvers are strongly coupled in the sense that $\mathbf{d}_I$ must satisfy both fluid and solid equations within a certain tolerance. Therefore an iterative loop of FSI cycles is employed until the $\mathbf{d}_I$ residual reaches the tolerance imposed. Figure 4.2 shows how the fluid structure interaction scheme is structured.

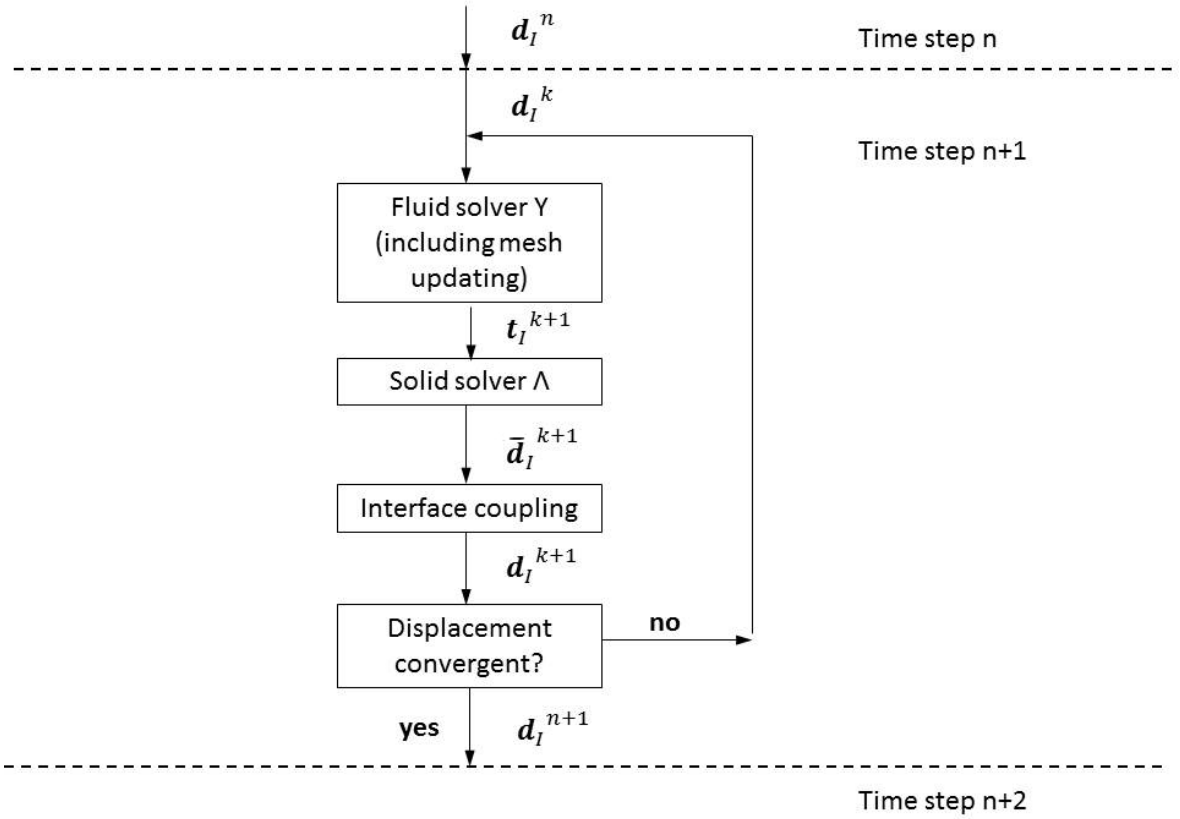

Figure 4.2: Partitioned strongly coupled fluid structure interaction scheme. For each FSI iteration the fluid and solid systems exchange information twice through the interface. The fluid remeshing is carried out according to $\mathbf{d}_I$, and this step takes place within (just before) the fluid solver. Once the fluid solution is computed, the fluid traction is passed to the solid boundary as prescribed load. The solid solution $\bar{\mathbf{d}}_I$ is then adjusted by means of a coupling technique. Once the interface displacement $\mathbf{d}_I$ has been computed, it is compared against the previous $\mathbf{d}_I$. If the residual is lower than the tolerance, the FSI loop ends and the current values of $\mathbf{d}_I$ are used for the next time step. If the residual check fails, $\mathbf{d}_I$ is transmitted again to the fluid solver, restarting a new FSI cycle.

Coupling technique

The *fixed point method with relaxation* is a straightforward technique to apply. This scheme corrects the approximation of $\bar{\mathbf{d}}_I$ in the following way

$$\mathbf{d}^{k+1} = \bar{\mathbf{d}}_I^{k+1} + \omega_R(\mathbf{d}_I^k - \bar{\mathbf{d}}_I^{k+1}) \tag{4.31}$$

where ω_R is a relaxing factor.

If the scale of the FSI problem is large, it may be convenient to apply a more sophisticated technique, in order to increase the efficiency and accuracy of the calculation. In this study we adopted the *Multi Vector Quasi-Newton* (MVQN) method proposed in [81]. In this case the interface displacement is computed as:

$$\mathbf{d}_I^{k+1} = \mathbf{d}_I^k - \mathbf{J}_I^{k+1}\mathbf{R}^k \tag{4.32}$$

where $\mathbf{R}^k$ is the displacement residual vector whilst $\mathbf{J}_I^{k+1} = (\frac{\partial \mathbf{R}}{\partial \mathbf{d}_I})^{-1}$ is the Jacobian of the system.

Information transfer

Traction The evaluation of fluid load induced to the structure $\mathbf{t}_I$ is described below. The tractions are calculated at the fluid nodes and are then projected to the structural nodes. Such a conservative method, valid for non-conforming meshes, is extensively described in [158]. Along the interface each fluid node is paired to a single wet solid element; then natural coordinates for such fluid (ξ) are calculated. The load $t_{I,k}$ at k^{th} solid node can be then evaluated as:

$$t_{I,k} = \sum_{l=1}^{l=l_F} \Phi_{pF} N_k(\xi_l) \tag{4.33}$$

where Φ_{pF} is the numerical pressure flux at l^{th} fluid node:

$$\Phi_{pF} = \int_{\Gamma_I} N_l(-pn_j + \tau_{F,ij}n_j)ds \tag{4.34}$$

As linear triangular elements are adopted for the fluid system, all the integrals in Equation (4.34) can be performed in a direct way.

Displacement As reported previously, RBF is able to pass accurately rigid motion between two systems. We therefore adopt this technique for passing the computed displacement from solid to fluid at the interface nodes.

4.5 Simulation results

The following section provides a validation of the FSI framework and presents simulations of a pressure wave propagating along an artery. The validation of the solution procedure is carried out by testing component by component against benchmark cases from the literature.

4.5.1 Cook's membrane

This problem is useful for assessing the convergence properties of the FE scheme under a mixture of bending and shear strains. A membrane is subjected on the right edge to a uniformly distributed vertical load F equal to 100 N (see Figure 4.3) and is fixed on the opposite edge. The applied force remains vertical throughout the loading programme. For this problem plane strain condition is assumed and a generalised Neo-Hookean material with shear modulus μ_S = 80.1938 $dyne/cm^2$ and bulk modulus (which in this study is also the penalty number) κ =40.0942 10^4 $dyne/cm^2$ adopted. Convergence of the solution with mesh refinement is assessed by employing four different meshes. Each of these has the same number of elements per edge. Figure 4.3 shows a mesh of 4 by 4 elements and the problem geometry.

In this problem the configuration is analysed at stationary conditions. The vertical displacement of the membrane's top right corner for different type of meshes is shown in Figure 4.4. This shows that there is a critical mesh size beyond which the displacement does not vary much. The values obtained from simulations are in good agreement with literature results, with the absolute relative error less than 2 %.

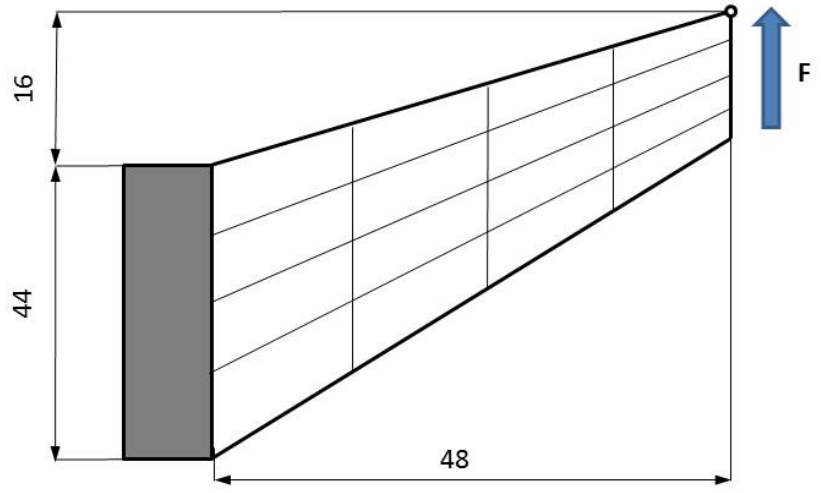

Figure 4.3: Cook's membrane. Geometry of the problem, expressed in *cm*.

4.5.2 Oscillations of a rigid beam

With this particular problem we intend to study the transient response of the solid scheme. More specifically, this case allows us to assess the energy conservation along the process. Figure 4.5 depicts the geometry of the problem. No load is applied on the boundary but initial velocity along the x axis (u) is prescribed. The initial velocity on the y axis is set equal to zero. This is distributed uniformly along the thickness (x axis) and varies linearly along the vertical axis (y axis) from 10 cm/s at the top to 0 cm/s at the bottom. The material is considered Neo-Hookean, with Young's modulus Y equal to 17000000.0 N/mm^2 and Poisson's ratio ν_{Pois} equal to 0.3. The density of the material ρ_S is equal to 1.1 g/cm^3. The time step Δt adopted was 10^{-3} s.

To assess the quality of the time-integration scheme we plotted the time evolution of both

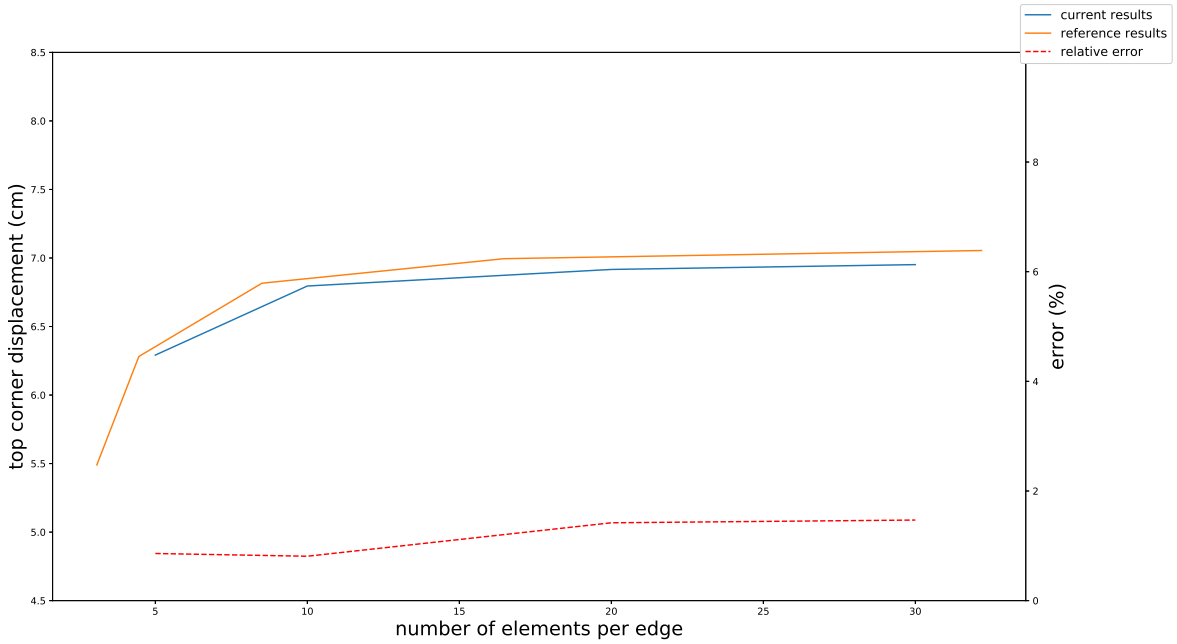

Figure 4.4: Cook's membrane. Vertical displacement of the top right corner vs number of element employed per edge. Reference results are from [3].

kinetic and potential energies for different coefficient ρ_∞^h (see Figure 4.6). We note that these energies present an oscillatory pattern which is specular but out of phase. For both ρ_∞^h=0 and ρ_∞^h=0.5 cases a gradual reduction in kinetic and potential energy along the time axis is recorded. This is because the schemes corresponding to such ρ_∞^h choice include dissipation and thus the total energy is not conserved. The situation is different for ρ_∞^h=1.0. In this case, since no damping is accounted for, the beam is destined to oscillate periodically around its vertical axis. The sum of kinetic and potential energy remains constant over time.

4.5.3 Flow in a rigid tube

A classic fluid mechanics problem of flow transport along a rigid tube is presented here. The geometry of the problem is depicted in Figure 4.7. A Poiseuille velocity profile is prescribed at the inlet of the tube, with an average amplitude equal to 1 cm/s. The dynamic viscosity μ_F is set equal to 0.035 *poise*, whilst the fluid density ρ_F =1.0 10^{-2} g/cm^3. No-slip condition is

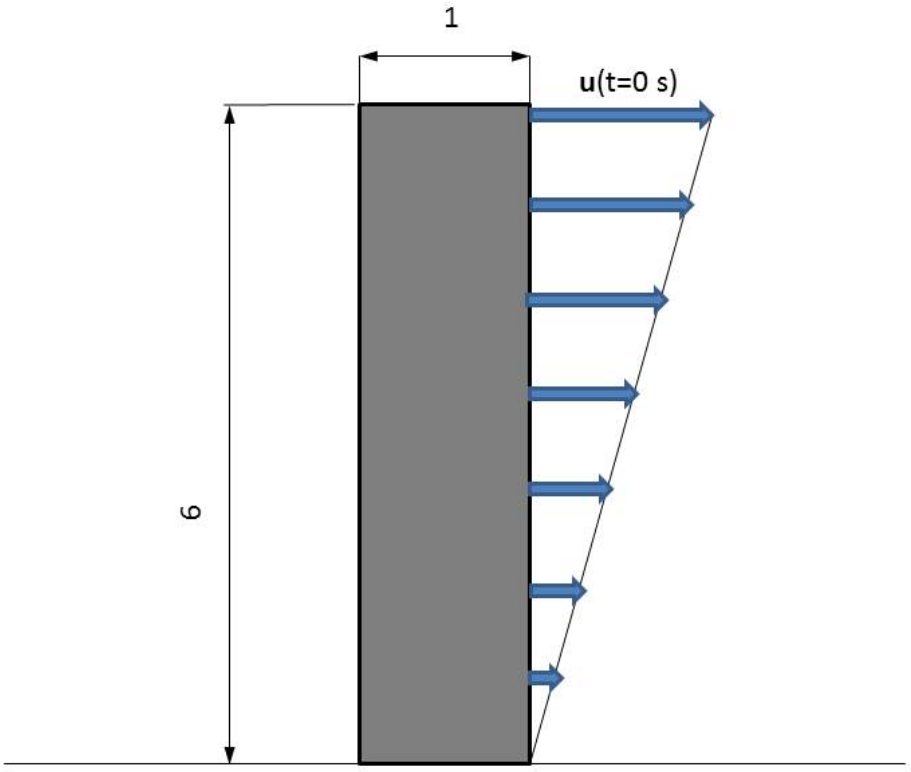

Figure 4.5: Oscillations of a rigid beam. Geometry of the problem, expressed in *cm*.

applied at the top of the lateral wall edge whilst symmetric flow condition is imposed for the bottom wall edge.

In Figures 4.8 and 4.9 the velocity and pressure fields are plotted after 1.4 *s* the beginning of the transient. The latter figure shows that the isobaric lines are parallel, as expected for a developed flow.

4.5.4 Flow passing a circular cylinder

This case represents a popular testing scenario of a numerical scheme for a flow transient problem. Through this example we intend also to verify how the fluid traction is transmitted

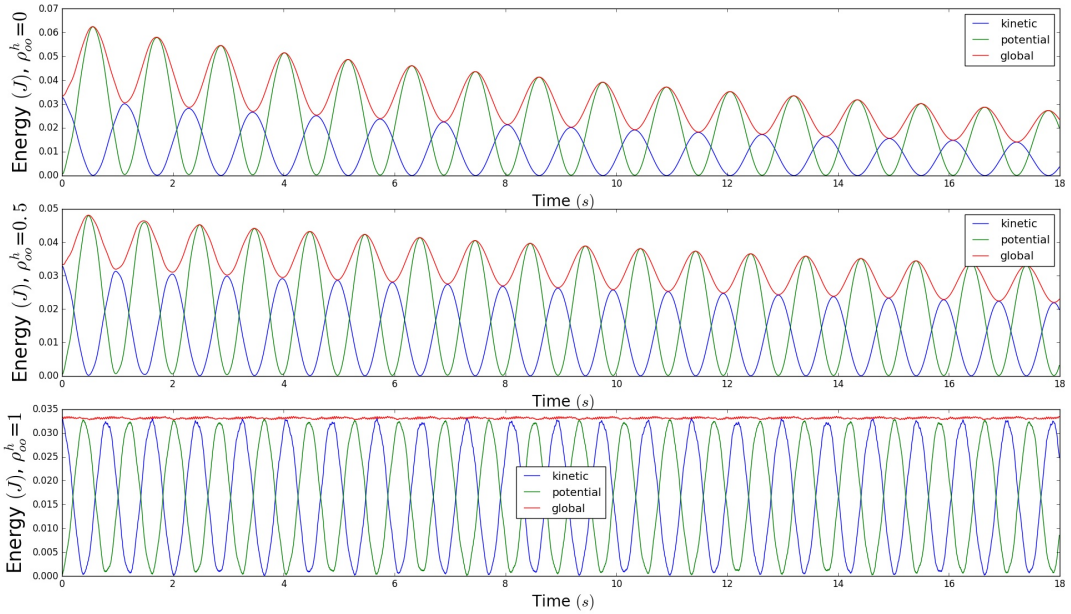

Figure 4.6: Oscillations of a rigid beam. Temporal evolutions of the kinetic energy, potential energy and global energy for different ρ_∞^h.

to a rigid body. In addition, this case allows us to assess the accuracy of the AC explicit CBS against the quasi-implicit version. The definition of the problem is standard (see Figure 4.10 for the definition of the problem's geometry). The flow at the inlet is uniform and the cylinder is placed at a centerline between two walls where no-slip condition is assumed. The distance from the inlet to the centre of the cylinder is $4D$, where D is the diameter of the cylinder. The total length of the domain is $16D$. No-slip condition is applied on the cylinder surface. The explicit scheme does not require the imposition of pressure boundary conditions at the outlet. For this scheme the minimum number of pseudo-time steps is one hundred whilst the real time step is set equal to 0.166 s. For the quasi-implicit version, a time step equal to 0.00333 s is employed.

Figure 4.11 shows the evolution in time of the drag and lift coefficients for both fully explicit and quasi-implicit CBS versions. Note that the plotted variables C_D and C_L are in non-dimensional scales. The results are in agreement with simulated results reported in [153]. The results for the quasi-implicit approach are more diffused than the ones obtained with the

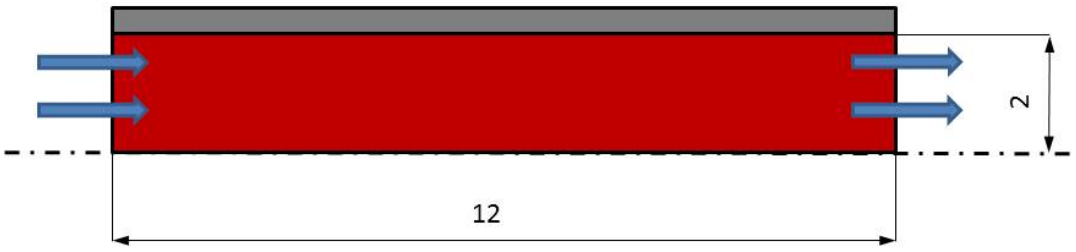

Figure 4.7: Flow in a rigid tube. Geometry of the problem, expressed in *cm*.

fully explicit case. Between these 2 methods (explicit case as reference), the relative errors of C_D (in average value) and C_L (in amplitude) are respectively 1.7 % and 1.8 %.

The efficiency of the two CBS versions is compared in Figure 4.12. The fully explicit CBS-AC converges faster, requiring less than one third of the computational time needed by the quasi-implicit version. This makes CBS-AC a valuable candidate for performing large scale fluid simulations. We note that for the quasi-implicit method the time step chosen is very close to the limit imposed by the CFL (Courant-Friedrichs-Lewy) condition. By using dual time stepping, the CBS version has no strict limitation on the real time step. This gives a great computational advantage, especially if a detailed evolution of the transient is not necessary.

The computational time required for each of these two time steps is different and does not substantially change along the transient (see Figure 4.13).

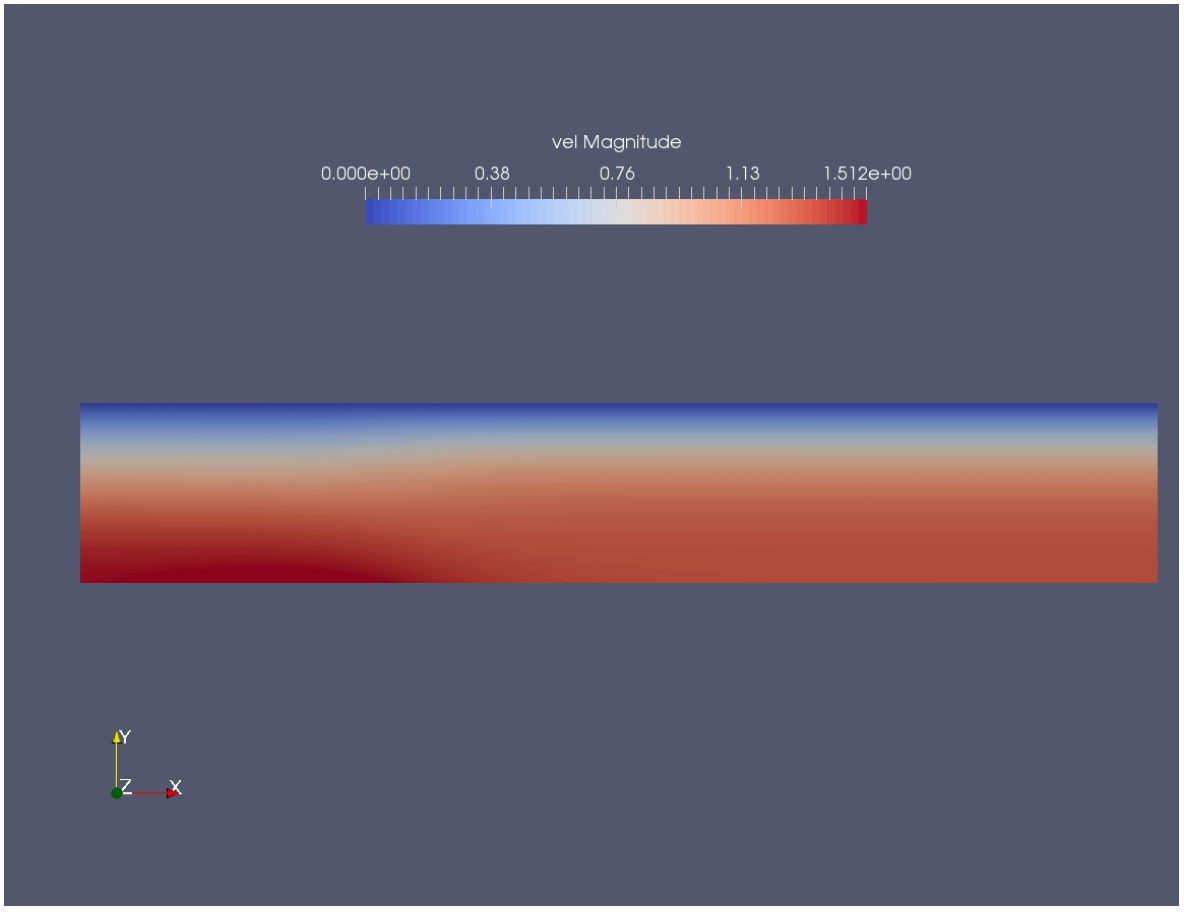

Figure 4.8: Flow in a rigid tube. Velocity magnitude field after 1.4 s, expressed in (cm/s)..

4.5.5 Vortex-induced vibrations of a flexible beam

Both solid and fluid solvers have been validated separately against reference testing cases, as suggested in [74]. In order to validate the integrated framework, we employ the well-known benchmark case proposed in [159]. It consists of a beam anchored to a block located in the middle of a channel (see Figure 4.14). The numerical experiment settings are as follows: The dynamic viscosity of the fluid (μ_F), the fluid and solid densities (ρ_F,ρ_S) are assumed respectively equal to μ_F=1.82 10^{-4} $Pa\ s$, ρ_F=1.18 10^{-3} g/cm^3 and ρ_S=0.1 g/cm^3. The other material parameters set are the solid Young's modulus (Y=2.5 10 6 N/cm^2) and the Poisson's ratio (ν_{Pois}=0.35). Plane stress conditions are assumed to hold for the solid. The inflow velocity is chosen as u_{inl}=51.3 cm/s. The Reynolds number is thus

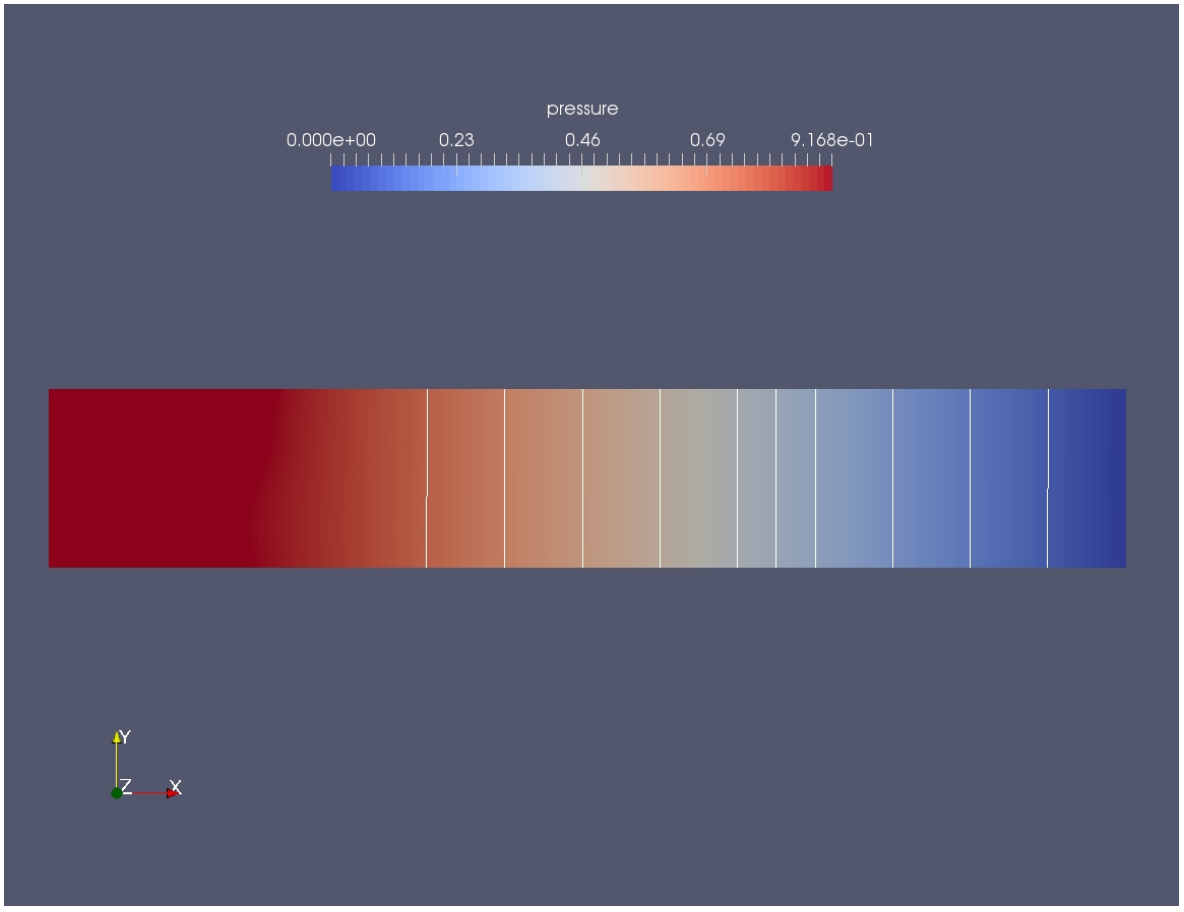

Figure 4.9: Flow in a rigid tube. Isobaric lines ($dyne/cm^2$) after 1.4 s.

$Re = \frac{\rho_F D u_{inl}}{\mu_F}$=333, whereby D=1 is the characteristic length of the square rigid body. For the domain discretization we adopted 3920 nodes and 4013 linear element for the fluid, while 46 nodes and 24 linear elements for the solid. In Figures 4.15 and 4.16 the velocity magnitude and pressure fields are reported for t=1.2 s. In the non-deformed configuration the beam is aligned with the far field flow. The vortices, which separate from the corners of the rigid body, generate lift forces which excite oscillations of the flexible beam. To verify the scheme accuracy we consider the vertical displacement of the beam (see Figure 4.17). The results obtained are in agreement with those reported in the reference work [74], in which the recorded maximum tip displacement and frequency are, respectively, 1.1 cm and 2.96 Hz. The corresponding relative errors are 17.2 % and 1.4 %, respectively. It is worth noticing that the difference in amplitude may be due to the different polynomial order adopted for the

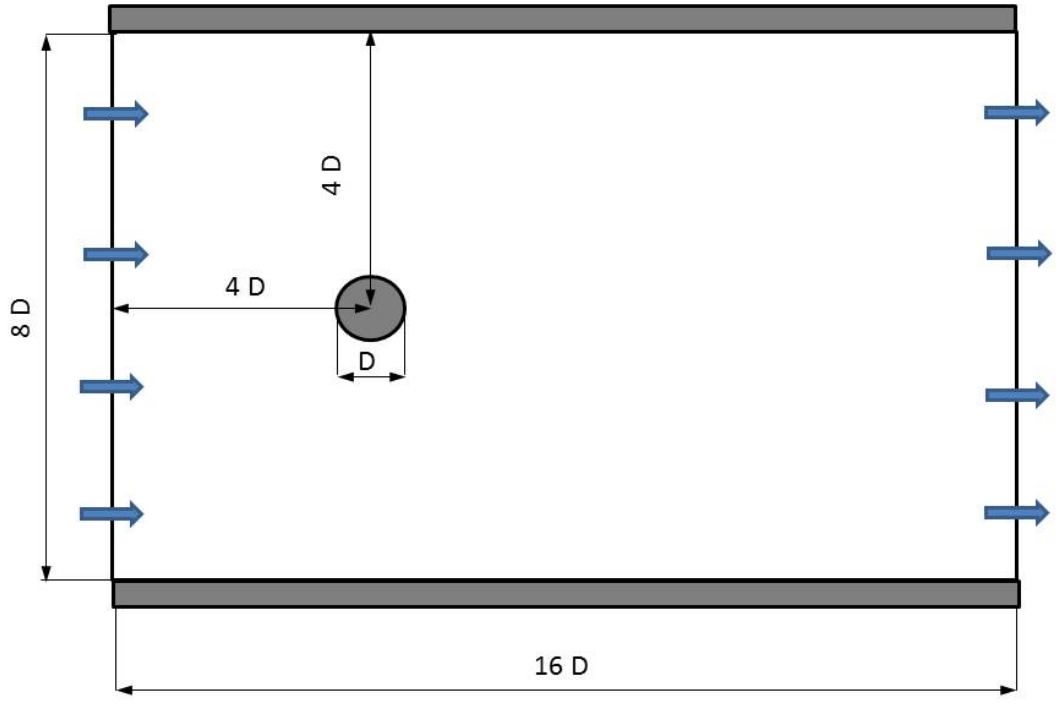

Figure 4.10: Flow passing a circular cylinder. Geometry of the problem, expressed in *cm*. Blue arrows indicate the direction of the velocity at the boundaries.

spatial discretization and the method used for dealing with the incompressibility constrain.

4.5.6 Pressure wave along an artery

The case of a 2-D vessel architecture is used to approximate flow and pressure distribution within an artery. For this numerical experiment all the constitutive data have been taken from the work by Zulliger et al. [47, 160]. The following parameters are set as constant: the dynamic viscosity of the blood (μ_F=1.82 10^{-3} $Pa\ s$), the fluid density (ρ_F =1.0 10^{-2} $g/cm3$), the solid density (ρ_S =1.0 g/cm^3) and the Poisson's ratio (ν_{Pois} = 0.35). The parameter we let vary is the Young's modulus; we consider a case with extremely stiff wall (Y=3.0 10^6 N/cm^2) and a case in which the wall is much more flexible (Y=5.0 10^5 N/cm^2). These distinct cases

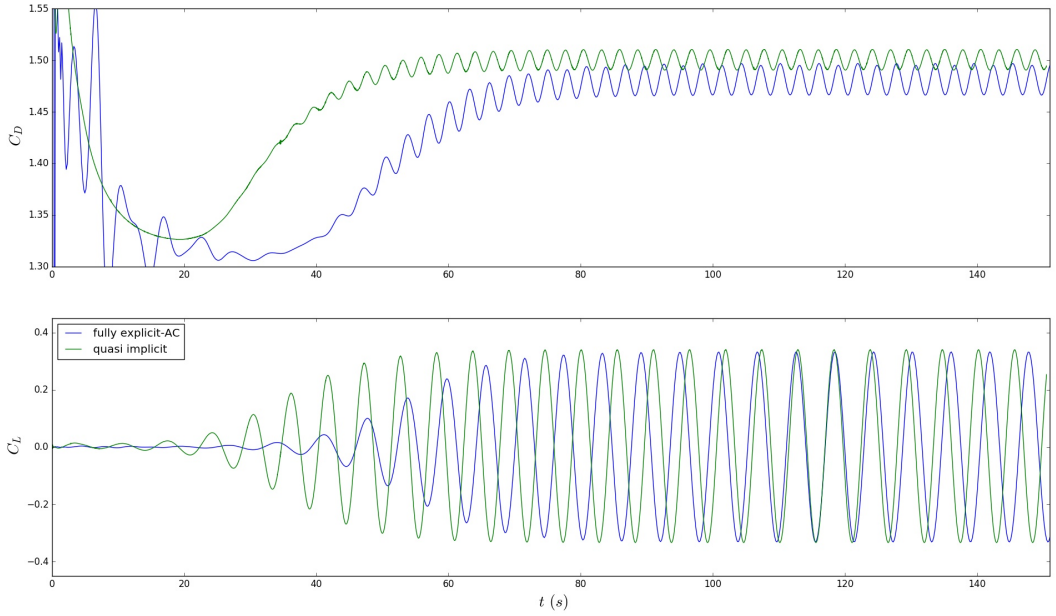

Figure 4.11: Flow passing a circular cylinder. Temporal evolution of drag and lift coefficients (C_D and C_L respectively). For the explicit CBS case the real time step Δt is equal to 0.166 s, while for the quasi-implicit case Δt is set equal to 0.00333 s.

provide a good perspective on the range of wall and flow responses. At the inlet a Poiseuille signal is applied and the Reynolds number is set equal to 400.

Figures 4.19, 4.20, 4.21, 4.22 present snapshots of the pressure and velocity magnitude fields for both cases. We note that these results are at 1.0 s and therefore transients are not yet fully eliminated. We observe that in case of a stiff artery (Figures 4.19 and 4.21) a small deformation of the wall occurs, while the pressure and velocity exhibit uniform patterns. In the case of a much more elastic vessel (Figures 4.20 and 4.22), the behaviour is significantly different. The wall swells due to momentary force impairment at the interface, followed by structure collapsing. At the shrinkage tract the flow accelerates and the velocity increases also in the radial direction, due to momentum conservation.

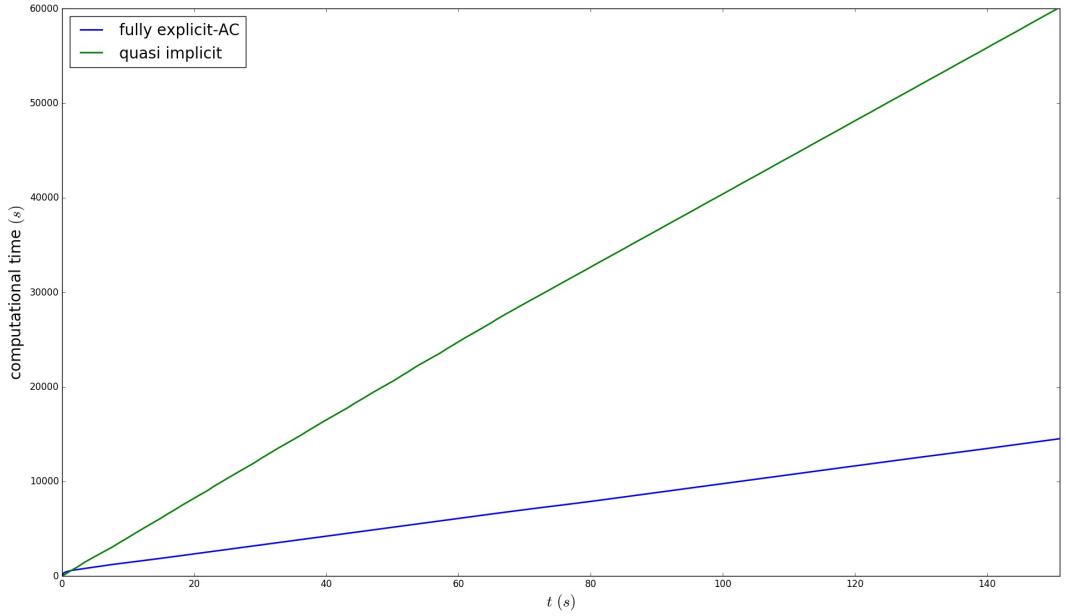

Figure 4.12: Flow passing a circular cylinder. Computational time vs real time. For the explicit CBS case the real time step Δt is equal to 0.166 s, while for the quasi-implicit case Δt is set equal to 0.00333 s.

4.6 Concluding remarks

A novel methodology has been developed and validated against literature benchmarks. Results from both solid and fluid solvers are in good agreement with the literature. The CBS-AC emerges as one of the most promising methods to be employed in large scale simulations. Moreover, results for the case presented in Section 4.5.5 prove the temporal stability of the global FSI framework. The fully explicit CBS method results are shown to be suitable for handling an FSI scheme. This methodology has also been used to represent an arterial vessel with elastic walls. In this study the constitutive parameter E has been varied along simulations and the findings qualitatively match observations. In the future we intend to employ this methodology to account for full 3D arterial geometries, and to incorporate the active contractile dynamics of the arterial wall. We also note that in accordance to current state of art the library is ran in serial mode. A future code parallelization would further enhance the software performance.

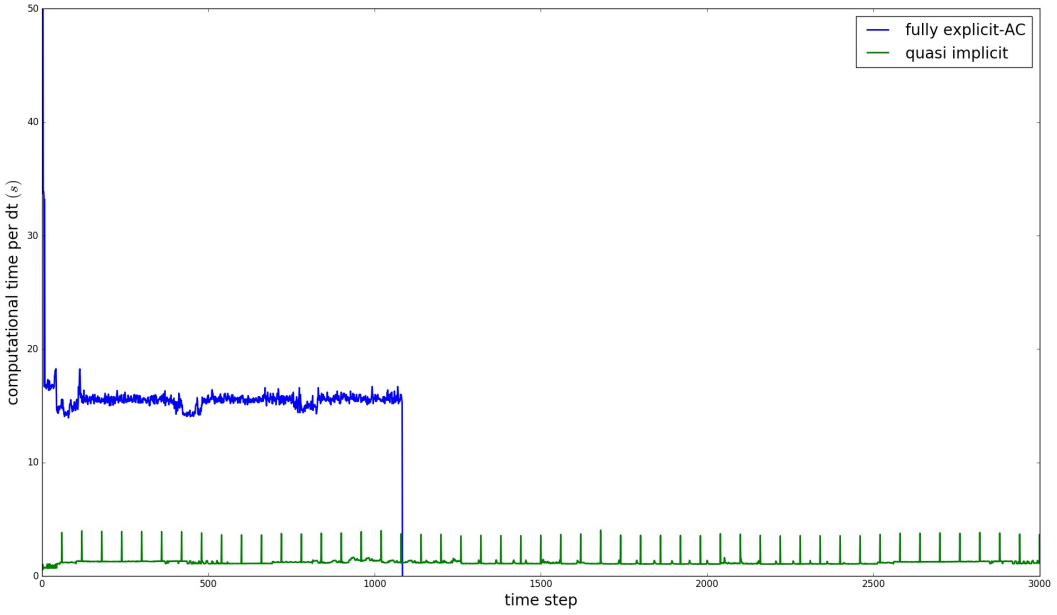

Figure 4.13: Flow passing a circular cylinder. Computational time per step vs real time. For the explicit CBS case the real time step Δt is equal to 0.166 s, while for the quasi-implicit case Δt is set equal to 0.00333 s.

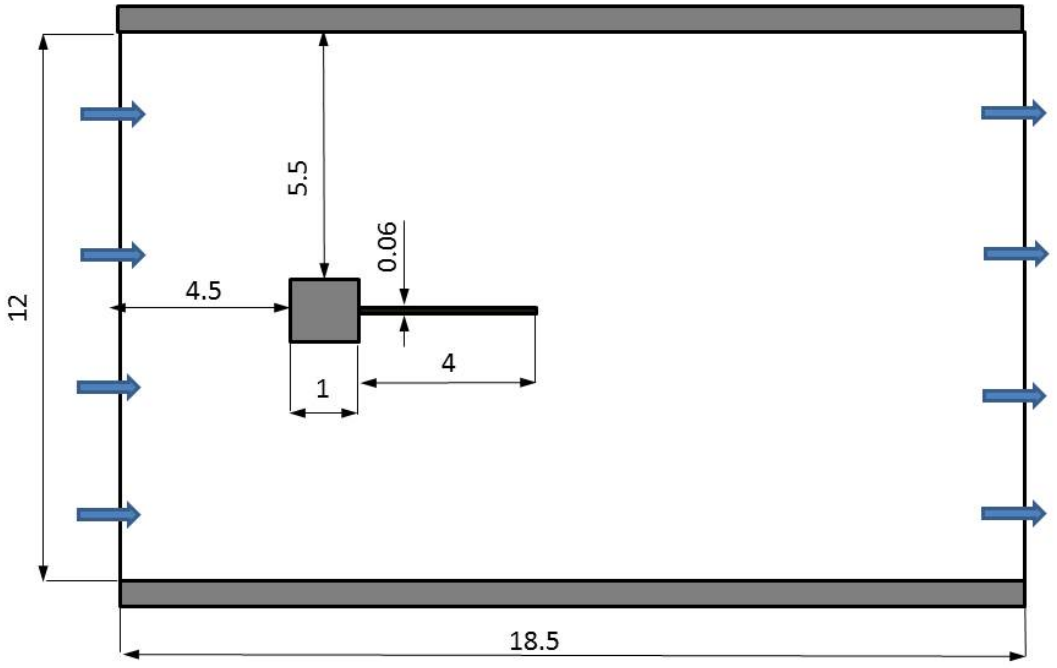

Figure 4.14: Vortex-induced vibrations of a flexible beam. Geometry of the problem, expressed in *cm*.

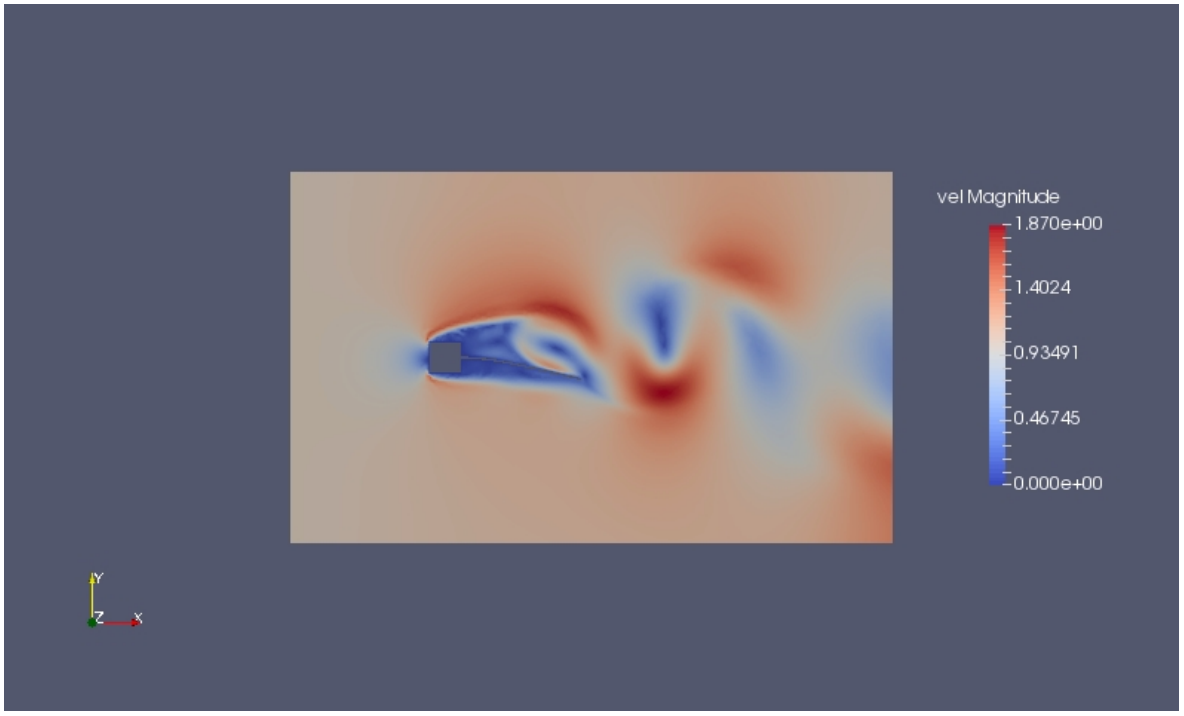

Figure 4.15: Vortex-induced vibrations of a flexible beam. Velocity magnitude field at t=1.2 *s*.

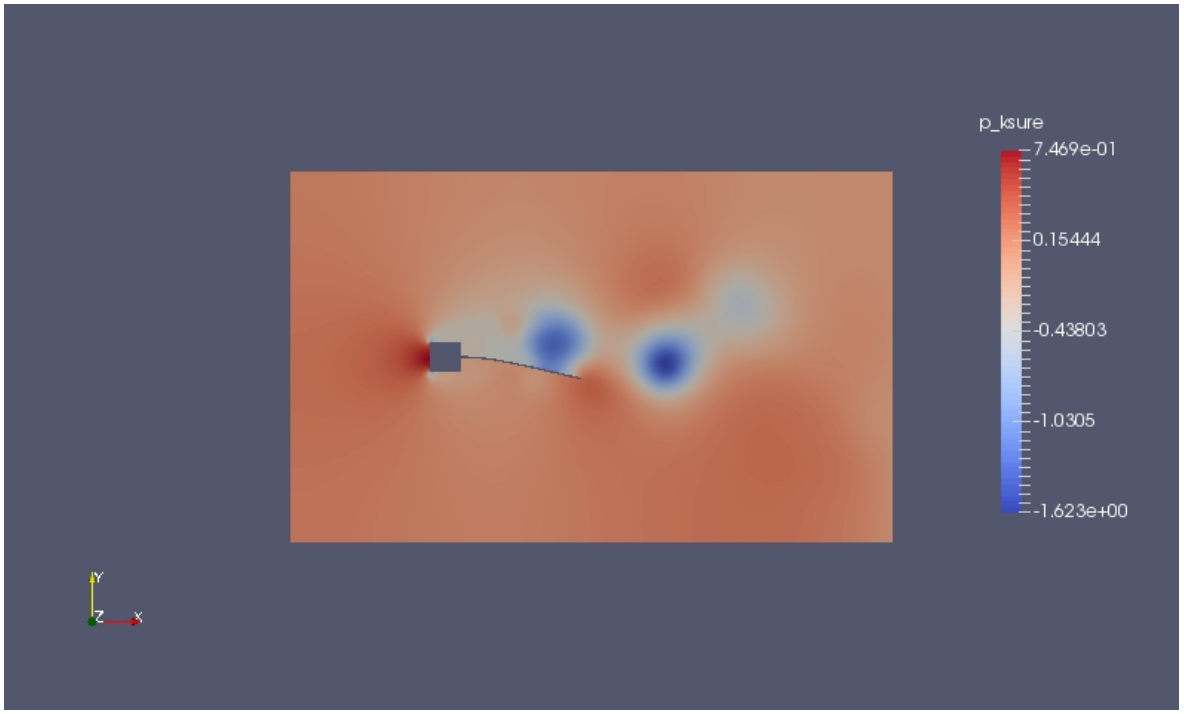

Figure 4.16: Vortex-induced vibrations of a flexible beam. Pressure field at t=1.2 *s*.

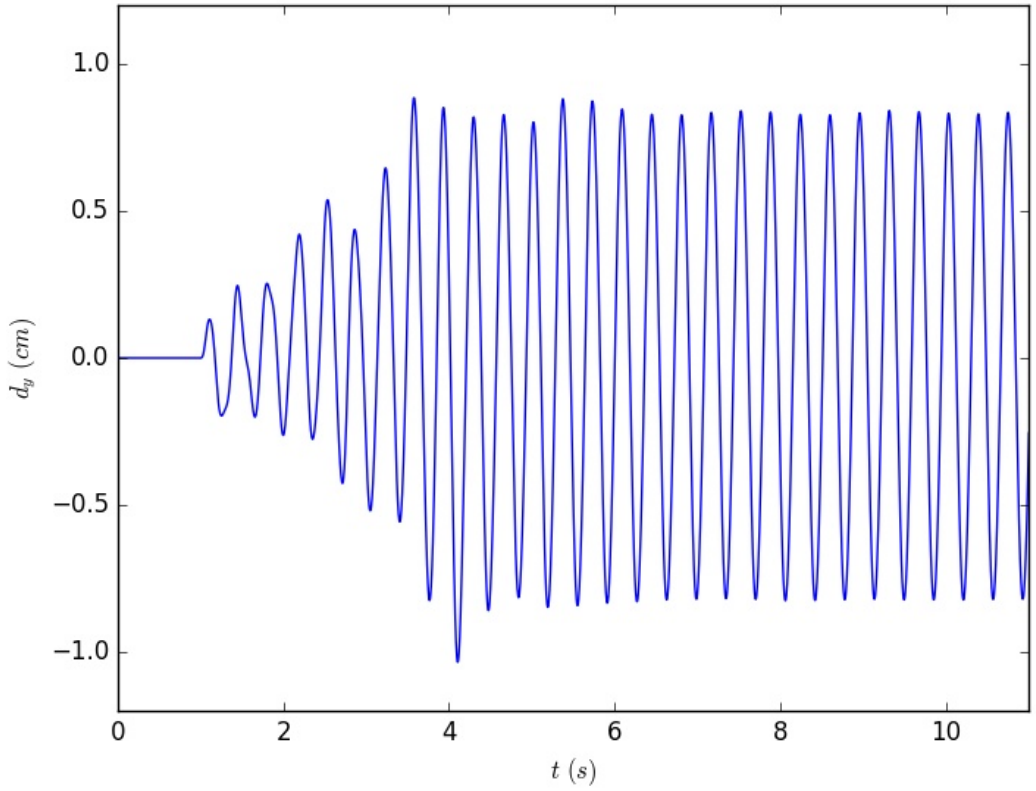

Figure 4.17: Vortex-induced vibrations of a flexible beam. Beam vertical displacement in time. For this case the real time step Δt is equal to 0.005 s.

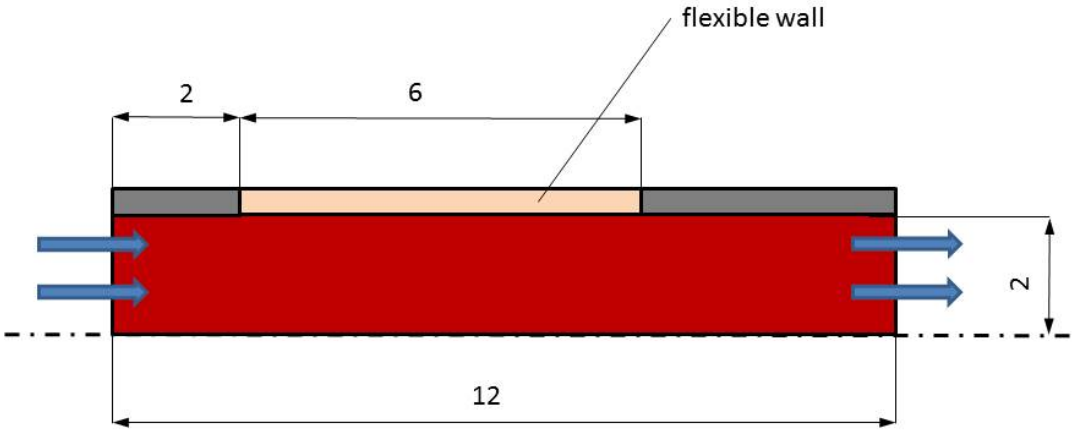

Figure 4.18: Pressure wave along an artery. Geometry of the problem (in *cm*).

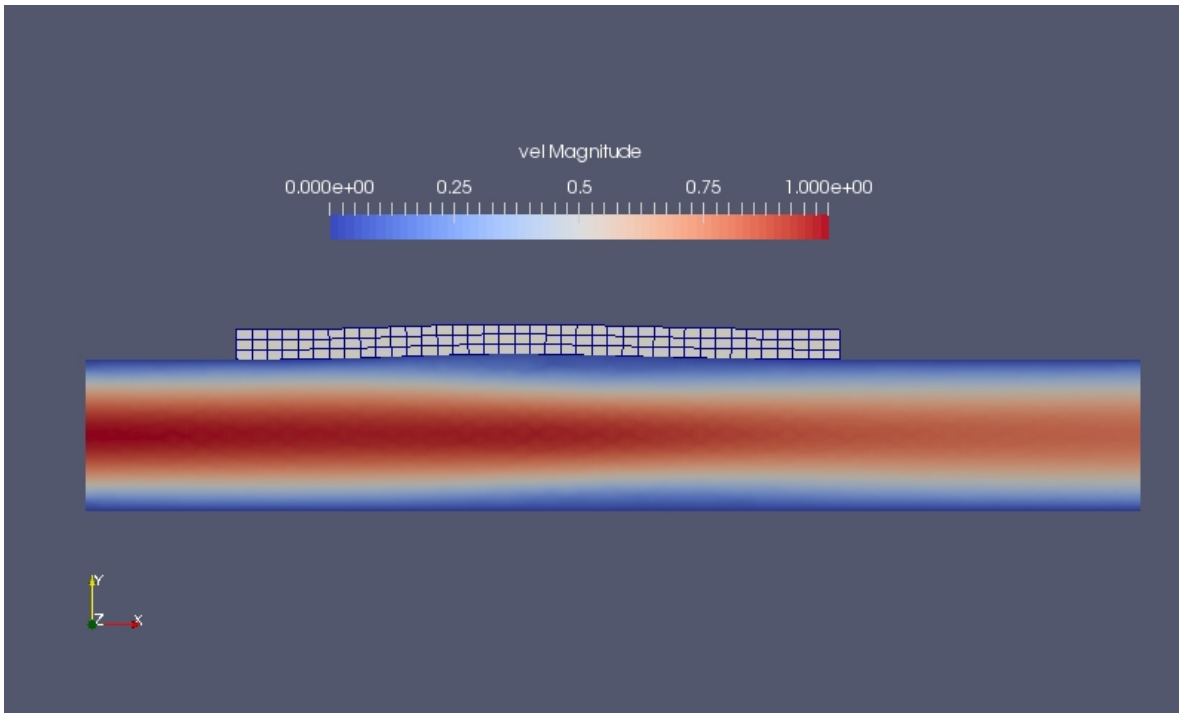

Figure 4.19: Pressure wave along an artery. Velocity magnitude field at t=1.0 s **(**Y**=3** 10^6 N/cm^2**).**

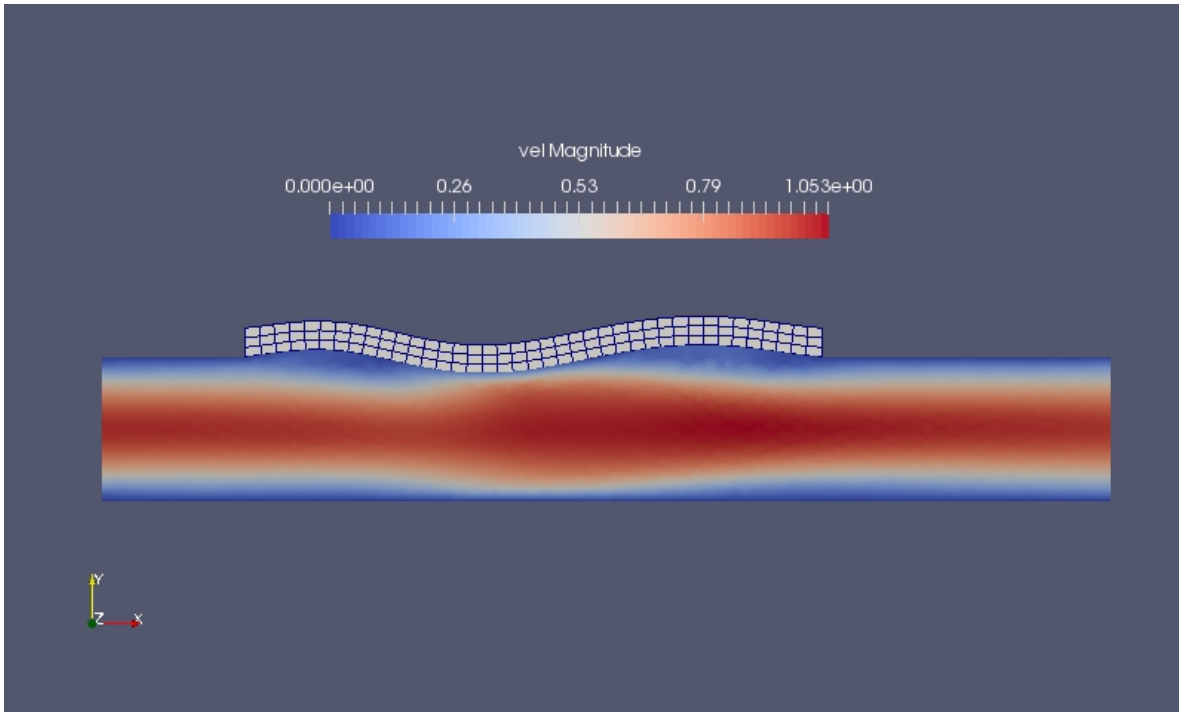

Figure 4.20: Pressure wave along an artery. Velocity magnitude field at t=1.0 s **(**Y**=3** 10^5 N/cm^2**).**

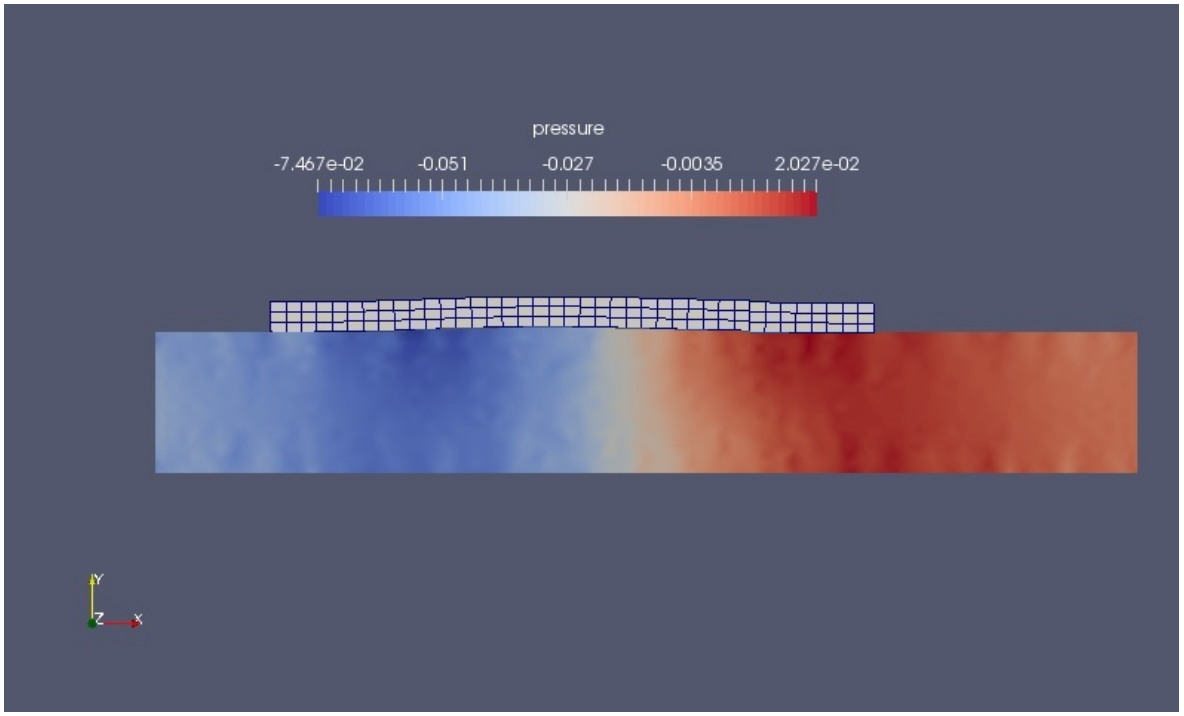

Figure 4.21: Pressure wave along an artery. Pressure field at t=1.0 s **(**Y**=3** 10^6 N/cm^2**).**

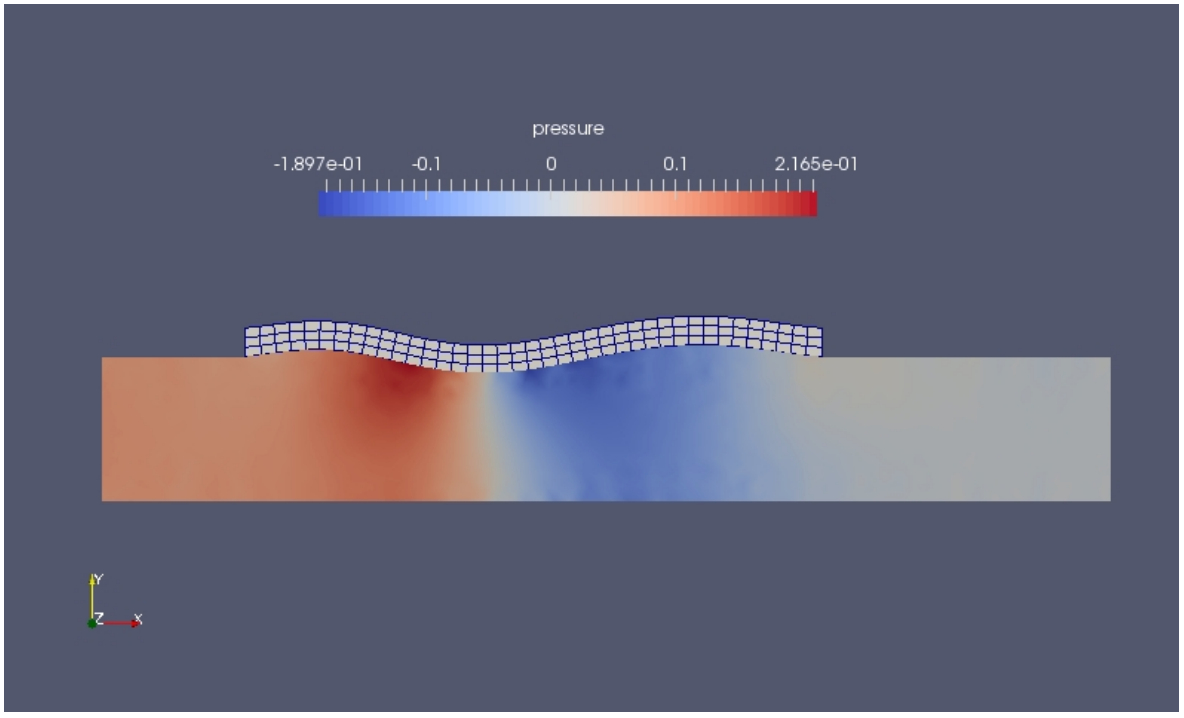

Figure 4.22: Pressure wave along an artery. Pressure field at t=1.0 s **(**Y**=3** 10^5 N/cm^2**).**

Chapter 5

Modelling energy transport within the human body

As anticipated in Section 1.3, computing blood transport along the arterial tree requires a multiscale approach for representing the vascular network. The methodology developed in Chapters 3 and 4, able to calculate accurately blood flow variables in a localized region of the vasculature, can be coupled with a reduced order (1-D) model representing the whole systemic circulation. This also allows the prescription of realistic boundary conditions. In this chapter, we report a model based on such a 1-D vessel framework, which allows to compute the transport of a blood property (in this case energy) within the solid tissues.

5.1 Background

The review of human body bio-heat transfer, presented in the Introduction, highlights the need for a step change in the modelling approach. A new generation model is therefore required as a basis for future development. In this regard, the present work combines a state of the art systemic circulation model with heat transfer to a segmentation model for body tissue. The methodology thus developed has been conceived as a combination of a multi segmental solid model, derived mostly from Fiala [101] and the arterial modelling methodology proposed by Mynard and Nithiarasu [64]. For the thermo-regulatory equations we refer to Smith [99]. The blood flow is considered laminar and a non-linear wall law is used for describing blood-wall interaction. With these assumptions, the final expressions of governing equations depend only on cross-sectional area, velocity and temperature of blood. The physical model of the arterial system is adopted from Low et al. [1], where the flow and pressure distributions in the arterial system are extensively compared to measurement data. The methods for dealing with ventricle, valve, bifurcations, coronary arteries and peripheral boundaries are detailed in [64, 161].

5.2 Objectives

As the present methodology is based on two robust models, it is able to respond to a wide spectrum of conditions without losing integrity of the solution. An example to this effect is the straightforward calculation of conduction in the solid system. The inherent robustness of the proposed model is one of its main advantages when compared to relevant recent works such as Salloum et al. [106] and Karaki et al. [107]. It would be fair to say that these modelling works have demonstrated good performance in simulating various situations, such as the evaluation of local thermal comfort and human physiological responses to cold water immersion. By comparison, the main aim of the proposed work is not to provide an analysis of the thermal performance of a specific subsystem, but to characterise the heat exchanges occurring within the multi-layer solid tissues. A further aim is to investigate how the two intrinsically coupled subsystems interact whenever the body is exposed to a range of external conditions (especially during non-thermal neutral settings). We were thus able to demonstrate that, depending on the conditions, flow may have either a rewarming or cooling effect on the surrounding tissues. These results have emphasised the modulatory role of arterial inner convection. Although processes involving cold induced vasodilation (CIVD) and arterio-venous anastomoses (AVA) would improve the predictive quality of our model, they were not incorporated in the formulation as they would disproportionately complicate the proposed methodology. Indeed, the main aim of this work is to provide a robust tool able to evaluate temperature distribution along tissues, which offers a different perspective in the study of bio-heat transfer within the human body, rather than to improve on the accuracy of existing models.

The aims of the work can be summarised in the following points:

- to present a one-dimensional thermo-fluid model for an elastic tube and tube network
- to investigate the influence of structural properties of the vessel wall and network singularities on property transport

- to deliver a comprehensive methodology for predicting the energy/property transport within the human body
- to investigate the role of internal convection on the global body thermal balance
- to validate the proposed model for different conditions against experimental/literature data

In Section 5.3 we present the methodology developed. Then in Section 5.4 the numerical procedure is outlined. Results and discussion are reported in Section 5.5, followed by the concluding remarks (Section 5.6).

5.3 Mathematical formulation of the problem

The human body bio-heat transfer can be modelled using a combination of "passive" and "active" systems. The passive part consists of transport in arteries and solid tissues while the active system is the thermo-regulatory part of the model that attempts to keep the body temperature within predetermined boundaries. This section starts by introducing the governing equations valid for a monodimensional elastic vessel, which represents the fundamental element of the global methodology. This is followed by a description of the system circulation, solid tissues, and thermo-regulatory system.

5.3.1 Flow in 1-D elastic vessel

The variables considered in the system are cross sectional area (A), the average values of velocity (u), fluid pressure (p) and temperature (T) over the cross section (see Figure 5.1). The density (ρ_F) of the fluid and wall are considered constant due to the incompressible nature of the materials assumed. The viscosity (μ_F) of the fluid is also assumed to be a

constant. Due to the one-dimensional nature of the model, the shear stress is evaluated using Poiseuille's flow assumption, i.e.,

$$\frac{d\tau_F}{dx} = -\frac{8\pi\mu_F u(x,t)}{A(x,t)} \tag{5.1}$$

where $Q = Au$ is the volume flow rate averaged over a cross-section. Due to the simplified assumptions, the model is not valid for cases in which flow is non-Newtonian or turbulent. In order to reduce the number of parameters, specific heat (c_F) and thermal conductivity (k_F) of the materials are also assumed to be constant.

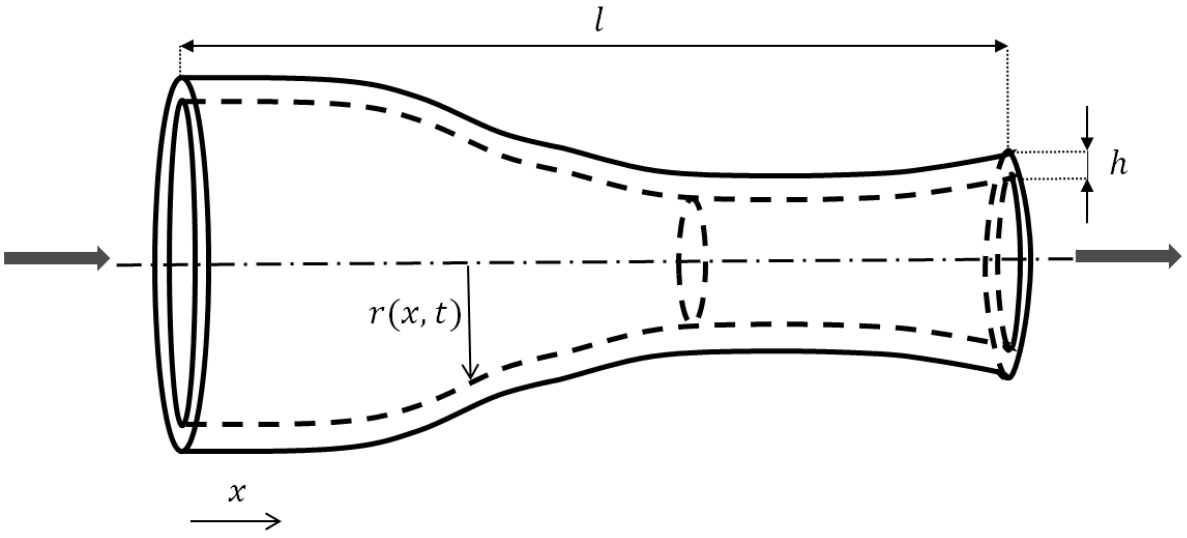

Figure 5.1: Schematic representation of flow and energy transport in a flexible tube (from [4]).

The full problem could be described by four equations: the conservation laws of mass, momentum and energy and a constitutive elastic wall model to define the relationship between the fluid pressure and the cross section area. Following the existing literature [162], the equations of mass and momentum for an elastic vessel can be written as

$$\frac{\partial A(x,t)}{\partial t} + \frac{\partial Q(x,t)}{\partial x} = 0 \tag{5.2}$$

$$\frac{\partial u(x,t)}{\partial t} + u(x,t)\frac{\partial u(x,t)}{\partial x} + \frac{1}{\rho_F}\frac{\partial p(x,t)}{\partial x} - \frac{1}{\rho_F}\frac{\partial \tau_F(x,t)}{\partial x} = 0 \tag{5.3}$$

It is important to note that these equations are valid for an infinitesimal cylindrical element of area A and length dx. For relating pressure and cross sectional area, a non-linear relation used by Formaggia et al. [163] and Olufsen et al. [62] is employed, i.e.,

$$p(x,t) = p_{ext} + \beta\left(\sqrt{A(x,t)} - \sqrt{A_0(x)}\right) \tag{5.4}$$

where p_{ext} is the external pressure acting on the walls of the tube, A_0 is the unstressed cross-section area and β is the characteristic property of elastic material, defined as

$$\beta = \frac{\sqrt{\pi}hY}{A_0(1-\nu_{Pois}^2)} \tag{5.5}$$

where Y is Young's modulus of the wall material, h is the wall thickness (see Figure 5.1) and ν_{Pois} the Poisson ratio of the wall material. By inserting Equations (5.1) and (5.4) into Equation (5.3), it is possible to express the momentum equation only in terms of area and velocity:

$$\frac{\partial u(x,t)}{\partial t} + u(x,t)\frac{\partial u(x,t)}{\partial x} + \frac{\beta}{2\rho_F\sqrt{A(x,t)}}\frac{\partial A(x,t)}{\partial x} + \frac{8\pi\mu_F}{\rho_F}\frac{u(x,t)}{A(x,t)} = 0 \tag{5.6}$$

Considering the 1-D elastic vessel shown in Figure 5.1, the integral balance of energy can be written as:

$$\begin{aligned}\dot{\Phi}_{conv}(t) =& \dot{W}_{wall}(t) + \dot{W}_{shear}(t) + \dot{\Phi}_{cond}(0,t) - \dot{\Phi}_{cond}(l,t) \\ &+ \rho_F Q(l,t)\left(E_s(l,t) + \frac{p(l,t)}{\rho_F}\right) - \rho_F Q(0,t)\left(E_s(0,t) + \frac{p(0,t)}{\rho_F}\right) \\ &+ \rho_F \frac{\partial}{\partial t}\int_0^l A(x,t)E_s(x,t)\,dx\end{aligned} \tag{5.7}$$

where E_s represents the specific energy of the fluid obtained as a sum of the specific internal energy and the kinetic energy ($E_s = e + \frac{u^2}{2}$), $\dot{\Phi}_{cond}$ is the conduction fluxes in the fluid, while $\dot{\Phi}_{conv}$, $\dot{W}_{wall}$ and $\dot{W}_{shear}$ are respectively the thermal flux exchanged by convection, integral quantities along the tube due to fluid forces on the walls and viscous losses. After simplification, the differential one-dimensional energy conservation equation for an infinitesimal tube (without considering viscous effects) can be written as,

$$\frac{\partial T(x,t)}{\partial t} + u(x,t)\frac{\partial T(x,t)}{\partial x} - \alpha_F \frac{\partial^2 T(x,t)}{\partial x^2} = \frac{2h_{in}}{\rho_F c_F \sqrt{A(x,t)/\pi}}(T_{w,in}(x,t) - T(x,t)) \quad (5.8)$$

where α_F is the thermal diffusivity of the fluid, h_{in} is the heat transfer coefficient at the inner surface of the wall and $T_{w,in}$ is the inner wall temperature. The full system of equations composed of Equations (5.2), (5.6) and (5.8) is non-linear and the first and second equations are strongly coupled. However, the mass and momentum conservation equations do not depend on the temperature. Thus, it is possible to split the solution process into two steps: in the first step one can calculate the velocity, cross sectional area and pressure using Equations (5.2) and (5.6) before computing the temperature in the second step.

Characteristic system

In order to assign boundary conditions and to apply the Taylor Galerkin method, it is convenient to write the whole system in a linearized de-coupled form. In Formaggia et al. [164] and Sherwin et al. [162], the system composed of mass and momentum conservation equations is written in a quasi linear form. Incorporating the energy equation requires a similar procedure. The system of Equations (5.2), (5.6) and (5.8) may be written as

$$\frac{\partial \bar{\mathbf{U}}_F}{\partial t} + \mathbf{H}_F \frac{\partial \bar{\mathbf{U}}_F}{\partial x} + \frac{\partial \bar{\mathbf{G}}_F}{\partial x} = \bar{\mathbf{S}}_F \quad (5.9)$$

with:

$$\bar{\mathbf{U}}_F = \begin{bmatrix} A \\ u \\ T \end{bmatrix}; \quad \mathbf{H}_F = \begin{bmatrix} u & A & 0 \\ \frac{\beta}{2\rho_F\sqrt{A}} & u & 0 \\ 0 & 0 & u \end{bmatrix}; \quad \bar{\mathbf{G}}_F = \begin{bmatrix} 0 \\ 0 \\ -\alpha_F \frac{\partial T}{\partial x} \end{bmatrix} \text{ and } \bar{\mathbf{S}}_F = \begin{bmatrix} 0 \\ -\frac{8\pi\mu_F}{\rho_F}\frac{u}{A} \\ \frac{2h_{in}}{\rho_F c_F \sqrt{A/\pi}}(T_{w,in} - T) \end{bmatrix}$$

where $\bar{\mathbf{U}}_F$, $\bar{\mathbf{G}}_F$ and $\bar{\mathbf{S}}_F$ are the vectors of primitive variables, the diffusive and source terms, while $\mathbf{H}_F$ is the matrix associated to convective term. If diffusion and sources are considered negligible ($\frac{\partial \bar{\mathbf{G}}_F}{\partial x} = 0$ and $\bar{\mathbf{S}}_F = 0$), the characteristic variables of Equation (5.9) may be determined.

Eigenvalues ($\bar{\Lambda}_{F,i}$) and eigenvectors ($L_{F,i}$) of the characteristic system are evaluated respectively by solving $|\bar{\mathbf{\Lambda}}_F \mathbf{I}_d - \mathbf{H}_F| = 0$ and $L_{F,i}\mathbf{H}_F = \bar{\Lambda}_{F,i} L_{F,i}$ [165]. In this case all eigenvalues associated to matrix $\mathbf{H}_F$ are real numbers, i.e.,

$$\bar{\mathbf{\Lambda}}_F = \begin{bmatrix} \bar{\Lambda}_{F,1} \\ \bar{\Lambda}_{F,2} \\ \bar{\Lambda}_{F,3} \end{bmatrix} = \begin{bmatrix} u + c_s \\ u - c_s \\ u \end{bmatrix} \tag{5.10}$$

where c_s is the intrinsic wave speed associated with the flexible wall material, expressed as

$$c_s = \sqrt{\frac{\beta\sqrt{A}}{2\rho_F}} \tag{5.11}$$

Eigenmatrix is:

$$\bar{\mathbf{L}}_F = \begin{bmatrix} c_s/A & 1 & 0 \\ -c_s/A & 1 & 0 \\ 0 & 0 & 1 \end{bmatrix} \tag{5.12}$$

The characteristic variables are defined as

$$dw_i = L_{F,i}\bar{\mathbf{U}}_F \tag{5.13}$$

and integration gives,

$$\begin{bmatrix} w_1 \\ w_2 \\ w_3 \end{bmatrix} = \begin{bmatrix} u+4c_s \\ u-4c_s \\ T \end{bmatrix} \tag{5.14}$$

By rearranging the above equations, it is possible to express the primitive variables in terms of the characteristic variables as

$$A = \frac{(w_1 - w_2)^4}{1024}\left(\frac{\rho_F}{\beta}\right)^2, \quad u = \frac{1}{2}(w_1 + w_2) \quad \text{and} \quad T = w_3 \tag{5.15}$$

Writing Equation (5.9) in terms of characteristic variables allows one to understand how information is transported in the domain considered. The physical interpretation of the first and second characteristic variables is that pressure and velocity wave fronts propagate forward (towards the exit) at a speed of $u + c_s$ and backwards (towards the inlet) at $u - c_s$. A wave front may be considered to be a particular point on a pulse [166] (for example, the peak or the foot). The third characteristic variable instead, has the eigenvalue equal to the velocity u. Thus it means that the temperature is a property transported by the flow with the effective velocity of the fluid u.

These relationships are employed at the boundaries to apply boundary conditions.

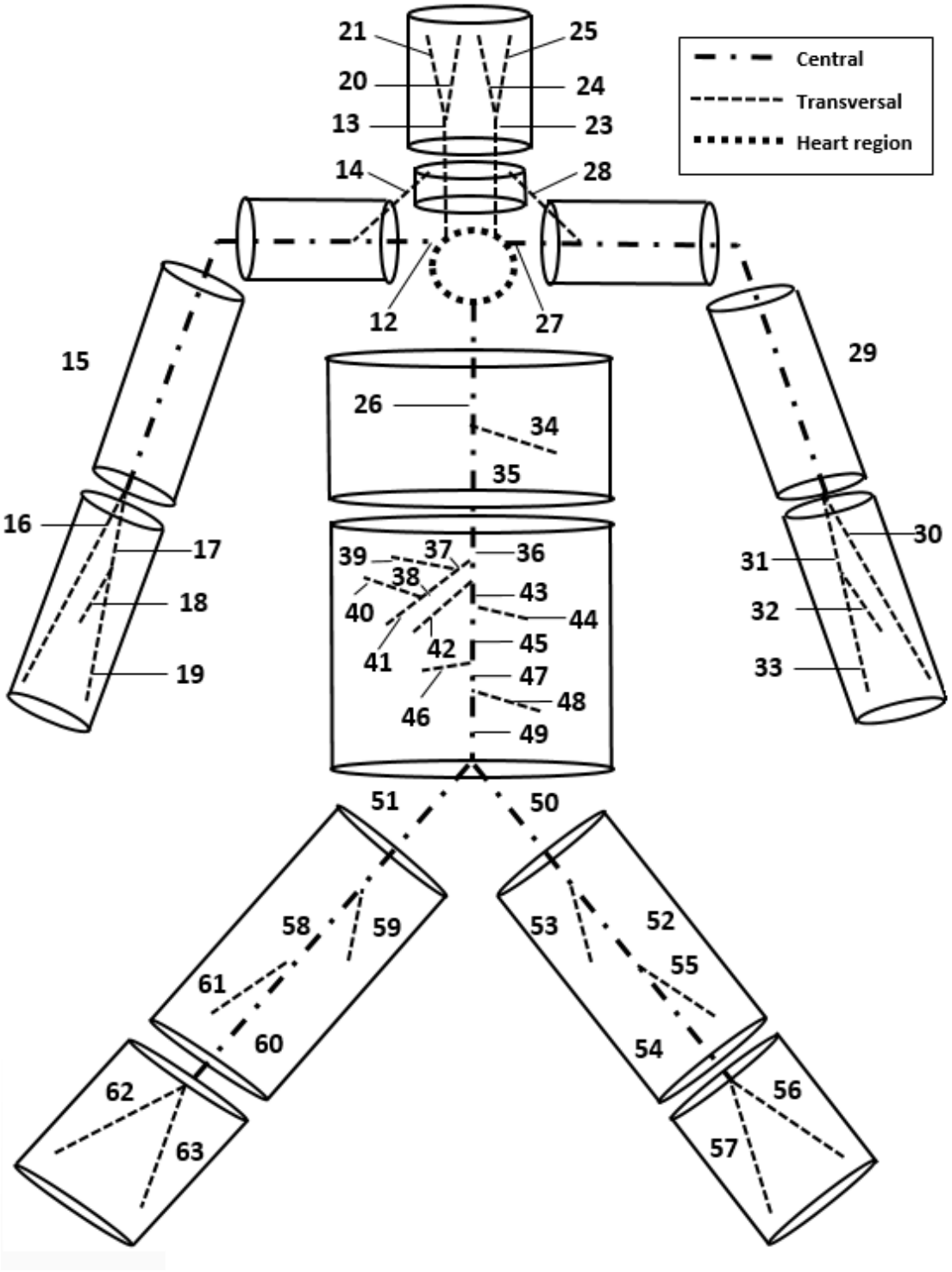

Figure 5.2: Arterial network considered (from [5]).

5.3.2 Systemic circulation

Arterial network

The systemic circulation is subdivided into large and small vessels. The large arteries are shown in Figure 5.2 as proposed in Low et al. [1]. In the present study, only major arteries are included. The microcirculation is represented by tapering vessels at the extremities of the network [64] and the energy exchange occurs only through a perfusion mechanism. The venous system is not included for the reasons mentioned previously. The whole network is composed by 91 segments (28 are tapering vessels), 6288 elements and 6379 nodes. Full details about the parameters and dimensions of the network are reported in [1].

Inlet flow conditions

Modelling the heart's pumping action is implemented by employing the method proposed in [64, 1]. The action of the heart allows one to set inlet boundary conditions and the system includes the left ventricle (LV) and aortic valve (AV) models. The LV is treated as a prescribed forward pressure source, which describes the cardiac cycle and the number of heart beats per unit time or heart rate (HR). The input of the model is a ventricular (forward) pressure prescribed in the ventricle's point just before the valve. Prescribing inlet and outlet variables is carried out by means of characteristic variables. By rearranging formulations in Equations (5.4) and (5.14) and prescribing forward pressure (p_{in}), it is possible to evaluate the forward characteristic at the inlet (w_{1in}):

$$w_{1in}^{n+1} = w_2^0 + 4\sqrt{\frac{2}{\rho_F}}\sqrt{(p_{in}^{n+1} - p_{ext}) + \beta\sqrt{A_0}} \tag{5.16}$$

where w_2^0 is the initial value of w_2 and is also equal to the value of w_2 at any time, if no backward-running waves reach the inlet. The backward characteristic variable (w_2) may be

evaluated via linear extrapolation in the $x-t$ plane, where for the next time step $n+1$,

$$w_2^{n+1}|_{x=x_0} = w_2^n|_{x=x_0-\bar{\Lambda}_{F,2}^n \Delta t} \tag{5.17}$$

Primitive variables A and u at the inlet node can be evaluated by using Equation (5.15). The behaviour of the AV is represented by a time-varying transmitter and reflector at the inlet. For each impedance of the network, a characteristic reflection coefficient (R_z) could be defined as

$$R_z = -\frac{\Delta w_2}{\Delta w_1} = \frac{w_2^{n+1} - w_2^0}{w_1^{n+1} - w_1^0} \tag{5.18}$$

where w_1^0 is the initial value (corresponding to no-pulse situation). Including the contribution from the AV, the total forward characteristic variable (w_{1in}^*) can be written as

$$w_{1in}^* = w_{1p} + w_{1r} + w_1^0 \tag{5.19}$$

where w_{1p} is the change in the incoming characteristic associated with the ventricular pump and w_{1r} is the change associated with backward-travelling waves that are partially or completely reflected from the valve.

Using Equation (5.18) to model the AV impedance, it is possible to write:

$$w_{1r} = R_{Vr}(t)\Delta w_2 \tag{5.20}$$

where $R_{Vr}(t)$ is a time-varying valve reflection coefficient for backward-travelling waves. It is assumed that $R_{Vr} = 0$ when the valve is open, $R_{Vr} = 1$ when it is closed, and that this value varies exponentially when the valve is opening or closing. Further details on the boundary conditions may be obtained from [64, 1].

Extremities and branching points

To model branch ending, tapering vessels are used. These terminal tubes present multiple step decreases in A_0 or step increases in β. Thus characteristic reflections of the downstream vasculature are accounted for. Calculation of the backward characteristic variable on the exit node may also be performed by prescribing reflections at the exit. The reflection coefficient of the terminal vessel (R_t) can be determined again by means of Equation (5.18), while the value of w_1 for the next time step $(t = n+1)$ is extrapolated. Thus the unknown (w_2^{n+1}) is

$$w_2^{n+1} = w_2^0 - R_t(w_1^{n+1} - w_1^0) \tag{5.21}$$

In the present work, R_t is set equal to 0 for each tapering vessel. Further details on the flow boundary conditions may be obtained from relevant published work [64]. At the extremities, we assume that the incoming flow is in thermal equilibrium with the surrounding tissue nodes. When the flow is outgoing from the system, the temperature at the downstream point is assigned by characteristic variable extrapolation. As tapering vessels used at the exit boundaries represent microcircualtion, adiabatic conditions are assumed within these vessels (no heat exchange through convection occurs). Robust modelling requires consideration of branching points such as bifurcations or discontinuities in geometrical and material properties. The works of Mynard and Nithiarasu [64] are adopted in the present work.

5.3.3 Solid tissues

For the solid tissue representation, we follow the work of Fiala et al. [100]. The body consists of fourteen multi-layered cylindrical elements representing head, neck, shoulders, thorax, abdomen, arms, forearms, thighs and legs (details are reported in Table 5.1). The segments representing shoulders, legs, thighs, arms and forearms are constituted by four layers of materials with different properties; from inside to outside the cylinder consists of bone, muscle, fat tissue and skin layers. In the head, thorax and abdomen segments, inner

organs, brain, lung and viscera respectively are also included. We note that some geometrical parameters differ because cylinders have been adapted to the arterial tree.

Cylinder	Tissues	Layer radii (*cm*)	Length (*cm*)
head	brain, bone, fat, skin	6.6, 7.6, 7.8, 8.0	23.5
neck	bone, muscle, fat, skin	1.9, 5.4, 5.6, 5.8	7.9
thorax	lung, bone, muscle, fat, skin	7.7, 8.9, 12.3, 12.6 12.9	15.6
abdomen	viscera, bone, muscle, fat, skin	7.9, 8.3, 10.9, 12.4, 12.6	24.8
shoulder	bone, muscle, fat, skin	3.7, 3.9, 4.4, 4.6	13.4
arm	bone, muscle, fat, skin	1.5, 3.4, 4.0, 4.2	29.6
forearm	bone, muscle, fat, skin	1.5, 3.4, 4.0, 4.2	23.7
thigh	bone, muscle, fat, skin	2.2, 4.8, 5.3, 5.5	58.5
leg	bone, muscle, fat, skin	2.2, 4.8, 5.3, 5.5	34.3

Table 5.1: Tissue distribution within body. Note that the thorax length is smaller than the real average size as heart region is not included.

We note that, in agreement with [100], we model the head as a cylinder and not a sphere; thus the layer radii are resized in order to keep the head volume constant.

In the current model a local thermal equilibrium between the venous blood and the tissue temperatures is assumed. The heat transfer by perfusion is assumed to be proportional to the temperature difference between arterial blood entering the tissue and the tissue itself. In order to evaluate tissue temperature (T_t), the one-dimensional bio-heat transfer equation in cylindrical coordinates is solved. For a single layer, the heat conduction is described by the following expression [167]

$$\rho_t c_t \frac{\partial T_t}{\partial t} - k_t \frac{1}{r}\frac{\partial}{\partial r}(r\frac{\partial T_t}{\partial r}) = q_m + \phi_{perf}\rho_F c_F (T - T_t) \tag{5.22}$$

In the above equation, r is the radial coordinate, q_m is the volumetric heat generation associated with the metabolism and ρ_t, c_t, k_t, ϕ_{perf} are respectively the density, specific heat, thermal conductivity and perfusion coefficient of the tissue. The metabolism term q_m represents mainly the energy generation due to biological processes. If the body is subjected to work, an enhancement of metabolism in muscle tissue occurs.

5.3.4 Thermo-regulatory system

Studies show that a state of thermo-neutrality exists when the core and mean skin temperatures of the body are respectively 36.8^{o}C and 33.7^{o}C [9]. When an imbalance in energy exchange between the body and environment occurs, the thermo-regulatory system is activated to maintain the body homeostasis. The core body temperature is controlled by the thermo-regulatory system consisting of thermoreceptors and the hypothalamus. Three control mechanisms, shivering (lower skin temperatures), sweating (higher skin temperatures) and vasomotion (flow control), are considered here. We define T_{core} as the mean temperature between the first layer inner nodes of head, neck, thorax and abdomen, while T_{skin} is the average value on the skin surface. With these integral variables, we can evaluate the shivering and vasomotion contributions [99]. The shivering heat per unit volume, q_{shiv}, may then be obtained by dividing the total segmental heat production by muscle volume. In the present study, the basal and vasomotor blood flows are taken from [99]. The corresponding perfusion rate ϕ_{perf} is evaluated by dividing the flow rate by the skin mass of the segment considered. The total evaporative heat loss q_{swe} is computed following [168]. For these calculations we assume that the vapour pressure on skin is equal to that of saturated water vapour at skin temperature [169]), while the evaporative heat transfer coefficient (h_{swe}) is taken from ([170]). We include also the clothing model proposed in [9]. The most relevant equations for modelling the regulatory processes are reported here.

Shivering

From [99] it is assumed that the shivering temperature, T_{shiv}, is a function of the core temperature, i.e.,

$$\begin{cases} T_{shiv} = 35.5^oC \;\; if \;\; T_{core} < 35.8\ ^oC \\ T_{shiv} = -10222 + 570.9\ T_{core} - 7.9455\ T_{core}^2\ (^oC) \\ \;\; if \;\; 35.8\ ^oC \leq T_{core} \leq 37.1\ ^oC \end{cases} \tag{5.23}$$

It should be noted that for T_{core} greater than 37.1^oC, shivering does not occur. The maximum increase in total metabolic heat generation caused by shivering ($Q_{shiv,max}$) can be written as

$$Q_{shiv,max} = \frac{1}{3600}(-1.1861\ 10^9 + 6.552\ 10^7\ T_{core} - 9.0418\ 10^5\ T_{core}^2)\ (W) \tag{5.24}$$

The shivering metabolic heat generation Q_{shiv} can now be calculated as

$$Q_{shiv} = Q_{shiv,max}[1 - (\frac{T_{skin} - 20}{T_{shiv} - 20})^2]\ (W)\ \ if\ \ (40 - T_{shiv}) \leq T_{skin} \leq T_{shiv}\ (^oC) \tag{5.25}$$

Vasodilation and vasoconstriction

Vasodilation and vasoconstriction increase and decrease, respectively, arterial flow in the skin layers. To model these processes we follow the method proposed in [99]. At thermoneutrality condition, flow assumes a basal value ($\dot{m}_{skin,bas}$). Whenever core temperature increases over its neutral value, vasodilation occurs. When the core temperature reaches 37.2 ^{o}C, the maximum flow in the skin layer is recorded ($\dot{m}_{skin,max}$). Between the core temperatures of 36.8 ^{o}C and 37.2 ^{o}C, the skin blood flow follows the core temperature linearly. As mean skin temperature falls below its neutral value of 33.7 ^{o}C, vasoconstriction occurs. The state of maximum vasoconstriction is recorded for a mean skin temperature equal to 10.7 ^{o}C [99]. At this temperature the skin blood flow assumes a minimum value ($\dot{m}_{skin,min}$). Between skin temperatures of 33.7^oC and 10.7^oC the skin blood flow is assumed to vary linearly with temperature.

The evaluation of vasodilation and vasoconstriction flows ($\dot{m}_{skin,dil}$ and $\dot{m}_{skin,con}$) for a body

segment can be calculated via the following expressions:

$$\begin{cases} \dot{m}_{skin,dil} = \dot{m}_{skin,bas}\ (kg/s)\ \ if\ \ T_{core} < 36.8^oC \\ \dot{m}_{skin,dil} = \frac{T_{core}-36.8}{37.2-36.8}(\dot{m}_{skin,max} - \dot{m}_{skin,bas}) \\ +\dot{m}_{skin,bas}\ (kg/s)\ \ if\ \ 36.8^oC \leq T_{core} \leq 37.2^oC \\ \dot{m}_{skin,dil} = \dot{m}_{skin,max}\ (kg/s)\ \ if\ \ T_{core} > 37.2^oC \end{cases} \tag{5.26}$$

and

$$\begin{cases} \dot{m}_{skin,con} = \dot{m}_{skin,min}\ (kg/s)\ \ if\ \ T_{skin} < 27.8^oC \\ \dot{m}_{skin,con} = \frac{T_{skin}-27.8}{33.7-27.8}(\dot{m}_{skin,bas} - \dot{m}_{skin,min}) \\ +\dot{m}_{skin,min}\ (kg/s)\ \ if\ \ 27.8^oC \leq T_{skin} \leq 33.7^oC \\ \dot{m}_{skin,con} = \dot{m}_{skin,bas}\ (kg/s)\ \ if\ \ T_{skin} > 33.7^oC \end{cases} \tag{5.27}$$

Sweating

The sweating threshold T_{swe} is approximated as a function of mean skin temperature as [168]:

$$\begin{cases} T_{swe} = 42.084 - 0.15833\ T_{skin}\ (^oC) \\ \ \ if\ \ T_{skin} \leq 33.0\ ^oC \\ T_{swe} = 36.85\ ^oC\ \ if\ \ T_{skin} > 33.0\ ^oC \end{cases} \tag{5.28}$$

The sweat rate $\dot{m}_{swe}$ may now be evaluated as

$$\dot{m}_{swe} = \frac{45.8 + 739.4(T_{core} - T_{swe})}{3.6\ 10^6}\ (kg/s)\ \ if\ \ T_{core} > T_{swe} \tag{5.29}$$

The relative skin wetness w_{skin} is given as

$$w_{skin} = 0.06 + \frac{\dot{m}_{swe}(1-0.06)}{0.000193} \tag{5.30}$$

The total evaporative heat loss q_{swe} may now be written as [168]

$$q_{swe} = \frac{w_{skin}(p_{skin} - p_{out})}{R_{swe,cl} + \frac{1}{f_{cl} h_{swe}}} \ (W/m^2) \tag{5.31}$$

where p_{skin} is water vapour pressure on skin, $R_{swe,cl}$ is the evaporative heat transfer resistance of the clothing layer, f_{cl} is the clothing area factor (the surface of the clothed body divided by the area of the bare body), and h_{swe} is the evaporative heat transfer coefficient.

5.4 Numerical schemes

5.4.1 Fluid discretization

A brief overview on the numerical method employed is provided in this section. The details of the isothermal formulation are discussed in reference [171]. Equation (5.9) requires a scheme with a stabilisation term to obtain a stable solution. Thus, in this study the Locally Conservative Taylor Galerkin (LCG) method is used, which is the finite element equivalent of Lax-Wendroff stabilisation in finite difference discretization. Using this method, the semi-discrete form of Equation (5.9) can be written as,

$$\begin{aligned} \frac{\bar{\mathbf{U}}_F^{n+1} - \bar{\mathbf{U}}_F^n}{\Delta t} = & -\left[\mathbf{H}_F^n \frac{\partial \bar{\mathbf{U}}_F^n}{\partial x} + \frac{\partial \bar{\mathbf{G}}_F^n}{\partial x} - \bar{\mathbf{S}}_F^n\right] \\ & + \frac{\Delta t^2}{2}\left\{\frac{\partial}{\partial x}\left[\mathbf{H}_F^n\left(\mathbf{H}_F^n \frac{\partial \bar{\mathbf{U}}_F^n}{\partial x} - \bar{\mathbf{S}}_F^n\right)\right] - \mathbf{Q}_F^n\left(\mathbf{H}_F^n \frac{\partial \bar{\mathbf{U}}_F^n}{\partial x} + \frac{\partial \bar{\mathbf{G}}_F^n}{\partial x} - \bar{\mathbf{S}}_F^n\right)\right\} \end{aligned} \tag{5.32}$$

where $\mathbf{Q}_F$ is the Jacobian matrix of the source. Applying LCG method, Equation (5.32) can be written as [172, 173]:

$$\int_{\Omega_e} \mathbf{N}^T \Delta\bar{\mathbf{U}}_F^{n+1} dx = -\Delta t \int_{\Omega_e} \mathbf{N}^T \left[\mathbf{H}_F^n \frac{\partial \bar{\mathbf{U}}_F^n}{\partial x} + \frac{\partial \bar{\mathbf{G}}_F^n}{\partial x} - \bar{\mathbf{S}}_F^n \right] dx + \frac{\Delta t^2}{2} \int_{\Omega_e} \mathbf{N}^T \left\{ \frac{\partial}{\partial x} \left[\mathbf{H}_F^n \left(\mathbf{H}_F^n \frac{\partial \bar{\mathbf{U}}_F^n}{\partial x} - \bar{\mathbf{S}}_F^n \right) \right] + \mathbf{Q}_F^n \left(\mathbf{H}_F^n \frac{\partial \bar{\mathbf{U}}_F^n}{\partial x} + \frac{\partial \bar{\mathbf{G}}_F^n}{\partial x} - \bar{\mathbf{S}}_F^n \right) \right\} dx \tag{5.33}$$

The evaluation of Equation (5.33) for mass or momentum has been discussed by Mynard and Nithiarasu [171] in detail. The final discrete form of Equation (5.33) can now be written as

$$[\mathbf{M}_e]\{\Delta\mathbf{U}_F\}^{n+1} = \Delta t \left([\mathbf{K}_e]\{\mathbf{F}_F\}^n + [\mathbf{L}_e]\{\mathbf{S}_F\}^n + \mathbf{f}_{\Gamma_e}{}^n \right) \tag{5.34}$$

where $[\mathbf{M}_e]$, $[\mathbf{K}_e]$ and $[\mathbf{L}_e]$ are the element mass matrix, the coefficient matrix for convection, Taylor-Galerkin and source terms for the coupled continuity and momentum equations, respectively. These element matrices of the system of equations are solved on individual elements, independent of surrounding elements. Information is transmitted between elements via the numerical flux term ($\mathbf{f}_{\Gamma_e}$) that is imposed along the boundaries of each element [171, 172]. As mentioned previously, the energy equation may be decoupled from the other equations due to the one way nature of the coupling. If decoupled, the energy Equation (5.33) may be discretized as

$$[\mathbf{M}_{eT}]\{\Delta\mathbf{T}\}^{n+1} = \Delta t \{ ([\mathbf{K}_{eT}] + [\mathbf{D}_{eT}] + [\mathbf{L}_{eT}])\{\mathbf{T}\}^n + \mathbf{q}_{\Gamma_e}^n \} \tag{5.35}$$

where the matrix $[\mathbf{D}_{eT}]$ is the coefficient matrix for diffusion and $\mathbf{q}_{\Gamma_e}$ is the numerical conduction flux exchanged between two adjacent elements. The time step restrictions of the numerical scheme employed may be computed using the condition [171],

$$\Delta t = 0.9 \frac{\Delta x_{min}}{c_{max}} \tag{5.36}$$

5.4.2 Solid discretization

For the problem of heat conduction in the wall, the standard forward Euler method is used. The method uses the central difference scheme for spatial discretization and a first order discretization for the time term. Thus, the discrete form of Equation (5.22) for a node i may be written as

$$\begin{aligned} &T^n_{t,i-1}\frac{\Delta t k_t}{\rho_t c_t r_i}(-\frac{r_i}{\Delta r^2}+\frac{1}{2\Delta r})+T^n_{t,i}(1+\frac{2\Delta t k_t}{\rho_t c_t \Delta r^2})-T^n_{t,i+1}\frac{\Delta t k_t}{\rho_t c_t r_i}(\frac{r_i}{\Delta r^2}+\frac{1}{2\Delta r}) \\ &=\frac{\Delta t}{\rho_t c_t}q_m+T^{n-1}_{t,i}, \quad i=1,2,..m \end{aligned} \tag{5.37}$$

Since the matrix of the linear system is tridiagonal, Thomas algorithm is used to solve the above system.

5.4.3 Coupling blood with solid systems

The coupling between the blood vessels and surrounding tissue is critical to obtain sensible results. As mentioned previously, a one-dimensional bio-heat transfer model along the radial direction of body segment is used. The blood vessels are embedded into these segments as shown in Figure 5.2. This approach is considerably more advanced than the common assumption of a single core node, which implies that in each cylinder all types of convection losses are depending only on a scalar value. Furthermore, such a model is a good compromise between computational cost and accuracy [174].

The locations of arteries within the solid body are estimated from [175]. As reported previously, the heart represents the inlet to the fluid system and is not part of any cylindrical segment. The large arteries proposed in [1] are subdivided into three categories of heart region, central and transversal vessels. As arteries in the heart region are not included in the tissue discretization, no heat transfer with solid tissues occurs; the only exception is represented by the inlet flow node (which is isothermal with surrounding tissues). Each and every central artery is

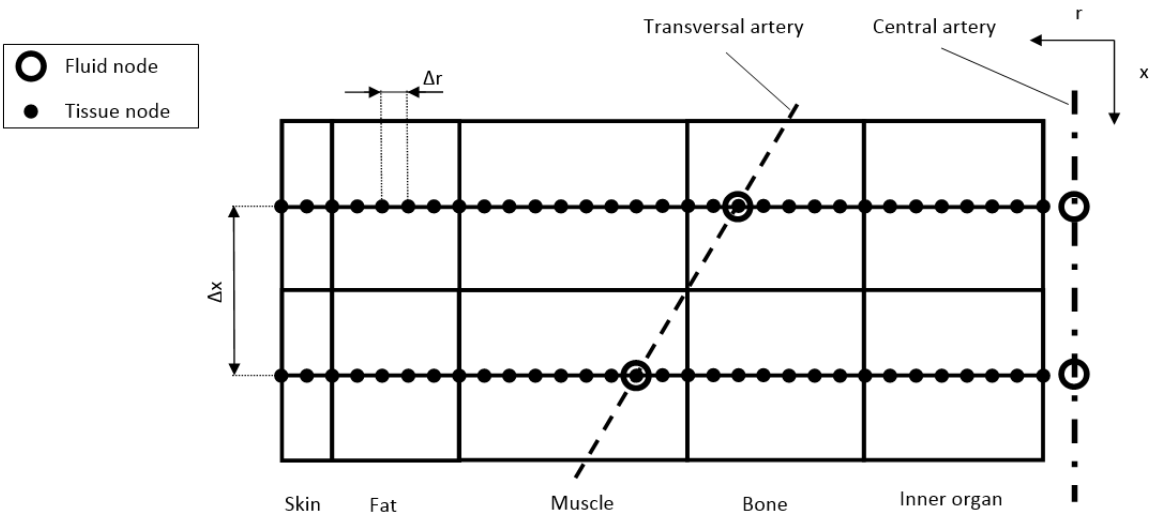

Figure 5.3: Longitudinal and radial discretizations for one cylinder (from [5]).

assumed to coincide with the axis of one or more cylindrical segments, while transversal vessels cross transversely one or more cylinders. The arrangement of these vessels within the cylindrical segment is shown in Figure 5.2, where central arteries are depicted as chained lines while transversal ones are represented by dashed lines. Figure 5.3 shows a typical section of the cylindrical segment with embedded central and transversal arteries. It should also be noted that while the geometrical and mechanical properties of elastic vessel may be allowed to change along the longitudinal coordinate, the solid tissue properties along the axial direction of the cylindrical segment are fixed. In addition, cylindrical segments are not considered deformable. The geometrical, thermophysical and basal physiological properties of tissue materials and the body features are adopted from [100]. The inner wall heat transfer coefficient is set up following [176] (Nusselt number is assumed be equal to 4).

Figure 5.3 shows the spatial discretization adapted in the present study. The body is assumed to be axisymmetric and the nodes of the central arteries are linked to the first node of the surrounding tissue layers as shown via a convective boundary condition. For every node along the central artery, a matching radial set of nodes are introduced into the surrounding solid tissues. Each central vessel node is therefore identified by two coordinates, a longitudinal and radial coordinate. As shown, the transversal vessels are embedded into the cylindrical

segment and at the intersecting point of tissue mesh and transversal artery, a flow node is introduced that coincides with the solid node (see Figure 5.3).

The temperature calculation at fluid-solid interface nodes includes the following steps. The temperature transported through the systemic circulation network forms the basis for the boundary condition to Equation (5.22). The fluid inlet node (first node of seg. 1) is assumed to be in thermal equilibrium with a tissue node located in the middle of the thorax, having radial coordinate equal to 8 cm. The nodal temperatures of the central arteries provide the wall temperature for the convective boundary condition between the blood and arterial wall (first tissue node). Where a transversal vessel node coincides with the tissue node, a volumetric source term is explicitly evaluated based on the expected convection contribution and added to the discrete heat conduction equation of the tissue (increasing the term q_m). In cylinders representing head, neck, legs and forearms there are no central arteries. Thus, along the axis of these cylindrical segments an adiabatic condition is adopted.

The perfusion in solid tissue segments is modelled through the perfusion coefficients (see Equation (5.22)). The temperature difference in the perfusion term is calculated as the difference between the section average blood (mean between all vessels crossing the section) and tissue temperatures. Equation (5.22) is applied to all tissue nodes by setting the appropriate material constants k_t, ρ_t, and c_t, q_m and ϕ_{perf}. It should be noted that q_m and ϕ_{perf} are variables regulated by the thermo-regulatory system (for further details see Subsection 5.3.4). In the present study, the tissue temperatures are computed after the evaluation of blood temperatures at every time step. All the components of q_m are evaluated before computing the tissue temperature at each time step.

The respiration losses are incorporated by considering a negative volumetric heat source q_{bre} at all lung nodes. To estimate such losses the following formulation has been used [99]

$$q_{bre} = \frac{1}{V_{lung}} [0.0014\ Q_{m,glob}\ (34 - T_{out}) + 0.0173\ Q_{m,glob}\ (5.87 - p_{out})]\ (W/cm^3) \quad (5.38)$$

where $Q_{m,glob}$ is the global metabolic heat generation rate, V_{lung} is the lung volume (respectively 58.2 W/m^2 and 5631.41 cm^3) and p_{out} is the ambient water vapour pressure. Further details may be found in [99].

5.4.4 Heat exchanged with the environment

The body exchanges heat with the environment through the skin and breathing. The skin is represented by the outer most part of the cylindrical segment. The flux exchanged between the skin layer and outside environment q_{skin} is the sum of the convection ($q_{con,out}$), radiation (q_{rad}) and evaporation (q_{swe}) losses. The Neumann boundary condition used in the present study is

$$-k_t A_{out} \frac{\partial T_t}{\partial r}|_{r_{out}} = q_{con,out} + q_{rad} + q_{swe} \tag{5.39}$$

For the evaluation of $q_{con,out}$ and q_{rad} the methodology proposed by Fiala et al. [100] is followed. The convective heat transfer between skin node and the external environment may be evaluated with the following expression.

$$q_{con,out} = h_{con,out}(T_t(r_{out}) - T_{out}) \tag{5.40}$$

where $h_{out,con}$ is the convection heat transfer coefficient and it is a function of the node location in the body, the air velocity and the temperature difference between the outer surface and environment. For the radiative exchange the evaluation of the mean temperature of the surrounding surfaces ($T_{sur,m}$) is necessary before applying

$$q_{rad} = h_{rad}(T_t(r_{out}) - T_{sur,m}) \tag{5.41}$$

where h_{rad} is the radiative heat transfer coefficient depending on the temperatures, the emission coefficients and the view factors of the surrounding surfaces considered.

5.4.5 System interconnections and solution procedure

Here we describe how all the subsystems are interconnected and coupled (see Figure 5.4). The thermo-regulatory response is evaluated by knowing T_{core} and T_{skin} of the previous time step and comparing them with thermo-neutrality reference values. Such a control system is able to modify tissue balance through shivering heat source, increment or decrement of skin perfused flow, sweating losses. As blood variables are evaluated in an explicit way, we use T_t of the previous time step for prescribing interacting wall and fluid inlet temperatures. Once the blood system output is calculated, tissue temperatures are calculated before starting a new cycle.

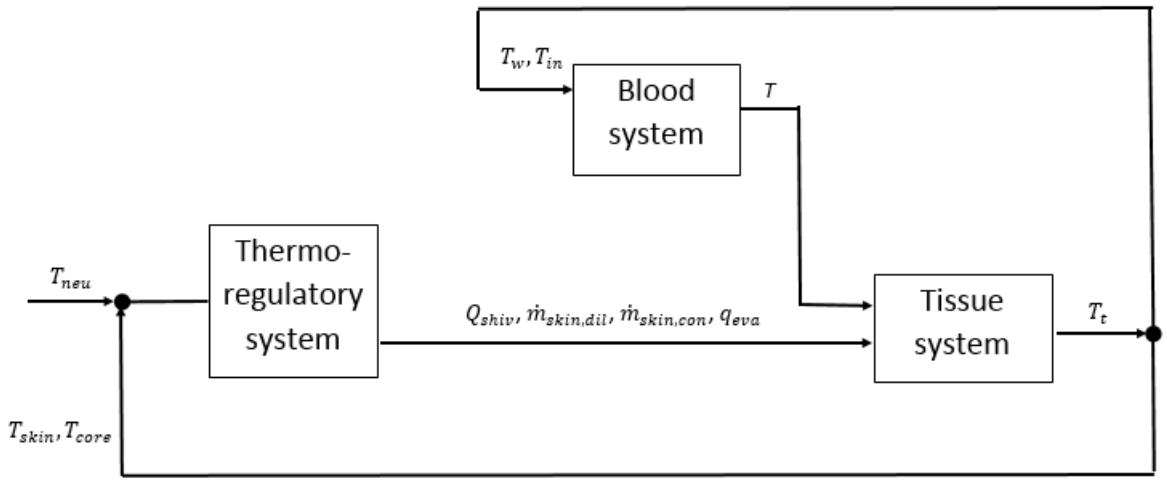

Figure 5.4: Global system (from [5]).

The calculation procedure for evaluating temperatures of the global system at each time step is carried out as follows:

1. T^{n+1} is calculated explicitly by means of third equation of (5.9) using $T^n_{w,in}$;
2. At the extremities of fluid network T^{n+1} are assigned equal to T^n_t of the interacting tissue nodes;
3. T_{core} and T_{skin} are derived from T^n_t field;

4. Convection from transversal vessels, breathing, sweating and shivering contributions are calculated using T^{n+1} and T_t^n;

5. T_t^{n+1} is computed implicitly with Equation (5.22).

5.5 Results

5.5.1 Convection in an elastic tube

The energy transport results obtained for straight and bifurcating vessels are reported in the following subsections. The Locally Conservative Taylor Galerkin method used in the present study is extensively tested previously for fluid flow, and a detailed discussion on the accuracy of the method is provided in references [171, 1]. Thus, no further validation for accuracy is reported here. The fluid properties used for the simulations are summarised in Table 5.5. The fluid motion is generated by applying an inlet pressure signal to the first node of the domain. It should be reiterated that other primitive variables at the inlet and exit are computed via the characteristic variables. This is the more natural way of determining the boundary conditions at the inlet and exit of the domain. The inlet temperature of the fluid is set at 37 °C to reflect the human body temperature. The external pressure acting on the wall is taken equal to zero.

Density of fluid, ρ_F (g/cm^3)	1.06
Viscosity of fluid, μ_F $(poise)$	$3.5\text{x}10^{-2}$
Thermal conductivity of fluid, k_F (W/cm^oC)	0.05
Specific heat of fluid, c_F (J/g^oC)	3.9
Inner wall heat transfer coefficient, h_{in} $(W/^oCcm^2)$	0.01

Table 5.2: Fluid parameters and properties used in simulations.

Poisson's ratio, ν_{Pois}	0.5
Unstressed area, A_0 (cm^2)	1.0
Material wall parameter, β $(dyne/cm^2)$	2.26974 10^5
Wall thickness, h (cm)	0.05
Tube length, L (cm)	20
Finite element size, l_e (cm)	2.0x10^{-2}

Table 5.3: Geometrical and material properties of the vessel used.

Solid wall density, ρ_t (g/cm^3)	1.30
Solid wall thermal conductivity, k_t (W/cm^oC)	0.075
Solid wall specific heat, c_t (J/g^oC)	3.0
Outside atmosphere temperature, T_{out} (^oC)	20.0
Outside wall heat transfer coefficient, h_{ext} $(W/^oCcm^2)$	0.001 - 0.01

Table 5.4: Solid parameters and the outside conditions.

Constant inner wall temperature

In order to check the performance of the method, a simple problem of straight tube with constant inlet temperature is considered first. In this case the inner wall temperature is assumed to be constant in space and time ($T_{w,in}$=35.3 °C). All the parameters related to the straight tube problem are listed in Table 5.3. All the variables are monitored at the midpoint of the segment.

The effects of a constant and pulsatile flow on temperature field are compared in Figure 5.5. The periodic signal is characterised by a pressure pulse with a width equal to 0.43 s. For both cases, pressure, area, velocity and temperature evolutions in time at midpoint are shown in Figure 5.5. As discussed in Section 5.3.1, A, u and p waveforms propagate in time along the tube at an intrinsic wave speed velocity of c, while T is transported by velocity field u. For the case in which velocity is constant, the temperature reaches an expected steady and stable value, slightly lower than the inlet temperature due to lower inner wall temperature. With a periodic pressure pulse, the behaviour is completely different. While there are no surprises in the velocity, area and pressure value distributions, very small local oscillations in temperature are observed. This is inline with the variations in velocity values, as reported in [177]. When the velocity value peaks, it introduces a reduced cooling effect

resulting in a slightly higher temperature than average temperature. However, when the velocity value is reduced, increased flow stagnation decreases the temperature value. This decrease in temperature is a result of enhanced heat transfer between the fluid and the wall due to reduced velocity. Such behaviour continues according to the prescribed pressure pulse in a cyclic manner as shown in Figure 5.5.

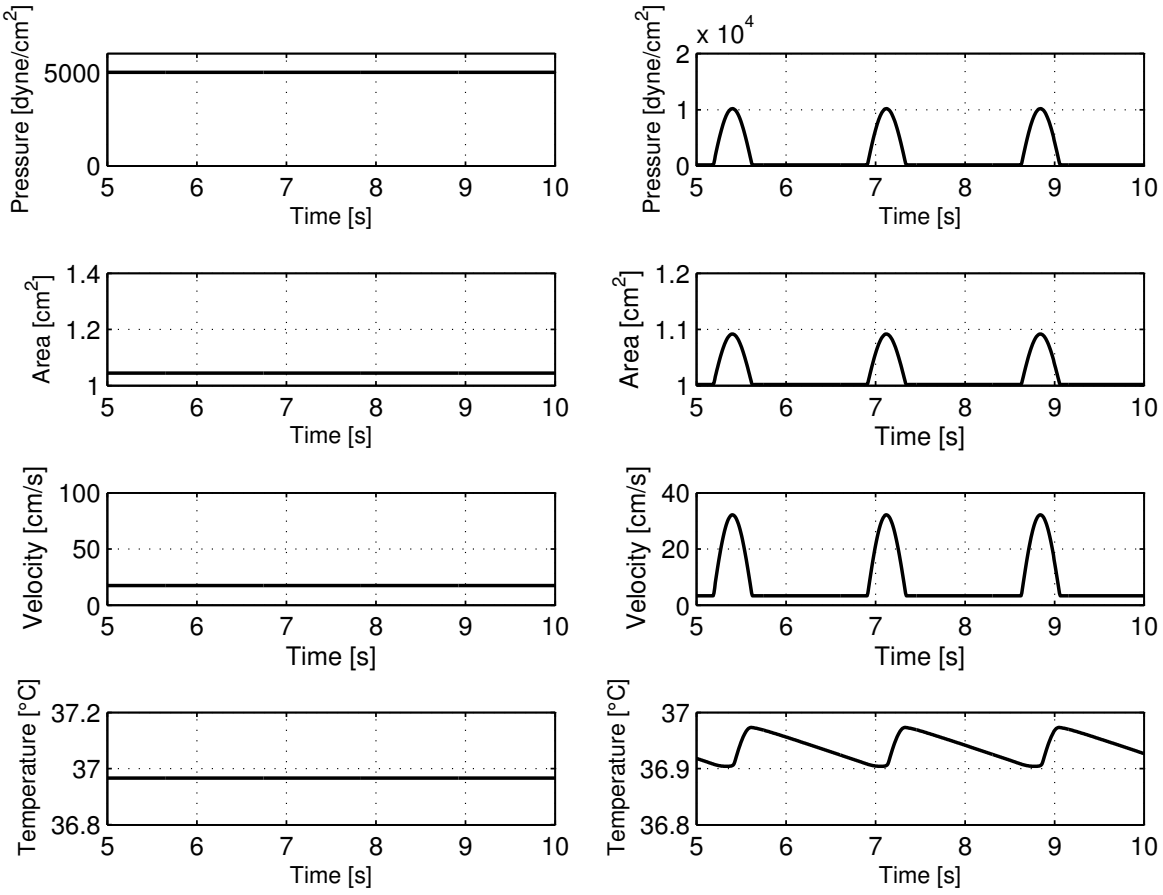

Figure 5.5: Flow and heat transfer in a flexible tube with a constant inner wall temperature (from [4]). Pressure, area, velocity and temperature variations for constant (left) and pulsating (right) pressure inputs.

To investigate the effects of reflections on heat transfer, three cases with prescribed exit reflection coefficients are examined next. A case without reflection (R_t=0), partial reflection (R_t=0.5) and total reflection (R_t=1) are studied. The results are shown in Figure 5.6. As seen, the flow and heat transfer results with zero reflection coefficient are not different from the one discussed previously. However, as the wave reflection is introduced at the exit the reverse

wave produces a strong cooling effect on the fluid. This is due to the fact that the reflected flow waves increase the fluid contact duration with the cold inner wall surface. This cooling effect is particularly pronounced when the wave is fully reflected. It is worth mentioning that setting R_t different from 0 is physiologically more correct, because in this case the reflected wave also depends on the forward characteristic variable.

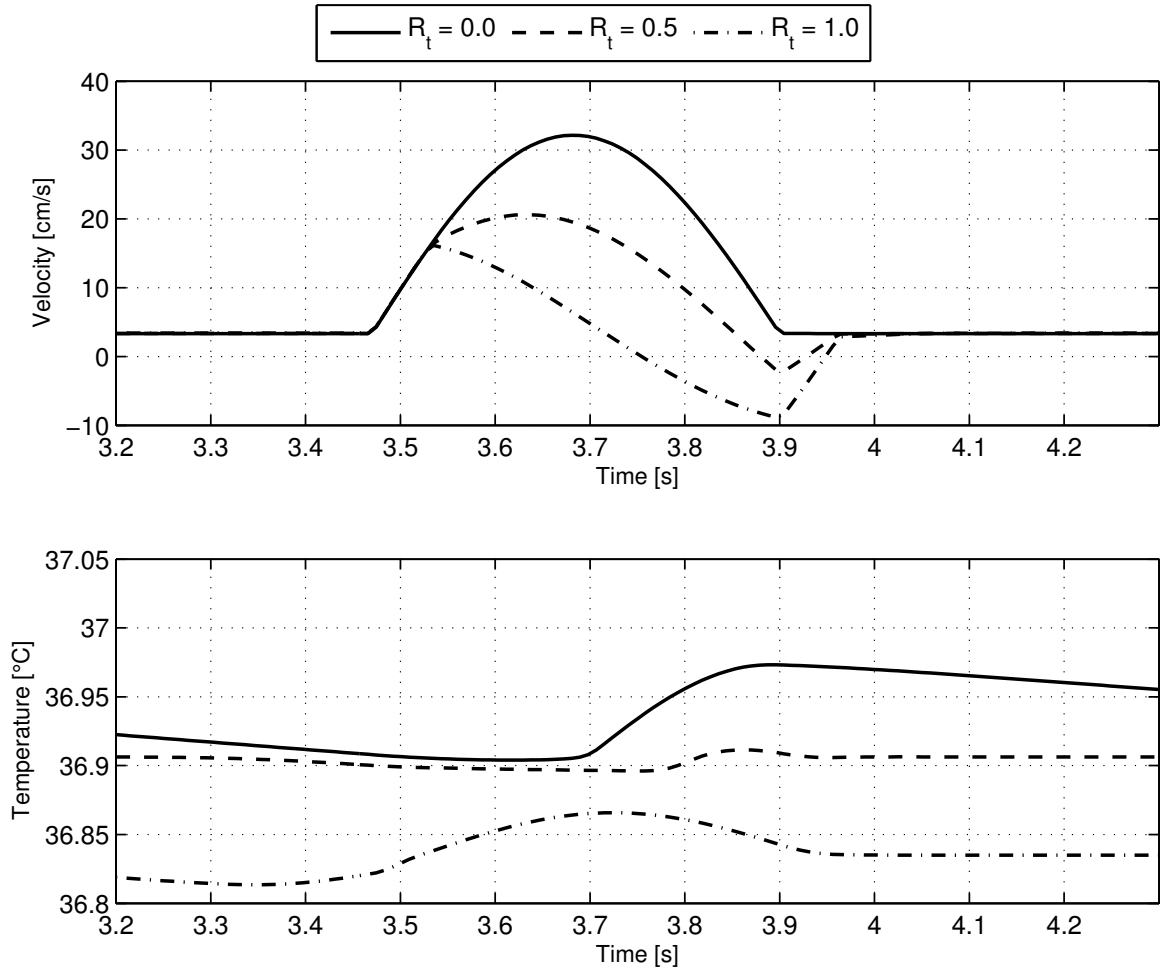

Figure 5.6: Flow and heat transfer in a flexible tube with a constant inner wall temperature (from [4]). Effects of reflections on velocity and temperature.

Convective inside/outside wall conditions

In this problem, the inner wall surface temperature is allowed to vary in time and space. Thus, the heat conduction model for the surrounding wall material is now invoked. The

model parameters and the outside conditions are reported in Table 5.4. All the remaining parameters for the study are the same as in the previous section.

To study the influence of the external heat transfer coefficient, the temperature is monitored at three points at the mid cross section of the vessel as shown in Figure 5.7. To clearly quantify the influence of external heat transfer coefficient, all other parameters, including internal wall heat transfer coefficient are fixed as given by Tables 5.5, 5.3 and 5.4. In Figure 5.7, temperature evolutions at points 1, 2 and 3 are shown for different heat transfer coefficients. As seen, the cooling effect is enhanced as the heat transfer coefficient is increased. Also, the temperature pattern with respect to time in the fluid is very similar to the previously observed pattern. However, the difference here is that the reduction in temperature is controlled by the external heat transfer coefficient at the outer surface of the vessel. In all cases, the time taken for the temperature to reach a steady state is much higher than the previously observed constant wall temperature example. Moreover, the temperature of the fluid shows minor oscillatory activity representing the pulsatile motion of the fluid. This activity is especially enhanced at higher external heat transfer coefficient values.

Next, we investigate the effect of wall properties on heat transfer. A combination of wall properties may be represented through the material parameter β. However, the wall thickness (h), unstressed area (A_0) and Young's modulus of the material (Y) may also be changed along with β. Apart from β, other parameters used in the calculations remain the same. The effect of wall thickness and corresponding β variation on flow and heat transfer is shown in Figure 5.8. As seen, both the velocity and temperature exhibits pulsatile behaviour. It is clear that when β decreases, the higher elasticity increases the average flow speed. The average fluid temperature also slightly decreases with β value. However, the peak temperature values slightly increase with decrease in β values. This may be due to the increased flow speed and reduced contact time between fluid and cold wall. The pulsating behaviour of the temperature remains the same as in the problem with constant inner wall temperature.

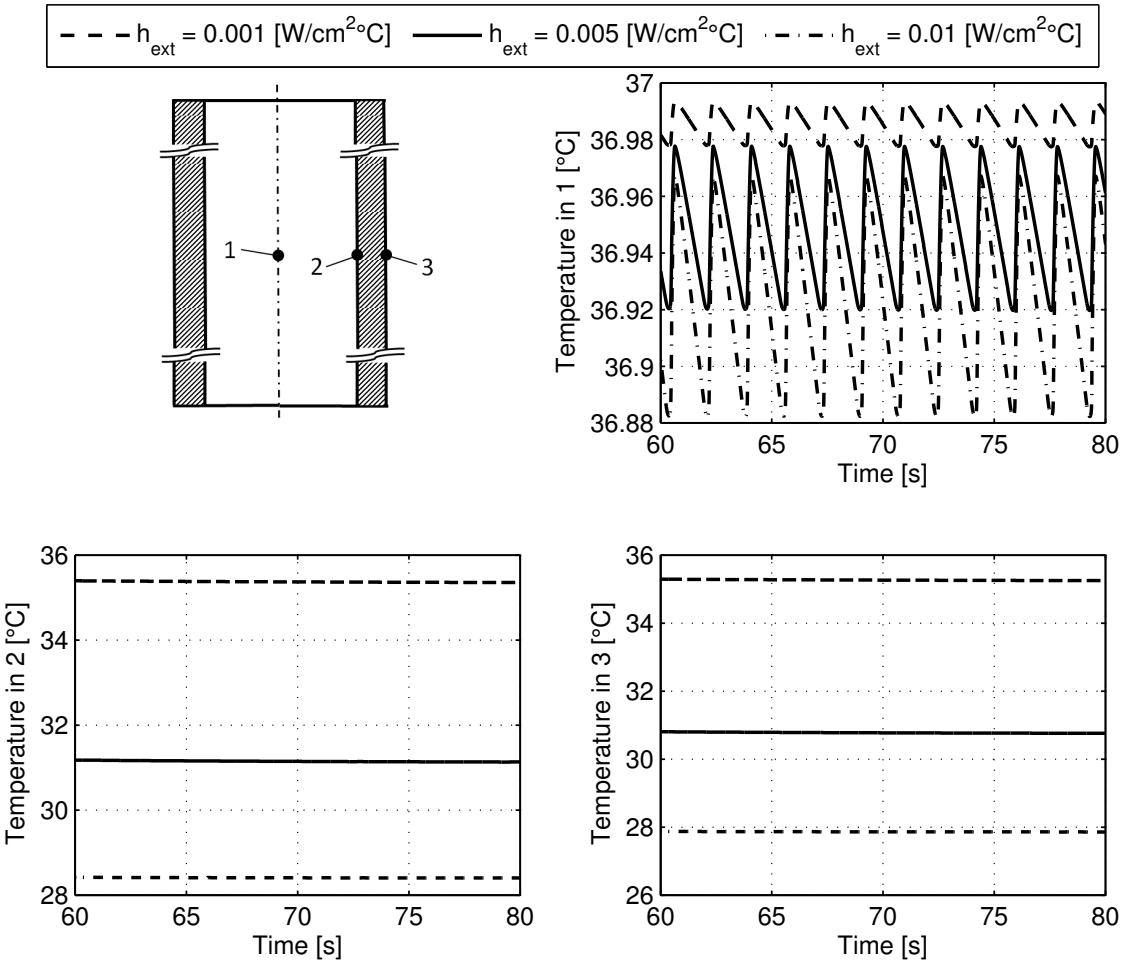

Figure 5.7: Flow and heat transfer in a flexible tube with convective wall conditions (from [4]). Effect of h_{ext} on temperature at points 1 (top right), 2 (bottom left) and 3 (bottom right).

Vessel branching

In this section, the effect of introducing a bifurcation is studied. The system considered includes three tubes that are linked by means of a bifurcation. Each of them has a length equal to 10 *cm*. Monitoring points (4 and 5) are positioned at the midpoint of the segment, as shown in Figure 5.9. The tube associated with the point 5 has an unstressed area (A_0) that is equal to half of the unstressed area of point 4. A comparison is carried out against a straight tube of identical total length with monitoring points at 6 and 7, as shown in Figure 5.9. In the straight tube case, the unstressed area is equal to the area at point 4. The heat transfer

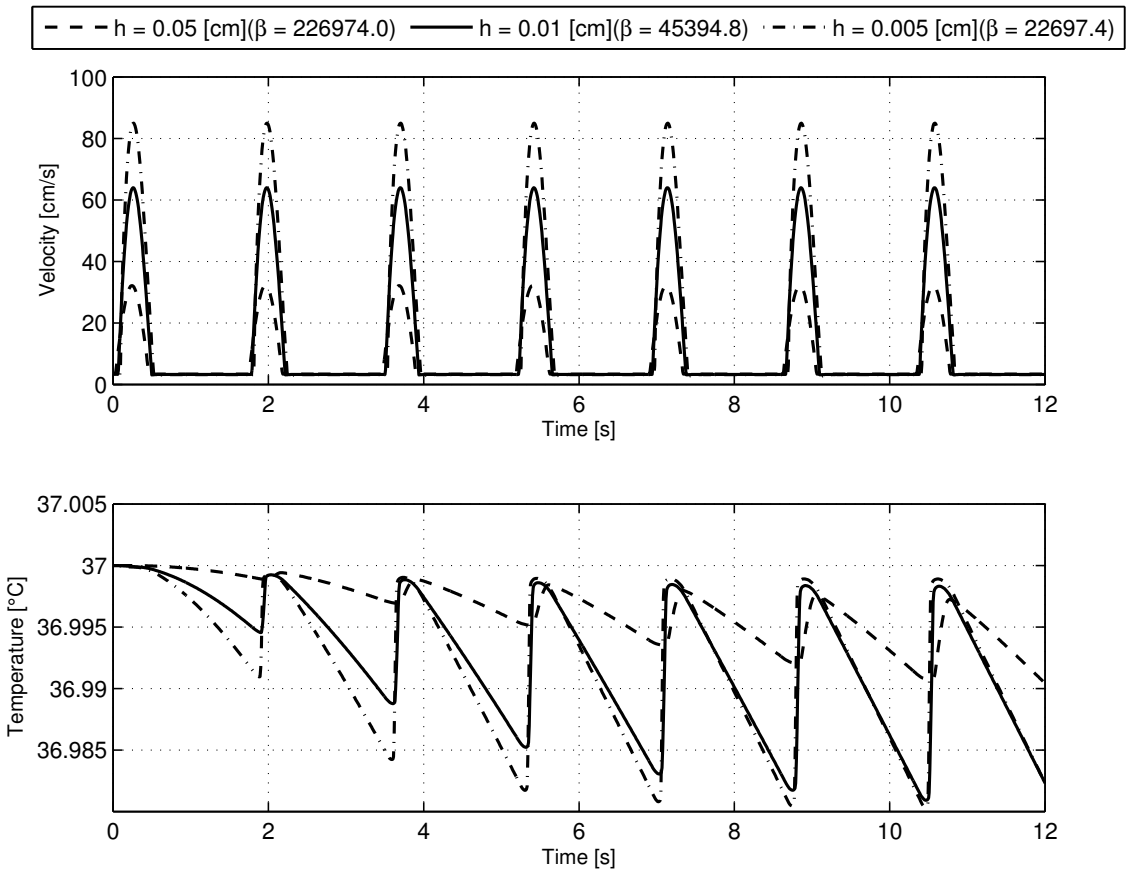

Figure 5.8: Flow and heat transfer in a flexible tube with a constant inner wall temperature (from [4]). Effects of wall thickness (h) on fluid velocity and temperature.

results are also shown in Figure 5.9. As expected, the bifurcation modifies the velocity field slightly. Both the velocity amplitude values, before and after the bifurcation, have been reduced in comparison to the straight tube value. While there is no significant difference in heat transfer between the parent vessel of the bifurcation and the straight tube, a reduction in temperature is observed in the daughter vessels. This is the result of smaller velocity in comparison to the straight tube and also due to an increase in the ratio between surface area and cross sectional area of daughter vessels.

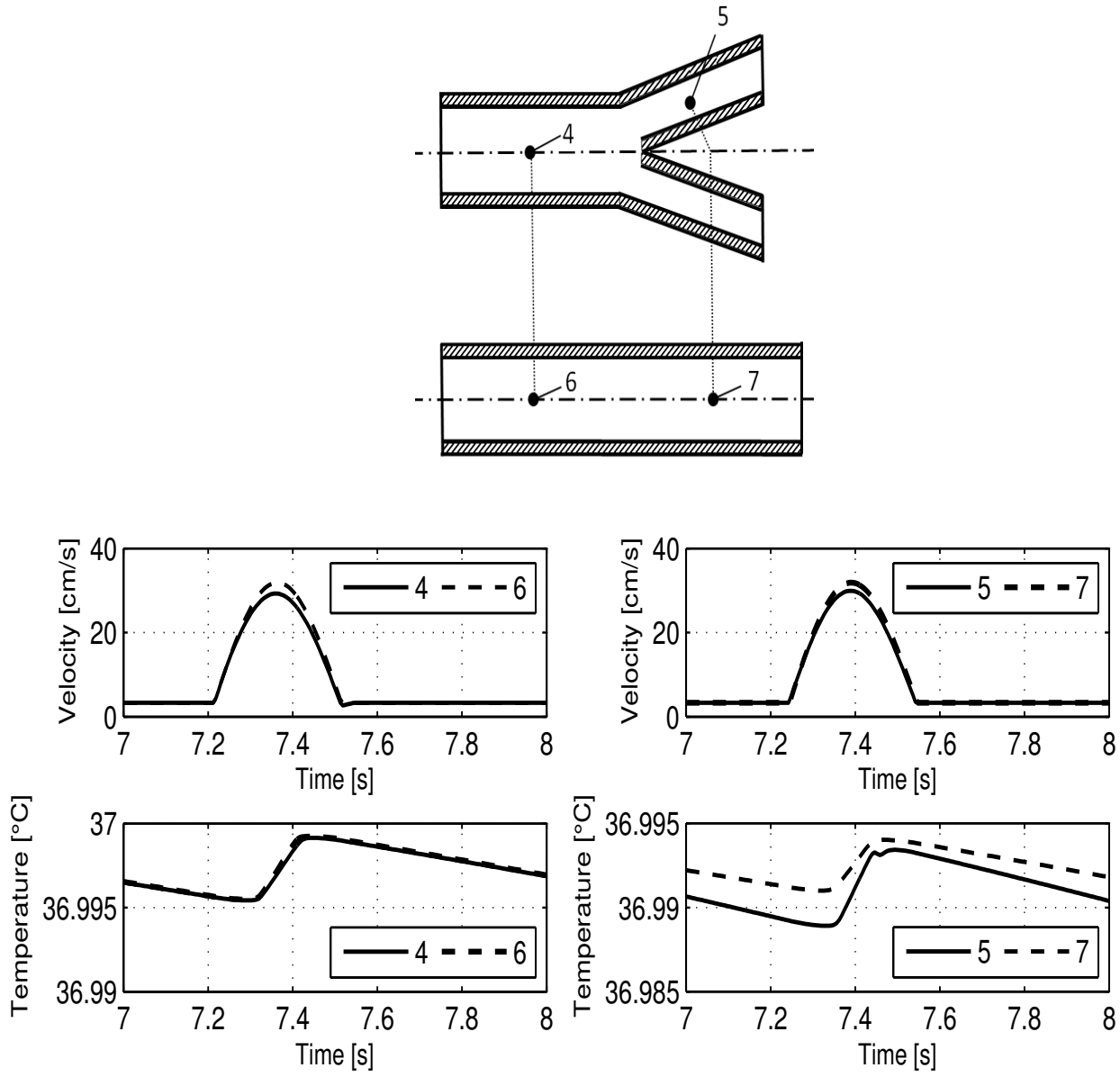

Figure 5.9: Flow and heat transfer in a bifurcating vessel with convective wall conditions (from [4]). Velocity and temperature in a bifurcation.

5.5.2 Energy transport within the human body

Although the model proposed in the present work is novel, different components of the methodology have undergone extensive testing in the past. The systemic circulation model, for example, has been extensively used in different studies and compared against experimental flow and pressure measurements [64, 1]. Thus, the focus of the results in the present study

is the bio-heat transfer within a human body for various governing parameters. We consider a bare body and thus $R_{swe,cl}$ and f_{cl} are set equal to 0 and 1, respectively. For the cases considered, we assume the same radiative parameters presented in [100], while air velocity (v_{air}) is set equal to 4 m/min. The initial temperature at all nodes is set at 36.8^{o}C in order to reflect an initial thermo neutral condition. The fluid properties and outside conditions used in the study are listed in Tables 5.5 and 5.6.

Density of fluid, ρ_F (g/cm^3)	1.060
Viscosity of fluid, μ_F $(poise)$	0.035
Thermal conductivity of fluid, k_F (W/cm^oC)	0.050
Specific heat of fluid, c_F (J/g^oC)	3.900

Table 5.5: Fluid parameters and properties used in the simulations.

Tissue	c_t (J/gK)	$q_{m,0}$ (W/cm^3)	ρ_t (g/cm^3)	k_t (W/cmK)	ϕ_{perf} $(1/s)$
brain	3.850	0.013400	1.080	0.0049	0.011320
lung	3.718	0.000600	0.550	0.0028	0.004310
viscera	3.697	0.004100	1.000	0.0053	0.000500
bone	1.700	0.000000	1.375	0.0075	0.000000
muscle	3.700	0.000727	1.085	0.0042	0.000538
fat	2.300	0.000003	0.850	0.0016	0.000004
skin	3.680	0.001096	1.085	0.0047	*variable*

Table 5.6: Solid properties used in the simulations. For the cutaneous perfusion we adopted a specific coefficient for each cylinder (more details can be found in [9]).

A comparison of the current model for various atmospheric conditions against measurement, is provided in the following subsection. This is followed by an investigation on the contribution of inner convection to the body thermal balance and finally the thermo-regulatory response of the body in a cold environment is quantified.

Comparison against measurements

At first a validation of the model with experimental data is presented. For doing this the relevant works by Stolwijk and Hardy [95], and Hardy and Stolwijk [178] are used. In these studies volunteers have undergone exposure to various environmental conditions. Temperatures were recorded for the tympanic and rectal regions and also the evaporative losses (sweating

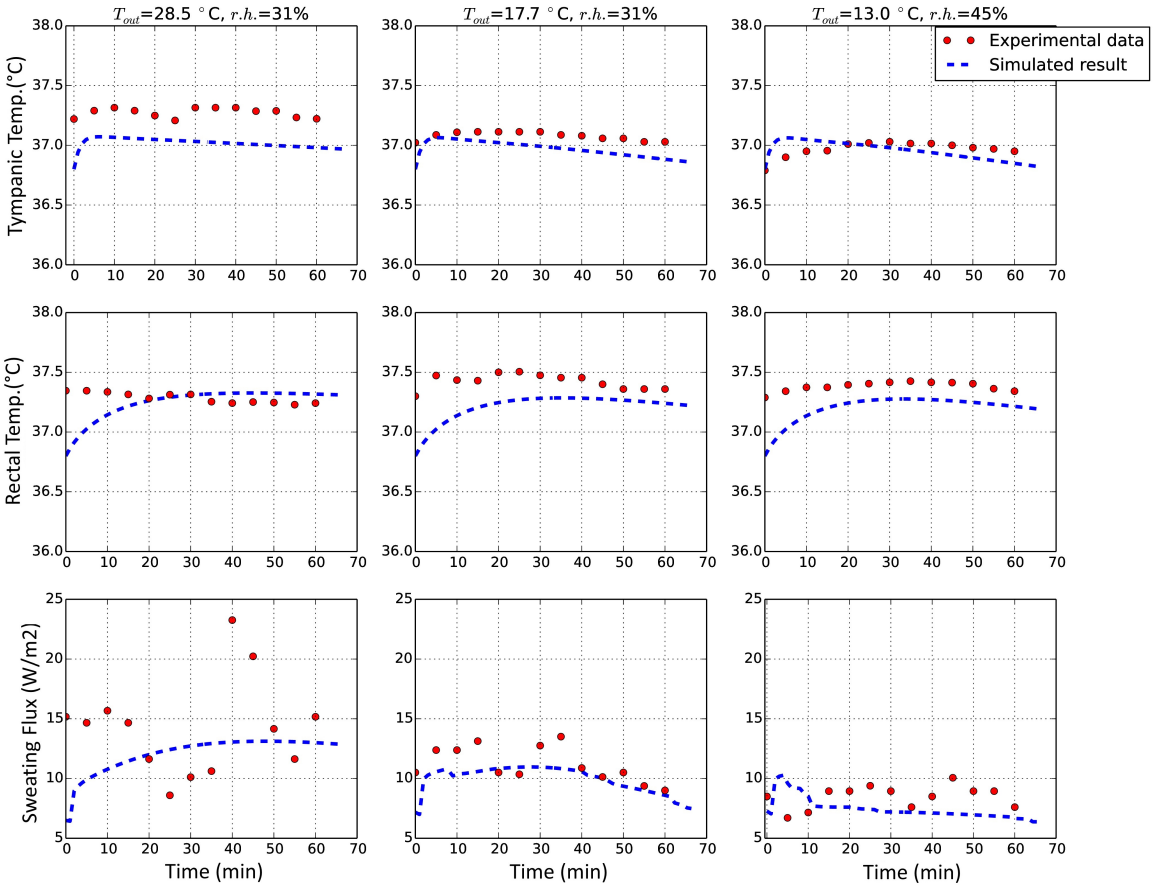

Figure 5.10: Tympanic and rectal temperatures for various external conditions (from [5]).

and breathing latent losses) were evaluated. In order to test systematically the current model, we simulate the body response for three different external exposures. The considered conditions are (T_{out}=28.5^{o}C-$r.h.$=31%), (T_{out}=17.7^{o}C-$r.h.$=31%) and (T_{out}=13.0^{o}C-$r.h.$=45%). For the rectal temperature calculation, we use the tissue node at an axial distance of 22 *cm* from the top of abdominal cylinder and at a radius of r=3.5 *cm*. The tympanic site is assumed to be at a distance of 12 *cm* from the bottom of the head cylinder and at r=5.0 *cm*. The evaporative losses are evaluated by summing the contributions of each cylinder section and then dividing by the total skin surface. We note that the initial temperature field imposed slightly differs from the one of a body under thermo neutral conditions. However, after a long transient all

results have to converge to the same value range.

In Figure 5.10 the time evolutions of tympanic, rectal temperatures and evaporative losses are reported. For all exposure conditions considered, the simulated results are in agreement with the experimental data. For the tympanic and rectal temperatures, the maximum relative errors are 0.7 % and 1.1 %, respectively. It can be seen that the temperature errors decrease significantly with time. At quasi-steady state, the largest difference in temperature is less than 0.25^oC. The accuracy of the evaporative losses calculated is difficult to evaluate as the experimental data is widely scattered.

Next, we report the thermal body response under controlled external conditions providing comparisons with experimental measurements and other numerical models. Specifically, the model is tested under exposure to heat for 1 hour at (28.1^oC,43% r.h.), 2 hours at (47.8^oC,27% r.h.) and 1 hour at (28.3^oC,44% r.h.). Findings for these simulated conditions are compared with experimental data [178] and solutions provided by "Smith" and "Karaki" models, respectively presented in [99, 107]. The core and mean skin temperature responses in time are shown in Figure 5.11. Our simulation results are in line with expectations. The maximum relative errors for core and mean skin temperatures are, respectively, 1.3 % and 3.6 %. As seen the mean skin temperature curve rises suddenly as the step change occurs but then it remains within an acceptable range of temperatures.

The model is also tested when the naked body is exposed to cold conditions. The core temperature prediction is compared against the findings reported in one of the most recent works [107]. Here the body is exposed to (13^oC,45% r.h.) for 65 *min*. The results are reported in Figure 5.12. This figure shows a good agreement between experimental and numerical results, with a maximum relative error ~ 0.8 %.

Role of inner convection

To understand the temperature changes in blood, four representative arteries, Abdominal Aorta II (seg. 43, abdomen), Left external carotid (seg. 25, head), Right External Iliac (seg.

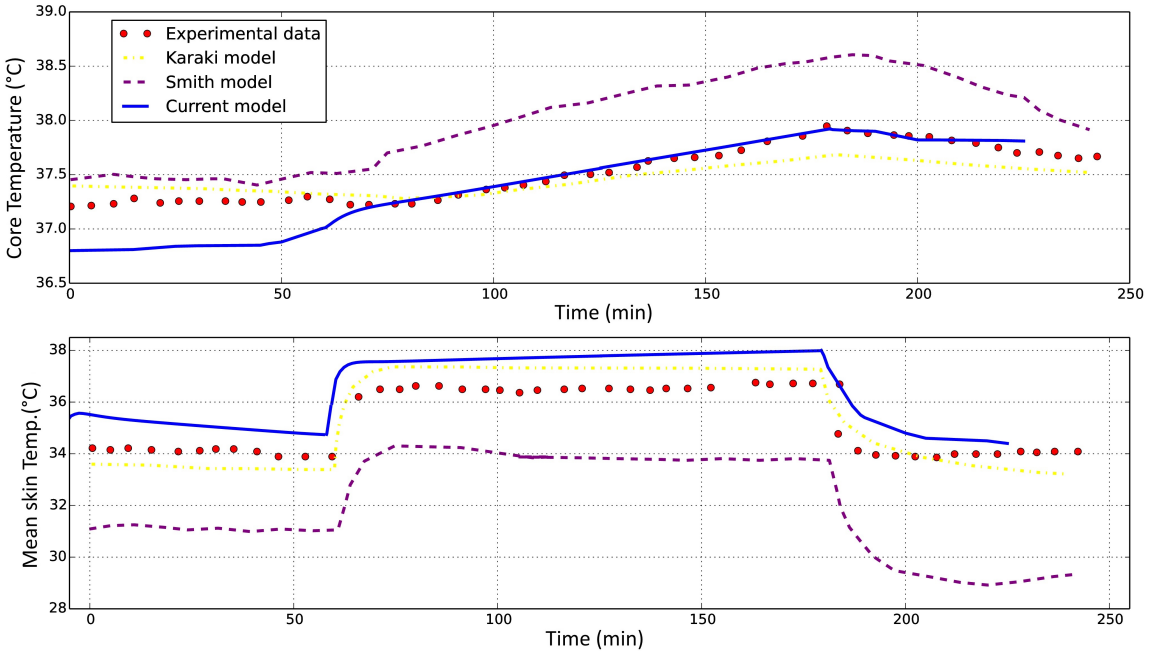

Figure 5.11: Benchmark case for naked body under heat exposure (from [5]).

58, right thigh) and Right Radial (seg. 16, right arm) are selected (for more detail about artery labelling see [1]). The temperatures at these locations are recorded once a quasi-steady state is reached. The tissue temperature distributions are recorded for the sections corresponding to the nodes selected in the arteries mentioned (abdomen, head, thigh, and arm).

Since the flow is pulsatile in nature [1], pulsatility of temperature is also anticipated. In addition, the wave nature of the flow leads to reflected temperature waves. Although a number of different parameters such as elastic properties of the vessels can be tested using the proposed model, all the material properties, heart rate and flow boundary conditions at the extremities are fixed to produce an understanding of normal human body behaviour. Note that describing bio-heat transfer in a body subjected to some disease states or extreme environmental conditions needs parameter changes.

Figure 5.13 shows the blood temperature at three selected monitoring points in the systemic circulation. As anticipated, the temperature follows a mild periodic pattern in line with the

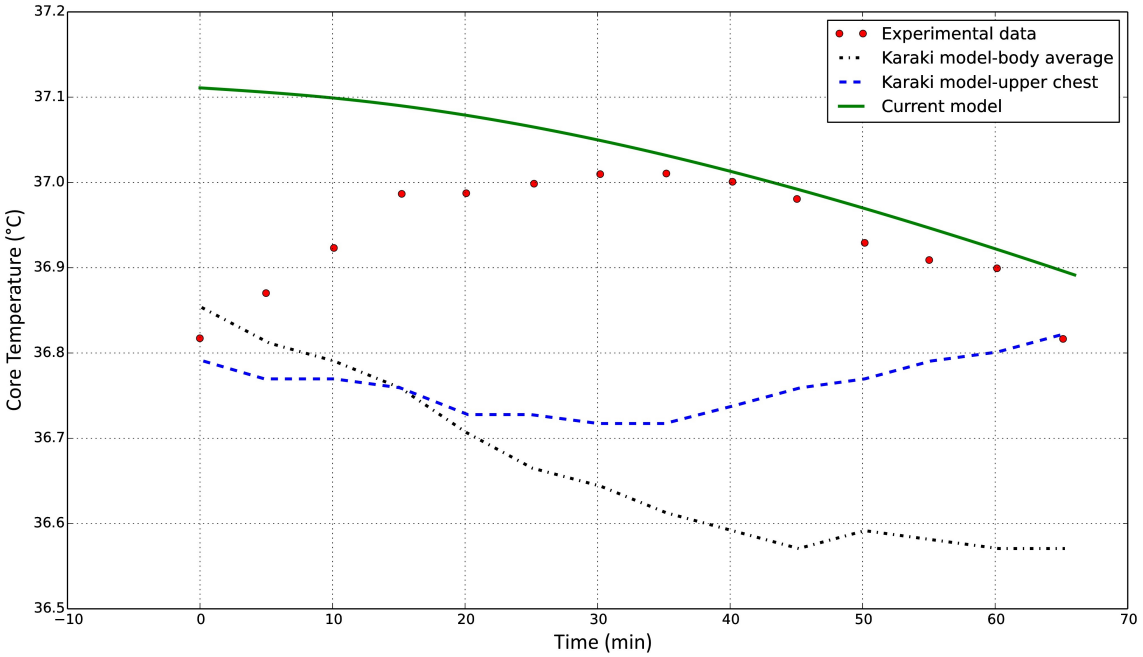

Figure 5.12: Benchmark case for naked body under cold exposure (from [5]).

velocity changes. As seen the frequency and amplitude of oscillations differ for different environmental conditions. In general the amplitude of the temperature waves is low and thus no dramatic local change in temperature is possible. The blood temperature is mildly influenced by the atmospheric temperature in the core part of the body. The pronounced effect in the radial artery is due to the smaller dimensions of the forearm and to the absence of any metabolic active tissue.

In order to evaluate the effect of heat convection on tissues, the results obtained from the proposed model are compared to the approach used in other reference works [100, 103] where heat conduction is exclusively used to model heat transfer occurring between blood and tissue system. Figure 5.14 shows the temperature distribution with and without heat convection and perfusion in arteries. As seen a local temperature variation of more than 1.0^{o}C is observed in tissues in the abdominal area. Although this variation decays as we approach the skin layer, this finding is important for further investigation. In the abdomen and head, convection involves a smaller average tissue temperature compared to the case without

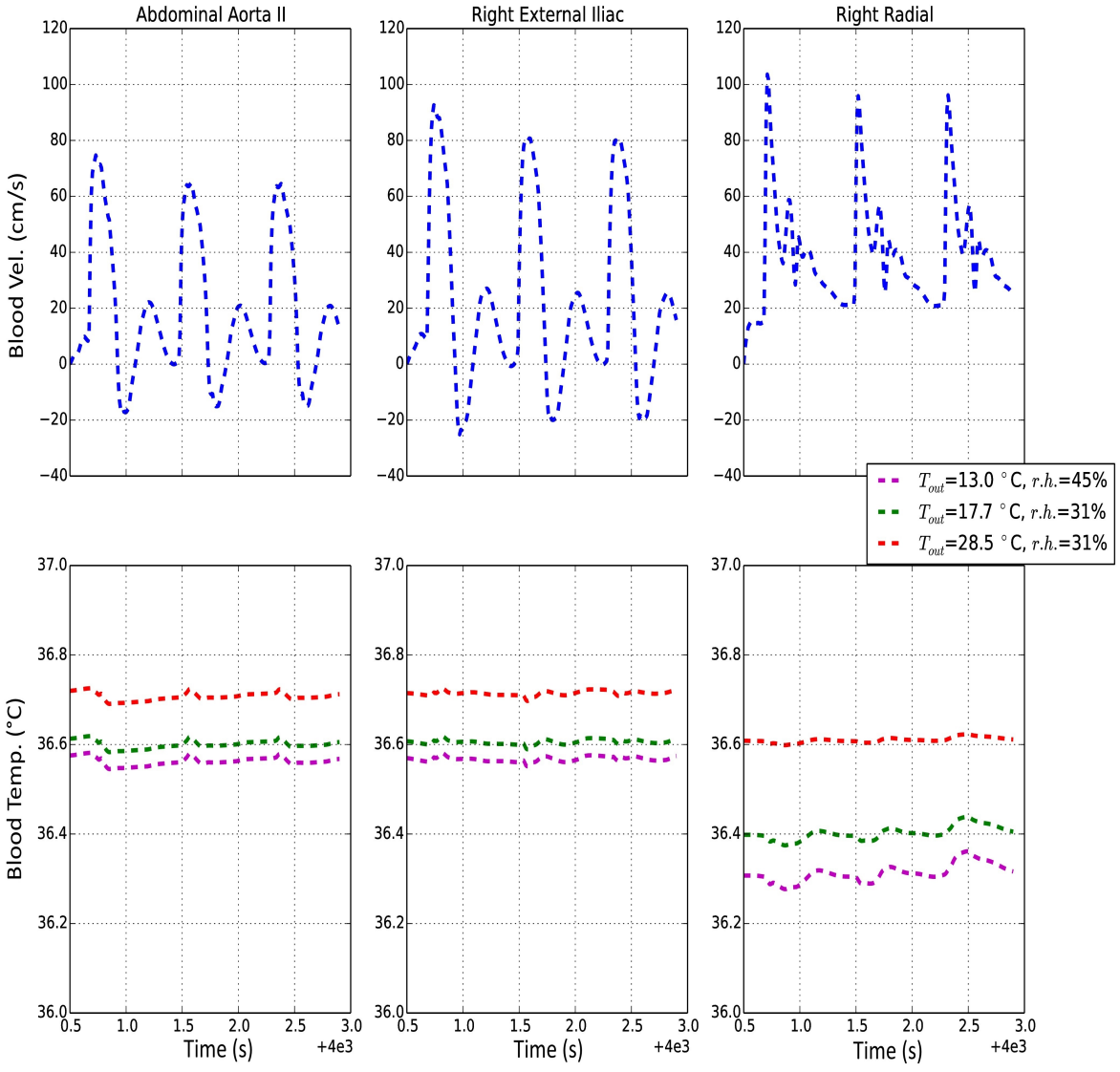

Figure 5.13: Blood velocity and temperature along the arterial tree for various external conditions (from [5]).

convection. The situation in the arm instead is the opposite. This can suggest that, with convection, a more uniform energy redistribution is enforced. It can therefore be reasonably concluded that flow and convection heat transfer play an important regulatory role that may be further enhanced in abnormal conditions such as high blood pressure and stiffer arteries.

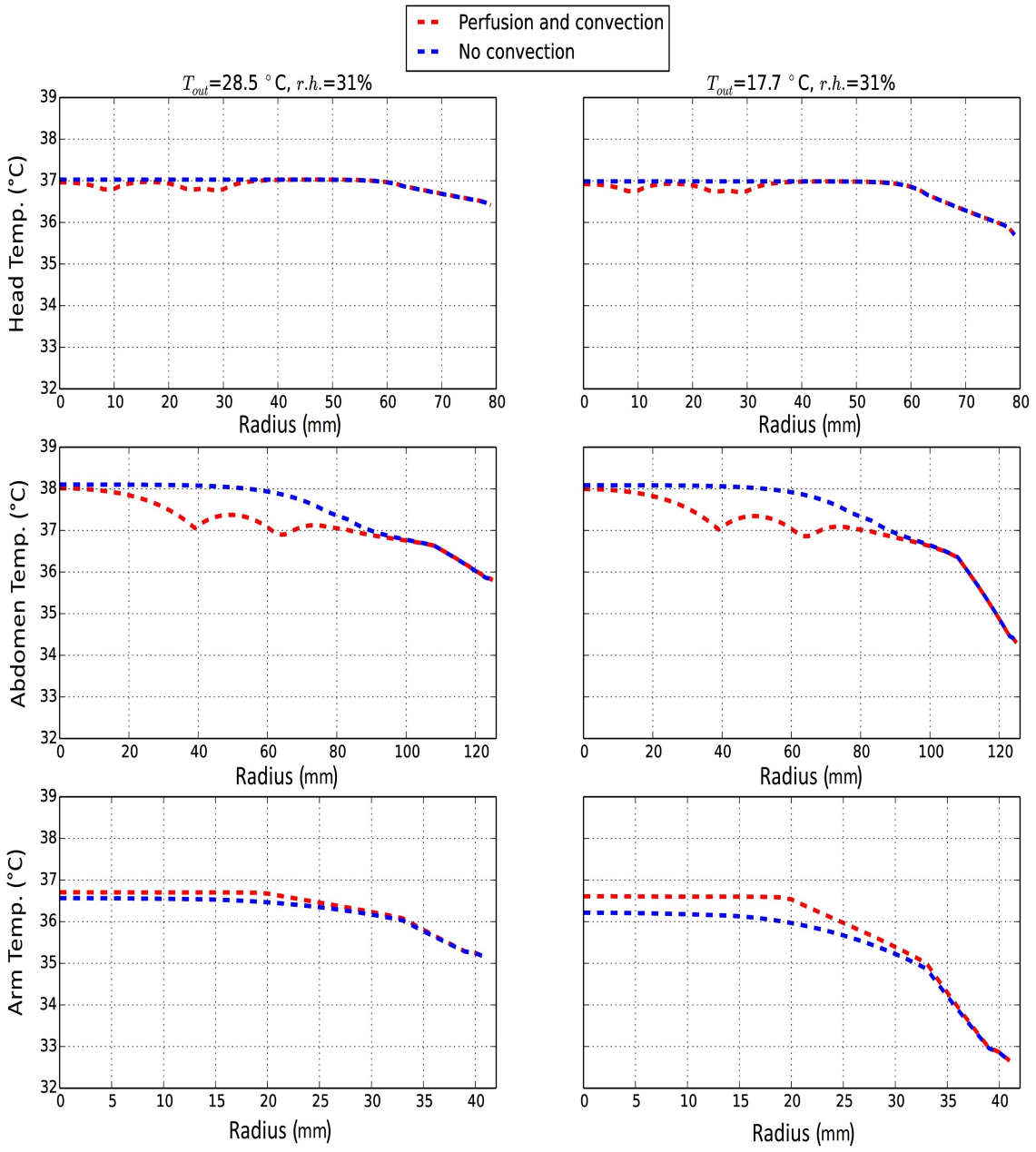

Figure 5.14: Tissue temperatures for two different modelling approaches at t=33.0 *min* (from [5]).

Influence of thermo-regulation

It is often difficult to evaluate the effect of thermo-regulation as this is highly coupled with different external parameters. Thus, in this section an example is provided to demonstrate the

effect of thermo-regulation when the body is subjected to cold exposure. To achieve this, we consider also a case in which all control mechanisms (shivering, cutaneous vasomotion and sweating) are shut down. All other parameters are assumed to be the same as in the previous subsections.

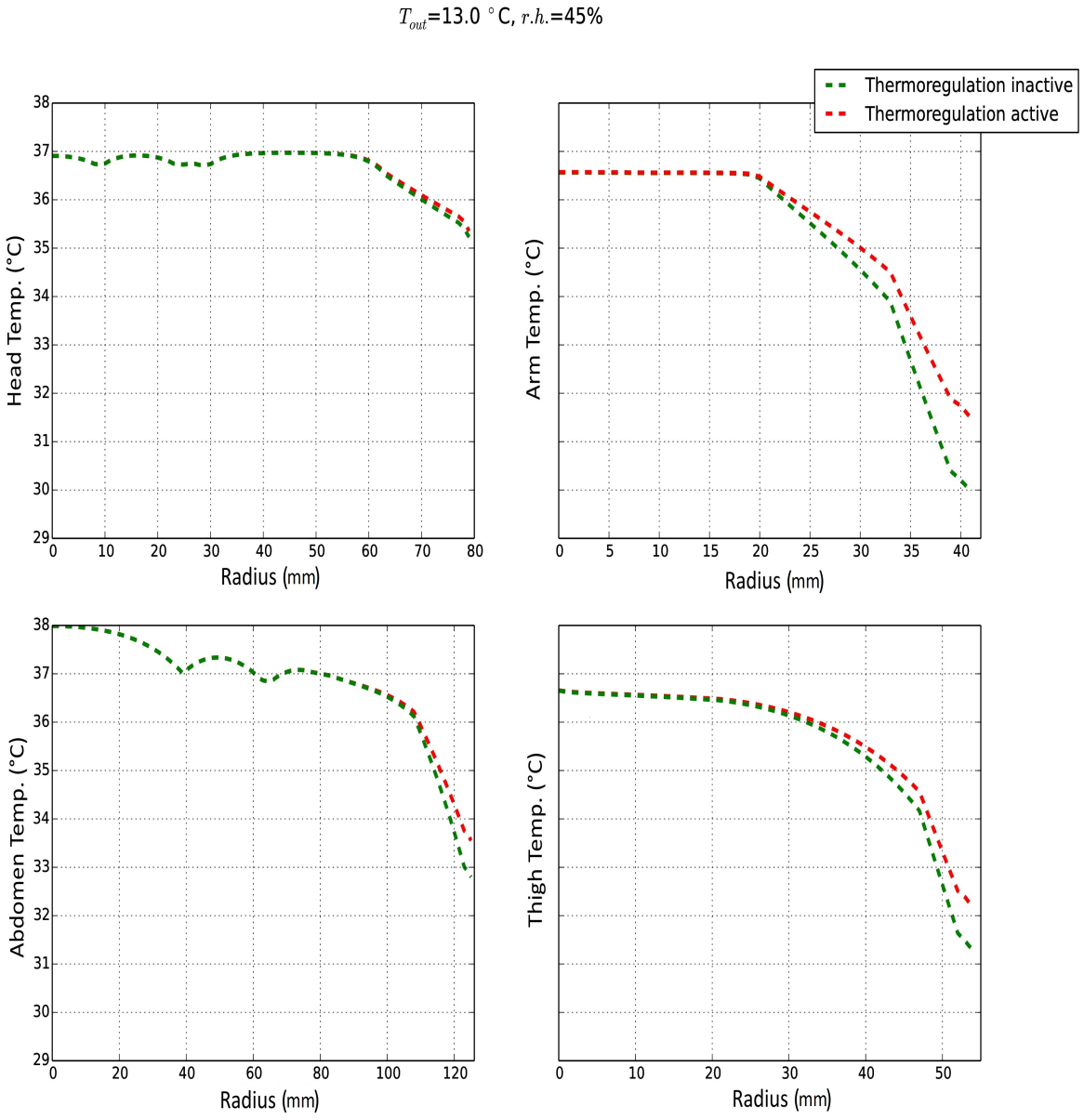

Figure 5.15: Thermo-regulation effects (active/inactive) on tissue temperatures at t=33.0 *min* (from [5]).

Figure 5.15 highlights the influence of the thermo-regulatory system in all four regions considered. While the core temperature remains approximately the same, the temperature at the periphery has dropped without thermo-regulation. Most consistent temperature variations occur in the peripheral body cylinders (arm and thigh). The reduction after 33.0 *min* is as high as 1^{o}C. The shivering effect is not included as the core temperature needed to trigger shivering has not been reached. For a longer time or more extreme external conditions, such profiles could change significantly.

5.6 Concluding remarks

A novel computational framework able to predict the energy transport within the human body has been developed and tested. The systemic circulation embedded human body model is more comprehensive than existing models. Further improvements are nevertheless possible by including more generations of arteries and veins. The proposed model in its present form can test various parameters including arterial stiffness, blood pressure, various branching architectures, tissue properties, surrounding conditions and many more. The results produced clearly highlight the effect of arterial heat convection on the surrounding tissues. The heat convection and perfusion enhances the energy exchange between the blood and surrounding tissues. As expected surrounding temperature-changes significantly affect the skin temperature; however, the control system limits the rapid variation of temperature whenever external conditions are far from a thermally neutral equilibrium.

There are numerous potential applications of the proposed model, such as better understanding of hyperthermia/hypothermia and the detailed study of resulting temperature transport and distribution. Furthermore, the proposed model can study the influence of disease conditions such as hypertension and arterial dysfunction and even ageing on energy exchange. The model can also be used to evaluate the effects of changing environments as a condition for enhanced quality of life.

Chapter 6

Global discussion

A summary of the results presented in the previous chapters is provided along with further and general conclusions. Potential future studies for the continuation of the present work are also proposed and discussed.

6.1 Results summary

The work presented in this thesis provides a number of key steps towards the integration of arterial wall mechanics and cellular signalling into a virtual arterial framework, able to test hypotheses on the origins of vascular disease and assist with the design of novel pharmacological and bio-mechanical probes. An important component of this modelling approach is the evaluation of the combined response due to the mechano-elastic properties of the vasculature with the active contractile response of the smooth muscle layer of the arterial wall, as presented in Chapter 3. The numerical methodology proposed combines dynamics and mechanics occurring at different scales, either under mechanical load or pharmacological stimuli, incorporating specific numerical solution strategies for each component. A number of specific outcomes are highlighted here. We were able to demonstrate the role of cell-cell communication (described by diffusion coefficients α_V and α_C) in emergent large scale synchronisation within the arterial wall. These findings highlighted the role of Ca^{2+} concentration distribution along the network, with the formation of localised contractile responses evolving into travelling waves for low and high coupling scenarios, respectively. Specific pharmacological probes (i.e., phenylephrine, CPA, ryanodine) able to either stimulate or inhibit smooth muscle contractile activity, were employed to evaluate the performance of the numerical framework. The combined passive (structural) response and active contractile response of SMC tissue accurately reproduced the distinct effects associated with the administration of the three pharmacological interventions. The role of the endothelium has not been accounted by the present methodology and will form a future addition to the model. To overcome this simplifying assumption, all experiments were performed in the presence of L-NAME which suppressed the NO endothelium production. In this study all experimental data were obtained from arterial samples maintained under isometric conditions. This allowed us to deal with a

simplified system where the inertia force is null, and the estimation of material parameters, such as densities of media and adventitia, was not necessary. In addition, any issue related to the time stability was also avoided. For the current study, several arterial ring experiments under isometric conditions have been carried out, each involving four rings ≈ 2 mm in length excised from the same animal. In spite of efforts to maintain identical conditions, variability was present, particularly between individual animals. With respect to the four arterial rings from the same arterial sample (e.g., Figure 3.9), experimental and biological variability that could not be eliminated was due to differences in length, diameter (all rings were from adjacent sections, but there is, inevitably, a reduction in diameter as you descend the vessel), and purely initial condition considerations, such as Ca^{2+} and ionic uptake levels, which have been shown both theoretically and experimentally to greatly affect the oscillatory response of the arterial wall [7, 56, 179]. Due to these factors, each arterial ring is at a different initial contractile state, reflected in variable unloaded geometry.

A novel, dual time step Fluid Structure Interaction framework is proposed in Chapter 4. This includes an extensive validation with several benchmark cases in order to test each subsystem. For the first time a quantitative comparison on the efficiency between standard and AC based CBS algorithms is carried out, showing, for the latter method, significant computational time savings on the problem analysed. Implementation of the proposed methodology demonstrated that it is possible to employ dual time stepping within the solution procedure. We need to note that the computational efficiency was not compared against any other segregated approaches employing a different fluid solver. Moreover, the methodology was not tested for any problem characterised by added mass effect. Importantly the use of a matrix free method for the fluid solver allows significant RAM memory savings, becoming an ideal candidate for large size problems.

Methodology for the incorporation of a one-dimensional vessels network into a solid tissue model is presented in Chapter 5. Firstly the model valid for a single 1-D elastic vessel surrounded by tissue is formulated. This formulation is subsequently extended to a realistic human body model. By contrast to the existing pure conduction/perfusion based models,

the present methodology couples the arterial fluid dynamics of a human body with a multi-segmental bio-heat model of surrounding solid tissues. More than a dozen segments are employed to represent the heat conduction in the surrounding tissues and each segment is constituted by a multi-layered circular cylinder. Multi-layers allow flexible delineation of the geometry and incorporation of properties of different tissue types. The global passive system is conjugated to the thermo-regulatory system, which is assumed to be underpinned by shivering, sweating, and perfusion changes. The extended framework allows for computation of the transport of a scalar field (i.e. the fluid temperature) along the arterial blood stream. The blood input was diffused within the tissues by coupling at the interfaces of the fluid and solid subsystems. Important features like fluid pulsatility and regulatory mechanisms were also accounted for. Initially we performed a sensitivity analysis on the vessel properties and parameters affecting the heat transfer between fluid and surrounding tissues. This analysis showed that vessel elasticity can affect the energy transfer due to changes in the contact time between the fluid and wall. For a tube of greater elasticity we obtained higher velocity and thus a smaller cooling effect (when the fluid is warmer than the surrounding tissues). On the other hand, by increasing the reflection coefficient at the vessel extremity, the fluid alternates direction promoting thermal exchange. Heat transfer was then simulated within the whole human body for different internal (i.e., internal convection thermo-regulation active/inactive) and external conditions. We proposed different cases for validating the methodology including cold and hot stress exposures. Blood temperature was monitored along the tree, as well as tissue temperature distribution along the radial section. The global body thermal response was evaluated by means of indicators, such as core and average skin temperatures. In spite of the model parameter uncertainty, the predicted results agreed with the experimental observations. Computational results show that the convection introduces pulsatility to the temperature distribution within the solid tissues in the vicinity of the arteries. This finding suggests that the inner convection has a more predominant role in the human body heat balance than previously believed.

6.2 Potential future work

The methodology developed embodies a number of crucial steps towards the development of a comprehensive computational platform for the in silico testing of mechanistic theories on the pathophysiology and progression of vascular and cardiac disease. At the fundamental level, this approach has incorporated intra- and inter-cellular signalling within the smooth muscle layer of the arterial wall. Upscaling allowed us to quantify the global manifestation of cellular processes in the arterial wall contractile response. At this fundamental level, a more comprehensive approach will require to account for the regulatory action of the endothelial layer, which plays a key role as the interface between blood flow and contractile media layer. The precise way in which the endothelium regulates the contractile apparatus of arterial smooth muscle by releasing a number of chemical agents is still not completely understood and needs further experimental and computational investigation. Coupling of the smooth muscle and endothelial layers, operating as distinct entities will require a multi-physics interface approach. Further integration of a comprehensive vascular wall model with a robust and computationally efficient Fluid Structure Interaction framework would allow us to quantify the effect of the muscle contractility on the vessel lumen. A fully responsive virtual artery incorporating blood flow will thus become feasible. This inclusive system would allow the detailed study of the effects of vascular disease on peripheral tissue perfusion and oxygenation. Generalisation of such a broad scheme to realistic branching architectures, would inevitably be very expensive computationally. A way to significantly reduce the computational effort, would be to couple the current multidimensional model, valid for any specific arterial region of interest, with a reduced order model representing an extended and comprehensive arterial network. With such a multiscale approach the computed results of the 1D model would be used as boundary conditions for a detailed domain analysis by the 3-D model. This strategy would maintain a sufficient degree of accuracy and, at the same time, will not be limited by computational efficiency issues. As an integrated framework the proposed modelling methodology has important potential healthcare applications. From a heuristic point of view, it can be employed as a testing

ground for the evolution of vascular disease, such as observed in diabetes and ageing. From a functional point of view, it can be employed to predict the transport of pharmacological compounds along the full arterial network, accounting for elastic, muscular-contractile and peripheral resistance vessels. Similarly it can be used to evaluate oxygen and nutrient transport to organs/specific tissues for healthy and diseased contractile response states. Additionally it can help to elucidate fundamental physiological concepts such as the precise role of arterial vasomotion in the optimisation of blood transport.

Bibliography

[1] K. Low, R. van Loon, I. Sazonov, R. L. T. Bevan, and P. Nithiarasu. An improved baseline model for a human arterial network to study the impact of aneurysms on pressure-flow waveforms. *International Journal for Numerical Methods in Biomedical Engineering*, 28:1224–1246, 2012.

[2] A. Coccarelli, D.H. Edwards, A. Aggarwal, P. Nithiarasu, and D. Parthimos. A multiscale active structural model of the arterial wall accounting for smooth muscle dynamics. *Journal of the Royal Society Interface*, 15(http://dx.doi.org/10.1098/rsif.2017.0732):20170732, 2018.

[3] E.A. de Souza Neto, D. Peric, G.C. Huang, and D.R.J. Owen. Remarks on the stability of enhanced strain elements in finite elasticity and plasticity. In D.R.J. Owen and E. Oñate, editors, *Computational Plasticity IV: Fundamentals and Applications*, pages 361–372. Pineridge Press, 1995.

[4] A. Coccarelli and P. Nithiarasu. A robust finite element modelling approach to conjugate heat transfer in flexible elastic tubes and tube networks. *Numerical Heat Transfer, Part A Applications*, 67:513–530, 2015.

[5] A. Coccarelli, E. Boileau, D. Parthimos, and P. Nithiarasu. An advanced computational bioheat transfer model for a human body with an embedded systemic circulation. *Biomechanics and Modeling in Mechanobiology*, 15(5)(DOI: 10.1007/s10237-015-0751-4):1173–1190, 2016.

[6] Boileau E., George C. H., Parthimos D., Mitchell A. N., Aziz S., and Nithiarasu P. Synergy between intercellular communication and intracellular Ca2+ handling in arrhythmogenesis. *Ann Biomed Eng*, 43(10.1007/s10439-014-1243-x):1614–1625, 2015.

[7] Parthimos D., Edwards D. H., and Griffith T. M. Minimal model of arterial chaos generated by coupled intracellular and membrane Ca2+ oscillators. *Am. J. Physiol*, 277:H1119–44, 1999.

[8] Murtada S.-I. and Holzapfel G. A. Investigating the role of smooth muscle cells in large elastic arteries: a finite element analysis. *J Theor Biol*, 358:1–10, 2014.

[9] R. Holopainen. *A human thermal model for improved thermal comfort*. PhD thesis, VTT, Technical Research Centre of Finland, 2012.

[10] Wetterer E., Bauer R. D., and Russe R. Arterial dynamics. *Cardiovascular and Pulmonary Dynamics*, 71:17–42, 1977. Euromech 92.

[11] Fung Y.C., editor. *Biomechanics: Circulation, (chap 4.9, pag 247)*. Springer-Verlag New York Inc., 2 edition, 1997.

[12] Caro C. G., Pedley T. J., Schroter R. C., Seed W. A., and Parker K. H. *The Mechanics of the Circulation*. CUP, second edition, 2012.

[13] Clifford P. S., Ella S. R., Stupica A. J., Nourian Z., Li M., Martinez-Lemus L. A., Dora K. A., Yang Y., Davis M. J., Pohl U., Meininger G. A., and Hill M. A. Small artery elastin distribution and architecture-focus on three dimensional organization. *Arterioscler. Thromb. Vasc. Biol.*, 31(12):2889–96, 2011.

[14] Hill M. A., Nourian Z., Ho I. L., Clifford P. S., Martinez-Lemus L., and Meininger G. A. Small artery elastin distribution and architecture-focus on three dimensional organization. *Microcirculation*, 23(8):614–620, 2016.

[15] Cox R. H. Regional variation of series elasticity in canine arterial smooth muscles. *Am. J. Physiol.*, 234:H542–H551, 1978.

[16] C. A. Taylor and J. D. Humphrey. Open problems in computational vascular biomechanics: Hemodynamics and arterial wall mechanics. *Computer Methods in Applied Mechanics and Engineering*, 198 (45-46):3514–3523, 2009.

[17] O. M. Costello and K. Fronek. Morphometry of the amount of smooth muscle cells in the media of various rabbit arteries. *Journal of Ultrastructure Research*, 91:1–12, 1985.

[18] John K.-J. Li. *Dynamics of the Vascular System*. World Scientific, first edition, 2004. Series on Bioengineering and Biomedical Engineering: Volume 1.

[19] Holzapfel G. A., Gasser T. C., and Ogden R. W. A new constitutive framework for arterial wall mechanics and a comparative study of material models. *Journal of Elasticity*, 61:1–48, 2000.

[20] Roach M. R. and Burton A. C. The reason for the shape of distensibility curve of arteries. *Canadian journal of biochemistry and physiology*, 35(8):681–690, 1957.

[21] Fung Y.C., editor. *Biomechanics: Mechanical properties of living tissues*. Springer-Verlag New York Inc., 1 edition, 1981.

[22] Pries A. R., Mulvany M. J., and Bakker E. N. T. P. Mbec special issue on microcirculation "engineering principles of vascular networks". *Med. Biol. Eng. Comput.*, 46:407–409, 2008.

[23] P. Segers, E. R. Rietzschel, M. L. De Buyzere, S. J. Vermeersch, D. De Bacquer, L. M. Van Bortel, and et al. Noninvasive (input) impedance, pulse wave velocity, and wave reflection in healthy middle-aged men and women. *Hypertension*, 49:1248–55, 2007.

[24] Meininger G. A. and Davis M. J. Cellular mechanisms involved in the vascular myogenic response. *Am. J. Physiol.*, 263(3 Pt 2):H647–59, 1992.

[25] Speden R. N. and Warren D. M. Myogenic adaptation of rabbit ear arteries to pulsatile internal pressures. *J. Physiol.*, 391:313–23, 1987.

[26] Griffith T. M., Edwards D. H., Davies R. L., Harrison T. J., and Evans K. T. Edrf coordinates the behaviour of vascular resistance vessels. *Nature*, 329:442–445, 1987.

[27] Achakri H., Rachev A., Stergiopulos N., and Meister J.-J. A theoretical investigation of low frequency diameter oscillations of muscular arteries. *Ann. Biomed. Eng.*, 22:253–263, 1994.

[28] Ursino M. and Fabbri G. Role of the myogenic mechanism in the genesis of microvascular oscillations (vasomotion): analysis with a mathematical model. *Microvasc. Res.*, 43:156–177, 1992.

[29] Stergiopulos N., Porret C. A., de Brouwer S., and Meister J. J. Arterial vasomotion: effect of flow and evidence of nonlinear dynamics. *Am. J. Physiol. (Heart Circ. Physiol. 43)*, 274:1858–1864, 1998.

[30] Funk W. and Intaglietta M. Spontaneous arteriolar vasomotion. *Prog. Appl. Microcirc.*, 3:66–82, 1983.

[31] Intaglietta M. Arteriolar vasomotion: implications for tissue ischemia. *Blood Vessels*, 28:1–7, 1991.

[32] Porret C. A., Stergiopulos N., Hayoz D., Brunner H. R., and Meister J. J. Simultaneous ipsilateral and contralateral measurements of vasomotion in conduit arteries of human upper limbs. *Am. J. Physiol.*, 269 (Heart Circ. Physiol. 38):H1852–H1858, 1995.

[33] Ross G., Stinson E., Schroeder J., and Ginsburg R. Spontaneous phasic activity of isolated human coronary arteries. *Cardiovasc. Res.*, 14:613–618, 1980.

[34] Intaglietta M. Vasomotor activity, time-dependent fluid exchange and tissue pressure. *Microvasc. Res.*, 21:153–164, 1981.

[35] Secomb T. W, Intaglietta M., and Gross J. F. Effects of vasomotion on microcirculatory mass transport. *Prog. Appl. Microcirc.*, 15:49–61, 1989.

[36] Tardy Y., Meister J. J., Perret F., Brunner H. R., and Arditi M. Non-invasive estimate of the mechanical properties of peripheral arteries from ultrasonic and photoplethysmographic measurements. *Clin. Phys. Physiol. Meas.*, 12:39–54, 1991.

[37] Nilsson H. and Aalkjaer C. Vasomotion: mechanisms and physiological importance. *Mol. Interv.*, 3:79–89, 2003.

[38] Achakri H., Stergiopulos N., Hoogerwerf N., Hayoz D., Brunner H. R., and Meister J. J. Intraluminal pressure modulates the magnitude and the frequency of induced vasomotion in rat arteries. *J. Vasc. Res.*, 32:237–246, 1995.

[39] T. M. Griffith and Edwards D. H. Modulation of chaotic pressure oscillations in isolated resistance arteries by edrf. *Eur. Heart J.*, 14, Suppl. I:60–67, 1993.

[40] Osol G. and Halpern W. Spontaneous vasomotion in pressurized cerebral arteries from genetically hypertensive rats. *Am. J. Physiol*, 254 (Heart Circ. Physiol. 23):H28–H33, 1988.

[41] Gonzalez-Fernandez J. M. and Ermentrout B. On the origin of the vasomotion of small arteries. *Math. Biosci.*, 119:127–167, 1994.

[42] Griffith T. M. Chaos and fractals in vascular biology. *Vasc. Med. Rev.*, 5:161–182, 1994.

[43] Mulvany M. J. Functional characteristics of vascular smooth muscle. *Prog. Appl. Microcirc.*, 3:4–18, 1983.

[44] Fung Y. C., Fronek K., and Patitucci P. Pseudoelasticity of arteries and the choice of its mathematical expression. *Am. J. Physiol. Heart Circ. Physiol.*, 237(5):H620–631, 1979.

[45] Takamizawa K. and Hayashi K. Strain energy density function and uniform strain hypothesis for arterial mechanics. *Journal of Biomechanics*, 20(1):7–17, 1987.

[46] Holzapfel G. A. and Weizsäcker H. W. Biomechanical behavior of the arterial wall and its numerical characterization. *Computers in Biology and Medicine*, 28(4):377–392, 1998.

[47] Zulliger M. A., Rachev A., and Stergiopulos N. A constitutive formulation of arterial mechanics including vascular smooth muscle tone. *Am J Physiol Heart Circ Physiol*, 287:1335–1344, 2004.

[48] G. A. Holzapfel, T. C. Gasser, and M. Stadler. A structural model for the viscoelastic behavior of arterial walls: Continuum formulation and finite element analysis. *European Journal of Mechanics A-Solids*, 21 (3):441–463, 2002.

[49] Gasser T. C. and Holzapfel G. A. A rate-independent elastoplastic constitutive model for biological fiber-reinforced composites at finite strains: continuum basis, algorithmic formulation and finite element implementation. *Computational Mechanics*, 29:340–360, 2002.

[50] Gasser T. C., Ogden R. Y., and Holzapfel G. A. Hyperelastic modelling of arterial layers with distributed collagen fibre orientations. *J. R. Soc. Interface*, 3:15–35, 2006.

[51] Rachev A. and Hayashi K. Theoretical study of the effects of vascular smooth muscle contraction on strain and stress distributions in arteries. *Annals of Biomedical Engineering*, 27(4):459–468, 1999.

[52] Stålhand J., Klarbring A., and Holzapfel G. A. Smooth muscle contraction: Mechanochemical formulation for homogeneous finite strains. *Progress in Biophysics and Molecular Biology*, 96:465–81, 2008.

[53] Murtada S.-I., Kroon M., and Holzapfel G. A. A calcium-driven mechanochemical model for prediction of force generation in smooth muscle. *Biomech Model Mechanobiol*, 9:749–762, 2010.

[54] Schmitz A. and Böl M. On a phenomenological model for active smooth muscle contraction. *J. Biomech.*, 44(11):2090–5, 2011.

[55] Murtada S.-I., Arner A., and Holzapfel G. A. Experiments and mechanochemical modeling of smooth muscle contraction: Significance of filament overlap. *J Theor Biol*, 297:176–186, 2012.

[56] Parthimos D., Haddock R. E., Hill C. E., and Griffith T. M. Dynamics of a three-variable nonlinear model of vasomotion: comparison of theory and experiments. *Biophys. J.*, 93:1534–1556, 2007.

[57] George C. H., Parthimos D., and Silvester N. C. A network-oriented perspective on cardiac calcium signaling. *Am. J. Physiol. Cell. Physiol.*, 303:897–910, 2012.

[58] Boileau E., Parthimos D., and Nithiarasu P. An extended computational framework to study arterial vasomotion and its links to vascular disease. In *Lecture Note in Applied and Computational Mechanics*. Springer, 2014.

[59] Vito R. P. and Dixon S. A. Blood vessel constitutive models. *Annual Review of Biomedical Engineering-1995-2002*, 5(1):413–439, 2003.

[60] Holzapfel G. A. and Ogden R. W. Constitutive modelling of arteries. *Proc. R. Soc. Lond.*, A 466:1551–1597, 2010.

[61] Ursino M. Interaction between carotid baroregulation and the pulsating heart: a mathematical model. *Am. J. Heart Circ. Physiol.*, 275:H1733–H1747, 1998.

[62] M.S. Olufsen, C.S. Peskin, W.Y. Kim, E.M. Pedersen, A. Nadim, and J. Larsen. Numerical simulation and experimental validation of blood flow in arteries with structured-tree outflow conditions. *Annals of Biomedical Engineering*, 28:1281–1299, 2000.

[63] L. Formaggia, D. Lamponi, and A. Quarteroni. One-dimensional models for blood flow in arteries. *Journal of Engineering Mathematics*, 47:251–276, 2003.

[64] J.P. Mynard and P. Nithiarasu. A 1D arterial blood flow model incorporating ventricular pressure, aortic valve and regional coronary flow using locally conservative Galerkin (LCG) method. *Communications in Numerical Methods in Engineering*, 24:367–417, 2008.

[65] Reymond P., Merenda F., Perren F., Rufenacht D., and Stergiopulos N. Validation of a one-dimensional model of the systemic arterial tree. *American Journal of Physiology Heart and Circulatory Physiology*, 297:H208–H222, 2009.

[66] J. P. Mynard and J. J. Smolich. One-dimensional haemodynamic modeling and wave dynamics in the entire adult circulation. *Ann Biomed Eng*, 43 (6)(DOI: 10.1007/s10439-015-1313-8):1443–60, 2015.

[67] H. M. Hasan, A. Coccarelli, and P. Nithiarasu. Novel semi-implicit, locally conservative galerkin (silcg) methods: Application to blood flow in a systemic circulation. *Computer Methods in Applied Mechanics and Engineering*, 332:217–233, 2018.

[68] Taylor C. A., Hughes T. J. R., and Zarins C.K. Finite element modeling of blood flow in arteries. *Computer Methods in Applied Mechanics and Engineering*, 158(1-2):155–196, 1998.

[69] X. Y. Xu, Long Q., Collins M. W., Bourne M., and Griffith T. M. Reconstruction of blood flow patterns in human arteries. *Proc Inst Mech Eng H, Journal of Engineering in Medicine*, 213(5):411–421, 1999.

[70] A. Quarteroni, M. Tuveri, and A. Veneziani. Computational vascular fluid dynamics: problems, models and methods. *Computing and Visualization in Science*, 2(4):163–197, 2000.

[71] Figueroa C. A., Vignon-Clementel I. E., Jansen K. E., Hughes T. J. R., and Taylor C. A. A coupled momentum method for modeling blood flow in three-dimensional deformable arteries. *Computer Methods in Applied Mechanics and Engineering*, 195(DOI:10.1016/j.cma.2005.11.011):5685–5706, 2006.

[72] Alastruey J., Xiao N., For H., Schaeffter T., and Figueroa C. A. On the impact of modelling assumptions in multi-scale, subject-specific models of aortic haemodynamics. *J. R. Soc. Interface*, 13, 2016.

[73] A. Quarteroni, A. Veneziani, and C. Vergara. Geometric multiscale modeling of the cardiovascular system, between theory and practice. *cmame*, 302:193–252, 2016.

[74] Dettmer W. and Perić D. A computational framework for fluid-structure interaction: Finite element formulation and applications. *Computer Methods in Applied Mechanics and Engineering*, 195:5754–5779, 2006.

[75] Heil M, Hazel AL., and Boyle J. Solvers for large-displacement fluid-structure interaction problems: Segregated versus monolithic approaches. *Computational Mechanics*, 43:91–101, 2008.

[76] Küttler U., Förster Ch. Gee M., Comerford A., and Wall WA. Coupling strategies for biomedical fluid-structure interaction problems. *International Journal for Numerical Methods in Biomedical Engineering*, 26:305–321, 2010.

[77] C. Kadapa, W. G. Dettmer, and D. Perîc. A fictitious domain/distributed lagrange multiplier based fluid-structure interaction scheme with hierarchical b-spline grids. *Computer Methods in Applied Mechanics and Engineering*, 301:1–27, 2016.

[78] G. Guidoboni, R. Glowinski, N. Cavallini, and S. Canic. Stable loosely-coupled-type algorithm for fluid-structure interaction in blood flow. *Journal of Computational Physics*, 228:6916–6937, 2009.

[79] E. Burman and M. A. Fernández. Stabilization of explicit coupling in fluid-structure interaction involving fluid incompressibility. *Computer Methods in Applied Mechanics and Engineering*, 198:766–784, 2009.

[80] Dettmer W. and Perić D. A new staggered scheme for fluid-structure interaction. *International Journal for Numerical Methods in Engineering*, 93:1–22, 2013.

[81] A.E.J. Bogaers. *Efficient and robust partitioned schemes for fluid-structure interactions*. PhD thesis, The University of Cape Town, Cape Town, South Africa, 2015.

[82] Causin P., Gerbeau JF, and Nobile F. Added-mass effect in the design of partitioned algorithms for fluid-structure problems. *Computer Methods in Applied Mechanics and Engineering*, 194:4506–4527, 2005.

[83] Küttler U., Förster C., and Wall W. A. A solution for the incompressibility dilemma in partitioned fluid-structure interaction with pure dirichlet fluid domains. *Comput. Mech.*, 38:417–429, 2006.

[84] C. Förster, W. A. Wall, and E. Ramm. Artificial added mass instabilities in sequential staggered coupling of nonlinear structures and incompressible viscous flows. *Computer Methods in Applied Mechanics and Engineering*, 196:1278–1293, 2007.

[85] Bazilevs Y., Takizawa K., and Tezduyar TE. *Computational Fluid-Structure Interaction Methods and Applications*. Wiley, 2013.

[86] Y. Bazilevs, V.M. Calo, and N.C. Silvester. Isogeometric fluid-structure interaction analysis with applications to arterial blood flow. *Computational Mechanics*, 38:310–322, 2006.

[87] Y. Zhang, Y. Bazilevs, S. Goswamia, C.L. Bajajb, and T.J.R. Hughes. Patient-specific vascular nurbs modeling for isogeometric analysis of blood flow. *Computer Methods in Applied Mechanics and Engineering*, 196(29–30):2943–2959, 2007.

[88] Calo V., Brasher N., Bazilevs Y., and Hughes T. J. R. Multiphysics model for blood flow and drug transport with application to patient-specific coronary artery flow. *Computational Mechanics*, 43(1):161–177, 2008.

[89] L. Formaggia, J.F. Gerbeau, F. Nobile, and A. Quarteroni. On the coupling of 3D and 1D Navier-Stokes equations for flow problems in compliant vessels. *Computer Methods in Applied Mechanics and Engineering*, 191(6-7):561–582, 2001.

[90] P.B. Wells, S. Thomsen, M.A. Jones, S. Baek, and J.D. Humphrey. Histological evidence for the role of mechanical stress in modulating thermal denaturation of collagen. *Biomechanics and Modeling in Mechanobiology*, 4:201–210, 2005.

[91] T.I. Zohdi. Modeling electrical power absorption and thermally-induced biological tissue damage. *Biomechanics and Modeling in Mechanobiology*, 13:115–121, 2014.

[92] L. Zhu, L. Pang, and L.X. Xu. Simultaneous measurements of local tissue temperature and blood perfusion rate in the canine prostate during radio frequency thermal therapy. *Biomechan Model Mechanobiol*, 4:1–9, 2005.

[93] A.P. Gagge, J.A.J. Stolwijk, and J.D. Hardy. Comfort and thermal sensation and associated physiological responses at various ambient temperatures. *Environmental Research*, 1:1–20, 1967.

[94] J.A.J. Stolwijk. A mathematical model of physiological temperature regulation in man. Technical Report NASA CR-1855, National Aeronautics and Space Administration, 1971.

[95] J.A.J. Stolwijk and J.D. Hardy. Partitional calorimetric studies of responses of man to thermal transients. *Journal of Applied Physiology*, 21:967–977, 1966.

[96] J.A.J. Stolwijk. Control of body temperature. In *Handbook of Physiology-Reaction to Environmental Agents*, pages 45–67. 1977.

[97] E.H. Wissler. A mathematical model of the human thermal system. *Bulletin of Mathematical Biophysics*, 62:66–78, 1964.

[98] E.H. Wissler. *Mathematical simulation of human thermal behaviour using whole-body models*. Plenum Press, New York, 1985.

[99] C. Smith. *A transient, Three Dimensional Model of the Human Thermal System*. PhD thesis, Kansas State University, 1991.

[100] D. Fiala. A computer model of human thermoregulation for a wide range of environmental conditions: The passive system. *Journal of Applied Physiology*, 87:1957–1972, 1999.

[101] D. Fiala, K.J. Lomas, and M. Stohrer. Computer prediction of human thermoregulatory and temperature response to a wide range of environmental conditions. *International Journal of Biometeorology*, 45:143–159, 2001.

[102] P.C. Cropper, T. Yang, M.J. Cook, D. Fiala, and R. Yousaf. Exchange of simulation data between cfd programmes and a multisegmented human thermal comfort model. In *Proceedings of Conference: Air Conditioning and the Low Carbon Cooling Challenge*, Cumberland Lodge, Windsor, UK, 27-29, July 2008.

[103] S. Tanabe, K. Kobayashi, J. Nakano, Y. Ozeki, and M. Konishi. Evaluation of thermal comfort using combined multi-node thermoregulation (65mn) and radiation models and computational fluid dynamics (cfd). *Energy and Buildings*, 34:637–646, 2002.

[104] C. Huizenga, Z. Hui, and E. Arens. A model of human physiology and comfort for assessing complex thermal environments. *Building and Environment*, 36:691–699, 2001.

[105] J.P. Rugh, R.B. Farrington, D. Bharathan, A. Vhalinos, R. Burke, C. Huizenga, and H. Zhang. Predicting human thermal comfort in a transient nonuniform thermal environment. *European Journal of Applied Physiology*, 92:721–727, 2004.

[106] M. Salloum, N. Ghaddar, and K. Ghali. A new transient bioheat model of the human body and its integration to clothing model. *International Journal of Thermal Sciences*, 46:371–384, 2007.

[107] W. Karaki, N. Ghaddar, K. Ghali, K. Kalev, I. Holmer, and L.L. Vanguard. Human thermal response with improved ava modeling of the digits. *Int J Therm Sci*, 67:41–52, 2013.

[108] M. Rida, W. Karaki, N. Ghaddar, K. Ghali, and J. Hoballah. A new mathematical model to simulate ava cold-induced vasodilation reaction to local cooling. *Int. J. Biometeorol.*, 58:1905–1918, 2014.

[109] H.A.M. Daanen. Arterio-venous anastomoses and thermoregulation. Report no. izf 1991 b-12, TNO Institute for Perception Group: Thermophysiology, Soesterberg, Netherland, 1991.

[110] V.S. Koscheyev, S. Paul, G.R. Leon, D. Tanchida, T.J. Taylor, and I.V. Koscheyev. Body surface temperature tuning as a comfort support system in space and other extreme environments. In *Proceedings of the 28th International Conference on Environmental Systems, pp. 1e8, SAE Technical Paper Series 981723*, Danvers, MA, 13-16, July 1998.

[111] Vanggaard L., Kuklane K., Holmer I., and Smolander J. Thermal responses to whole-body cooling in air with special reference to arteriovenus anastomoses in fingers. *Clin. Physiol. Funct. Imaging*, 32(6):463–469, 2012.

[112] X. Sun. *Development of an Improved Thermal Model of the Human Body and an Experimental Investigation of Heat Transfer from a Moving Cylinder*. PhD thesis, Kansas State University, 2012.

[113] M.S. Ferreira and J.I. Yanagihara. A transient three-dimensional heat transfer model of the human body. *International Communications in Heat and Mass Transfer*, 36:718–724, 2009.

[114] M.S. Ferreira and J.I. Yanagihara. A heat transfer model of the human upper limbs. *International Communications in Heat and Mass Transfer*, 39:196–203, 2012.

[115] J.W. Mitchell and G.E. Myers. An analytical model of the counter-current heat exchange phenomena. *Biophysical J.*, 8:897–911, 1968.

[116] Vanggaard L. Physiological reactions to wet cold. *Aviat. Space Environ. Med.*, 46(1):33–36, 1975.

[117] O.I. Craciunescu and S.T. Clegg. Pulsatile blood flow effects on temperature distribution and heat transfer in rigid vessels. *Trans. ASME, J. Biomech. Eng.*, 123:500–505, 2001.

[118] M. Bommadevara and L. Zhu. Temperature difference between the body core and arterial blood supplied to the brain during hyperthermia or hypothermia in humans. *Biomechanics and Modeling in Mechanobiology*, 1:137–149, 2002.

[119] H. Ying, L. Hao, and H. Ryutaro. A one-dimensional thermo-fuid model of blood circulation in the human upper limb. *International Journal of Heat and Mass Transfer*, 47:2735–2745, 2004.

[120] O.C. Zienkiewicz, R.L. Taylor, and J.Z. Zhu. *The Finite Element Method: The Basis and Fundamentals*. Elsevier, Oxford, 7th edition, 2013.

[121] T.J.R. Hughes. *The Finite Element Method: Linear Static and Dynamic Analysis*. Dover Publications, New York, 2000.

[122] K.-J. Bathe. *Finite Element Procedures*. Prentice Hall, Englewood Cliffs, N.J., 1996.

[123] O.C. Zienkiewicz and R.L. Taylor. *The Finite Element Method: Solid Mechanics*, volume 2. Butterworth-Heinemann, Oxford, 5th edition, 2000.

[124] J. Bonet and R.D. Wood. *Nonlinear Continuum Mechanics for Finite Element Analysis*. Cambridge University Press, Cambridge, 1997. ISBN 0-521-57272-X.

[125] Newmark N. M. A method of computation for structural dynamics. *J. Engineering Mechanics, ASCE*, 85:67–94, 1959.

[126] Quarteroni A., Saleri F., and Gervasio P. *Scientific Computing with MATLAB and Octave*. Springer-Verlag, fourth edition, 2014.

[127] Buus N. H., VanBavel E., and Mulvany M. J. Differences in sensitivity of rat mesenteric small arteries to agonists when studied as ring preparations or as cannulated preparations. *Br. J. Pharmacol.*, 112:579–87, 1994.

[128] Griffith T. M. and Edwards D. H. Edrf suppresses chaotic pressure oscillations in isolated resistance artery without influencing intrinsic complexity. *Am. J. Physiol.*, 266 (Heart Circ. Physiol.):H1786–H1800, 1994.

[129] Rezakhaniha R., Fonck E., Genoud C., and Stergiopulos N. Role of elastin anisotropy in structural strain energy functions of arterial tissue. *Biomech. Model. Mechanobiol.*, 10(4):599–611, 2011.

[130] Bers D. Cardiac excitation-contraction coupling. *Nature*, 415:198–205, 2002.

[131] Efremov R. G., Leitner A., Aebersold R., and Raunser S. Architecture and conformational switch mechanism of the ryanodine receptor. *Nature*, 517:39–43, 2015.

[132] Peng W., Shen H., Wu J., Guo W., Pan X., Wang R., Chen S. R., and Yan N. Structural basis for the gating mechanism of the type 2 ryanodine receptor ryr2. *Science*, 354:aah5324, 2016.

[133] Valentin A., Cardamone L., Baek S., and Humphrey J. D. Complementary vasoactivity and matrixremodelling in arterial adaptations to altered flow and pressure. *J. R. Soc. Interface*, 6(32):293–306, 2009.

[134] Weisbecker H., Unterberger M. J., and Holzapfel G. A. Constitutive modelling of arteries considering fibre recruitment and three-dimensional fibre distribution. *J. R. Soc. Interface*, 12:1–11, 2015.

[135] Bellini C., Ferruzzi J., Roccabianca S., Di Martino E. S., and Humphrey J. D. A microstructurally motivated model of arterial wall mechanics with mechanobiological implications. *Ann. Biomed. Eng.*, 42(3):488–502, 2014.

[136] Stålhand J., McMeeking R. M., and Holzapfel G. A. A microstructurally motivated model of arterial wall mechanics with mechanobiological implications. *Journal of the Mechanics and Physics of Solids*, 94:490–503, 2016.

[137] Holzapfel G. A., Sommer G., Gasser C. T., and Regitnig P. Determination of layer-specific mechanical properties of human coronary arteries with nonatherosclerotic intimal thickening and related constitutive modeling. *Am. J. Physiol. Heart Circ. Physiol.*, 289:2048–2058, 2005.

[138] Sommer G. and Holzapfel G. A. 3d constitutive modeling of the biaxial mechanical response of intact and layer-dissected human carotid arteries. *Journal of the Mechanical Behavior of Biomedical Materials*, 5:116–128, 2012.

[139] Fischer S. A. Vascular smooth muscle phenotypic diversity and function. *Physiol. Genomics.*, 42A(3):169–187, 2010.

[140] Hai C. M. and Murphy R. A. Cross-bridge phosphorylation and regulation of latch state in smooth muscle. *J. Appl. Physiol.*, 254:C99–C106, 1988.

[141] Hai C. M. and Murphy R. A. Regulation of shortening velocity by cross-bridge phosphorylation in smooth muscle. *Am. J. Physiol.*, 255:C86–C94, 1988.

[142] Berman R. S. and Griffith T. M. Spatial heterogeneity in the mechanisms contributing to acetylcholine-induced dilatation in the rabbit isolated ear. *British Journal of Pharmacology*, 124:1245–1253, 1998.

[143] Lee C.-H., Poburko D., Sahota P., Sandhu J., Ruehlmann D. O., and van Breemen C. The mechanism of phenylephrine-mediated [Ca2+] oscillations underlying tonic contraction in the rabbit inferior vena cava. *J. Physiol.*, 534(Pt 3):641–650, 2001.

[144] De Brouwer S., Edwards D. H., and Griffith T. M. Simplification of the quasiperiodic route to chaos in agonist-induced vasomotion by iterative circle maps. *Am. J. Physiol.(Heart Circ. Physiol. 43)*, 274:1315–1326, 1998.

[145] Griffith T. M. Temporal chaos in the microcirculation. *Cardiovasc. Res.*, 31:342–358, 1996.

[146] Shaw L., O'Neill S., Jonesc C. J., Austin C., and Taggart M. J. Comparison of u46619-, endothelin-1- or phenylephrine-induced changes in cellular Ca2+ profiles and Ca2+ sensitisation of constriction of pressurised rat resistance arteries. *Br. J. Pharmacol*, 141:678–688, 2004.

[147] Griffith T. M., Parthimos D., and Edwards D. H. Non-linear analysis and modelling of the cellular mechanisms that regulate arterial vasomotion. *N. Proc. IMechE*, 220:C:367–383, 2006.

[148] Wu K. D., Bungard D., and Lytton J. Regulation of serca Ca2+ pump expression by cytoplasmic [Ca2+] in vascular smooth muscle cells. *Am. J. Physiol. Cell. Physiol.*, 280:C843–C851, 2001.

[149] H. G. Matthies, R. Niekamp, and J. Steindorf. Algorithms for strong coupling procedures. *Computer Methods in Applied Mechanics and Engineering*, 195:2028–2049, 2007.

[150] M. A. Fernández, J. F. Gerbau, and C. Grandmont. A projection semi-implicit scheme for the coupling of an elastic structure with an incompressible fluid. *International Journal for Numerical Methods in Engineering*, 69:794–821, 2007.

[151] S. Badia, F. Nobile, and C. Vergara. Fluid-structure partitioned procedures based on robin transmission conditions. *Journal of Computational Physics*, 227:7027–7051, 2008.

[152] P. Nithiarasu, R. Codina, and O. C. Zienkiewicz. The Characteristic-Based Split (CBS) scheme - a unified approach to fluid dynamics. *International Journal for Numerical Methods in Engineering*, 66:1514–1546, 2006.

[153] P. Nithiarasu. An efficient artificial compressibility (ac) scheme based on the characteristic based split (cbs) method for incompressible flows. *International Journal for Numerical Methods in Engineering*, 56:1815–1845, 2003.

[154] R. L. T. Bevan and P. Nithiarasu. Accelerating incompressible flow calculations using a quasi-implicit scheme: local and dual time stepping approaches. *Computational Mechanics*, 50(6, SI):687–693, 2012.

[155] Bogaers A. E. J., Kok S., Reddy B. D., and Franz T. Quasi-newton methods for implicit black-box fsi coupling. *Comp. Meth. Appl. Mech. and Engineering*, 279:112–132, 2014.

[156] Küttler U. and Wall WA. Fixed-point fluid-structure interaction solvers with dynamic relaxation. *Computational Mechanics*, 43:61–72, 2008.

[157] Bevan R. L. T. and Nithiarasu P. A dual time stepping approach to eliminate first order error in fractional step methods for incompressible flows. *International Journal of Numerical Methods for Heat & Fluid Flow*, 26:556–570, 2016.

[158] Farhat C., Lesoinne M., and Le Tallec P. Load and motion transfer algorithms for fluid/ structure interaction problems with non-matching discrete interfaces: Momentum and energy conservation, optimal discretization and application to aeroelasticity. *Comp. Meths. Appl. Mech. Engng*, 157:95–114, 1998.

[159] W.A. Wall. *Fluid-Struktur-Interaktion mit stabilisierten Finiten Elementen.* Dissertation, Institut für Baustatik, Universität Stuttgart, Stuttgart, 1999.

[160] Zulliger M. A.and Fridez P., Hayashi K., and Stergiopulos N. A strain energy function for arteries accounting for wall composition and structure. *Journal of Biomechanics*, 37:989–1000, 2004.

[161] E. Boileau, P. Nithiarasu, J.B. Blanco, L.O. Muller, F. E.E. Fossans, L.R. Helleviks, W.P. Doners, W. Huberts, M. Willemet, and J. Alastruey. A benchmark study of 1-d numerical schemes for arterial blood flow modelling. *International Journal for Numerical Methods in Biomedical Engineering*, e02732(DOI: 10.1002/cnm.2732), 2015.

[162] S. J. Sherwin, L. Formaggia, J. Peiró, and V. Franke. Computational modelling of 1D blood flow with variable mechanical properties and its application to the simulation of wave propagation in the human arterial system. *International Journal for Numerical Methods in Fluids*, 43(6-7):673–700, 2003. b.

[163] L. Formaggia, F. Nobile, A. Quarteroni, and A. Veneziani. Multiscale modelling of the circulatory system: a preliminary analysis. *Computing and Visualization in Science*, 2:75–83, 1999.

[164] L. Formaggia, F. Nobile, and A. Quarteroni. A one dimensional model for blood flow: Application to vascular prosthesis. In Babuska I., Miyoshi T., and Ciarlet P.G., editors, *Mathematical Modeling and Numerical Simulation in Continuum Mechanics, Lecture Notes in Computational Science and Engineering*. Springer-Verlag, Berlin, 2002.

[165] Hirsch C. *Numerical computation of internal and external flows: II Computational method for inviscid and viscous flows*. Wiley series in numerical methods in engineering. John Wiley and Sons, Chichester, UK, 1990.

[166] M. Anliker, R.L. Rockwell, and E. Ogden. Nonlinear analysis of flow pulses and shock waves in arteries, part i: Derivation and properties of mathematical model. *Zeitschrift für Angewandte Mathematik und Physik (ZAMP)*, 22(2):217–246, 1971.

[167] H. Pennes. Analysis of tissue and arterial blood temperatures in the resting human forearm. *Journal of applied physiology*, 1:91–122, 1948.

[168] Refrigerating American Society of Heating and Air-Conditioning Engineers. Physiological principles and thermal comfort, 1993.

[169] P.O. Fanger. *Thermal Comfort*. New York: McGraw-Hill, 1970.

[170] D.M. Kerslake. *The Stress of Hot Environments*. Cambridge: University Press, 1972.

[171] Mynard J. P. and Nithiarasu P. A 1D arterial blood flow model incorporating ventricular pressure, aortic valve and regional coronary flow using the locally conservative Galerkin (LCG) method. *Communications in Numerical Methods in Engineering*, 24:367–417, 2008.

[172] P. Nithiarasu. A simple locally conservative galerkin (LCG) finite-element method for transient conservation equations. *Numerical Heat Transfer Part B - Fundamentals*, 46(4):357–370, 2004.

[173] C. G. Thomas and P. Nithiarasu. An element-wise, locally conservative galerkin (lcg) method for solving diffusion and convection-diffusion problems. *International Journal for Numerical Methods in Engineering*, 73:642–664, 2008.

[174] C.K. Charny, S. Weinbaum, and R. L. Levin. An evaluation of the weinbaum-jiji bioheat equation for normal and hyperthermic conditions. *ASME J. Biomech. Eng.*, 112:80–87, 1990.

[175] R. Uflacker. *Atlas of Vascular Anatomy: An Angiographic Approach*. Lippincott Williams & Wilkins, 2006.

[176] A. Shitzer and R.C. Eberhart. *Heat transfer in medicine and biology–analysis and applications*. Plenum Press, New York, USA., 1985.

[177] Y He, H Liu, and R Himeno. A one-dimensional thermo-fluid model of blood circulation in the human upper limb. *International Journal for Heat and Mass Transfer*, 47:2735–2745, 2004.

[178] J.D. Hardy and J.A.J. Stolwijk. Partitional exposures calorimetric studies of man during to thermal transients. *Journal of Applied Physiology*, 21:1799–1806, 1966.

[179] Griffith T. M. and Edwards D. H. Fractal analysis of role of smooth muscle Ca2+ fluxes in genesis of chaotic arterial pressure oscillations. *Am. J. Physiol.*, 266:H1801–H1811, 1994.